

MODEL-ORDER REDUCTION TECHNIQUES FOR THE NUMERICAL SOLUTION OF ELECTROMAGNETIC WAVE SCATTERING PROBLEMS

by

Patrick J Bradley

A dissertation submitted to Dublin City University
for the degree of
Doctor of Philosophy
2009

Research Supervisors:

Dr. Conor Brennan
Dr. Marissa Condon

Declaration

I hereby certify that this material, which I now submit for assessment on the programme of study leading to the award of Doctor of Philosophy, is entirely my own work, that I have exercised reasonable care to ensure that the work is original, and does not to the best of my knowledge breach any law of copyright, and has not been taken from the work of others save and to the extent that such work has been cited and acknowledged within the text of my work.

Signed:

ID No:

Date:

Abstract

It is the aim of this work to contribute to the development of model-order reduction (MOR) techniques for the field of computational electromagnetics in relation to the electric field integral equation (EFIE) formulation. The ultimate goal is to enable a fast-sweep analysis.

In a fast-sweep problem, some parameter on which the original problem depends is varying and the problem must be solved as the parameter changes over a desired parameter range. The complexity of the original model prohibits its direct use in simulation to compute the results at every required point. However, one can use MOR techniques to generate reduced-order models (ROMs), which can be rapidly solved to characterise the parameter-dependent behaviour of the system over the entire parameter range.

This thesis focus is to implement robust, fast and accurate MOR techniques with strict error controls, for application with varying parameters, using the EFIE formulations. While these formulations result in matrices that are significantly smaller relative to differential equation-based formulations, the matrices resulting from discretising integral equations are very dense. Consequently, EFIEs pose a difficult proposition in the generation of low-order accurate reduced-order models.

The MOR techniques presented in this thesis are based on the theory of Krylov projections. They are widely accepted as being the most flexible and computationally efficient approaches in the generation of ROMs. There are three main contributions attributed to this work.

- The formulation of an approximate extension of the Arnoldi algorithm to produce a ROM for an inhomogeneous contrast-sweep and source-sweep analysis.
- Investigation of the application of the Well-Conditioned Asymptotic Waveform Evaluation (WCAWE) technique to problems in which the system matrix has a nonlinear parameter dependence for EFIE formulations.
- The development of a fast full-wave frequency sweep analysis using the WCAWE technique for materials with frequency-dependent dielectric properties.

“Ever tried. Ever failed. No matter. Try again. Fail again. Fail better.”

Samuel Beckett

To my Family

Contents

Declaration	i
Abstract	ii
Contents	v
1 Introduction	1
1.1 Contribution	7
1.2 Notation	8
2 Model-Order Reduction	9
2.1 Mathematical statement of model-order reduction problem	9
2.2 Krylov subspace iteration	10
2.3 Residual minimising methods	13
2.4 Review of Asymptotic Waveform Evaluation via Padé approxi- mation	16
2.4.1 Numerical sensitivity	18
2.5 Galerkin Asymptotic Waveform Evaluation	22
2.6 Linearisation of the nonlinear MOR parameters	25
3 EFIE formulations	27
3.1 Differential form of Maxwell's equations	27
3.2 Time-Harmonic form of Maxwell's equations	29
3.3 Volume equivalence principle	30
3.4 Method of Moments	36
3.5 Volume EFIE for a two-dimensional homogeneous dielectric ob- ject for a TM^z polarisation	39
3.6 Green's function singularity	45
3.6.1 Analytical evaluation of Green's function singularity us- ing circle cell approximation	45
3.6.2 Numerical evaluation of Green's function singularity us- ing triangular cells	47

3.7	TM ^z analytical solution for two-dimensional homogeneous dielectric circular cylinder	51
3.8	TM ^z example for two-dimensional homogeneous dielectric circular cylinder	53
4	Fast contrast-sweep analysis using the Arnoldi MOR algorithm	57
4.1	Problem statement	58
4.2	The Arnoldi method	59
4.2.1	Orthogonal reduction of G to Hessenberg form H	62
4.2.2	Re-orthogonalised Arnoldi algorithm	63
4.3	Model-order reduction for a homogeneous body	66
4.4	Model-order reduction for an inhomogeneous body	68
4.4.1	Equation 4.36 approximation	69
4.4.2	Computational analysis	70
4.4.3	Terminating the iteration	73
4.5	Numerical results and validations	76
4.5.1	Case Study 1: Bi-static scattering homogeneous cylinder - Medium 1	76
4.5.2	Case Study 1: Mono-static scattering homogeneous cylinder - Medium 1	82
4.6	Shift-and-invert Arnoldi	87
4.6.1	Case Study 2: Mono-static scattering homogeneous cylinder - Medium 1	90
4.6.2	Case Study 3: Bi-static scattering inhomogeneous cylinder - Medium 1,2,3,4	94
4.6.3	Case Study 4: Mono-static scattering from an inhomogeneous cylinder - Medium 1,2,3,4	99
5	Well-Conditioned Asymptotic Waveform Evaluation	104
5.1	Well-Conditioned Asymptotic Waveform Evaluation (WCAWE)	104
5.1.1	Summary of terms	106
5.2	WCAWE algorithm	108
5.2.1	Summary of terms	110
5.3	Example showing that the WCAWE algorithm matches moments	112
5.4	Recursive formulation of the matrix derivatives	115
5.5	Numerical results and validations	117
5.5.1	Case Study 1: Homogeneous cylinder - Medium 1	117
5.6	Multipoint Well-Conditioned Asymptotic Waveform Evaluation (MWCAWE)	125
5.6.1	Case Study 2: Inhomogeneous square - Medium 1,2	127

5.7	Three-dimensional surface EFIE for a perfectly conducting object	133
5.8	Numerical results and validations	133
5.8.1	Case Study 1: Perfect electrically conducting square	133
6	Fast frequency-sweep analysis for object with frequency-dependent dielectrics	139
6.1	Frequency dependence of the dielectric properties	139
6.2	Dielectric ceramic $\text{Ba}_x\text{La}_4\text{Ti}_{2+x}\text{O}_{12+3x}$	141
6.3	Recursive formulation of the matrix derivatives	141
6.4	Numerical results and validations	143
6.4.1	Case Study 1: Homogeneous cylinder - Medium 1	143
6.4.2	Case Study 2: Inhomogeneous cylinder - Medium 1,2	150
7	Conclusions	153
7.1	Future study	156
A	Basic definitions and proofs	158
B	Acronyms	166
	Bibliography	168
	Publications	176
	Acknowledgements	177

List of Figures

2.1	Galerkin condition	15
3.1	An inhomogeneous obstacle illuminated by an incident field. . .	35
3.2	TM ^z wave scattering from a partial discretised structure.	44
3.3	Analytical circle-cell approximation.	46
3.4	Numerical evaluation of Green's function singularity using triangular cells.	50
3.5	Part A: Two-dimensional homogeneous dielectric circular cylinder	54
3.6	Part B: Comparison of the Method of Moments using the numerical evaluation against the analytical evaluation for a two-dimensional homogeneous dielectric circular cylinder	55
3.7	Part C: Comparison of the Method of Moments using the numerical evaluation against the analytical evaluation for a two-dimensional homogeneous dielectric circular cylinder	56
4.1	Inhomogeneous discretised structure with two homogenous regions.	72
4.2	Case study 1 setup - Homogeneous cylinder illuminated by a TM ^z incident wave.	75
4.3	Case study 1 Part A: Bi-static scattering from a homogeneous cylinder with $r = 1.5\lambda_0$, $q = 250$ and $\zeta = 1.1$ ($\epsilon_r = 2.1$), comparing MoM and MGSR.	78
4.4	Case study 1 Part B: Bi-static scattering from a homogeneous cylinder with $r = 1.5\lambda_0$, $q = 250$ and $\zeta = 1.1$ ($\epsilon_r = 2.1$), comparing MoM and MGSR.	79
4.5	Case study 1 Part C: Bi-static scattering from a homogeneous cylinder with $r = 1.5\lambda_0$, $q = 250$ and $\zeta = 1.1$ ($\epsilon_r = 2.1$), comparing MoM and MGSR.	80
4.6	Case study 1 Part D: Bi-static scattering from a homogeneous cylinder with $r = 1.5\lambda_0$, $q = 250$ and $\zeta = 1.1$ ($\epsilon_r = 2.1$), comparing MoM and MGSR.	81

4.7	Case study 1: Mono-static scattering from a homogeneous cylinder with $r = 1.5\lambda_0$, $q = 150, 250$ and $\zeta = 1.1 : 0.1 : 4$, comparing MoM and MGSr.	85
4.8	Case study 1: Scattering from a homogeneous cylinder with constant contrast and varying source location, comparing MoM and MGSr.	86
4.9	Case study 2: Mono-static scattering from a homogeneous cylinder with $r = 1.5\lambda_0$, $q = 250$ and $\zeta = 1.1 : 0.25 : 10$, comparing MoM, MGSr and SIMGSr.	91
4.10	Case study 2 Part A: Error analysis of the approximate eigenvalues of the ROM created using the MGSr and SIMGSr for a range of ζ values.	92
4.11	Case study 2 Part A: Error analysis of the approximate eigenvalues of the ROM created using the MGSr and SIMGSr for a range of ζ values.	93
4.12	Case study 3 Part A: Bi-static scattering from an inhomogeneous cylinder with $r = 1.5\lambda_0$, $q = 250$, $\zeta_1 = 4$, $\zeta_2 = 3$, $\zeta_3 = 2$ and $\zeta_4 = 1.1$	95
4.13	Case study 3 Part B: Bi-static scattering from an inhomogeneous cylinder with $r = 1.5\lambda_0$, $q = 250$, $\zeta_1 = 4$, $\zeta_2 = 3$, $\zeta_3 = 2$ and $\zeta_4 = 1.1$	96
4.14	Case study 3 Part C: Bi-static scattering from an inhomogeneous cylinder with $r = 1.5\lambda_0$, $q = 250$, $\zeta_1 = 4$, $\zeta_2 = 3$, $\zeta_3 = 2$ and $\zeta_4 = 1.1$	97
4.15	Case study 3 Part D: Bi-static scattering from an inhomogeneous cylinder with $r = 1.5\lambda_0$, $q = 250$, $\zeta_1 = 4$, $\zeta_2 = 3$, $\zeta_3 = 2$ and $\zeta_4 = 1.1$	98
4.16	Case study 3: Mono-static scattering from an inhomogeneous cylinder with $r = 1.5\lambda_0$, $q = 250, 150$, $\zeta = 1.1:0.1:4$, $\zeta_1 = 4$, $\zeta_2 = 3$ and $\zeta_3 = 2$	102
4.17	Case study 4: Scattering from an inhomogeneous cylinder with constant contrast and varying source location.	103
5.1	Case study 1 Part A: Single point expansion - Homogeneous cylinder.	121
5.2	Case study 1 Part B: Single point expansion - Homogeneous cylinder.	122
5.3	Case study 1 Part C: Single point expansion - Homogeneous cylinder.	123
5.4	Case study 1 Part D: Single point expansion - Homogeneous cylinder.	124
5.5	Multipoint WCAWE procedure.	126
5.6	Case study 2 Part A: Single point expansion - Inhomogeneous square.	130

5.7	Case study 2 Part A: Multipoint expansion - Inhomogeneous square.	131
5.8	Case study 2 Part B: Multipoint expansion - Inhomogeneous square.	132
5.9	Case study 1 Part A: Single point expansion - Homogeneous square.	136
5.10	Case study 1 Part B: Single point expansion - Homogeneous square.	137
5.11	Case study 1 Part C: Single point expansion - Homogeneous square.	138
6.1	Microwave dielectric properties of $\text{Ba}_x\text{La}_4\text{Ti}_{2+x}\text{O}_{12+3x}$ as a function of frequency for two specific values of x	146
6.2	Case study 1 Part A: Single point expansion - Homogeneous cylinder.	147
6.3	Case study 1 Part B: Single point expansion - Homogeneous cylinder.	148
6.4	Case study 1 Part C: Single point expansion - Homogeneous cylinder.	149
6.5	Case study 2: Multipoint expansion - Inhomogeneous cylinder. .	152
A.1	Example A - The construction of \mathbf{v}_3 from \mathbf{z}_3 and \mathbf{W}_2	164
A.2	Modified Gram-Schmidt when \mathbf{Z} is 2×2 matrix.	165

List of Tables

2.1	Condition number analysis of Padé coefficient matrix \mathbf{P}_f for Case study 1 in Section 5.5.1	21
2.2	Galerkin Asymptotic Waveform Evaluation Algorithm (GAWE).	24
4.1	Arnoldi - modified Gram-Schmidt algorithm (AMGS).	61
4.2	Arnoldi - modified Gram-Schmidt algorithm with re-orthogonalisation (AMGSR).	65
4.3	Arnoldi CPU time analysis for case study 1,2: Mono-static scattering homogeneous cylinder - Section 4.5.2 and 4.6.1	84
4.4	Shift and invert Arnoldi - modified Gram-Schmidt algorithm with re-orthogonalisation (SIMGSR)	89
4.5	Arnoldi CPU time analysis for case study 3,4: Bi-static, Mono-static scattering inhomogeneous cylinder - Section 4.6.2 and 4.6.3	101
5.1	AGAWE Algorithm.	107
5.2	Well-Conditioned Asymptotic Waveform Evaluation Algorithm (WCAWE).	111
5.3	WCAWE CPU time analysis for Case study 1: Homogeneous cylinder - Section 5.5.1	120
5.4	WCAWE volume EFIE CPU time analysis for case study 2: Inhomogeneous cylinder - Section 5.6.1	129
5.5	WCAWE surface EFIE CPU time analysis for case study 1: Perfect Electrically Conducting square - Section 5.8.1	135
6.1	WCAWE lossy volume EFIE CPU time analysis for case study 1: Homogeneous cylinder - Section 6.4.1	145
6.2	WCAWE lossy volume EFIE CPU time analysis for case study 2: Inhomogeneous cylinder - Section 6.4.2	151
A.1	The classical Gram-Schmidt (CGS) algorithm.	163
A.2	The modified Gram-Schmidt (MGS) algorithm.	163

Chapter 1

Introduction

“God runs electromagnetics by wave theory on Monday, Wednesday, and Friday, and the Devil runs them by quantum theory on Tuesday, Thursday, and Saturday. ”

Sir William Bragg

Electromagnetics has been at the forefront of technological innovations during the 20th and in the 21st century. Thus, much effort has been invested in developing tools for electromagnetic (EM) analysis.

The list of factors that engineers and manufacturers must consider during the design of new systems has expanded rapidly. Therefore, there is a growing need for efficient and accurate computational electromagnetic (CEM) analysis tools to aid engineers during the design process. CEM applications of particular interest are EM scattering problems, which arise in several areas of research including radar cross-section computation [1–3], inverse scattering [4–6], and medical imaging [7,8]. These all require CEM analysis to understand the interaction of EM fields and waves with arbitrary structures. This is achieved by EM wave scattering solvers generating models that characterise the current induced when a source EM wave interacts with a scattering structure. From the induced currents, other scattering qualities of interest can then be computed.

Modelling and simulation play a decisive role in the design and solution of CEM problems. After the relevant physical laws have been formulated into finite linear equations that a computer can solve, modelling of the behaviour of the system is possible in various scenarios. In this simulation phase, one tries to predict the behaviour of the system and, if any shortcomings are foreseen, the design can be changed accordingly.

Obviously, any speed-up in the simulation phase of the design and solution to EM problems is beneficial. One approach is to use a smaller model to describe the CEM problem, which results in reduced simulation times. Smaller models

are models that describe the behaviour of a system accurately, without the disadvantage of unnecessary detail. This enables the simulation of complex CEM problems in a reasonable time. These models should be smaller than the original models and their behaviour should be comparable to the behavior of the original model. The use of smaller models is in some configurations inevitable due to the size of the original models. This is the case for very complex geometries at high frequencies where a very fine discretisation is required. To model the EM fields accurately, the size of the discretisation cells must be small compared to the wavelength; approximately no larger than $\lambda/10$ (where λ denotes wavelength in the dielectric material) [9]. Also, in cases where a very detailed current distribution across the object is not of interest, a smaller model may capture adequate information for the early stages of a design process.

Another main reason for using MOR is to enable a fast-sweep capability. In a fast-sweep problem, some parameter on which the original problem depends is variable and the problem must be solved as the parameter changes over a desired parameter range. However, the complexity of the original model is such that its computation for every parameter value would be prohibitive.

A very fine resolution may be required in order to reduce the risk of failing to capture a region that produces rapidly varying fields. Therefore, one can use MOR techniques to generate ROMs which can be rapidly solved to characterise the parameter-dependent behaviour of the system over the entire parameter range. When MOR is applied, it is essential that the dominant characteristic of the original system, with respect to the varying parameter, is captured in the ROM so that the approximation is accurate. In addition, since the ROM has fewer unknowns than the original system, it is more computationally efficient to solve the ROM for many different values of the varying parameter than to solve the original system over the entire parameter range. Two fast-sweep problems in electromagnetism that will be investigated in this thesis are contrast-and frequency-sweep problems.

Contrast-sweep problems are associated with scattering analysis where the material properties such as the permittivity, permeability and conductivity are varied over a range, to produce the scattered fields. There has been very limited research in the field of fast contrast-sweep problems. Much of the research has been restricted to the solution of inverse problems through the direct simulation of the forward problem [6]. This requires the repeated solution of full-scattering problems for the total fields at each step in contrast. Recently published work by [4, 5] circumvented this particular computational problem by using Krylov subspace methods to produce a ROM for a homogeneous structure. This is an

object which has an uniform material properties throughout its structure. Conversely inhomogeneous objects consist of materials that are not of the same kind. In this work, an approximate extension that accounts for wave scattering from an inhomogeneous object using a two-dimensional volume integral formulation is presented. The approximation is shown to be exact in the limit as the level of reduction approaches zero.

The second application considered is frequency-sweep analysis, which is a very popular area of research with numerous applications. In many areas such as radar applications, it is necessary to determine the fields scattered from an object over a wide-frequency band. Since the system is frequency-dependent, this produces a nonlinear parameter dependence and precludes the use of several standard linear MOR techniques.

In this work, a new MOR technique produced by Slone [10,11] called Well-Conditioned Asymptotic Waveform Evaluation (WCAWE) is examined. In particular, its application to fast-frequency analysis for the EFIE formulation is investigated. Additionally, this approach is extended to account for the frequency dependence of dielectric properties in a fast-frequency analysis. This is of particular importance, as frequency-dependent dielectric variations occur in all materials and no research to date has treated this variation in a frequency sweep analysis using MOR.

There are a wide variety of mathematical processes to derive ROMs which form the field of MOR. These techniques try to capture the essential features of a system. This means that, after a small number of iterations in a MOR procedure, the most important information of the original model must be captured in the ROM. A MOR procedure should

- produce a robust low-order ROM
- be able to be generated and implemented in an efficient manner
- achieve an accurate approximation
- have automatic error controls

In the past decade, MOR techniques have been at the foreground of research to reduce the computational complexity associated with numerical electromagnetic simulations. The fundamental methods in the area of MOR were published in the 1980s and 1990s. However, the basis for many of today's MOR techniques is rooted in the Arnoldi [12] and Lanczos [13] algorithms first developed back in the 1950s. These techniques were used to reduce a matrix to Hessenberg and tridiagonal form, respectively. The techniques were not applied to produce a

ROM until the mid-1990s. Methods based on Truncated Balance Realisation (TBR) [14] and Proper Orthogonal Decomposition (POD) [15] were proposed in 1981 and 1987 respectively, as a means to produce ROMs.

TBR [16] is a method developed in the area of system and control theory and is applied to ordinary differential equation sets (ODEs). The TBR method calculates the largest singular values of a system and uses a similarity transform to achieve a ROM. POD [15] was developed within the area of computation fluid dynamics and is applied to nonlinear partial differential equations (PDEs). These methods use the time response outputs of a system to certain inputs as a means to build an orthogonal basis onto which the system may be projected. These projections are subsequently used to create the ROM.

In 1989, Model-Based Parameter Estimation (MBPE) [17] was introduced. It [18–20] is primarily used in conjunction with the method of moments (MoM). This method creates a ROM by matching a rational polynomial to data available from the MoM. A model is interpolated between, or extrapolated from, samples of this data. The major drawback of this technique is that the sampling points and interpolation order are not known *a priori*. Therefore the procedure is not automated and essentially requires running several simulations before choosing the best ROM.

The following year, the first methods based on the Asymptotic Waveform Evaluation (AWE) [21] were published. The focus of this method was the explicit computation of moments which are then converted into a Padé approximation. AWE was introduced to perform MOR on circuit analysis problems by matching moments in a Taylor series for the system transfer function. However, the use of this expansion is limited to the radius of convergence of the Taylor series. In such cases, the rational function approach is used to improve the accuracy of the numerical solution. The Padé representations have a larger radius of convergence and therefore can provide a broader extrapolation as they include poles as well as zeros in the response and as such can match the resonant behaviour far better than a truncated power series [1, 22–24]. This technique was later used for fast-frequency sweep analysis using electric field integral equations in [1]. However, it has been well documented [22, 23] that the AWE process of sequentially evaluating moments is inherently ill-conditioned, which results in limited bandwidth. Then, in 1994, techniques based on the Lanczos process were introduced. The proposed Padé via Lanczos (PVL) [25] method developed the relation between the Padé approximation and the Krylov subspaces without explicitly forming the ill-conditioned moments. In 1995, another Krylov-based method, the Projection via Arnoldi (PVA) [26] method based on the Arnoldi

methods of the early 1950s, was introduced. These techniques were initially applied to circuit analysis but later were adopted for use in computational electromagnetics [4,27]. However, PVL and PVA suffer from an inherent limitation which requires the original model to be a linear function of the ROM varying parameter.

In more recent years, much research has been done in the area of MOR. Many of these new techniques are tailored to specific applications and formulations while others are more general. The use of Krylov subspace techniques is widely accepted as being the most flexible and computationally efficient approach to MOR and has been widely used in various formulations and applications. Since the essential features of the original system are captured at the early stage of the iteration, Krylov subspace algorithms can produce very accurate low-order models. One such avenue of research is the work in [10,11] which has developed the Well-Conditioned Asymptotic Waveform Evaluation (WCAWE) method which circumvents the ill-condition properties of the moment matching sequence. This is achieved by deriving an AWE-Arnoldi based hybrid algorithm which builds an orthogonalised Krylov subspace that can still match moments. WCAWE, unlike AWE, does not suffer degradation in the moment matching power with increasing order. In addition, it does not require the original model to be a linear function of the ROM varying parameter.

For nonlinear systems, where the dependence on the MOR parameter is nonlinear, much of the recent research has centred on either linearising the problem and then using a linear Krylov-based technique such as the PVA or otherwise directly using an AWE variant. Although various linearisation techniques have been successfully implemented in Finite Element Method (FEM) simulations and subsequently reduced using the PVA algorithm [11,28], it has been the experience of this author that this approach has several deficiencies. (These numerical issues will be discussed in the next section.) Therefore, in this thesis, the WCAWE techniques will be used as the primary MOR approach to nonlinear dependence. This technique has been shown to be a stable and robust method for finite element simulations. It is one of the objectives of this thesis to apply and extend the WCAWE technique to various EFIE formulations and applications for nonlinear MOR parameters.

Although much work has been done in the area of MOR, application of these techniques to the EFIE formulation of EM wave scattering problems has been limited. Integral equations (IEs) can be solved by the Method of Moments (MoM) [9,29], in which the unknown field function is expanded in a set of expansion or testing functions. The dot product of both sides of the integral equa-

tion with a set of testing functions is subsequently achieved, and the results are integrated over the object domain. This leads to a system of linear algebraic equations that can be solved using direct discrete numerical solution methods such as Gaussian Elimination (GE) [9, 30] or suitable iterative techniques such as Conjugate Gradient (CG) methods [9, 30]. While these formulations result in matrices that are significantly smaller relative to differential equation-based formulations, the matrices resulting from discretising IEs are dense.

Additionally several other approaches can be used in conjunction with MOR to reduce the computational expense of solving complicated systems over a desired parameter range. To permit simulation, IE-based tools accelerate computations by using iterative methods [30, 31] to solve the system in conjunction with sparsification algorithms. Sparsification techniques, such as the precorrected fast Fourier transform (PFFT) [32, 33] and fast multipole method (FMM) [34] approximate the discretised model of the original system when computing matrix-vector products. These methods can reduce the number of operations required by a matrix-vector product from $\mathcal{O}(m^2)$ to almost $\mathcal{O}(m)$ [28, 35]. For systems with Toeplitz matrices (each descending diagonal from left to right is constant), the Conjugate Gradient Fast Fourier Transform (CG-FFT) implementation is very effective and can reduce the matrix-vector product to $\mathcal{O}(m \log m)$ operations [34]. By orchestrating different approaches such as sparsification techniques, iterative methods, preconditioning [9, 31, 36], and parallelisation [37–39], extremely large-scale scattering problems in the order of millions of unknowns can be rapidly solved [40].

Alternatively, using higher-order MoM techniques can achieve well-conditioned system matrices of reduced-order which can significantly reduce computational expense. These higher-order MoM schemes comprise higher-order basis functions and an accurate representation of the structure by higher-order curvilinear elements [9, 41, 42]. Recently, this approach has been successfully used for an accelerated computation of the response of microwave circuits over a wide-frequency band [43].

We conclude this section with summaries of the material in each of the remaining chapters.

The next chapter provides the context necessary to understand the algorithms presented in the following chapters. Specifically, traditional MOR techniques such as Krylov subspace iteration and Asymptotic Waveform Evaluation are introduced.

Chapter 3 traces the development from the appropriate Maxwell’s laws into EFIE formulations.

Chapter 4 introduces the Arnoldi algorithm and then outlines how to generate ROMs for use with contrast sweep problems. An approximate extension of this algorithm to produce a ROM for inhomogeneous contrast-sweep analysis is formulated. This approximation is shown to be exact in the limit as the level of reduction approaches zero. A ROM for source sweep problems is also developed using the Arnoldi algorithm where for a fixed contrast profile the location of the source is varied. Other topics, including automatic error control, re-orthogonalisation, and Spectral Transformations, are also discussed.

Chapter 5 is dedicated to the application of the WCAWE algorithm for use with the volume and surface EFIE in a fast-frequency sweep analysis. A multipoint automatic WCAWE method is also demonstrated which can produce an accurate solution over a much broader bandwidth. Several numerical examples are given which illustrate the accuracy and robustness of the proposed methods.

Chapter 6 extends MOR to account for frequency-dependent dielectric properties in a fast-frequency analysis using the WCAWE. In particular, the variation in the dielectric properties of the ceramic $\text{Ba}_x\text{La}_4\text{Ti}_{2+x}\text{O}_{12+3x}$ in the sub 1 GHz frequency range is investigated for various values of x in a frequency sweep analysis.

Some concluding remarks and a summary of this research are presented in the final Chapter 7.

1.1 Contribution

It is the aim of this work to contribute to the development of model-order reduction (MOR) techniques suitable for use for fast-sweep analysis of EM wave scattering problems in relation to EFIEs. The main contributions of this thesis are described in Chapters 4, 5 and 6 and can be summarised as follows:

- The formulation of an approximate extension of the Arnoldi algorithm to produce a ROM for an inhomogeneous contrast and source sweep analysis.
- The application of the WCAWE technique to achieve a fast-frequency sweep analysis for electric field integral equation applications.
- The development of a fast full-wave frequency sweep analysis using the WCAWE technique for materials with frequency-dependent dielectric properties.

1.2 Notation

Bold capital and bold lower-case letters denote matrices and vectors, respectively, while lower-case italics denote scalars. The transpose of a vector \mathbf{x} is denoted by \mathbf{x}^T , and \mathbf{x}^H denotes the conjugate transpose. The Euclidean norms are denoted by $\|\cdot\|_2$ while the range of a matrix \mathbf{A} is denoted by $\mathcal{R}(\mathbf{A})$. For the sake of clarity the subscript $\mathbf{U}_{m \times q}$ will be used to explicitly indicate the size of the relevant matrix/vector. This notation will be used only when the relevant matrix/vector is first introduced and the short hand \mathbf{U}_q will be used thereafter. This is required due to the adaptive nature of the algorithm being used in this thesis, where the size of a matrix/vector is directly determined by the number of iteration taken. In this example since m is fixed and q is adaptive, this short hand is appropriate. For the case of fixed size matrices/vectors this notation will not be adopted.

Chapter 2

Model-Order Reduction

“The question is not what you look at, but what you see”

Henry David Thoreau

This chapter provides the background material necessary to understand the algorithms presented in the following chapters. Specifically, it introduces traditional model-order reduction techniques such as Krylov subspace iteration and Asymptotic Waveform Evaluation. Finally, a review is given of the framework of how these methods can generate reduced-order models for linear and nonlinear parameter dependence.

2.1 Mathematical statement of model-order reduction problem

In computational modelling of electromagnetic fields for practical applications, typically a large system of linear equations must be solved. This system originates from the discretised integral equation. In formal notation, such a system can be written as

$$\mathbf{Z}\mathbf{x} = \mathbf{b} \tag{2.1}$$

where \mathbf{Z} is an $m \times m$ matrix containing coupling information between the basis functions, \mathbf{b} is a vector of size m containing information about the incident field while \mathbf{x} represent the unknown amplitudes of the m basis functions. We are interested in the situation where this problem must be solved for a large number of sampled values of some parameter. MOR is a technique for generating a ROM of size q , which retains parameter dependencies of the original system across a desired parameter range as well as certain properties of the original model. One can readily compute an accurate approximation to desired scattering quantities, which characterise the original system, from the unknown fields

yielded by solving the ROM at a given parameter point. Since a smaller system of equations can be solved more rapidly than the original system of equations, an accurate approximation to the behaviour of the original system across the desired parameter range can be quickly computed by solving the ROM at each point in a parameter range.

2.2 Krylov subspace iteration

In this section, projection methods using Krylov subspaces are considered. Krylov subspace algorithms exploit projection processes in order to extract approximate solutions from a specified low-dimensional subspace. Certain conditions are required in order to be able to extract these approximations; however, once constrained, a reduced-order matrix problem can be obtained. Krylov methods have their origins in eigenvalue computation and in particular, in eigenvalue estimations. This will be the premise for how the Krylov techniques described in this section obtain accurate low-order approximations. To start this analysis, the rationale for using Krylov subspace methods is described. A review of how to extract information about a matrix via matrix-vector multiplication and the numerical problems associated with such routines will be useful in illustrating the reason why Krylov techniques are used. To extract an approximation to \mathbf{Z} requires the iterative computation of the sequence of matrix-vector products

$$\mathbf{K} = [\mathbf{b}, \mathbf{Z}\mathbf{b}, \dots, \mathbf{Z}^{m-1}\mathbf{b}] \quad (2.2)$$

where \mathbf{K} is an $m \times m$ matrix. This sequence is inherently ill-conditioned. In a direct implementation, finite precision arithmetic causes each newly created vector to converge towards the eigenvector that is associated with the dominant eigenvalue of \mathbf{Z} . As a result, each new vector will contain only information corresponding to one eigenvalue of \mathbf{Z} . Assuming \mathbf{K} is nonsingular and not orthogonal then

$$\mathbf{Z}\mathbf{K} = \mathbf{K}\mathbf{K}^{-1}\mathbf{Z}\mathbf{K} = \mathbf{K}\mathbf{C} = \mathbf{K} \begin{pmatrix} 0 & 0 & \cdots & -c_1 \\ 1 & 0 & \cdots & -c_2 \\ 0 & 1 & \cdots & \vdots \\ \vdots & \cdots & 1 & -c_m \end{pmatrix} \quad (2.3)$$

where \mathbf{C} is an $m \times m$ companion matrix [36, 44]. \mathbf{Z} has now been reduced to a simpler form, and the eigenvalues of \mathbf{Z} can now be found easily by finding the zeros of the characteristic polynomial of \mathbf{C} [36, 44]

$$p(x) = x^m + \sum_{i=1}^m c_i x^{i-1} \quad (2.4)$$

This simpler form is not useful in practice as \mathbf{K} is in many cases very ill-conditioned, resulting in an inaccurate computation. This is due to the fact that the space formed in Equation 2.2 is created by a power series method [44]. As such, the columns of \mathbf{K} will converge to an eigenvector corresponding to the largest eigenvalue of \mathbf{Z} [36,44,45]. Thus, the columns of \mathbf{K} will lose linear independence (see Appendix A) and each newly formed column of \mathbf{K} will not add any useful information to the approximation. From this analysis it is clear that, to achieve an accurate approximation, the columns of \mathbf{K} must be linearly independent. The space spanned by the columns is called a Krylov subspace,

$$\mathcal{K}(\mathbf{Z}, \mathbf{u}_1) = \text{span}\{\mathbf{u}_1, \mathbf{Z}\mathbf{u}_1, \dots, \mathbf{Z}^{m-1}\mathbf{u}_1\} \quad (2.5)$$

$$\text{span}\{\mathbf{u}_1, \dots, \mathbf{u}_m\} = \text{span}\{\mathbf{u}_1, \mathbf{Z}\mathbf{u}_1, \dots, \mathbf{Z}^{m-1}\mathbf{u}_1\} \quad (2.6)$$

where \mathbf{u}_m is the m^{th} column of the $m \times m$ orthonormal matrix \mathbf{U} . In what follows \mathbf{K} will be replaced with an orthonormal matrix \mathbf{U} such that for all m , the leading m columns of \mathbf{K} and \mathbf{U} span the same space. Since each column of the \mathbf{U} matrix is formed to be orthonormal to all the previous ones, the columns are linearly independent. Due to its structure, the \mathbf{U} matrix is subsequently well-conditioned and easy to invert. Furthermore, the sequence of vector-matrix multiplications in Equation 2.5 does not have the same numerical instability issues as Equation 2.2. However, as with all explicit vector-matrix multiplications, round-off error will exist which will result in loss of orthogonality amongst the columns of the \mathbf{U} matrix. This is rectified by the introduction of a re-orthogonalisation process in the Krylov iteration which will be discussed in detail in Chapter 4.

In the context of MOR, it should be noted that only the leading columns of \mathbf{U} that will obtain an accurate approximation are produced in a Krylov routine (This will be discussed in greater detail later in this section). This means a ROM can be created which is an accurate approximation to the original model.

In order to show how \mathbf{Z} can be approximated by using an orthonormal matrix \mathbf{U} , a \mathbf{QR} decomposition of \mathbf{K} [44] is applied. From Equation 2.3

$$\begin{aligned}
\mathbf{C} &= \mathbf{K}^{-1}\mathbf{Z}\mathbf{K} \\
&= \mathbf{R}^{-1}\mathbf{Q}^H\mathbf{Z}\mathbf{Q}\mathbf{R} & (\mathbf{Q}^{-1} = \mathbf{Q}^H) \\
&= \mathbf{R}^{-1}\mathbf{U}^H\mathbf{Z}\mathbf{U}\mathbf{R} & \mathbf{U} \equiv \mathbf{Q}
\end{aligned} \tag{2.7}$$

implying

$$\mathbf{U}^H\mathbf{Z}\mathbf{U} = \mathbf{R}\mathbf{C}\mathbf{R}^{-1} = \mathbf{H}. \tag{2.8}$$

If \mathbf{Z} is nonsymmetric, then \mathbf{H} is a $m \times m$ upper Hessenberg matrix. On the other hand if \mathbf{Z} is symmetric, then it is tridiagonal [44]. This procedure will be used in Chapter 4 to produce a ROM by using the orthogonal transformation matrix \mathbf{U} to reduce the \mathbf{Z} matrix to upper Hessenberg form.

2.3 Residual minimising methods

After q steps of a Krylov process have been performed, a $m \times q$ orthonormal matrix $\mathbf{U}_{m \times q}$ and the corresponding upper Hessenberg matrix $\mathbf{H}_{q \times q}$ will have been obtained. As stated earlier this notation is used due to the adaptive nature of the algorithm being used in this thesis. This notation will be used only when the relevant matrix/vector is first introduced and the short hand \mathbf{U}_q and \mathbf{H}_q will be used thereafter.

How can these matrixes be used to produce a reduced order approximation? A Krylov subspace based technique extracts an approximate solution of dimension q from the subspace $\mathcal{K}_{m \times q}$. In order to achieve an accurate approximation, the solution is chosen from \mathcal{K}_q so that q constraints are satisfied. Typically, the constraints require that the residual is orthogonal to subspace \mathcal{K}_q . This subspace can be represented by an orthonormal matrix \mathbf{U}_q whose columns form a basis for the subspace \mathcal{K}_q . This orthonormal matrix is then used to project the original system onto the subspace \mathcal{K}_q . This projection is known as an orthogonal similarity transformation (see Appendix A) which produces the ROM. Creation of a reduced-order model via projection will be addressed in greater detail in Chapter 4. In this section a review of how an optimum approximation is extracted from the Krylov subspace \mathcal{K}_q is undertaken.

For the linear system in Equation 2.1, the Krylov space technique generates an approximate solution \mathbf{x}_q to \mathbf{x} the $m \times 1$ vector and corresponding residuals

$$\mathbf{r}_q = \mathbf{b} - \mathbf{Z}\mathbf{x}_q \quad (2.9)$$

so that $\mathbf{x}_q \in \mathcal{K}_q$ and \mathbf{x}_q approximates \mathbf{x} in q steps [31, 44, 46, 47].

In order to extract an approximation from the \mathbf{U}_q and \mathbf{H}_q matrices, certain constraints have to be imposed to ensure a unique solution. To this end Galerkin conditions are imposed on the residual vector.

Because $\mathbf{x}_q \in \mathcal{K}_q$, \mathbf{x}_q can be expressed as a linear combination of the columns of \mathbf{U}_q with coefficient vectors $\mathbf{a}_{q \times 1}$ [31, 44, 47]. As such, an approximation to \mathbf{x} can be made in terms of these q basis vectors of the form

$$\mathbf{x}_q = \sum_{n=1}^q \mathbf{u}_n \alpha_n = \mathbf{U}_q \mathbf{a}_q \quad (2.10)$$

where $\mathbf{a} = [\alpha_1, \alpha_2, \dots, \alpha_q]^H$. To find the optimal approximate solution, there are several approaches to constraining \mathbf{x}_q , resulting in different Krylov-based algorithms [44]. A typical way to impose these constraints is to ensure that \mathbf{x}_q minimises the 2-norm of the residual $\|\mathbf{r}_q\|_2$: this can be achieved by imposing

q independent orthogonality conditions [44]. Specifically, the residual vector is constrained to be orthogonal to the q linearly independent vectors \mathbf{u}_n . This is known as the orthogonal residual property, or a Galerkin condition [44]

$$\mathbf{r}_q \perp \mathcal{K}_q \quad \mathbf{U}_q^H \mathbf{r}_q = 0. \quad (2.11)$$

The orthogonality relation imposed on the residual is illustrated in Figure 2.1. It is clear from this figure that the residual \mathbf{r}_q is minimised when the residual is orthogonal to the space \mathcal{K}_q . This is confirmed in the following Theorem [44]

Theorem 2.3.1. Let \mathbf{Z} be symmetric, $\mathbf{H}_q = \mathbf{U}_q^H \mathbf{Z} \mathbf{U}_q$ and $\mathbf{r}_q = \mathbf{b} - \mathbf{Z} \mathbf{x}_q$, where $\mathbf{x}_q \in \mathcal{K}_q$. If \mathbf{H}_q is nonsingular and $\mathbf{x}_q = \mathbf{U}_q \mathbf{H}_q^{-1} \mathbf{e}_1 \|\mathbf{b}\|_2$, where $\mathbf{e}_q = [1, 0, \dots, 0]^T$, then $\mathbf{U}_q^H \mathbf{r}_q = 0$.

Proof. Let $\mathbf{a}_q = \mathbf{H}_q^{-1} \mathbf{e}_q \|\mathbf{b}\|_2$, $\mathbf{x}_q = \mathbf{U}_q \mathbf{H}_q^{-1} \mathbf{e}_q \|\mathbf{b}\|_2 \equiv \mathbf{Z}^{-1} \mathbf{b}$ (because the first column of \mathbf{U}_q is $\mathbf{b}/\|\mathbf{b}\|_2$ and its other columns are orthogonal to \mathbf{b} therefore $\mathbf{U}_q \mathbf{b} = \mathbf{e}_q \|\mathbf{b}\|_2$), $\mathbf{r}_q = \mathbf{b} - \mathbf{Z} \mathbf{x}_q$ and we assume that $\mathbf{H}_q = \mathbf{U}_q^H \mathbf{Z} \mathbf{U}_q$ is nonsingular. We confirm that $\mathbf{U}_q^H \mathbf{r}_q = 0$ by computing

$$\begin{aligned} \mathbf{U}_q^H \mathbf{r}_q &= \mathbf{U}_q^H (\mathbf{b} - \mathbf{Z} \mathbf{x}_q) &= \mathbf{U}_q^H \mathbf{b} - \mathbf{U}_q^H \mathbf{Z} \mathbf{x}_q \\ &= \mathbf{e}_q \|\mathbf{b}\|_2 - \mathbf{U}_q^H \mathbf{Z} (\mathbf{U}_q \mathbf{H}_q^{-1} \mathbf{e}_q \|\mathbf{b}\|_2) \\ &= \mathbf{e}_q \|\mathbf{b}\|_2 - (\mathbf{U}_q^H \mathbf{Z} \mathbf{U}_q) \mathbf{H}_q^{-1} \mathbf{e}_q \|\mathbf{b}\|_2 \\ &= \mathbf{e}_q \|\mathbf{b}\|_2 - (\mathbf{H}_q) \mathbf{H}_q^{-1} \mathbf{e}_q \|\mathbf{b}\|_2 \\ &= 0. \end{aligned} \quad (2.12)$$

□

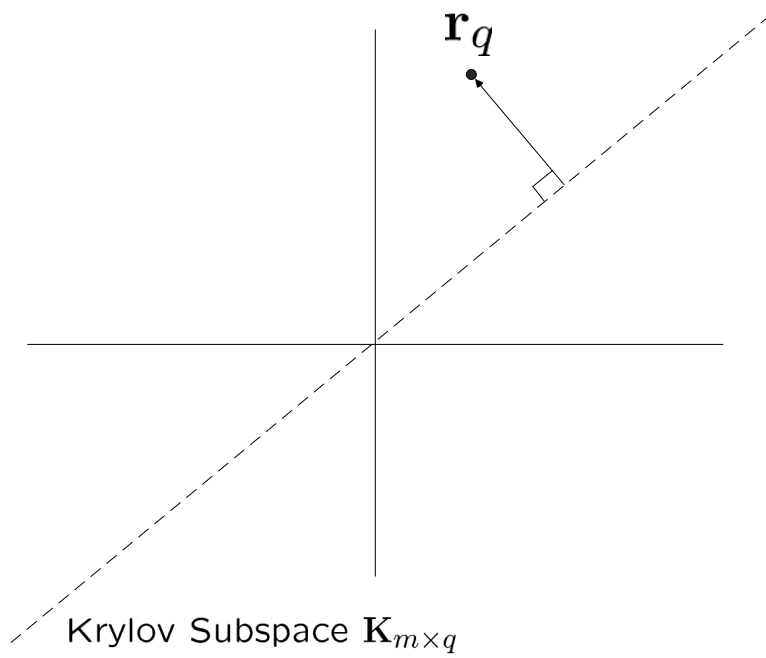


Figure 2.1: Galerkin condition

2.4 Review of Asymptotic Waveform Evaluation via Padé approximation

For nonlinear systems where the dependence on the MOR parameter is nonlinear

$$\mathbf{Z}(k) \mathbf{x}(k) = \mathbf{b}(k) \quad (2.13)$$

much of the recent research has centred on either linearising the problem and then using linear Krylov-based techniques such as the PVA, or directly using an AWE variant. In Equation 2.13, the \mathbf{Z} matrix and the vectors \mathbf{x}, \mathbf{b} are clearly dependent on frequency, where k is the free-space wave number. In this work, a new MOR technique produced in [10,11] called the Well-Conditioned Asymptotic Waveform Evaluation (WCAWE) and its application to the fast-frequency analysis of the EFIE formulation is investigated. In order to understand this algorithm, the basis of the AWE process and its limitations will be reviewed.

The AWE is a method that extracts information about the system behaviour over a wide frequency range from the solution at one or several frequency points [1, 22–24]. This is possible because coefficients of the matrix equation, describing the system behaviour, are known functions of frequency. The AWE method approximates the frequency response at wave number k_b by expanding $\mathbf{x}(k)$ into a Taylor series around k_b

$$\mathbf{x}(k) = \sum_{n=0}^q \mathbf{m}_n \beta^n. \quad (2.14)$$

Where \mathbf{m}_n are the moments of $\mathbf{x}(k)$, k is the wave number, q is the order of the Taylor series expansion and $\beta = (k - k_b)$, where k_b is the wave number at the expansion frequency. By substituting Equation 2.14 into Equation 2.13, expanding the impedance matrix $\mathbf{Z}(k)$ and the excitation vector $\mathbf{b}(k)$ into a Taylor series, Equation 2.13 can be re-written as

$$\sum_{n=0}^q \left(\mathbf{Z}^{[n]} \beta^n \right) \sum_{n=0}^q \mathbf{m}_n \beta^n = \sum_{n=0}^q \left(\mathbf{b}^{[n]} \beta^n \right). \quad (2.15)$$

Vector $\mathbf{b}^{[q]}(k_b)$ denotes the q^{th} derivative with respect to k of $\mathbf{b}(k)$ evaluated at k_b divided by $q!$. Similarly $\mathbf{Z}^{[q]}(k_b)$ denotes the q^{th} derivative of $\mathbf{Z}(k)$ evaluated at k_b divided by $q!$. For the sake of clarity, $\mathbf{Z}^{[q]}(k_b)$ and $\mathbf{b}^{[q]}(k_b)$ and will be denoted by $\mathbf{Z}^{[q]}$ and $\mathbf{b}^{[q]}$.

Finally, equating the coefficients of equal powers of β on both sides of Equation 2.15 yields the moments of Equation 2.14

$$\begin{aligned}
\mathbf{w}_1 &= \mathbf{Z}^{-1}(k_b) \mathbf{b}(k_b) \\
\mathbf{w}_2 &= \mathbf{Z}^{-1}(k_b) \left[\mathbf{b}^{[1]}(k_b) - \mathbf{Z}^{[1]}(k_b) \mathbf{w}_1 \right] \\
\mathbf{w}_3 &= \mathbf{Z}^{-1}(k_b) \left[\mathbf{b}^{[2]}(k_b) - \mathbf{Z}^{[1]}(k_b) \mathbf{w}_2 - \mathbf{Z}^{[2]}(k_b) \mathbf{w}_1 \right] \\
&\vdots \\
\mathbf{w}_q &= \mathbf{Z}^{-1}(k_b) \left[\mathbf{b}^{[q-1]}(k_b) - \sum_{n=1}^{q-1} \mathbf{Z}^{[n]}(k_b) \mathbf{w}_{q-n} \right].
\end{aligned} \tag{2.16}$$

From the above recursive relation, the moment vectors \mathbf{m} in Equation 2.14 are given by

$$\mathbf{m}_n = \mathbf{w}_{n+1} \quad \text{for } 0 \leq n \leq q-1. \tag{2.17}$$

Once the moment vectors are obtained, the value of $\mathbf{x}(k)$ at other frequencies can be calculated using Equation 2.14. However, the use of this expansion is limited to the radius of convergence of the Taylor series. In such cases, the rational function approach is used to improve the accuracy of the numerical solution. The Padé representations have a larger radius of convergence and therefore can provide a broader extrapolation as they include poles as well as zeros in the response and as such can match the resonant behaviour far better than a truncated power series [1, 22–24]. Typically c is used for the number of zeros and f is the number of poles in the rational function. The aforementioned Padé approximations are given by

$$\mathbf{x}(k) = \sum_{n=0}^q \mathbf{m}_n \beta^n = \sum_{n=0}^{c+f+1} \mathbf{m}_n \beta^n = \frac{\sum_{i=0}^c \mathbf{d}_i \beta^i}{1 + \sum_{j=1}^f \mathbf{e}_j \beta^j}. \tag{2.18}$$

Matching the coefficients of equal powers of $\beta^{c+1}, \dots, \beta^{c+f}$ leads to a matrix equation containing the Padé coefficient matrix $\mathbf{P}_{f \times f}$, which allows for the solution of \mathbf{e}_j to be obtained [22].

$$\mathbf{P}_f \begin{pmatrix} e_1 \\ e_2 \\ e_3 \\ \vdots \\ e_f \end{pmatrix} = - \begin{pmatrix} m_{c+1} \\ m_{c+2} \\ m_{c+3} \\ \vdots \\ m_{c+f} \end{pmatrix} \tag{2.19}$$

where

$$\mathbf{P}_f = \begin{pmatrix} m_c & m_{c-1} & m_{c-2} & \cdots & m_{c-f+1} \\ m_{c+1} & m_c & m_{c-1} & \cdots & m_{c-f+2} \\ m_{c+2} & m_{c+1} & m_c & \cdots & m_{c-f+3} \\ \vdots & \vdots & \vdots & \ddots & \vdots \\ m_{c+f-1} & m_{c+f-2} & m_{c+f-3} & \cdots & m_c \end{pmatrix}. \quad (2.20)$$

Having found the \mathbf{e}_j , the unknown coefficients d_i can be calculated as:

$$\begin{aligned} d_0 &= m_0 \\ d_1 &= m_1 + e_1 m_0 \\ d_2 &= m_2 + e_1 m_1 + e_2 m_0 \\ &\vdots \\ d_i &= m_i + \sum_{j=1}^i e_j m_{i-j}. \end{aligned} \quad (2.21)$$

Equation 2.19 and 2.21 are repeatedly solved for each element d_i and e_j of the \mathbf{d}_i and \mathbf{e}_j vectors. After the Padé approximations have been formed, the solution at each frequency is found using Equation 2.18. Unfortunately, although the solution of Equation 2.19 requires solving a relatively small matrix problem, the Padé coefficient matrix \mathbf{P}_f is poorly conditioned, reducing the accuracy of the final solution. Various solutions are presented in the following sections to circumvent the numerical sensitivity in the AWE process.

2.4.1 Numerical sensitivity

The AWE moment matching subspace, $\mathcal{W}_{m \times q}$, generated from the recursive Equation 2.16, is given by

$$\mathcal{W}_q = \{\mathbf{w}_1, \mathbf{w}_2, \dots, \mathbf{w}_q\}. \quad (2.22)$$

It has been well documented [22, 23, 27] that the process of sequentially evaluating \mathbf{w}_q is inherently ill-conditioned, leading to instability in the computation of the Padé approximation. In a direct implementation, finite precision arithmetic causes each newly created moment vector \mathbf{w}_q to converge towards the eigenvector that is associated with the dominant eigenvalue of \mathbf{Z} . As a result, the moments \mathbf{w}_q contain only information corresponding to one eigenvalue of \mathbf{Z} . As

a consequence, the coefficient matrix \mathbf{P}_f becomes rapidly ill-conditioned. Subsequently, the solution of Equation 2.19 becomes unattainable, thus restricting its use to approximations of relatively low order, typically for values of $q < 20$. Indeed, typically one can expect the process to start to stagnate for values of $q > 10$.

The above observation is confirmed by analysing the condition number of the coefficient matrix \mathbf{P}_f of Equation 2.19, $\text{cond}(\mathbf{P}_f)$. The condition number is a measure of the extent to which round-off error affects the accuracy of the numerically computed solution of Equation 2.19. It has been shown in [25] that an increase of $\text{cond}(\mathbf{P}_f)$ by a factor of 10 signals the loss of one decimal digit of accuracy in the computed solution. In particular, if double-precision with 16 decimal digits is used, then the computed solution must be expected to be meaningless if $\text{cond}(\mathbf{P}_f) > \mathcal{O}(10^{16})$. In Table 2.1, a list of the $\text{cond}(\mathbf{P}_f)$ for the Padé coefficient matrix for the simulation example in Section 5.5.1 is displayed. From this table it is clear that for small values of q , the coefficient matrix can be extremely ill-conditioned. One approach to remedy this problem is to use scaling [25]. The original recursive form for the moments \mathbf{w}_q , generated by Equation 2.16, is replaced with

$$\mathbf{w}_q = \mathbf{Z}^{-1} \left[\frac{\mathbf{b}^{[q-1]}}{\xi^{q-1}} - \sum_{m=0}^{q-1} \frac{(1 - \delta_{q0}) \mathbf{Z}^{[m]} \mathbf{w}_{q-m}}{\xi^m} \right] \quad (2.23)$$

where ξ is a scaling factor used to improve the conditioning of the Padé coefficient matrix \mathbf{P}_f . The subsequent Padé via AWE with adaptive Zeta approximation is given by

$$\sum_{n=0}^{c+f+1} \mathbf{m}_n (\xi\beta)^n = \frac{\sum_{i=0}^c \mathbf{d}_i (\xi\beta)^i}{1 + \sum_{j=1}^f \mathbf{e}_j (\xi\beta)^j} \quad (2.24)$$

The scaling factor is chosen such that all the moments \mathbf{m}_n are of the same order of magnitude. This improves the conditioning of \mathbf{P}_f and is given by

$$\xi = \frac{\|\mathbf{m}_1\|_2}{\|\mathbf{m}_0\|_2}. \quad (2.25)$$

This requires the computation of the first two moments before finding ξ and then re-calculating the second moment vector with the scaling factor. In addition, expanding the Taylor series in terms of the wave number instead of frequency will significantly reduce the effect of scaling in the derivation of the moments for cases where $f \gg k$ [25]. Scaling the moments by a high frequency amplifies any errors that exist during the computation of the moments. While scaling reduces

the effect of ill-conditioning, the scaled moment matrix is still badly conditioned for small values of q as evident in column two of Table 2.1.

Moment order	Cond(Padé coefficient matrix without scaling)	Cond(Padé coefficient matrix with scaling)
$q = 5$	1	1
$q = 10$	$10.54e^6$	571.14
$q = 15$	$18.78e^{12}$	$67.38e^4$
$q = 20$	$22.81e^{19}$	$29.44e^6$

Table 2.1: Condition number analysis of Padé coefficient matrix \mathbf{P}_f for Case study 1 in Section 5.5.1

2.5 Galerkin Asymptotic Waveform Evaluation

Various enhancements to the AWE process have been presented recently. Amongst them are orthogonalised Krylov subspace methods such as the Galerkin Asymptotic Waveform Evaluation (GAWE) and WCAWE [48–50]. As discussed in the previous section, the accuracy of the numerically computed AWE approximation will only improve with increasing q , if an algorithm is able to recover information about more than one eigenvalue of \mathbf{Z} . It is hence necessary to implement the construction of the bases vectors in Equation 2.22 in a numerically stable way. This is generally done with the help of an orthogonalisation process, where, by imposing an orthogonality relation among the vectors, linear independence can be maintained. Consequently, high-order approximations can be constructed. The GAWE was originally proposed by [48] and is a hybrid Arnoldi AWE process. The GAWE algorithm, outlined in Table 2.2, generates the vectors of the orthonormal matrix

$$\overline{\mathbf{W}}_{m \times q} = [\bar{\mathbf{w}}_1, \bar{\mathbf{w}}_2, \dots, \bar{\mathbf{w}}_q] \quad (2.26)$$

iteratively by utilising a modified Gram-Schmidt process, whose columns define an orthonormal basis. This procedure computes the orthogonal projection of \mathbf{w}_q onto $\text{span}\{\bar{\mathbf{w}}_1 \ \bar{\mathbf{w}}_2 \ \dots \ \bar{\mathbf{w}}_{q-1}\}$. This projection is subtracted from the original vector and the result is normalised to obtain $\bar{\mathbf{w}}_q$. This is, by construction, orthogonal to all the previously computed vectors $\bar{\mathbf{w}}_1, \bar{\mathbf{w}}_2, \dots, \bar{\mathbf{w}}_{q-1}$ and has unit norm. After q iterations, an approximation to \mathbf{x} in Equation 2.14 can be made in terms of these q basis vectors of the form

$$\mathbf{x} \approx \mathbf{x}_q = \overline{\mathbf{W}}_q \mathbf{a}_q = \sum_{n=1}^q \bar{\mathbf{w}}_n \alpha_n \quad (2.27)$$

as explained in Section 2.3 where $\mathbf{a}_q = [\alpha_1, \alpha_2, \dots, \alpha_q]^H$. The quantities \mathbf{a}_q are chosen such that the approximation in Equation 2.27 minimises the residual

$$\mathbf{r}_q = \sum_{n=0}^q \left(\mathbf{Z}^{[n]} \beta^n \right) \sum_{n=1}^q \bar{\mathbf{w}}_n \alpha_n - \sum_{n=0}^q \left(\mathbf{b}^{[n]} \beta^n \right). \quad (2.28)$$

This is conditional on the careful selection of the associated \mathbf{a}_q - specifically, that the residual vector is constrained to be orthogonal to q linearly independent vectors

$$\mathbf{r}_q \perp \overline{\mathbf{W}}_q \quad (2.29)$$

A complete proof is given in [11,51], which shows that this condition is satisfied

by setting

$$\mathbf{a}_q = \left(\sum_{n=0}^q \overline{\mathbf{W}}_q^H \mathbf{Z}^{[n]} \overline{\mathbf{W}}_q \beta^n \right)^{-1} \left(\sum_{n=0}^q \overline{\mathbf{W}}_{m \times q}^H \mathbf{b}^{[n]} \beta^n \right). \quad (2.30)$$

This unique selection ensures that

$$\mathbf{x} \approx \overline{\mathbf{W}}_q \mathbf{a}_q. \quad (2.31)$$

```

 $\mathbf{w}_1 = \mathbf{Z}^{-1}\mathbf{b}$ 
 $\mathbf{H}_{[1,1]} = \|\mathbf{w}_1\|_2$ 
 $\bar{\mathbf{w}}_1 = \mathbf{w}_1\mathbf{H}_{[1,1]}^{-1}$ 
for  $n = 2, \dots, q$ 
   $\mathbf{w}_n = \mathbf{Z}^{-1}(\mathbf{b}^{[n-1]} - \sum_{m=1}^{n-1} \mathbf{Z}^{[m]} \mathbf{w}_{n-m})$ 
  for  $i = 1, \dots, n-1$ 
     $\mathbf{H}_{[i,n]} = \bar{\mathbf{w}}_i^H \mathbf{w}_n$ 
     $\tilde{\mathbf{w}}_n = \mathbf{w}_n - \mathbf{H}_{[i,n]} \bar{\mathbf{w}}_i$ 
  end  $i$ 
   $\mathbf{H}_{[n,n]} = \|\tilde{\mathbf{w}}_n\|_2$ 
   $\bar{\mathbf{w}}_n = \tilde{\mathbf{w}}_n \mathbf{H}_{[n,n]}^{-1}$ 
end  $n$ .

```

Table 2.2: Galerkin Asymptotic Waveform Evaluation Algorithm (GAWE).

2.6 Linearisation of the nonlinear MOR parameters

As an alternative to solving a nonlinear system directly using AWE, linearisation techniques can be used to linearise the nonlinear parameter. Once linearised, a Krylov subspace technique such as the Arnoldi or Lanczos algorithm can be applied. In this section, a linearisation procedure will be reviewed which will be used to linearise

$$\mathbf{Z}(k) \mathbf{x}(k) = \mathbf{b} \quad (2.32)$$

in terms of the nonlinear parameter k . For cases with both sides of Equation 2.32 having frequency-dependent terms, a suitable formulation is discussed later in this section. This technique was recently given in [28,52] and requires expanding the impedance matrix $\mathbf{Z}(k)$ into a Taylor series as:

$$\sum_{n=0}^q \left(\mathbf{Z}^{[n]} \beta^n \right) \mathbf{x}(k) = \mathbf{b} \quad (2.33)$$

$$\left(\mathbf{Z} + \mathbf{Z}^{[1]} \beta + \mathbf{Z}^{[2]} \beta^2 + \mathbf{Z}^{[3]} \beta^3 + \dots + \mathbf{Z}^{[q]} \beta^q \right) \mathbf{x}(k) = \mathbf{b}$$

where q is the order of the truncated Taylor series expansion, $\beta = (k - k_b)$ and $\mathbf{Z}^{[n]}$ denotes the n^{th} derivative of $\mathbf{Z}(k)$ evaluated at k_b and divided by $n!$. By the introduction of new state variables \mathbf{x}_q Equation 2.33 can now be written in matrix form as

$$\left[\begin{pmatrix} \mathbf{Z} & 0 & \dots \\ 0 & +\mathbf{I} & \ddots \\ \vdots & \ddots & \ddots \end{pmatrix} + \beta \begin{pmatrix} \mathbf{Z}^{[1]} & \mathbf{Z}^{[2]} & \mathbf{Z}^{[3]} & \dots & \mathbf{Z}^{[q]} \\ -\mathbf{I} & 0 & 0 & \dots & 0 \\ 0 & -\mathbf{I} & 0 & \dots & 0 \\ \vdots & \ddots & \ddots & \ddots & 0 \\ 0 & 0 & 0 & -\mathbf{I} & 0 \end{pmatrix} \right] \begin{pmatrix} \mathbf{x} \\ \mathbf{x}_0 \\ \mathbf{x}_1 \\ \vdots \\ \mathbf{x}_q \end{pmatrix} = \begin{pmatrix} \mathbf{b} \\ 0 \\ 0 \\ \vdots \\ 0 \end{pmatrix}$$

where \mathbf{I} is a $m \times m$ identity matrix and \mathbf{x}_0 in the above formulation is equal to \mathbf{x} in Equation 2.33. The above formulation is referred to as the expanded Taylor approximation system (ETAS) and can be written in simplified notation as

$$\begin{aligned} [\mathbf{Z}\mathbf{e}\mathbf{1}_{g \times g} + \beta \mathbf{Z}\mathbf{e}\mathbf{2}_{g \times g}] \mathbf{x}_{e_{g \times 1}} &= \mathbf{b}_{e_{g \times 1}} \\ [\mathbf{I}_g + \beta \mathbf{Z}\mathbf{e}\mathbf{1}_g^{-1} \mathbf{Z}\mathbf{e}\mathbf{2}_g] \mathbf{x}_{e_g} &= \mathbf{Z}\mathbf{e}\mathbf{1}_g^{-1} \mathbf{b}_{e_g} \end{aligned} \quad (2.34)$$

where $\mathbf{Ze1}$ and $\mathbf{Ze2}$ are the corresponding expanded matrix of size $g \times g$ ($g = qm$ where q = order of Taylor series Equation 2.33 and m = number of basis function). Equation 2.34 is the starting point for applying a MOR technique such as the Arnoldi or Lanczos processes since the formulation is now linear with respect to β .

Although both techniques produce Krylov subspaces in the reduction process there is no general consensus on which technique is superior. After q steps of the Arnoldi or Lanczos iteration, an orthonormal matrix \mathbf{U}_q is used to generate a ROM of the form

$$\mathbf{x}(k) \approx \mathbf{x}_q(k) = \mathbf{U}_q [\mathbf{I} + \beta \mathbf{U}_q^H \mathbf{Ze1}_g^{-1} \mathbf{Ze2}_g \mathbf{U}_q^H]^{-1} \mathbf{U}_q^H \mathbf{Ze1}_g^{-1} \mathbf{be}_g \quad (2.35)$$

The above ROM can now be efficiently solved at each β rapidly, as the solution requires the inversion of a model $q \ll m$. The Arnoldi procedure is outlined in detail in Chapter 4 and [11, 26, 53], while a detailed analysis of the Lanczos iteration is given in [25, 27, 53, 54].

The Arnoldi and Lanczos algorithm has been shown to work well for linear parameters [25, 26]. However, it has been the experience of this author that when applied to a linearised model, the resultant ROM has several deficiencies. In order to linearise the problem, the size of the original model needs to be increased to several times its original size, which can prove prohibitive for largescale computations. Secondly, due to the increase in system size, achieving a relatively low-order approximation using the Arnoldi or Lanczos algorithm is not guaranteed. Finally, due to higher-order terms being truncated to linearise the problem, the accuracy of the resultant system can be limited.

Chapter 3

EFIE formulations

“The ideal engineer is a composite ... He is not a scientist, he is not a mathematician, he is not a sociologist or a writer; but he may use the knowledge and techniques of any or all of these disciplines in solving engineering problems.”

N. W. Dougherty

This chapter describes the formulation of the electric field integral equation (EFIE) from Maxwell’s laws which will be used extensively throughout this thesis. We present techniques to discretise these integral equations into systems of linear equations that can be solved numerically and consider in detail the singularity associated with EFIE formulations.

3.1 Differential form of Maxwell’s equations

To accurately analyse the electromagnetic behaviour of arbitrary structures, CEM solvers generate a model of the original system based on Maxwell’s equations. The relations and variations of the electric and magnetic fields, charges, and current associated with electromagnetic waves are governed by these equations [9, 34]. When modelling an electromagnetic system the solution of Maxwell’s equations for the unknown electric fields and magnetic fields is the ultimate objective. There are many ways to find solutions to Maxwell’s equations. Unfortunately, due to the complexity of Maxwell’s equations their analytical solution exists only for simple cases. For instance, analytical solutions exist for structures such as a homogeneous sphere or an infinite homogeneous circular cylinder. This limitation creates a necessity to solve Maxwell’s equation using numerical techniques. Due to the finite and discrete nature of computer computation, a CEM solver will approximate the geometry of the original system and approximate the solution space. Classification of CEM solvers is based on differences between the ways the known and unknown quantities are discretised

or converted from continuous functions to discrete representations that a computer can manipulate. These methods include the Finite Element Method (FEM), Finite-Difference Frequency Domain (FDTD) and Method of Moments (MoM).

The differential form of Maxwell's equations is the most widely used representation to solve electrometric problems and is given by

$$\nabla \times \mathcal{E}(\mathbf{r}, t) = -\mathcal{M}^i(\mathbf{r}, t) - \frac{\partial}{\partial t} \mathcal{B}(\mathbf{r}, t) \quad (3.1)$$

$$\nabla \times \mathcal{H}(\mathbf{r}, t) = +\mathcal{J}^i(\mathbf{r}, t) + \frac{\partial}{\partial t} \mathcal{D}(\mathbf{r}, t) \quad (3.2)$$

$$\nabla \cdot \mathcal{B}(\mathbf{r}, t) = 0 \quad (3.3)$$

$$\nabla \cdot \mathcal{D}(\mathbf{r}, t) = \rho_e(\mathbf{r}, t) \quad (3.4)$$

The quantities are

\mathcal{E}	=	electric field intensity (volts/meter)
\mathcal{H}	=	magnetic field intensity (amperes/meter)
\mathcal{D}	=	electric flux density (coulombs/square meter)
\mathcal{B}	=	magnetic flux density (webers/square meter)
\mathcal{J}^i	=	source electric current density (amperes/square meter)
\mathcal{M}^i	=	source magnetic current density (volts/square meter)
ρ_e	=	electric charge density (coulombs/cubic meter)

All these field quantities are assumed to be time-varying and each is a function of locations and times. Equation 3.1 is known as Faraday's law, and states that a time-varying magnetic flux generates an electric field. Ampere's law is described by Equation 3.2, and states that a time-varying electric flux generates a magnetic field. Equations 3.3 and 3.4 are the consequence of Gauss' law which is a statement of the conservation of flux, More specifically, Equation 3.4 implies that the electric flux \mathcal{D} is produced by a charge density ρ_e .

3.2 Time-Harmonic form of Maxwell's equations

In many practical problems involving electromagnetic waves, these time variations in Equations 3.1-3.4 are time-harmonic. These time variation can be represented by $e^{j\omega t}$ and the instantaneous fields can be related to their complex form by the relation

$$\mathcal{A}(\mathbf{r}, t) = \Re e \left(\mathbf{A}(\mathbf{r}) \exp^{j\omega t} \right) \quad (3.5)$$

where the corresponding complex form is only a function of position. By considering Maxwell equations for time-harmonic fields, Equations 3.1-3.4 subsequently become

$$\nabla \times \mathbf{E}(\mathbf{r}) = -\mathbf{M}^i(\mathbf{r}) - j\omega \mathbf{B}(\mathbf{r}) \quad (3.6)$$

$$\nabla \times \mathbf{H}(\mathbf{r}) = \mathbf{J}^i(\mathbf{r}) + j\omega \mathbf{D}(\mathbf{r}) \quad (3.7)$$

$$\nabla \cdot \mathbf{B}(\mathbf{r}) = 0 \quad (3.8)$$

$$\nabla \cdot \mathbf{D}(\mathbf{r}) = \rho_e(\mathbf{r}) \quad (3.9)$$

The corresponding field theory relations for the time-harmonic equations are given as

$$\mathbf{B}(\mathbf{r}) = \mu_0 \mu_r(\mathbf{r}) \mathbf{H}(\mathbf{r}) \quad \mathbf{D}(\mathbf{r}) = \epsilon_0 \epsilon_r(\mathbf{r}) \mathbf{E}(\mathbf{r}) \quad (3.10)$$

where $\mu(\mathbf{r})$ and $\epsilon(\mathbf{r})$ are the non-time varying permeability and permittivity of the medium which are functions of position. The permeability and permittivity are calculated relative to free space and are given by

$$\mu(\mathbf{r}) = \mu_0 \mu_r(\mathbf{r}) \quad \epsilon(\mathbf{r}) = \epsilon_0 \epsilon_r(\mathbf{r}). \quad (3.11)$$

These constitutive parameters are used to characterise the electrical properties of a material. Media where the constitutive parameters are not functions of position are known as homogeneous; otherwise they are referred to as inhomogeneous. Materials whose constitutive parameters are function of frequency are referred to as dispersive. All materials exhibit different degrees of variations in these parameters, this will be discussed in greater detail in Chapter 6.

3.3 Volume equivalence principle

To simplify the above formulation, it is convenient to replace the dielectric and magnetic material present in Equations 3.6-3.7 by equivalent sources radiating in free space. Through the use of the equivalent electric and magnetic current sources, the volume equivalence principle can be used to determine the scattered fields when a material object is introduced in a free-space environment as illustrated in Figure 3.1. In the previous Equation, the free-space environment sources \mathbf{J}^i and \mathbf{M}^i generated the electric and magnetic fields \mathbf{E}^i and \mathbf{H}^i . These sources satisfy Maxwell equations

$$\nabla \times \mathbf{E}^i(\mathbf{r}) = -\mathbf{M}^i(\mathbf{r}) - j\omega\mu_0\mathbf{H}^i(\mathbf{r}) \quad (3.12)$$

$$\nabla \times \mathbf{H}^i(\mathbf{r}) = \mathbf{J}^i(\mathbf{r}) + j\omega\epsilon_0\mathbf{E}^i(\mathbf{r}). \quad (3.13)$$

When these sources radiate in a medium represented by ϵ and μ they generate electric and magnetic fields that satisfy

$$\nabla \times \mathbf{E}(\mathbf{r}) = -\mathbf{M}^i(\mathbf{r}) - j\omega\mu\mathbf{H}(\mathbf{r}) \quad (3.14)$$

$$\nabla \times \mathbf{H}(\mathbf{r}) = \mathbf{J}^i(\mathbf{r}) + j\omega\epsilon\mathbf{E}(\mathbf{r}). \quad (3.15)$$

Subtracting Equations 3.12-3.13 from their corresponding Equations 3.14-3.15 gives

$$\nabla \times (\mathbf{E}(\mathbf{r}) - \mathbf{E}^i(\mathbf{r})) = -j\omega(\mu\mathbf{H}(\mathbf{r}) - \mu_0\mathbf{H}^i(\mathbf{r})) \quad (3.16)$$

$$\nabla \times (\mathbf{H}(\mathbf{r}) - \mathbf{H}^i(\mathbf{r})) = j\omega(\epsilon\mathbf{E}(\mathbf{r}) - \epsilon_0\mathbf{E}^i(\mathbf{r})). \quad (3.17)$$

After defining the difference between the total fields \mathbf{E} and incident fields \mathbf{E}^i , and \mathbf{H} and \mathbf{H}^i as the scattered fields \mathbf{E}^s and \mathbf{H}^s

$$\mathbf{E}^s(\mathbf{r}) = \mathbf{E}(\mathbf{r}) - \mathbf{E}^i(\mathbf{r}) \quad (3.18)$$

$$\mathbf{H}^s(\mathbf{r}) = \mathbf{H}(\mathbf{r}) - \mathbf{H}^i(\mathbf{r}) \quad (3.19)$$

yields the expression

$$\nabla \times \mathbf{E}^s(\mathbf{r}) = -\mathbf{M}(\mathbf{r}) - j\omega\mu_0\mathbf{H}^s(\mathbf{r}) \quad (3.20)$$

$$\nabla \times \mathbf{H}^s(\mathbf{r}) = \mathbf{J}(\mathbf{r}) + j\omega\epsilon_0\mathbf{E}^s(\mathbf{r}). \quad (3.21)$$

The volume equivalent electric and magnetic current densities are defined as

$$\mathbf{J}(\mathbf{r}) = j\omega(\epsilon - \epsilon_0)\mathbf{E}(\mathbf{r}) \quad (3.22)$$

$$\mathbf{M}(\mathbf{r}) = j\omega(\mu - \mu_0)\mathbf{H}(\mathbf{r}) \quad (3.23)$$

which exist only in the material itself ($\epsilon \neq \epsilon_0$ and $\mu \neq \mu_0$) and radiate in a free-space environment. The above equations are useful for finding the scattered fields due to the dielectric obstacles. They explicitly relate the scattered fields and the volume equivalent electric and magnetic current densities. Although the formulation has now been simplified, solving for the electric field \mathbf{E} and magnetic field \mathbf{H} is still difficult. In order to solve for the electric field \mathbf{E} and magnetic field \mathbf{H} in Equations 3.22 and 3.23, typically these fields are expressed in terms of the magnetic vector potential \mathbf{A} and the electric vector potential \mathbf{F} . It can be shown that these potentials satisfy the wave equation expressions

$$\nabla^2\mathbf{A} + k^2\mathbf{A} = -\mu\mathbf{J} \quad (3.24)$$

$$\nabla^2\mathbf{F} + k^2\mathbf{F} = -\epsilon\mathbf{M} \quad (3.25)$$

where the background wave-number is given by

$$k_b = \omega\sqrt{\mu_0\epsilon_0}. \quad (3.26)$$

A solution to Equations 3.24 and 3.25 for \mathbf{A} and \mathbf{F} can be written in the form

$$\mathbf{A}(\mathbf{r}) = \frac{\mu}{4\pi} \iiint_v \mathbf{J}(\mathbf{r}') \frac{e^{-jk_b|\mathbf{r}-\mathbf{r}'|}}{|\mathbf{r}-\mathbf{r}'|} dv' \quad (3.27)$$

$$\mathbf{F}(\mathbf{r}) = \frac{\epsilon}{4\pi} \iiint_v \mathbf{M}(\mathbf{r}') \frac{e^{-jk_b|\mathbf{r}-\mathbf{r}'|}}{|\mathbf{r}-\mathbf{r}'|} dv' \quad (3.28)$$

where the three-dimensional Green's function is given by

$$\mathbf{G}(\mathbf{r}, \mathbf{r}') = \frac{e^{-jk_b|\mathbf{r}-\mathbf{r}'|}}{4\pi|\mathbf{r}-\mathbf{r}'|}. \quad (3.29)$$

The introduction of these potentials simplifies the solution of the magnetic and electric fields. The total \mathbf{E} and \mathbf{H} fields are obtained by the superposition of the individual fields due to the vector potentials \mathbf{A} and \mathbf{F}

$$\mathbf{E} = \mathbf{E}_A + \mathbf{E}_F \quad (3.30)$$

$$\mathbf{H} = \mathbf{H}_A + \mathbf{H}_F \quad (3.31)$$

where

$$\mathbf{E}_A = -j\omega\mathbf{A} - j\frac{1}{\omega\mu\epsilon}\nabla(\nabla \cdot \mathbf{A}) = -j\omega\mathbf{A} - \nabla\phi_e \quad (3.32)$$

$$\mathbf{E}_F = -\frac{1}{\epsilon}\nabla \times \mathbf{F} \quad (3.33)$$

$$\mathbf{H}_A = \frac{1}{\mu}\nabla \times \mathbf{A} \quad (3.34)$$

$$\mathbf{H}_F = -\frac{1}{j\omega\mu}\nabla \times \mathbf{E}_F. \quad (3.35)$$

Now that an expression for the vector potential \mathbf{A} and \mathbf{F} has been formulated, a solution for the electric and magnetic fields can be defined by the mixed potential integral equations (MPIEs) as

$$\mathbf{E}(\mathbf{r}) = -j\omega\mathbf{A} - \frac{1}{\epsilon}\nabla \times \mathbf{F} - \nabla\phi_e \quad (3.36)$$

$$\mathbf{H}(\mathbf{r}) = \frac{1}{\mu}\nabla \times \mathbf{A} - \frac{1}{j\omega\mu}\nabla \times \mathbf{E}_F. \quad (3.37)$$

where ϕ_e is an electric scalar potential given by

$$\phi_e = \frac{1}{4\pi\epsilon_0} \iiint_v \rho_e(\mathbf{r}) \frac{e^{-jk_b|\mathbf{r}-\mathbf{r}'|}}{|\mathbf{r}-\mathbf{r}'|} dv'. \quad (3.38)$$

Combining Equations 3.18-3.19 and Equations 3.39-3.40 results in the volume electric field integral equation (EFIE) and magnetic field integral equation (MFIE) respectively

$$\begin{aligned}
\mathbf{E}^i(\mathbf{r}) &= \mathbf{E}(\mathbf{r}) + j\omega\mathbf{A} + \frac{1}{\epsilon}\nabla \times \mathbf{F} + \nabla\phi_e \\
&= \frac{\mathbf{J}(\mathbf{r})}{j\omega\epsilon_0(\epsilon_r - 1)} + \frac{j\omega\mu}{4\pi} \iiint_v \mathbf{J}(\mathbf{r}') \frac{e^{-jk_b|\mathbf{r}-\mathbf{r}'|}}{|\mathbf{r}-\mathbf{r}'|} dv' \\
&\quad + \frac{1}{\epsilon}\nabla \times \frac{\epsilon}{4\pi} \iiint_v \mathbf{M}(\mathbf{r}') \frac{e^{-jk_b|\mathbf{r}-\mathbf{r}'|}}{|\mathbf{r}-\mathbf{r}'|} dv' \\
&\quad + \nabla \frac{1}{4\pi\epsilon_0} \iiint_v \rho_e(\mathbf{r}) \frac{e^{-jk_b|\mathbf{r}-\mathbf{r}'|}}{|\mathbf{r}-\mathbf{r}'|} dv' \tag{3.39}
\end{aligned}$$

$$\begin{aligned}
\mathbf{H}^i(\mathbf{r}) &= \mathbf{H}(\mathbf{r}) - \frac{1}{\mu}\nabla \times \mathbf{A} + \frac{1}{j\omega\mu}\nabla \times \mathbf{E}_F \\
&= \frac{\mathbf{M}(\mathbf{r})}{j\omega\mu_0(\mu_r - 1)} - \frac{1}{\mu}\nabla \times \frac{\mu}{4\pi} \iiint_v \mathbf{J}(\mathbf{r}') \frac{e^{-jk_b|\mathbf{r}-\mathbf{r}'|}}{|\mathbf{r}-\mathbf{r}'|} dv' \\
&\quad + \frac{1}{j\omega\mu}\nabla \times -\frac{1}{\epsilon}\nabla \times \frac{\epsilon}{4\pi} \iiint_v \mathbf{M}(\mathbf{r}') \frac{e^{-jk_b|\mathbf{r}-\mathbf{r}'|}}{|\mathbf{r}-\mathbf{r}'|} dv'. \tag{3.40}
\end{aligned}$$

These equations are suitable for the analysis of an inhomogeneous material. For scatterers where the penetrable body is homogeneous with constant ϵ_r and μ_r , the problem can be formulated in terms of either the volume or surface EFIE. A detailed explanation of the derivation of the surface EFIE is given in [9, 29]. It should be noted, that in future chapters the expression $(\epsilon_r - 1)$ will be classified as the contrast ζ .

To solve the EFIE for the unknowns, the method of moments (MoM) technique will be applied which discretises the object into m basis cells. This procedure converts the continuous integral equation into a discrete matrix equation. The resulting matrix equation can then be solved by using either direct or iterative solver techniques to yield the unknown coefficients.

In particular, the surface integral equations (SIEs) are discretised by elements composed of a collection of points that are defined only on the surface of the structure. Basis functions are used to approximate the fields and sources locally on the surface discretisation cell. The weighted sum of all the basis functions will approximate quantities over the surface for the entire structure. The matrices formed are dense, but since unknowns are defined only on the surface of the structure, SIE formulations can reduce the number of unknowns. However, SIEs are limited for use with homogeneous structures. For inhomogeneous structures the use of volume integral equations (VIEs) is preferred. VIEs require the entire volume of the scattering object to be discretised. This approach will produce a dense matrix equation. In both cases however, the resulting model size m will be significantly reduced as compared to finite difference methods. This is due to the discretisation being restricted to the surface or volume of the scattering

object as opposed to the surrounding volume [28, 55, 56].

It should be noted that these methods are restricted to the numerical approximations of Maxwell equations at relatively low frequencies. In order to ensure practical engineering accuracy, at least ten discretisation points per wavelength are required [9]. It follows that, for moderately high frequencies, a large number of discretisation points are needed to be able to solve the problem. In such situations approximate ray-based techniques are used, such as the geometrical theory of diffraction and uniform theory of diffraction [29, 57]. These high-frequency methods are based on approximations of Maxwell's equations.

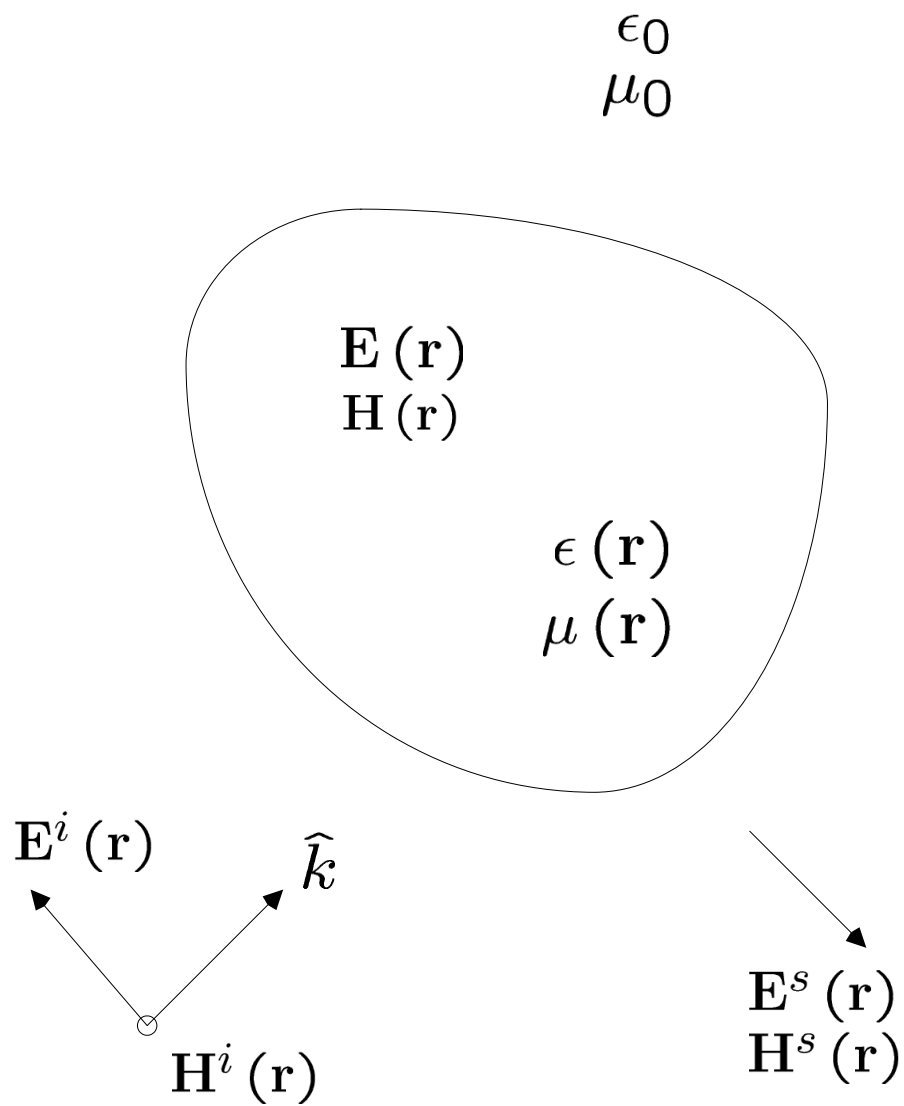


Figure 3.1: An inhomogeneous obstacle illuminated by an incident field.

3.4 Method of Moments

In this section, a numerical technique called the method of moments (MoM) is reviewed. This technique is used to convert the EFIE continuous integral equation from Section 3.3 into a discrete matrix equation. The resultant matrix equation can then be solved for the unknown vector by direct inversion or by utilising an iterative method. Consider the inhomogeneous equation

$$Lf = g \quad (3.41)$$

where L is a continuous linear operator, f is the unknown function to be determined and g represents the known excitation. An approximate solution of the above linear equation may be obtained by converting the unknown function f into a finite series of the form

$$f \cong \sum_{j=1}^m \alpha_j b_j \quad (3.42)$$

where α_i are now the unknown coefficients to be determined. The function

$$b = \{b_1, b_2, \dots, b_m\} \quad (3.43)$$

in Equation 3.42 represents the known basis functions that are defined over the m cells of the discretised structure. Equation 3.42 is now substituted into Equation 3.41 to obtain

$$L \sum_{j=1}^m \alpha_j b_j = g \quad (3.44)$$

and the subsequent residual

$$r_j = \sum_{j=1}^m \alpha_j Lb_j - g. \quad (3.45)$$

In order to minimise this residual over the entire structure, a set of testing functions

$$t = \{t_1, t_2, \dots, t_m\} \quad (3.46)$$

is utilised. Specifically, the residual is constrained to be orthogonal to the m linearly independent testing functions t . This is achieved by taking the inner product between the testing functions and Equation 3.44, which can be expressed as [9, 29, 58]

$$\sum_{j=1}^m \alpha_j \langle t_i, Lb_j \rangle = \langle t_i, g \rangle \quad i = 1, 2, \dots, m \quad (3.47)$$

In the above the inner product of two functions t and b is defined as

$$\langle t, b \rangle = \int_v t b dv. \quad (3.48)$$

Equation 3.47 results in a system of m linear equations each with M unknowns and can be written in matrix form as

$$\mathbf{Z}\mathbf{x} = \mathbf{b} \quad (3.49)$$

where

$$\mathbf{Z} = \begin{pmatrix} \langle t_1, Lb_1 \rangle & \langle t_1, Lb_2 \rangle & \cdots & \langle t_1, Lb_m \rangle \\ \langle t_2, Lb_1 \rangle & \langle t_2, Lb_2 \rangle & \cdots & \langle t_2, Lb_m \rangle \\ \vdots & \vdots & \ddots & \vdots \\ \langle t_m, Lb_1 \rangle & \langle t_m, Lb_2 \rangle & \cdots & \langle t_m, Lb_m \rangle \end{pmatrix} \quad (3.50)$$

$$\mathbf{x} = \begin{pmatrix} \alpha_1 \\ \vdots \\ \alpha_m \end{pmatrix} \quad (3.51)$$

$$\mathbf{b} = \begin{pmatrix} \langle t_1, g \rangle \\ \vdots \\ \langle t_m, g \rangle \end{pmatrix}. \quad (3.52)$$

Equation 3.49 can now be solved for the unknown vector \mathbf{x} by direct inversion or by utilising an iterative method.

The choice of basis and testing functions is the principle issue arising within a method of moment implementation. As discussed in [9, 29, 58], the basis functions b should be linear independent and chosen so that f can be reasonably approximated (Equation 3.42). The testing functions t should also be linearly independent to ensure that the m equations in Equations 3.47 are linearly independent. Furthermore, it is advantageous to choose a set of testing functions that will minimise the computations required to evaluate the inner product of Equation 3.48. A particular choice of testing function is the Dirac-Delta functions

$$t = \{\delta(\mathbf{r} - \mathbf{r}_1), \delta(\mathbf{r} - \mathbf{r}_2), \dots, \delta(\mathbf{r} - \mathbf{r}_m)\} \quad (3.53)$$

where \mathbf{r}_i represents a point at which the Equation 3.44 is to be constrained and the Dirac-Delta function is defined as

$$\delta(\mathbf{r} - \mathbf{r}_i) = \begin{cases} 1 & \text{if } \mathbf{r} - \mathbf{r}_i = 0 \\ 0 & \text{otherwise} \end{cases} \quad i = 1, 2, \dots, m. \quad (3.54)$$

Using the Dirac-Delta testing functions eliminates the integrations associated with the inner product of Equation 3.48 and reduces Equation 3.47 to

$$\sum_{j=1}^m \alpha_j \langle \delta(\mathbf{r} - \mathbf{r}_i), Lb_j \rangle = \langle \delta(\mathbf{r} - \mathbf{r}_i), g \rangle \quad (3.55)$$

$$\sum_{j=1}^m \alpha_j Lb_j|_{\mathbf{r}=\mathbf{r}_i} = g|_{\mathbf{r}=\mathbf{r}_i} \quad i = 1, 2, \dots, m. \quad (3.56)$$

This simplification ensures that the integral equation is constrained only at discrete points over the structure. For best results, this point is usually placed at the centre of the discretisation cell. Due to its acceptable accuracy, along with its computational advantages, this type of testing function is extensively used in electromagnetic problems. These and other computational complexities, associated with the Method of Moments, are discussed in detail in [9, 29, 58].

3.5 Volume EFIE for a two-dimensional homogeneous dielectric object for a TM^z polarisation

In this section, the scattering from a two-dimensional homogeneous dielectric object characterised by a permittivity ϵ and permeability μ using a volume integral formulation is considered. Following the volume equivalence principle as discussed in Section 3.3, the inhomogeneous dielectric and magnetic material present in the problem is replaced by equivalent induced currents and charges. We can now derive a specialised expression for the electromagnetic scattering from a two-dimensional dielectric object illuminated by transverse magnetic (TM^z) incident wave as illustrated in Figure 3.2. For the TM^z polarization, the EFIE appearing in Equation 3.39 can be specialised to

$$\mathbf{E}_z^i(\mathbf{r}) = \mathbf{E}_z(\mathbf{r}) + j\omega\mathbf{A}_z \quad (3.57)$$

where for the TM^z case the magnetic vector potential has been reduced to

$$A_z(\mathbf{r}) = \int_v J_z(\mathbf{r}') G(\mathbf{r}, \mathbf{r}') dv' \quad (3.58)$$

and the electric scalar potential $\phi_e = 0$. Subject to $\mu = \mu_0$ the electric vector potential now becomes

$$\mathbf{F} = 0. \quad (3.59)$$

Additionally, for the two-dimensional case the Green's function is now given by

$$G(\mathbf{r}, \mathbf{r}') = \frac{1}{4j} H_0^{(2)}(k_b |\mathbf{r} - \mathbf{r}'|). \quad (3.60)$$

where k_b is the background wave number defined in Equation 3.26 and $H_0^{(2)}$ is the zero-order Hankel function of the second kind. By substituting Equation 3.22 into Equation 3.57, the primary unknown in the EFIE can be posed in terms of the polarisation current density $J_z(\mathbf{r}')$ as

$$E_z^i(\mathbf{r}) = \frac{J_z(\mathbf{r}')}{j\omega\epsilon_0(\epsilon_r(\mathbf{r}) - 1)} + jk_b\eta \int_v J_z(\mathbf{r}') \frac{1}{4j} H_0^{(2)}(k_b |\mathbf{r} - \mathbf{r}'|) dv' \quad (3.61)$$

where η is the background impedance given by

$$\eta = \sqrt{\frac{\mu_0}{\epsilon_0}}. \quad (3.62)$$

To solve the EFIE for the unknown volume current density, the continuous EFIE

is discretised by the MoM as described in Section 3.4. By employing this discretisation procedure, the integral equation can be converted into a finite linear system of equations which approximate the original system. This approach requires the discretisation of the structure into m cells as illustrated in Figure 3.2. The unknown function $J_z(\mathbf{r}')$ are then expanded into a finite series of the form

$$J_z(\mathbf{r}') \cong \sum_{j=1}^m \alpha_j b_j(\mathbf{r}') \quad (3.63)$$

where pulse basis functions are utilised

$$b_j(\mathbf{r}') = \begin{cases} 1 & \text{if } \mathbf{r}' \in \text{cell } j \\ 0 & \text{otherwise.} \end{cases} \quad (3.64)$$

Substituting Equation 3.63 into Equation 3.61 yields

$$\begin{aligned} E_z^i(\mathbf{r}) &\cong \sum_{j=1}^m \alpha_j \frac{b_j(\mathbf{r}')}{j\omega\epsilon_0(\epsilon_r(\mathbf{r}) - 1)} + jk_b\eta \int_v \sum_{j=1}^m \alpha_j b_j(\mathbf{r}') \frac{1}{4j} H_0^{(2)}(k_b|\mathbf{r} - \mathbf{r}'|) dv' \\ &= \sum_{j=1}^m \alpha_j \left(\frac{b_j(\mathbf{r}')}{j\omega\epsilon_0(\epsilon_r(\mathbf{r}) - 1)} + jk_b\eta \int_v b_j(\mathbf{r}') \frac{1}{4j} H_0^{(2)}(k_b|\mathbf{r} - \mathbf{r}'|) dv' \right) \\ &= \sum_{j=1}^m \alpha_j \left(\frac{\eta b_j(\mathbf{r}')}{jk_b(\epsilon_r(\mathbf{r}) - 1)} + \frac{k_b\eta}{4} \int_v b_j(\mathbf{r}') H_0^{(2)}(k_b|\mathbf{r} - \mathbf{r}'|) dv' \right). \end{aligned} \quad (3.65)$$

As prescribed in Section 3.4, a set of testing functions t_i is applied to Equation 3.65, resulting in

$$\langle E_z^i(\mathbf{r}), t_i \rangle = \sum_{j=1}^m \alpha_j \left\langle \left(\frac{\eta b_j(\mathbf{r}')}{jk_b(\epsilon_r(\mathbf{r}) - 1)} + \frac{k_b\eta}{4} \int_v b_j(\mathbf{r}') H_0^{(2)}(k_b|\mathbf{r} - \mathbf{r}'|) dv' \right), t_i \right\rangle. \quad (3.66)$$

Using Dirac-Delta testing functions (Equation 3.53), Equation 3.66 can be written as

$$\begin{aligned}
\int_v E_z^i(\mathbf{r}) \delta(\mathbf{r} - \mathbf{r}_i) dv &= \sum_{j=1}^m \alpha_j \int_v \delta(\mathbf{r} - \mathbf{r}_i) \left(\frac{\eta b_j(\mathbf{r}')}{jk_b(\epsilon_r(\mathbf{r}) - 1)} \right. \\
&\quad \left. + \frac{k_b \eta}{4} \int_v b_j(\mathbf{r}') H_0^{(2)}(k_b |\mathbf{r} - \mathbf{r}'|) dv' \right) dv \\
E_z^i(\mathbf{r}_i) &= \sum_{j=1}^m \alpha_j \left(\frac{\eta b_j(\mathbf{r}')}{jk_b(\epsilon_r(\mathbf{r}_i) - 1)} \right. \\
&\quad \left. + \frac{k_b \eta}{4} \int_v b_j(\mathbf{r}') H_0^{(2)}(k_b |\mathbf{r}_i - \mathbf{r}'|) dv' \right) \\
E_z^i(\mathbf{r}_i) &= \sum_{j=1}^m \alpha_j \left(\frac{\eta}{jk_b(\epsilon_r(\mathbf{r}_i) - 1)} \right. \\
&\quad \left. + \frac{k_b \eta}{4} \int_{\text{cell } i} H_0^{(2)}(k_b |\mathbf{r}_i - \mathbf{r}'|) dv' \right). \quad (3.67)
\end{aligned}$$

Equation 3.67 produces m equations with m unknowns and can be represented in matrix form as

$$\begin{pmatrix} Z_{1,1} & Z_{1,2} & Z_{1,3} & \cdots & Z_{1,m} \\ Z_{2,1} & Z_{2,2} & Z_{2,3} & \cdots & Z_{2,m} \\ Z_{3,1} & Z_{3,2} & Z_{3,3} & \cdots & Z_{3,m} \\ \vdots & \vdots & \vdots & \ddots & \vdots \\ Z_{m,1} & Z_{m,2} & Z_{m,3} & \cdots & Z_{m,m} \end{pmatrix} \begin{pmatrix} \alpha_1 \\ \alpha_2 \\ \alpha_3 \\ \vdots \\ \alpha_m \end{pmatrix} = \begin{pmatrix} b_1 \\ b_2 \\ b_3 \\ \vdots \\ b_m \end{pmatrix}.$$

For ease of notation, the above matrix equation will be represented throughout this thesis by

$$\mathbf{Z}\mathbf{x} = \mathbf{b} \quad (3.68)$$

where the \mathbf{Z} matrix is referred to as the impedance matrix whose entries represent the coupling between different cells in the discretisation. It is given by

$$Z_{i,j} = \frac{k_b \eta}{4} \int_{\text{cell } i} H_0^{(2)}(k_b |\mathbf{r}_i - \mathbf{r}'|) dv' \quad i \neq j \quad (3.69)$$

and

$$Z_{i,j} = \frac{\eta}{jk_b(\epsilon_{ri} - 1)} + \frac{k_b \eta}{4} \int_{\text{cell } i} H_0^{(2)}(k_b |\mathbf{r}_i - \mathbf{r}'|) dv' \quad i = j. \quad (3.70)$$

The \mathbf{b} vector contains information about the incident fields. For a TM^z polarised

incident plane wave (see Figure 3.2), E_z^i can be expressed as

$$b_i = E_a \exp^{-j\mathbf{k} \cdot \mathbf{r}_i} \quad (3.71)$$

where E_a is the amplitude and \mathbf{k} is the propagation vector given by

$$\mathbf{k} = k_x \hat{x} + k_y \hat{y} + k_z \hat{z}. \quad (3.72)$$

Alternatively, for a line source, the elements are given by

$$b_i = \frac{j\omega\mu_0}{4} H_0^{(2)}(k_b |\mathbf{r}_i - \mathbf{r}_s|) \quad (3.73)$$

where \mathbf{r}_s is the source location. The plane wave incident field will be extensively used throughout this work since an analytical expression for the scattered field of select geometries is available for this type of source.

The solution of the matrix Equation 3.68 yields the coefficients α_j . Once the current density J_z is obtained, other quantities such as radar cross-section (RCS)

$$\sigma_{\text{TM}}(\phi) \cong \frac{k_b \eta^2}{4} \left[\sum_{i=1}^M \alpha_i \frac{2\pi a_i}{k_b} J_1(k_b a_i) e^{jk_b(x_i \cos\phi + y_i \sin\phi)} \right]^2, \quad (3.74)$$

can be calculated [9]. J_1 is the Bessel function of order 1, a_i is the equivalent radius for cell i (see Section 3.6.1) and x_i is the centroid x coordinates of cell i . The scattered field at any point in space E_z^s can now be obtained by using Equation 3.18.

In the next chapter, the EFIE of Equation 3.61 will be specialised to have the electric field E_z as the primary unknown, yielding

$$E_z^i(\mathbf{r}) = E_z(\mathbf{r}) + \frac{jk_b^2 \zeta}{4} \int_v E_z(\mathbf{r}) H_0^{(2)}(k_b |\mathbf{r} - \mathbf{r}'|) dv'. \quad (3.75)$$

As before, the integral equation is discretised using the MoM technique with m pulse basis functions and Dirac testing functions, leading to the matrix equation

$$(\mathbf{I} + \mathbf{GA}) \mathbf{x} = \mathbf{b} \quad (3.76)$$

where \mathbf{b} is a vector containing information regarding the incident fields and \mathbf{G} is a $m \times m$ matrix containing coupling information between the basis functions. The element in the i^{th} row and j^{th} column of \mathbf{G} is given by

$$G_{i,j} = \frac{jk_b^2}{4} \int_{\text{cell } i} H_0^{(2)}(k_b |\mathbf{r}_i - \mathbf{r}'|) dv'. \quad (3.77)$$

The contrast matrix \mathbf{A} in Equation 3.76 is a diagonal matrix with diagonal entries

given by

$$A_{i,i} = \zeta_i \quad (3.78)$$

where ζ_i is the contrast in the i^{th} pulse basis function domain

$$\zeta_i = (\epsilon_r - 1) = \left(\frac{\epsilon_i}{\epsilon_0} - 1 \right). \quad (3.79)$$

This formulation will be the starting point for the contrast-sweep analysis of the next chapter.

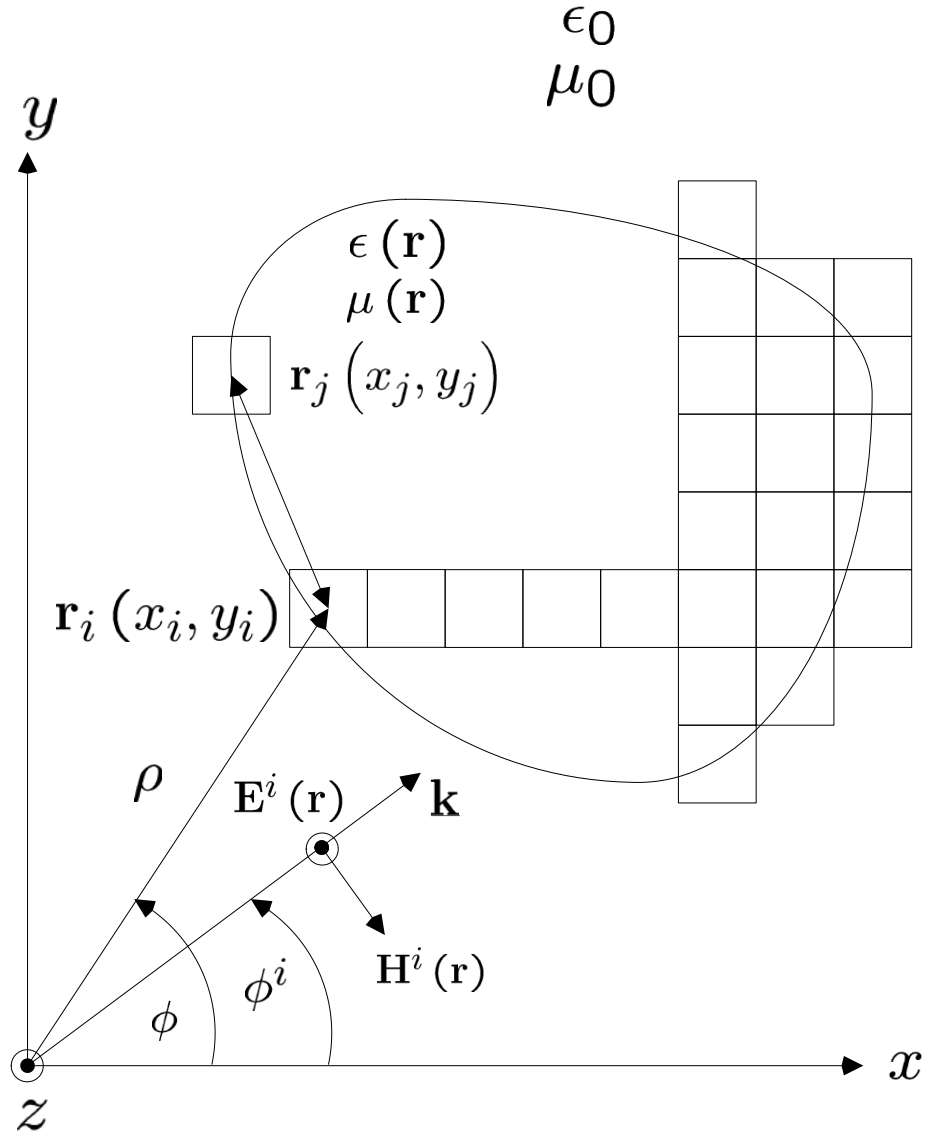


Figure 3.2: TM^z wave scattering from a partial discretised structure.

3.6 Green's function singularity

Due to the singularity of the Green's function, careful consideration of the evaluation of Equation 3.70 must be undertaken. This singularity is due to the Hankel function becoming singular for cases where $|\mathbf{r} - \mathbf{r}'| = 0$, which occurs in the diagonal elements of the impedance matrix. Due to the large contribution of the singular components it is important to evaluate its effect accurately. In this section, an overview of how to evaluate this singularity is discussed.

3.6.1 Analytical evaluation of Green's function singularity using circle cell approximation

If the discretisation cells are approximated by a circle of the same area, the integrals of Equations 3.69-3.70 can be evaluated analytically using [9]

$$\int_{\phi'=0}^{2\pi} \int_{\rho'=0}^a H_0^{(2)}(k_b |\mathbf{r} - \mathbf{r}'|) \rho' d\rho' d\phi' = \begin{cases} \frac{2\pi a}{k_b} J_0(k_b \rho) H_1^{(2)}(ka) - \frac{4j}{k_b^2} & \rho < a \\ \frac{2\pi a}{k_b} J_1(ka) H_0^{(2)}(k_b \rho) & \rho > a \end{cases} \quad (3.80)$$

where

$$\rho = \sqrt{(x_i - x')^2 + (y_i - y')^2}. \quad (3.81)$$

(ρ', ϕ') are polar coordinates based on a coordinate origin at the centre of cell j . Since we evaluate the singularity at the centre of the cell, the instant $\rho = a$ is not explicitly derived. The first solution given in Equation 3.80 applies if the observation point is at the centre of the circular cell as illustrated in Figure 3.3. The singularity is now replaced by analytically evaluating the contribution not from the centre of the cell but from the entire area of the cell $\rho' d\rho' d\phi'$. When ρ_{ij} is greater than the radius a of the circular region, the second solution is used. Substituting these approximations into Equations 3.69 and 3.70 yields

$$Z_{i,j} = \frac{\eta\pi a_i}{2} J_1(k_b a_i) H_0^{(2)}(k_b |\mathbf{r}_i - \mathbf{r}_j|) \quad i \neq j. \quad (3.82)$$

and

$$Z_{i,j} = \frac{\eta\pi a_i}{2} H_1^{(2)}(k_b a_i) - \frac{j\eta\epsilon_{ri}}{k_b (\epsilon_{ri} - 1)} \quad i = j. \quad (3.83)$$

Numerical calculation in [59] has shown that minimal error is incurred in approximating square cells with circular cells of the same area of cross-section.

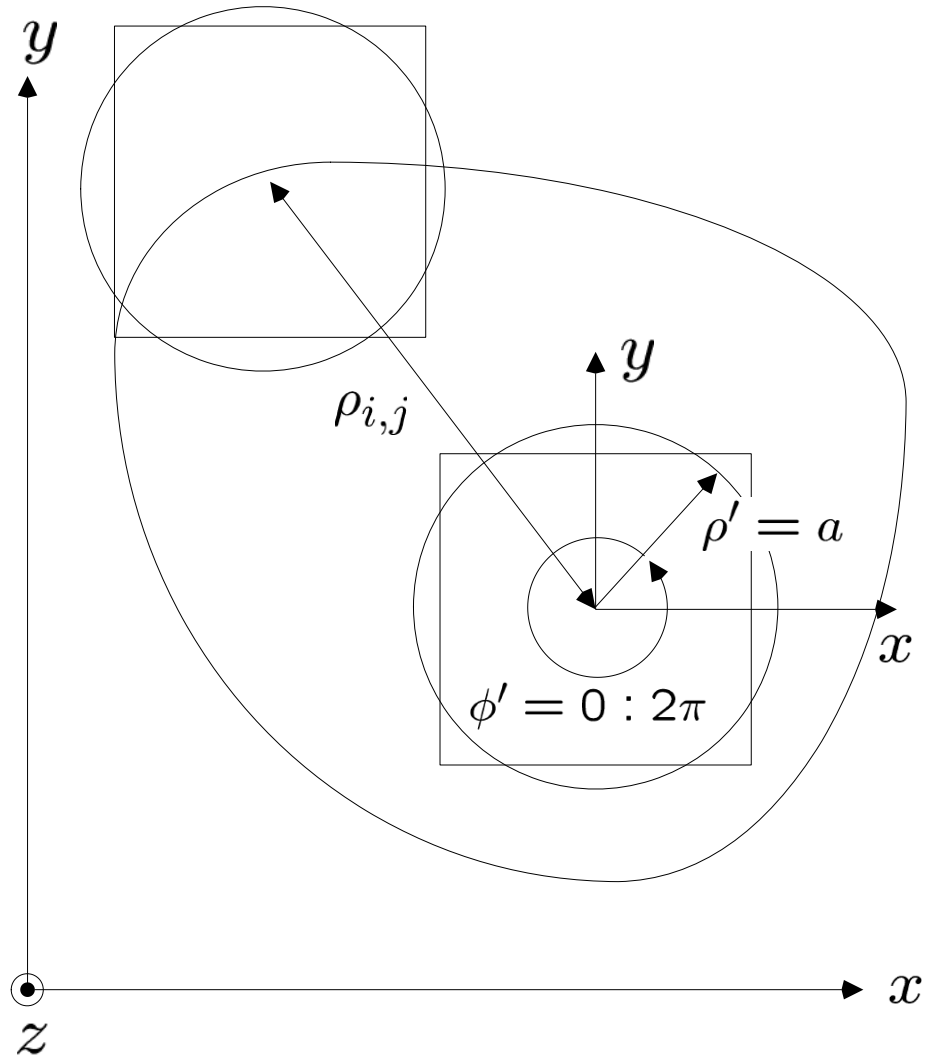


Figure 3.3: Analytical circle-cell approximation.

3.6.2 Numerical evaluation of Green's function singularity using triangular cells

The previous method makes approximations regarding the shape of the cell in order to remove the singularity. This introduces a modelling error into the analysis. In order to discretise a complex object accurately, it is recommended to use triangular cell discretisation. The following method is a fully numerical approach which has been implemented by [60]. This is more pertinent than an equivalent analytical approximation as no approximations regarding the shape of the object are made. In this section, the procedure by [60] is outlined which was derived for use with the three-dimensional surface EFIE. The results for the two-dimensional volume integral equation are presented.

Figure 3.4 illustrates the triangle T representing the self-interaction cell that is being evaluated. \mathbf{r}_0 and \mathbf{r}' are the observation point and integration points respectively, defined on a coordinate system (u, v) . The auxiliary polar coordinate system is defined by (ρ, ϕ) where ρ is the distance between the integration and observation points. ϕ_a^i and ϕ_b^i are the angles associated with the endpoints of δT_i relative to the coordinate system (u, v) . $R(\phi)$ is the distance of any point of δT_i to the observation point which is a function of ϕ , where $\phi_a^i < \phi < \phi_b^i$.

The singularity is isolated inside a disc of radius ϵ and evaluated analytically. The self contribution is evaluated numerically from the remaining area of the cell. This is achieved by splitting the triangle into three sub-triangles δT_i and summing the contribution from each sub-triangle. Observe that

$$\vartheta(\phi) = \vartheta_1(\phi) + \sum_{i=1}^3 \vartheta_2^i(\phi) \quad (3.84)$$

with

$$\vartheta_1(\phi) = \int_0^{2\pi} \lim_{\epsilon \rightarrow 0} \int_0^\epsilon \left(1 - j \frac{2}{\pi} \ln \left(\frac{\gamma k_b \rho}{2} \right) \right) \rho d\rho d\phi = 0 \quad (3.85)$$

$$\vartheta_2^i(\phi) = \int_{\phi_A^i}^{\phi_B^i} \lim_{\epsilon \rightarrow 0} \int_\epsilon^{R(\phi)} \left(1 - \frac{2j}{\pi} \ln \left(\frac{\gamma k_b \rho}{2} \right) \right) \rho d\rho d\phi. \quad (3.86)$$

Setting

$$x = \frac{\gamma k_b \rho}{2} \quad dx = \frac{\gamma k_b d\rho}{2} \quad \text{gives} \quad \rho = \frac{2x}{\gamma k_b} \quad d\rho = \frac{2dx}{\gamma k_b} \quad (3.87)$$

and interchanging the limits yields [61]

$$\vartheta_2^i(\phi) = \int_{\phi_A^i}^{\phi_B^i} \lim_{\epsilon \rightarrow 0} \frac{\rho^2}{2} \Big|_{\epsilon}^{R(\phi)} d\phi - \frac{2j}{\pi} \int_{\phi_A^i}^{\phi_B^i} \lim_{\epsilon \rightarrow 0} \int_{x=\frac{\gamma k_b \epsilon}{2}}^{\frac{\gamma k_b R(\phi)}{2}} \ln(x) \left(\frac{2}{k_b \gamma} \right)^2 x dx d\phi. \quad (3.88)$$

Using the identities

$$\int_{x=0}^{\frac{\gamma k_b R(\phi)}{2}} \ln(x) x dx = \left(\frac{x^2}{2} \ln(x) - \frac{x^2}{4} \right) \Big|_0^{\frac{\gamma k_b R(\phi)}{2}} \quad \lim_{x \rightarrow 0} \frac{x^2}{2} \ln(x) = 0 \quad (3.89)$$

produces

$$\begin{aligned} \vartheta_2^i(\phi) &= \int_{\phi_A^i}^{\phi_B^i} \lim_{\epsilon \rightarrow 0} \frac{R(\phi)^2 - \epsilon^2}{2} d\phi - \frac{2j}{\pi} \left(\frac{2}{k_b \gamma} \right)^2 \int_{\phi_A^i}^{\phi_B^i} \lim_{\epsilon \rightarrow 0} \left[\left(\left(\frac{\gamma k_b R(\phi)}{2} \right)^2 \right. \right. \\ &\quad \left. \frac{1}{2} \ln \left(\frac{\gamma k_b R(\phi)}{2} \right) - \left(\frac{\gamma k_b R(\phi)}{2} \right)^2 \frac{1}{4} \right) \\ &\quad \left. - \left(\left(\frac{\gamma k_b \epsilon}{2} \right)^2 \frac{1}{2} \ln \left(\frac{\gamma k_b \epsilon}{2} \right) - \left(\frac{\gamma k_b \epsilon}{2} \right)^2 \frac{1}{4} \right) \right] \\ &= \int_{\phi_A^i}^{\phi_B^i} \frac{R(\phi)^2}{2} d\phi - \frac{2j}{\pi} \int_{\phi_A^i}^{\phi_B^i} \left(\frac{R(\phi)^2}{2} \ln \left(\frac{\gamma k_b R(\phi)}{2} \right) - \frac{R(\phi)^2}{4} \right) d\phi \\ &= \int_{\phi_A^i}^{\phi_B^i} \frac{R(\phi)^2}{2} - \frac{j R(\phi)^2}{\pi} \ln \left(\frac{\gamma k_b R(\phi)}{2} \right) + \frac{j R(\phi)^2}{2\pi} d\phi \\ &= \int_{\phi_A^i}^{\phi_B^i} R(\phi)^2 \left[\frac{j}{2\pi} \left(1 - 2 \ln \left(\frac{\gamma k_b R(\phi)}{2} \right) \right) \right] d\phi. \end{aligned} \quad (3.90)$$

Once the integrals have been evaluated, they can be numerically implemented by using the Gaussian quadrature formula [60, 62]

$$\vartheta(\phi) = \sum_{i=1}^3 \vartheta_2^i(\phi) = \sum_{i=1}^3 \left(\sum_{j=1}^{\alpha} w_j f_i(\phi_j) \right) \quad (3.91)$$

where $\{w_j\}_{j=1,\dots,J}$ and $\{\phi_j\}_{j=1,\dots,J}$ are the weights and abscissas adopted for each ϕ^i . Substituting Equation 3.91 into Equation 3.70 yields the self-term impedance matrix terms

$$Z_{i,j} = \frac{\eta}{jk_b(\epsilon_{ri} - 1)} + \frac{k_b \eta}{4} \vartheta(\phi) \quad i = j. \quad (3.92)$$

The benefit of this technique is that no approximations are made regarding the shape of the basis cell. This technique results in an accurate evaluation of the

impedance matrix self-term elements for the two-dimensional volume integral equation.

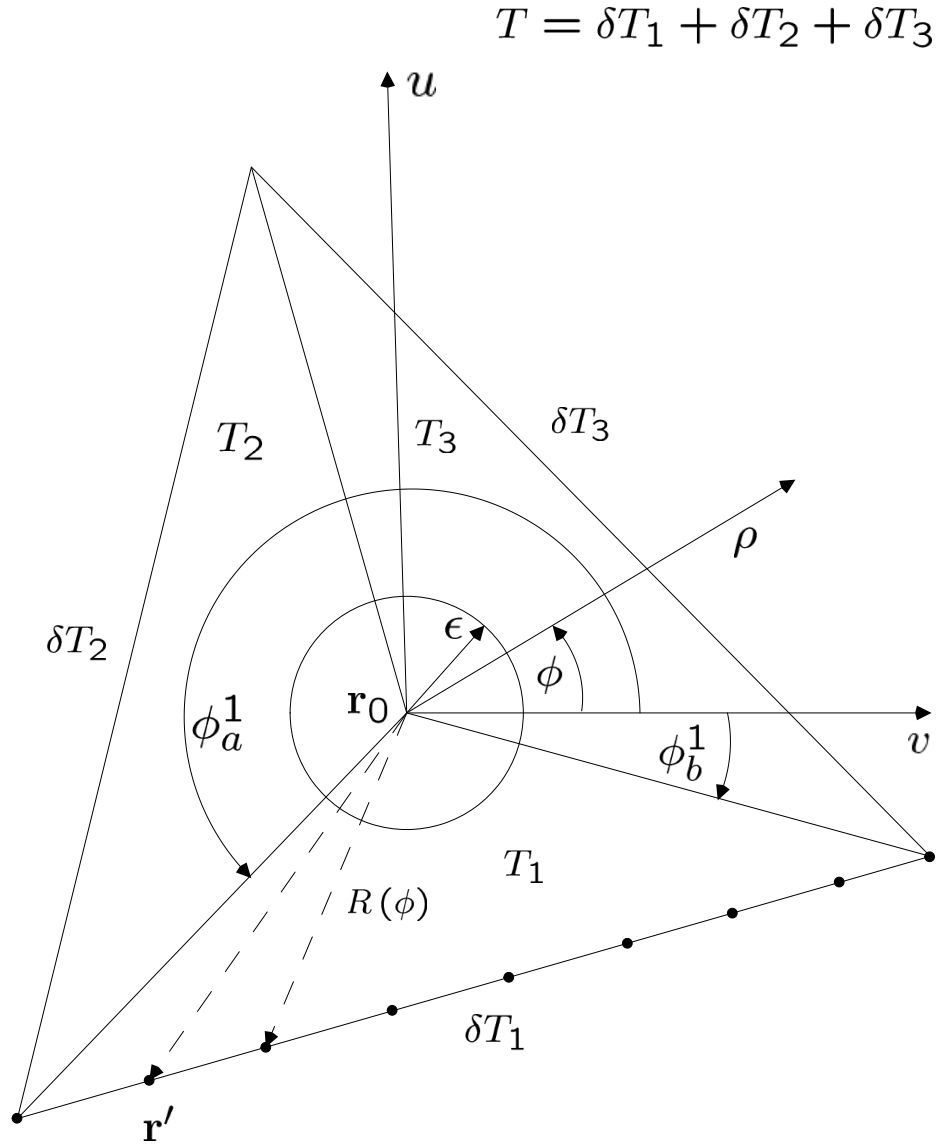


Figure 3.4: Numerical evaluation of Green's function singularity using triangular cells.

3.7 TM^z analytical solution for two-dimensional homogeneous dielectric circular cylinder

For select geometries, an analytical expression can be derived for the scattered fields. In this section, the analytical solution for scattering from a two-dimensional dielectric circular cylinder with radius a is presented [63, 64]. This expression provides a comparison for the numerical EFIE formulation. Let us first consider a TM^z polarised incident plane wave incident upon a dielectric circular cylinder that is

$$E_z^i = E_a \exp^{-j\mathbf{k} \cdot \mathbf{r}} \quad (3.93)$$

Using the wave transformation of [63], the incident field can be expressed as

$$E_z^i = \exp^{-j\mathbf{k} \cdot \mathbf{r}} = \sum_{n=-\infty}^{\infty} j^{-n} J_n(k\rho) \exp^{jn\phi} \quad (3.94)$$

where J_n is the Bessel function of order n . The analytical solution for the scattered field external to the cylinder E_z^s is given by

$$E_z^s = \sum_{n=-\infty}^{\infty} j^{-n} A_n^{\text{TM}^z} H_n^{(2)}(k\rho) \exp^{jn\phi} \quad (3.95)$$

with

$$A_n^{\text{TM}^z} = \frac{\frac{\eta_b}{\eta_d} J_n(ka) J_n^{[1]}(k_d a) - J_n^{[1]}(ka) J_n(k_d a)}{J_n(k_d a) H_n^{(2)[1]}(ka) - \frac{\eta_b}{\eta_d} J_n^{[1]}(k_d a) H_n^{(2)}(ka)} \quad (3.96)$$

where η_b and η_d are the background and dielectric wave impedances, while k_d is the wave number in the dielectric. $J_n^{[1]}$ and $H_n^{(2)[1]}$ represent the 1st derivatives of the Bessel and Hankel function, respectively given by

$$\Psi_n^{[1]}(x) = \frac{1}{2} \{ \Psi_{n-1}(x) - \Psi_{n+1}(x) \} \quad (3.97)$$

where $\Psi_n^{[1]}(x)$ denotes the 1st derivative of either J_n or $H_n^{(2)}$. Finally, the expression for the total scattered field inside the cylinder is given by

$$E_z = \sum_{n=-\infty}^{\infty} j^{-n} B_n^{\text{TM}^z} J_n(k(\rho)\rho) \exp^{jn\phi} \quad (3.98)$$

with

$$B_n^{\text{TM}^z} = \frac{\frac{-2j}{\pi ka}}{J_n(k_d a) H_n^{(2)[1]}(ka) - \frac{\eta_b}{\eta_d} J_n^{[1]}(k_d a) H_n^{(2)}(ka)}. \quad (3.99)$$

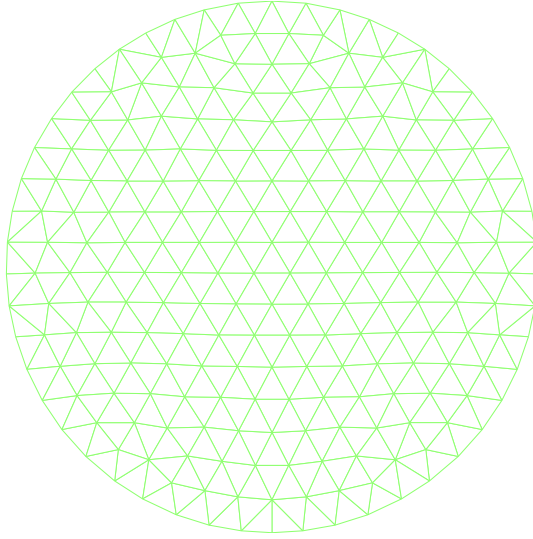
Expressions 3.95 and 3.98 will be referred to as the Mie series [63] and will be used extensively throughout this thesis.

3.8 TM^z example for two-dimensional homogeneous dielectric circular cylinder

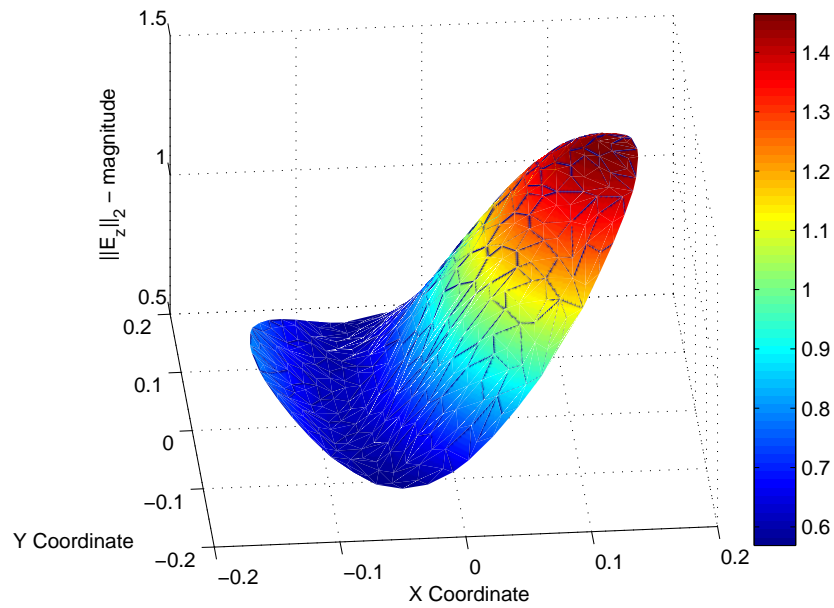
By way of illustrating some of the concepts described previously, a selection of plots are presented for a homogeneous dielectric cylinder of radius $0.16m$ centred at the origin and with a relative permittivity of $\epsilon_r = 2.5$. The cylinder is discretised using $m = 400$ triangular cells (Figure 3.5(a)). It is illuminated by a TM^z plane wave radiating at a frequency of $f = 300$ MHz. The Mie series, as described in Section 3.7, is used to independently evaluate the accuracy of the MoM solution. Specifically, the MoM solution using the numerical and analytical evaluation of the Green's function singularity is compared, as given in Sections 3.6.2 and 3.6.1 respectively.

Figure 3.5(b) shows the magnitude of the internal field $\|E_z\|_2$ obtained using the Mie series. Comparison of the Mie series against the MoM using the numerical and analytical evaluation of Green's function singularity for $\|E_z\|_2$ calculated at evenly spaced points along the x axis of the cylinder is displayed in Figure 3.6(a). It is apparent from this figure that there is minimal difference between these two techniques. This is confirmed in Figure 3.6(b), which indicates, on average, a 1% relative error.

The total scattered field E_z^s , at an observation radius of $0.32m$ and angles $\phi = 0 : 2\pi$, is illustrated in Figure 3.7(a). Finally, Figure 3.7(b) depicts the RCS using Equation 3.74 for a monostatic setup $\phi_s = 0 : 2\pi$ comparing the two singularity techniques. Monostatic is the term given to an experimental setup where the transmitter and receiver are in the same location. Conversely bistatic setup comprises of a transmitter and receiver located at different positions.

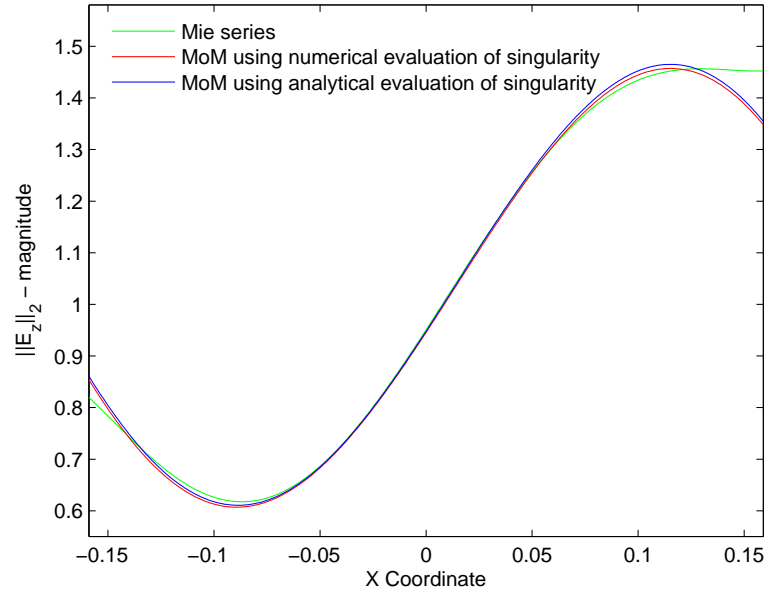


(a) Discretised cylinder using $m = 400$ triangular cells centred @ (0,0)

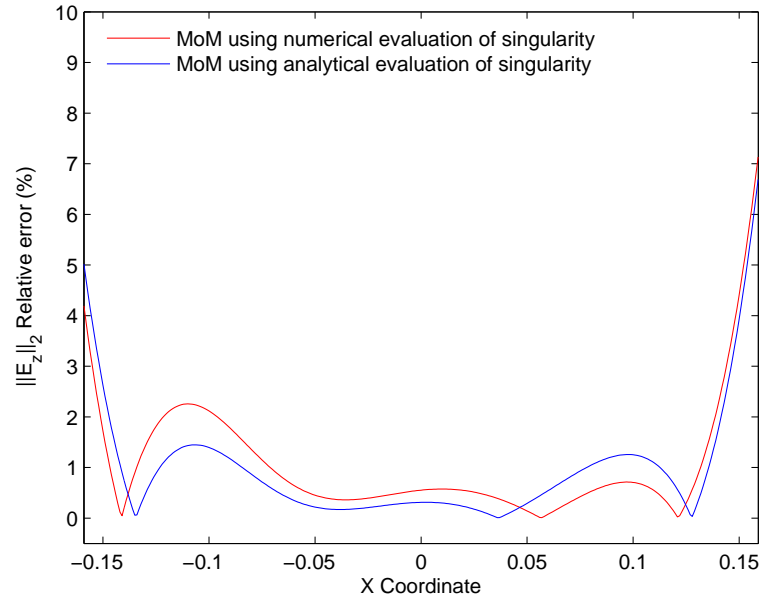


(b) Mie series $\|E_z\|_2$ - magnitude plot

Figure 3.5: Part A: Two-dimensional homogeneous dielectric circular cylinder

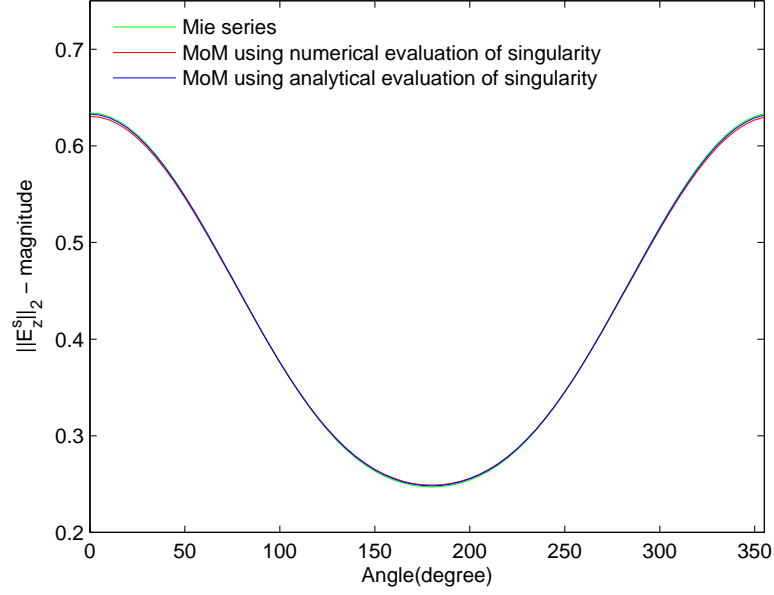


(a) $\|E_z\|_2$ along the x axis, comparing the Mie series against the Method of Moments, using the numerical and analytical evaluation of Green's function singularity from Sections 3.6.2 and 3.6 respectively.

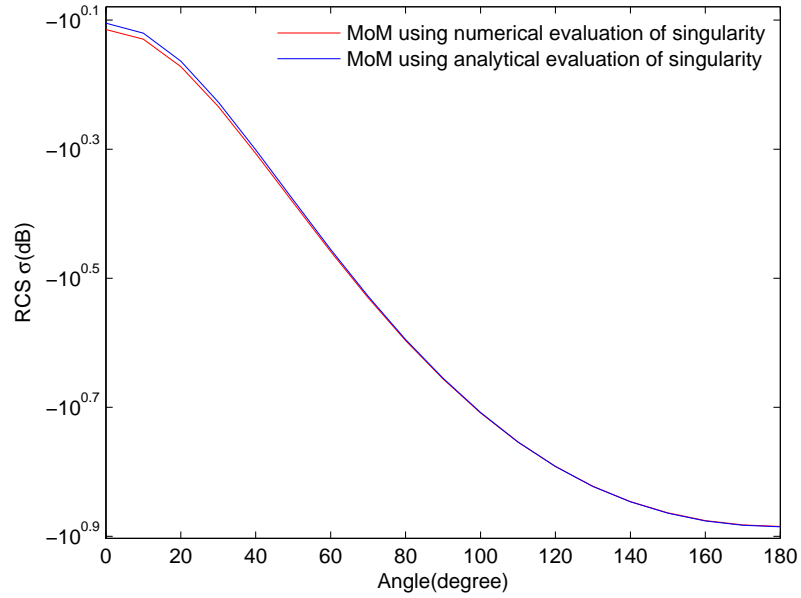


(b) Percentage relative error for Figure 3.6(a) comparing the MoM to the Mie series solution

Figure 3.6: Part B: Comparison of the Method of Moments using the numerical evaluation against the analytical evaluation for a two-dimensional homogeneous dielectric circular cylinder



(a) $\|E_z^s\|_2$ for bi-static scattering over range of angles $\phi = 0 : 2\pi$ at radius of $0.32m$, comparing the Mie series against the Method of Moments, using the numerical and analytical evaluation of Green's function singularity.



(b) $\sigma_{TM}(\Phi)$ RCS comparing Method of Moments using the numerical and analytical evaluation of Green's function singularity

Figure 3.7: Part C: Comparison of the Method of Moments using the numerical evaluation against the analytical evaluation for a two-dimensional homogeneous dielectric circular cylinder

Chapter 4

Fast contrast-sweep analysis using the Arnoldi MOR algorithm

“Do not worry about your difficulties in Mathematics. I can assure you mine are still greater.”

Albert Einstein

This chapter presents a MOR algorithm applicable to the volume EFIE formulation in a contrast-sweep analysis. The Arnoldi algorithm will be used to circumvent the computational complexity associated with the repeated numerical solution of full-scattering problems for the total fields at each step in contrast or source location. Contrast-sweep problems are associated with scattering analysis where the material properties such as the permittivity, permeability and conductivity are varied over a range, to produce the scattered fields.

The Arnoldi iterative method is based on the projection of an m -dimensional problem onto a lower-dimensional Krylov subspace. As this chapter will demonstrate, the Arnoldi algorithm can produce accurate low-order approximations for a relatively low computational cost.

It will be shown that this method can be used to produce ROMs for homogeneous structures. Additionally, an approximate extension that accounts for wave scattering from an inhomogeneous object using a two-dimensional volume integral formulation is also presented. This approximation will be shown to be exact in the limit as the level of reduction approaches zero. Application of the Arnoldi algorithm for simulations with multiple deviations of the source location, for a fixed contrast profile, will also be demonstrated. Finally, a shift-and-invert Arnoldi extension will be introduced which can improve the range of the Arnoldi iteration in a contrast-sweep analysis.

The chapter is organised as follows. The basic Arnoldi algorithm and factorisation are introduced in Section 4.2. The Hessenberg decomposition of the

impedance matrix \mathbf{G} using an orthogonal reduction is reviewed in Section 4.2.1. Loss of orthogonality amongst the Arnoldi vectors \mathbf{u}_n is investigated in Section 4.2.2. How to generate a reduced order model using the Arnoldi method for application to scattering from a homogeneous object is introduced in Section 4.3. The extension of the Arnoldi algorithm to wave scattering from an inhomogeneous object is derived in Section 4.4. Computational issues associated with the Arnoldi algorithm are analysed in Sections 4.4.1, 4.4.2, and 4.4.3. Numerical results and observations are presented in Section 6.4.

4.1 Problem statement

For the homogeneous case, it is assumed that the original system is described by the generalised matrix equation specified in Section 3.5

$$(\mathbf{I} + \mathbf{G}\zeta) \mathbf{x} = \mathbf{b}. \quad (4.1)$$

where \mathbf{I}, \mathbf{G} are $m \times m$ matrices and \mathbf{x}, \mathbf{b} are a $m \times 1$ vector. The above equation is repeatedly solved for each value of contrast ζ in a contrast-sweep analysis at extensive computational expense. In this chapter, the generation of an accurate low-order approximation of the corresponding form

$$(\mathbf{I}_{q \times q} + \tilde{\mathbf{G}}_{q \times q} \zeta) \tilde{\mathbf{x}}_{q \times 1} = \tilde{\mathbf{b}}_{q \times 1} \quad (4.2)$$

will be introduced, where $q \ll m$. The change of variable is defined as

$$\tilde{\mathbf{G}} = \mathbf{U}_{q \times m}^H \mathbf{G} \mathbf{U}_{m \times q} \quad \tilde{\mathbf{x}} = \mathbf{U}_{q \times m}^H \mathbf{x} \quad \tilde{\mathbf{b}} = \mathbf{U}_{q \times m}^H \mathbf{b}. \quad (4.3)$$

The orthogonal similarity transformation (see Appendix A) matrix \mathbf{U}_q is produced by the Arnoldi algorithm in Table 4.1 and is used to project the relevant variables into a lower-order Krylov subspace. Equation 4.2 can be solved rapidly over a range of contrast ζ for \mathbf{x} to determine the total fields $E_z(\mathbf{r})$ throughout the scatterer and elsewhere. This ROM representation is based on the shift invariance property [65] of the Arnoldi iteration. This means that the Arnoldi algorithm is applied only once with some particular choice of ζ . The resultant ROM is valid for a whole range of ζ values. The main computational cost associated with computing a solution for another ζ consists of inverting a system matrix of order q .

4.2 The Arnoldi method

The Arnoldi method is an orthogonal projection method that iteratively builds an orthonormal basis for the Krylov subspace [31,36,45,66]

$$\mathcal{K}_q(\mathbf{G}, \mathbf{u}_1) = \text{span}\{\mathbf{u}_1, \mathbf{G}\mathbf{u}_1, \dots, \mathbf{G}^{q-1}\mathbf{u}_1\} \quad (4.4)$$

for \mathbf{G} generated by the vector \mathbf{u}_1 . This algorithm generates a Hessenberg reduction

$$\mathbf{H}_{q \times q} = \mathbf{U}_q^H \mathbf{G} \mathbf{U}_q \quad (4.5)$$

where \mathbf{H}_q is an upper Hessenberg matrix [36]. To derive the columns of

$$\mathbf{U}_q = [\mathbf{u}_1, \mathbf{u}_2, \dots, \mathbf{u}_q] \quad (4.6)$$

iteratively, the Arnoldi process in Table 4.1 [31,36,45,66] is applied. In particular,

$$\mathbf{U}_q^H \mathbf{U}_q = \mathbf{I} \quad \mathbf{U}_q \mathbf{U}_q^H = \mathbf{I} \quad \text{for } q = m \quad (4.7)$$

implying

$$\mathbf{G} \mathbf{U}_q = \mathbf{U}_q \mathbf{H}_q \quad \text{for } q = m. \quad (4.8)$$

However, it should be noted that for $q \neq m$ the above relations do not hold

$$\mathbf{U}_q^H \mathbf{U}_q = \mathbf{I} \quad \mathbf{U}_q \mathbf{U}_q^H \neq \mathbf{I} \quad (4.9)$$

By comparing the q columns of the above equation the following relationship can be achieved

$$\mathbf{G} \mathbf{u}_q = \sum_{n=1}^{q+1} h_{n,q} \mathbf{u}_n \quad 1 \leq q \leq m-1 \quad (4.10)$$

where m is the number of basis cells, q is the order of the ROM and n is the control index of the Arnoldi algorithm. Isolating the last term in the summation gives

$$h_{q+1,q} \mathbf{u}_{q+1} = \mathbf{G} \mathbf{u}_q - \sum_{n=1}^q h_{n,q} \mathbf{u}_n \equiv \mathbf{w}_q \quad (\text{Line 8 Table 4.1}). \quad (4.11)$$

where since the \mathbf{u}_q are orthonormal, pre-multiplying both sides of the last equality by \mathbf{u}_n^H yields

$$h_{n,q} = \mathbf{u}_n^H \mathbf{G} \mathbf{u}_q \quad \text{for } n = 1 : q. \quad (4.12)$$

If $\mathbf{w}_q \neq 0$, then \mathbf{u}_{q+1} is specified by

$$\mathbf{u}_{q+1} = \mathbf{w}_q / h_{q+1,q} \quad (4.13)$$

These equations define the Arnoldi process outlined in Table 4.1. The \mathbf{u}_n computed by the Arnoldi algorithm are called the Arnoldi vectors and they define an orthonormal basis for the Krylov subspace $\mathcal{K}_q(\mathbf{G}, \mathbf{u}_1)$

$$\text{span}\{\mathbf{u}_1, \mathbf{u}_2, \dots, \mathbf{u}_q\} = \text{span}\{\mathbf{u}_1, \mathbf{G}\mathbf{u}_1, \dots, \mathbf{G}^{q-1}\mathbf{u}_1\}. \quad (4.14)$$

The Arnoldi procedure can be essentially viewed as a modified Gram-Schmidt process for building an orthogonal basis for the Krylov space $\mathcal{K}_q(\mathbf{G}, \mathbf{u}_1)$. The vectors \mathbf{u}_n are mutually orthonormal and have the property that the columns of the generated \mathbf{U}_q matrix span the Krylov subspace \mathcal{K}_q . The procedure has the advantage that it can be stopped part-way, leaving a partial reduction to Hessenberg form that is exploited to provide a reduced order model for Equation 4.1.

The modified Gram-Schmidt procedure orthonormalises each vector sequentially. The Arnoldi algorithm in Table 4.1 computes the orthogonal projection of \mathbf{w}_n onto $\text{span}\{\mathbf{u}_1 \ \mathbf{u}_2 \ \dots \ \mathbf{u}_n\}$. This projection is subtracted from the original vector and the result is normalised to obtain \mathbf{u}_{n+1} , which is, by construction, orthogonal to all previously computed Arnoldi vectors $\{\mathbf{u}_1, \mathbf{u}_2, \dots, \mathbf{u}_n\}$ with unit norm. A working example of the modified Gram-Schmidt procedure is given in Appendix A Example A.0.1.

After q steps, the Arnoldi process can be summarised by the q -step Arnoldi factorisation generated using Equation 4.11

$$\mathbf{G}\mathbf{U}_q = \mathbf{U}_q\mathbf{H}_q + \mathbf{u}_{q+1}h_{q+1,q}\mathbf{e}_q^T \quad (4.15)$$

$$= \mathbf{U}_q\mathbf{H}_q + \mathbf{w}_q\mathbf{e}_q^T \quad (4.16)$$

where $\mathbf{e}_q = \mathbf{I}_q(:, q)$, $h_{q+1,q}$ is the $(q+1, q)$ entry of the Hessenberg matrix \mathbf{H}_q , and the vector $h_{q+1,q}\mathbf{u}_{q+1}$ is the Arnoldi residual \mathbf{w}_q of the q -step Arnoldi factorisation and is orthogonal to the columns of \mathbf{U}_q .


```

 $\mathbf{u}_1 = \mathbf{b} / \|\mathbf{b}\|_2$ 
for  $n = 1, \dots, q$ 
     $\mathbf{w}_n = \mathbf{G}\mathbf{u}_n$  (compute next vector spanning the subspace);
    for  $i = 1, \dots, n$ 
         $h_{i,n} = \mathbf{u}_i^H \mathbf{w}_n$  (compute projections of new vector  $\mathbf{w}_n$  onto the previously
        calculated orthonormal vectors  $\mathbf{u}_i$ );
         $\mathbf{w}_n = \mathbf{w}_n - \mathbf{u}_i h_{i,n}$  (subtract the projections to make  $\mathbf{w}_n$  orthogonal to
        previously calculated orthonormal vectors  $\mathbf{u}_i$ );
    end  $i$ 
     $h_{n+1,n} = \|\mathbf{w}_n\|_2$ 
    if  $h_{n+1,n} = 0$  Quit
     $\mathbf{u}_{n+1} = \mathbf{w}_n / h_{n+1,n}$  (make  $\mathbf{u}_{n+1}$  a unit vector);
end  $n$ .
 $\mathbf{H} = h(1 : q, :)$ 

```

Table 4.1: Arnoldi - modified Gram-Schmidt algorithm (AMGS).

4.2.1 Orthogonal reduction of \mathbf{G} to Hessenberg form \mathbf{H}

Using the identity $\mathbf{U}_q^H \mathbf{U}_q = \mathbf{I}_q$ and the fact that $\mathbf{U}_q^H \mathbf{u}_{q+1} = 0$, an expression for \mathbf{H}_q can be derived

$$\mathbf{U}_q^H \mathbf{G} \mathbf{U}_q = \mathbf{H}_q \quad (4.17)$$

The matrix \mathbf{H}_q is the orthogonal similarity transformation (see Appendix A) of the matrix \mathbf{G} to Hessenberg form given by

$$\mathbf{H}_q = \begin{pmatrix} h_{1,1} & h_{1,2} & h_{1,3} & \cdots & h_{1,q} \\ h_{2,1} & h_{2,2} & h_{2,3} & \cdots & h_{2,q} \\ 0 & h_{3,2} & h_{3,3} & \cdots & h_{3,q} \\ \vdots & & \ddots & \ddots & \vdots \\ 0 & \cdots & \cdots & h_{q,q-1} & h_{q,q} \end{pmatrix}.$$

This matrix can be interpreted as the orthogonal projection of \mathbf{G} onto the q -dimensional subspace \mathcal{K}_q , whose leading eigenvalues are approximations to those of \mathbf{G}

$$\begin{aligned} \text{proj}_{\mathcal{K}_q} \mathbf{G} &= \mathbf{U}_q \mathbf{U}_q^H \mathbf{G} \\ \mathbf{H}_q &= \mathbf{U}_q^H \mathbf{U}_q \mathbf{U}_q^H \mathbf{G} \mathbf{U}_q = \mathbf{U}_q^H \mathbf{G} \mathbf{U}_q \quad (\text{see Theorem A.0.2}). \end{aligned} \quad (4.18)$$

From Definition A.0.5 it is clear that \mathbf{G} and \mathbf{H}_q are approximately unitarily similar if $q \neq m$. As $q \rightarrow m$, the number of eigenvalues $\lambda_n(\mathbf{H}_q)$ that constitute a good approximation for corresponding eigenvalues $\lambda_n(\mathbf{G})$ will improve. If $q = m$ then \mathbf{G} and \mathbf{H}_q are unitarily similar and $\lambda_n(\mathbf{H}_q) = \lambda_n(\mathbf{G})$. This eventuality is characterised by the residual $\|\mathbf{w}_n\|_2 = 0$ (calculated in line 8 of Table 4.1), at which point the algorithm is terminated. This signals the fact that \mathbf{w}_{n+1} is linearly dependent with respect to $\{\mathbf{w}_1 \ \mathbf{w}_2 \ \cdots \ \mathbf{w}_n\}$ [31, 45, 67]. However, this situation is very unlikely to occur in practice, due to finite-precision arithmetic. In this scenario ($\|\mathbf{w}_n\|_2 = 0$), $\mathcal{K}_q(\mathbf{G}, \mathbf{u}_1)$ is an exact invariant subspace (see Appendix A) of \mathbf{G} .

When the \mathbf{G} matrix is symmetric, then \mathbf{H}_q is symmetric and tridiagonal and the Arnoldi algorithm simplifies considerably. For such a case, there is an altered version of the Arnoldi algorithm, called the Lanczos algorithm. The Lanczos algorithm is similar to the Arnoldi algorithm. Unlike the Arnoldi algorithm, the Lanczos process only orthogonalises the most recent generated vector to the

previous vector. This results in the Lanczos algorithm being prone to loss of orthogonality, making it not as numerically stable as the Arnoldi algorithm. Consequently, the Arnoldi algorithm will be the technique of choice for producing an orthonormal basis for the Krylov subspace \mathcal{K}_q .

4.2.2 Re-orthogonalised Arnoldi algorithm

In exact arithmetic, each newly computed vector \mathbf{u}_{n+1} will be orthogonal to the columns of \mathbf{U}_q . The columns of \mathbf{U}_q form an orthonormal basis for the Krylov subspace \mathcal{K}_q and \mathbf{H}_q is the orthogonal projection of \mathbf{G} onto this space. However, in finite-precision arithmetic, this property will not hold true due to numerical instabilities associated with the modified Gram-Schmidt orthogonalisation process [31, 36, 67, 68]. This makes it necessary to re-orthogonalise \mathbf{u}_{n+1} against the columns of \mathbf{U}_q . Failure to maintain orthogonality leads to several numerical difficulties. If subsequent Arnoldi vectors are not forced to be orthogonal to the previous vectors, then spurious eigenvalues will appear in the spectrum of the projected matrix \mathbf{H}_q . Thus, a computational procedure that monitors the possible loss of orthogonality in an inexpensive manner is required. In addition, an efficient and stable computational procedure is needed to enforce orthogonality when required.

As stated earlier, as q increases the eigenvalues of the approximation matrix \mathbf{H}_q will converge to the eigenvalues of \mathbf{G} . The residual \mathbf{w}_n therefore is expected to decrease as the q increases until $\|\mathbf{w}_n\|_2 = 0$; when $q = m$. Loss of orthogonality amongst the generated Arnoldi vectors \mathbf{u}_n will however result in an increase in the residual \mathbf{w}_n . Therefore, the decision to perform another step of orthogonalisation is based on whether [68, 69]

$$\frac{\|\mathbf{w}_n\|_2}{\|\mathbf{w}_{n-1}\|_2} < \eta \quad (4.19)$$

is less than a prescribed tolerance η (as implemented in line 9 of Table 4.2). Subsequently, a re-orthogonalisation of \mathbf{w}_n against all the columns of \mathbf{U}_q is performed. The parameter η is chosen to satisfy $0 < \eta < 1$. Larger values result in a relaxing of the orthogonality between \mathbf{U}_q and the final \mathbf{w}_n . Work published in [68, 69] shows that orthogonality to working precision is accomplished with at most one step of re-orthogonalisation. A value for the parameter $\eta = 1/\sqrt{2}$ has been proposed by [69] which results in a good compromise maintaining an orthogonal set of Arnoldi vectors without an unnecessary amount of re-orthogonalisation. Loss of orthogonality of the matrix \mathbf{U}_q at each iteration step can be bounded [68, 70]

$$\|\mathbf{I} - \mathbf{U}_q^H \mathbf{U}_q\|_2 \leq \text{Tolerance}. \quad (4.20)$$

The computational cost of preserving the orthogonality near machine precision is approximately twice that of the standard Arnoldi algorithm. However, it will be shown in Section 6.4 that re-orthogonalisation is mandatory to obtain an accurate approximate solution. In Section 6.4, the loss of orthogonality of computed vectors $\|\mathbf{I} - \mathbf{U}_q^H \mathbf{U}_q\|_2$ for the Arnoldi algorithm with and without re-orthogonalisation is plotted.

```

u1 = b/||b||2
for n = 1, ..., q
    wn = Gun
    vn = ||wn||2
    for i = 1, ..., n
        yi,n = uiHwn
        wn = wn - uiyi,n
    end i
    if ||wn||2 < η * vn
        for i = 1, ..., n
            hi,n = uiTwn
            wn = wn - uihi,n
        end i
        hn,n = hn,n + yn,n
    endif
    hn+1,n = ||wn||2
    if hn+1,n = 0 Quit
    un+1 = wn/hn+1,n
end n.
H = h (1 : q, :)

```

Table 4.2: Arnoldi - modified Gram-Schmidt algorithm with re-orthogonalisation (AMGSR).

4.3 Model-order reduction for a homogeneous body

This section reviews the formation of a ROM for the case of scattering from a homogeneous object [5,31]. We note that computing the fields scattered from a homogeneous body requires independently solving

$$\mathbf{x} = (\mathbf{I} + \zeta \mathbf{G})^{-1} \mathbf{b} \quad (4.21)$$

for each value of ζ desired, where the diagonal contrast matrix \mathbf{A} has been reduced to a constant multiplicative factor ζ . The Arnoldi algorithm achieves this by iteratively computing the Hessenberg reduction

$$\mathbf{H}_q = \mathbf{U}_q^H \mathbf{G} \mathbf{U}_q \quad (4.22)$$

and using it to develop a ROM for the total field. As discussed in Section 2.3, after q steps of the Arnoldi algorithm, an approximation \mathbf{x}_q , to \mathbf{x} , can be made in terms of the q basis vectors

$$\mathbf{x} \approx \mathbf{x}_q = \sum_{n=1}^q \mathbf{u}_n \alpha_n = \mathbf{U}_q \mathbf{a}_q \quad (4.23)$$

where $\mathbf{a}_q = [\alpha_1 \ \alpha_2 \ \cdots \ \alpha_q]^T$ is a vector of expansion coefficients for the Arnoldi basis vectors \mathbf{u}_n that span the Krylov subspace. The residual \mathbf{r}_q that corresponds to this approximation is introduced as

$$\mathbf{r}_q = \mathbf{b} - (\mathbf{I} + \zeta \mathbf{G}) \mathbf{x}_q. \quad (4.24)$$

To find the optimal approximate solution, \mathbf{x}_q is constrained to ensure that \mathbf{x}_q minimises the residual \mathbf{r}_q . Specifically, the residual vector is constrained to be orthogonal to q linearly independent vectors known as the orthogonal residual property, or a Galerkin condition, as discussed in Section 2.3

$$\mathbf{r}_q \perp \mathcal{K}_q \quad \mathbf{U}_q^H \mathbf{r}_q = 0. \quad (4.25)$$

It is clear from Section 2.3 that the residual \mathbf{r}_q is minimised when the residual vector is orthogonal to the space \mathcal{K}_q . This requires substituting Equation 4.23 into Equation 4.24

$$\mathbf{r}_q = \mathbf{b} - (\mathbf{I} + \zeta \mathbf{G}) \mathbf{U}_q \mathbf{a}_q \quad (4.26)$$

and performing a Galerkin test, to give

$$\begin{aligned}
\mathbf{U}_q^H \mathbf{r}_q &= 0 \\
\mathbf{U}_q^H (\mathbf{b} - (\mathbf{I} + \zeta \mathbf{G}) \mathbf{U}_q \mathbf{a}_q) &= 0 \\
(\mathbf{U}_q^H + \zeta \mathbf{U}_q^H \mathbf{G}) \mathbf{U}_q \mathbf{a}_q &= \mathbf{U}_q^H \mathbf{b} \\
(\mathbf{I} + \zeta \mathbf{U}_q^H \mathbf{G} \mathbf{U}_q) \mathbf{a}_q &= \mathbf{U}_q^H \mathbf{b}
\end{aligned} \tag{4.27}$$

which, from the Arnoldi governing Equation 4.22, results in

$$\mathbf{a}_q = (\mathbf{I} + \zeta \mathbf{H}_q)^{-1} \mathbf{U}_q^H \mathbf{b}. \tag{4.28}$$

Clearly substituting Equation 4.28 into Equation 4.27 results in the residual being minimised as required

$$\mathbf{U}_q^H \mathbf{r}_q = \mathbf{U}_q^H \mathbf{b} - (\mathbf{I} + \zeta \mathbf{H}_q) (\mathbf{I} + \zeta \mathbf{H}_q)^{-1} \mathbf{U}_q^H \mathbf{b} = 0. \tag{4.29}$$

Therefore, substituting this into Equation 4.23 yields the ROM for the total field

$$\mathbf{x} \approx \mathbf{x}_q = \mathbf{U}_q (\mathbf{I} + \zeta \mathbf{H}_q)^{-1} \mathbf{U}_q^H \mathbf{b} \tag{4.30}$$

This formulation can be used for both contrast and source location sweep problems. However, this equation can be further reduced by choosing the first Arnoldi vector to be $\mathbf{u}_1 = \|\mathbf{b}\|_2^{-1} \mathbf{b}$

$$\mathbf{U}_q^H \mathbf{b} = \mathbf{e}_1 \|\mathbf{b}\|_2 = \begin{pmatrix} \|\mathbf{b}\|_2 \\ 0 \\ \vdots \\ 0 \end{pmatrix} \tag{4.31}$$

because all the remaining columns of \mathbf{U}_q are orthogonal to \mathbf{b} . As a result

$$\mathbf{x} \approx \mathbf{x}_q = \mathbf{U}_q (\mathbf{I} + \zeta \mathbf{H}_q)^{-1} \mathbf{e}_1 \|\mathbf{b}\|_2. \tag{4.32}$$

It should be noted that the contrast ζ appears as a parameter and neither \mathbf{U}_q nor matrix \mathbf{H}_q depends on ζ . As such, the \mathbf{U}_q matrix need only be generated once in a contrast-sweep analysis. Clearly, Equation 4.32 can be used to efficiently solve over a wide range of contrasts, as it requires the inversion of a matrix of order $q \ll m$ for each contrast value.

4.4 Model-order reduction for an inhomogeneous body

The MOR technique outlined in [5] is applied only to wave scattering from homogeneous bodies. This section extends the MOR technique of the previous section to the case of scattering from inhomogeneous bodies where application of the surface EFIE is not appropriate. We analyse scattering from a body composed of m distinct homogeneous basis function domains.

Solution of the scattering problem over a range of contrasts necessitates the ability to compute in an efficient manner the quantity

$$\mathbf{x} = (\mathbf{I} + \mathbf{GA})^{-1} \mathbf{b} \quad (4.33)$$

where \mathbf{A} is the diagonal contrast matrix given in Equation 3.78. Again, expand the approximation \mathbf{x}_q in terms of q orthonormal vectors generated by the Arnoldi algorithm as:

$$\mathbf{x} \approx \mathbf{x}_q = \sum_{n=1}^q \mathbf{u}_n \alpha_n = \mathbf{U}_q \mathbf{a}_q \quad (4.34)$$

Following the same steps as before, the residual can thus be written as

$$\mathbf{U}_q^H \mathbf{r}_q = \mathbf{U}_q^H (\mathbf{b} - (\mathbf{I} + \mathbf{GA}) \mathbf{U}_q \mathbf{a}_q) \quad (4.35)$$

and performing a Galerkin test gives

$$\begin{aligned} \mathbf{U}_q^H \mathbf{r}_q &= \mathbf{U}_q^H (\mathbf{b} - (\mathbf{I} + \mathbf{GA}) \mathbf{U}_q \mathbf{a}_q) \\ &= \mathbf{U}_q^H \mathbf{b} - (\mathbf{I} + \mathbf{U}_q^H \mathbf{GA} \mathbf{U}_q) \mathbf{a}_q \\ &\approx \mathbf{U}_q^H \mathbf{b} - (\mathbf{I} + \mathbf{U}_q^H \mathbf{G} \mathbf{U}_q \mathbf{U}_q^H \mathbf{A} \mathbf{U}_q) \mathbf{a}_q \end{aligned} \quad (4.36)$$

$$= \mathbf{U}_q^H \mathbf{b} - \left(\mathbf{I} + \mathbf{H}_q \tilde{\mathbf{A}}_{q \times q} \right) \mathbf{a}_q \quad (4.37)$$

where

$$\tilde{\mathbf{A}}_q = \mathbf{U}_q^H \mathbf{A} \mathbf{U}_q. \quad (4.38)$$

As a result of setting

$$\mathbf{a}_q = \left(\mathbf{I} + \mathbf{H}_q \tilde{\mathbf{A}}_q \right)^{-1} \mathbf{U}_q^H \mathbf{b} \quad (4.39)$$

the residual has been minimised

$$\mathbf{U}_q^H \mathbf{r}_q = \mathbf{U}_q^H \mathbf{b} - \left(\mathbf{I} + \mathbf{H}_q \tilde{\mathbf{A}}_q \right) \left(\mathbf{I} + \mathbf{H}_q \tilde{\mathbf{A}}_q \right)^{-1} \mathbf{U}_q^H \mathbf{b} = 0 \quad (4.40)$$

and assuming $\mathbf{u}_1 = \|\mathbf{b}\|_2^{-1} \mathbf{b}$ yields the following reduced form for the total field

$$\mathbf{x} \approx \mathbf{x}_q = \mathbf{U}_q \left(\mathbf{I} + \mathbf{H}_q \tilde{\mathbf{A}}_q \right)^{-1} \mathbf{e}_1 \|\mathbf{b}\|_2. \quad (4.41)$$

Equation 4.41 can be used for the solution of any inhomogeneous domain of the same dimension and discretisation. As before, for simulations where there is any deviation of source location for a fixed contrast profile, the total field is calculated by

$$\mathbf{x} \approx \mathbf{x}_q = \mathbf{U}_q \left(\mathbf{I} + \mathbf{H}_q \tilde{\mathbf{A}}_q \right)^{-1} \mathbf{U}_q^H \mathbf{b}. \quad (4.42)$$

4.4.1 Equation 4.36 approximation

In this section, the approximation of line 3 of Equation 4.36 will be substantiated. As stated earlier, for $q \neq m$ the following relations hold

$$\mathbf{U}_q^H \mathbf{U}_q = \mathbf{I} \quad \mathbf{U}_q \mathbf{U}_q^H \neq \mathbf{I}. \quad (4.43)$$

However, due to the independence of the columns of \mathbf{U}_q imposed by the re-orthogonalisation process, Equation 4.36 can be shown to be a valid approximation. As prescribed in [36], if the columns of \mathbf{U}_q are independent and the norm of the residual matrix

$$\mathbf{R} = \mathbf{A} \mathbf{U}_q - \mathbf{U}_q \mathbf{S}_{q \times q} \quad (4.44)$$

has been minimised for some choice of \mathbf{S}_q , then the columns of \mathbf{U}_q define an approximate subspace. The selection of $\mathbf{S}_q = \mathbf{U}_q^H \mathbf{A} \mathbf{U}_q = \tilde{\mathbf{A}}_q$ results in the norm of the residual being minimised

$$\min \|\mathbf{A} \mathbf{U}_q - \mathbf{U}_q \mathbf{S}_q\|_2 = \|(\mathbf{I} - \mathbf{U}_q \mathbf{U}_q^H) \mathbf{A} \mathbf{U}_q\|_F. \quad (4.45)$$

Thus, Equation 4.36 becomes a valid approximation with the property that, as $q \rightarrow m$, a better approximation is procured. This is validated numerically in the results section. Note that, when $q = m$, Equation 4.36 is exact as

$$\mathbf{U}_q^H \mathbf{U}_q = \mathbf{U}_q \mathbf{U}_q^H = \mathbf{I}. \quad (4.46)$$

4.4.2 Computational analysis

In this analysis, the shape of the object is known *a priori*. A variation in the contrast and source location is considered. For scattering problems where multiple approximate solutions for varying contrast with fixed-source location are required, it will be shown that significant computational saving can be achieved as compared to accelerated solver techniques, such as the Conjugate Gradient Normal Equation - Fast Fourier Transform (CGNE-FFT) [9]. Additionally, considerable time savings can be obtained for scattering with fixed contrast profiles and varying source location when compared with such accelerated solvers.

The main computational cost of this approach is incurred in generating the Krylov matrix \mathbf{U}_q . However, once generated it is stored and can be applied to scattering problems with the same geometry but different contrast configuration or source locations. The computation of the \mathbf{U}_q involves the multiplication of \mathbf{G} by $q - 1$ Arnoldi vectors \mathbf{u}_n , at a cost of $\mathcal{O}(2m^2q)$ operations. If a second orthogonalisation is performed at each iteration, the operation count is doubled (line 8 of Table 4.2). This represents the worst-case scenario; However, it is clear that the MGS with re-orthogonalisation is essential, as discussed in Section 4.2.2.

For inhomogeneous scattering problems, the computational cost is increased by the need to formulate the matrix $\tilde{\mathbf{A}}_q$ in Equation 4.38. This requires an initial operation cost of $\mathcal{O}((0.5q)^2 m)$ flops, which can be attributed to the sparse nature of the matrix \mathbf{A} and the symmetry of the matrix multiplication, $\mathbf{U}_q^H \mathbf{A} \mathbf{U}_q$. All subsequent solutions for domains with different contrast configurations require only the formation of an amended matrix $\tilde{\mathbf{A}}_q$. To demonstrate the computational overhead associated with the calculation of a new $\tilde{\mathbf{A}}_q$, a simple example is considered. The homogeneous region 1 ($\zeta_1 = \zeta_2 = \zeta_3$) in Figure 4.1 is kept constant, while the contrast in region 2 ($\zeta_4 = \zeta_5$) is varied. For this simple case of two homogeneous regions as illustrated in Figure 4.1, the arithmetic computation of $\tilde{\mathbf{A}}_q$ can be written in matrix form as

$$\tilde{\mathbf{A}}_q = \begin{bmatrix} \leftarrow & \mathbf{u}_1 & \rightarrow \\ \leftarrow & \mathbf{u}_2 & \rightarrow \end{bmatrix} \begin{bmatrix} \zeta_1 & 0 & 0 & 0 & 0 \\ 0 & \zeta_2 & 0 & 0 & 0 \\ 0 & 0 & \zeta_3 & 0 & 0 \\ 0 & 0 & 0 & \zeta_4 & 0 \\ 0 & 0 & 0 & 0 & \zeta_5 \end{bmatrix} \begin{bmatrix} \uparrow & \uparrow \\ \mathbf{u}_1 & \mathbf{u}_2 \\ \downarrow & \downarrow \end{bmatrix}$$

$$\tilde{\mathbf{A}}_q = \mathbf{U}_q^H \mathbf{A}_m \mathbf{U}_q. \quad (4.47)$$

Expanding Equation 4.47 yields

$$\hat{\mathbf{A}}_{m \times q} = \mathbf{A}\mathbf{U}_q = \begin{bmatrix} \zeta_1 \mathbf{u}_1 \\ \zeta_2 \mathbf{u}_2 \\ 0 \\ 0 \\ 0 \end{bmatrix} + \begin{bmatrix} 0 \\ 0 \\ \zeta_3 \mathbf{u}_3 \\ \zeta_4 \mathbf{u}_4 \\ \zeta_5 \mathbf{u}_5 \end{bmatrix} = \hat{\mathbf{A}}_1 + \hat{\mathbf{A}}_2 \quad (4.48)$$

$\tilde{\mathbf{A}}_q$ can now be written in terms of the direct computational cost associated with each new homogeneous region as

$$\tilde{\mathbf{A}}_q = \mathbf{U}_q^H \hat{\mathbf{A}}_1 + \mathbf{U}_q^H \hat{\mathbf{A}}_2. \quad (4.49)$$

As discussed earlier, the main computational cost of this approach is incurred in generating the Krylov matrix \mathbf{U}_q and the initial $\tilde{\mathbf{A}}_q$. However, once generated, the \mathbf{U}_q matrix and non-varying components of $\tilde{\mathbf{A}}_q$ can be used in subsequent simulations. Specifically, only the component of $\tilde{\mathbf{A}}_q$ associated with each varying homogeneous region needs to be re-calculated. For the above example $\mathbf{U}_q^H \hat{\mathbf{A}}_2$ is re-calculated for each simulation where the contrast value in region 2 is changing. Consequently, as the number of homogeneous regions increases, the computational cost of generating a new $\tilde{\mathbf{A}}_q$ is significantly reduced.

For fixed contrast scattering problems with varying source location, the additional computational cost is due to the formulation of the initial $\tilde{\mathbf{A}}_q$ and the generation of a new \mathbf{b} vector at each source location. An additional $\mathcal{O}(2q^2)$ operations are required to solve the resultant matrix equation in Equation 4.41 which can be efficiently solved over a wide contrast range or source location, as it requires the inversion of a matrix of order $q \ll m$. A complete time analysis is undertaken in Section 6.4. The computational time associated with the generation and solution of Equation 4.41 using Arnoldi and CG is compared against the solution of the original model, Equation 4.33, using an accelerated solver CGNE-FFT.

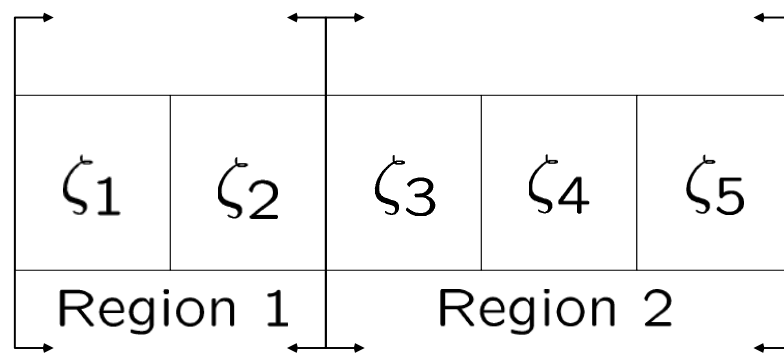


Figure 4.1: Inhomogeneous discretised structure with two homogenous regions.

4.4.3 Terminating the iteration

In order to choose an order of the Krylov subspace \mathcal{K}_q that can reflect the essential dynamics of the original model, an effective residual error must be considered as a stopping criterion to terminate the Arnoldi iteration process. Let the approximation residual error be defined as

$$r_q = \frac{\|\mathbf{b} - (\mathbf{I} + \mathbf{G}\mathbf{A}) \mathbf{x}_q\|_2}{\|\mathbf{b}\|_2} \quad (4.50)$$

If $r_q \leq \text{tol}_{r_q}$ for some pre-specified error tolerance value tol_{r_q} , the iteration process is terminated and hence, the ROM is considered to have converged to this tolerance.

In addition to monitoring the residual error, a procedure to detect when the process has stagnated is required. This means that \mathbf{u}_{q+1} will essentially offer no new information and therefore is not expected to improve the approximation. As discussed earlier, the Arnoldi algorithm approximates the eigenvalues of the \mathbf{G} in order of magnitude. The eigenvalues of largest magnitude are classified as the most dominant and contain the most amount of information describing the system. After the most dominant eigenvalues have been approximated, there is a decrease in the amount of new information introduced into the reduced order model. Consequently, there is a need to monitor the reduction in new information being gained by approximated any new eigenvalues. This can be achieved by monitoring the convergence of the eigenvalues of the approximation matrix $\lambda(\mathbf{H}_q)$ to the eigenvalues of $\lambda(\mathbf{G})$. The Arnoldi technique seeks an approximate eigenvalue $\tilde{\lambda}$ and eigenvector \tilde{y} that minimise the eigenvalue problem

$$\|(\mathbf{G} - \tilde{\lambda}_q \mathbf{I}) \tilde{y}\|_2. \quad (4.51)$$

When the Arnoldi residual $\|\mathbf{w}_n\|_2 = 0$, then the columns of \mathbf{U}_q define an exact invariant subspace of \mathbf{G} and the approximate eigenvalues and eigenvectors are exact. Otherwise, by using the relation

$$\mathbf{H}_q \tilde{y} = \tilde{\lambda} \tilde{y} \quad (4.52)$$

and the Arnoldi factorisation, a bound for the error of the approximation can be derived [36]. These yield the relation

$$\mathbf{G}\mathbf{U}_q = \mathbf{U}_q\mathbf{H}_q + \mathbf{u}_{q+1}h_{q+1,q}\mathbf{e}_q^T \quad (4.53)$$

$$\mathbf{G}\mathbf{U}_q = \mathbf{U}_q\mathbf{H}_q + \mathbf{w}_q\mathbf{e}_q^T \quad (4.54)$$

$$\mathbf{G}\mathbf{U}_q\tilde{\mathbf{y}} = \mathbf{U}_q\mathbf{H}_q\tilde{\mathbf{y}} + \mathbf{w}_q\mathbf{e}_q^T\tilde{\mathbf{y}} \quad (4.55)$$

$$\mathbf{G}\mathbf{U}_q\tilde{\mathbf{y}} = \mathbf{U}_q\tilde{\lambda}\tilde{\mathbf{y}} + \mathbf{w}_q\mathbf{e}_q^T\tilde{\mathbf{y}} \quad (4.56)$$

$$(\mathbf{G} - \tilde{\lambda}\mathbf{I})\mathbf{U}_q\tilde{\mathbf{y}} = \mathbf{w}_q\mathbf{e}_q^T\tilde{\mathbf{y}}. \quad (4.57)$$

The Ritz residual norm is subsequently given by [36, 45]

$$\|(\mathbf{G} - \tilde{\lambda}\mathbf{I})\mathbf{x}\|_2 = \|\mathbf{w}_q\mathbf{e}_q^T\tilde{\mathbf{y}}\|_2 \quad (4.58)$$

$$\|\mathbf{t}_q\|_2 = \|\mathbf{w}_q\mathbf{e}_q^T\tilde{\mathbf{y}}\|_2 \quad (4.59)$$

where $\mathbf{x} = \mathbf{U}_q\tilde{\mathbf{y}}$ and is known as the Ritz approximate eigenvector. Although this residual norm is not indicative of the actual error in the approximation eigenvalues, it is useful in monitoring the stagnation of the Arnoldi process. Additionally, obtaining the residual norm, as the algorithm progresses, is inexpensive due to the associated vectors being already generated within the Arnoldi algorithm. As q increases, the approximate eigenvalues will converge to the corresponding eigenvalues of the \mathbf{G} matrix and subsequently, the size of the residual norm will decrease. Typically, the process will start to stagnate after the most dominant eigenvalues have been approximated. Consequently, no additional useful information will be added by the generation of a new vector \mathbf{u}_q . To justify the generation of \mathbf{u}_{q+1} , the residual norm can be used to compare the current value of residual to that of s steps previous

$$\text{if } (\|\mathbf{t}_q - \mathbf{t}_{q-s}\|_2 \leq \text{tol}_{t_q}) \quad \text{Stagnation} = \text{True}. \quad (4.60)$$

Typically, a value for the tolerance $\text{tol}_{t_q} = 10^{-4}$ is used to determine stagnation and the subsequent termination of the Arnoldi algorithm.

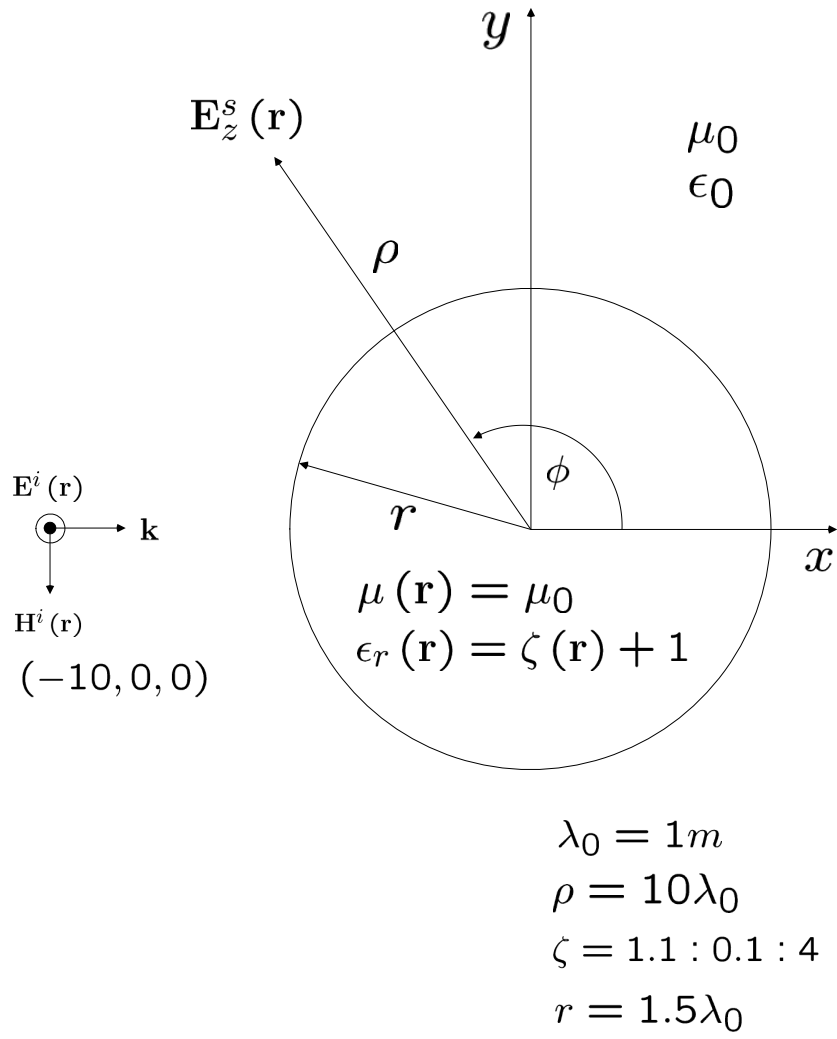


Figure 4.2: Case study 1 setup - Homogeneous cylinder illuminated by a TM^z incident wave.

4.5 Numerical results and validations

In this section, the scattered field E_z^s is calculated from a circular cylinder for a variety of contrast profiles and source locations. The numerical performance of the reduced order model, generated using the Arnoldi algorithm, are compared against an accelerated solver. Subsequently, these are validated against the direct solution using the MoM.

4.5.1 Case Study 1: Bi-static scattering homogeneous cylinder - Medium 1

We initially consider a homogeneous cylinder of radius $r = 1.5\lambda_0 = 1.5m$, centred at the origin and assumed to be embedded in free space (see Figure 4.2). It is illuminated by a TM^z plane wave radiating at a frequency of $f = 300$ MHz. The cylinder was discretised using $m = 2500$ cells and a bi-static backscattered field E_z^s field is computed for the particular case of contrast $\zeta = 1.1$, over an observation angle of $\phi = 0 : 2\pi$ using a fixed source location. The Mie series, as described in Section 3.7, is used to validate independently the accuracy of the MoM solution. The scattered field and associated percentage relative error are shown in Figures 4.3(a) and 4.3(b) respectively. The percentage relative error is defined as

$$\delta x = \frac{\|\mathbf{x}_q - \mathbf{x}\|_2}{\|\mathbf{x}\|_2} \times 100 \quad (4.61)$$

where \mathbf{x} is the true value and \mathbf{x}_q the approximation. The analytical solution is compared against the MoM and the modified Gram-Schmidt algorithm with re-orthogonalisation (MGSR) for $q = 250$. The MGSR represent a 90% reduction in system size while yielding approximately machine precision accuracy over the entire observation angle range.

When determining how to terminate the MGSR iteration, the approximation residual error t_q (Equation 4.50) and the Ritz residual norm (Equation 4.59) are utilised. On the approximation residual error r_q reaching the pre-specified tolerance of $\text{tol}_{r_q} = 10^{-3}$, the iteration is terminated. This indicates that the approximation solution $\tilde{\mathbf{e}}$ has converged to \mathbf{e} , within the tolerance tol_{r_q} .

As identified from Figure 4.4(a), a value of $q = 60$ results in $r_q < 10^{-3}$. Figure 4.4(b) clearly demonstrates that as q increases the approximate eigenvalues will converge to the corresponding eigenvalues of the \mathbf{G} matrix and subsequently the size of the residual norm will decrease. Stagnation in the iteration can be bounded by monitoring the Ritz residual stagnation check (Equation 4.59). Termination of the iteration will occur when the pre-specified $\text{tol}_{t_q} = 10^{-4}$ is reached ($q = 160$), signalling that no additional useful information will

be added by the generation of a new vector \mathbf{u}_q as illustrated in Figure 4.5(a).

By way of illustrating how the Arnoldi iteration process progresses, a plot of the approximation eigenvalue $\lambda(\mathbf{H}_q)$ and the corresponding eigenvalue $\lambda(\mathbf{G})$, in order of magnitude is compared in Figure 4.5(b). From this figure, it is clear that the Arnoldi iteration initially approximates the largest eigenvalues of the matrix \mathbf{G} .

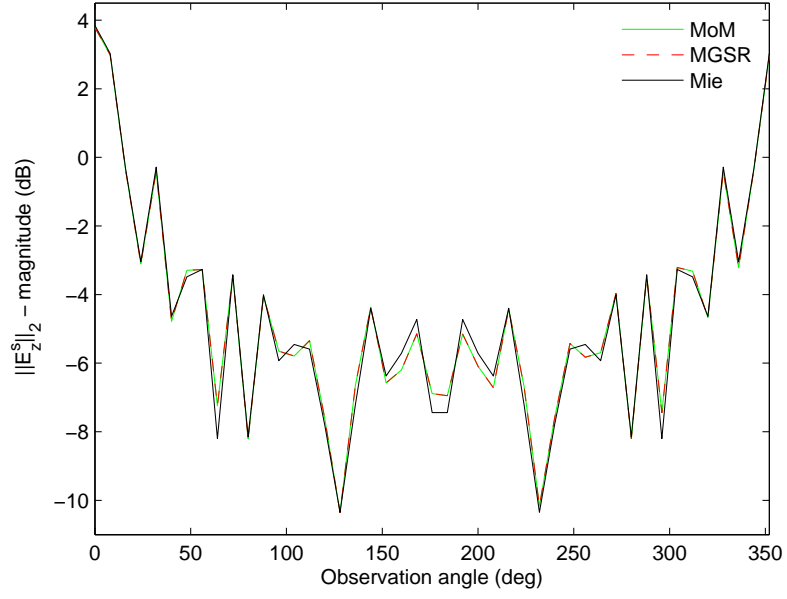
As q is increased, the process rapidly approximates these external eigenvalues (eigenvalues of the largest magnitude located in the outer spectrum) to a higher level of accuracy than the internal eigenvalues (eigenvalues closest to the origin). Although the external eigenvalues are the most dominant, it will be evident in the next section that the poor approximation to the internal eigenvalues (located around the origin) results in a limited contrast sweep range.

Loss of orthogonality of a computed Krylov matrix \mathbf{U}_n , utilising re-orthogonalisation at each iteration step is illustrated in Figure 4.6(a)

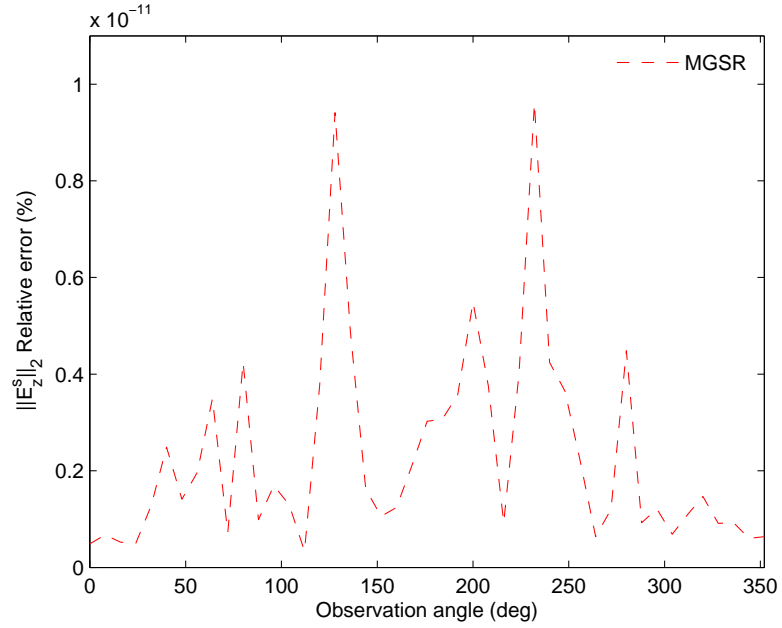
$$\|\mathbf{I}_n - \mathbf{U}_n^H \mathbf{U}_n\|_2 \quad \text{for all } 1 \leq n \leq q \quad (4.62)$$

where \mathbf{I}_n is a $n \times n$ identity matrix. We note the rapid loss of orthogonality in the Arnoldi process without the introduction of re-orthogonalisation. Additionally, it is evident that the MGS algorithm remains near-machine precision over the entire iteration process. The effect of loss of orthogonality in a contrast-sweep analysis will be demonstrated in the next section.

It should be noted that the stopping criteria, as discussed in this section, are subject to the ROM being analysed for a constant value of $\zeta = 1.1$. As ζ increases, there is no guarantee that the above analysis will produce an accurate approximation response over a contrast range. Additionally, repeated calculation of the approximation residual error for each contrast profile and iteration step will become computationally expensive. Instead, a closer inspection of the eigenvalue approximation in the proceeding sections will produce a means to produce an accurate approximation over an extended contrast range.

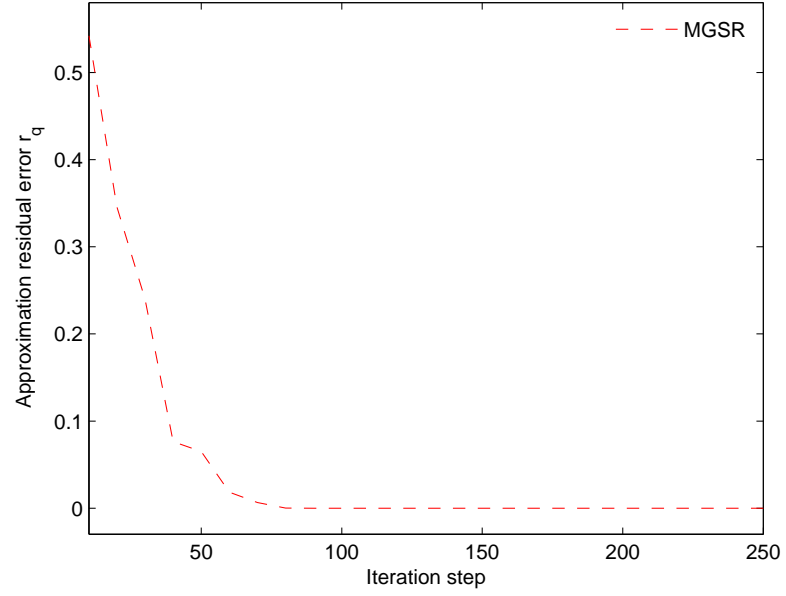


(a) $\|E_z^s\|_2$ - magnitude in dB for bi-static scattering over range of angle $\phi = 0 : 2\pi$ comparing MoM, MGSR and the Mie series for a constant contrast of $\zeta = 1.1$ ($\epsilon_r = 2.1$) from a homogeneous cylinder.

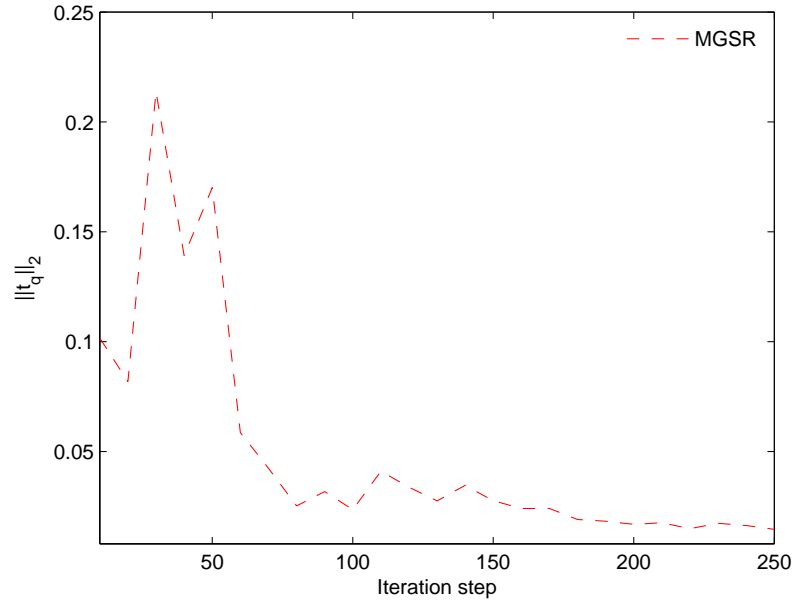


(b) Percentage relative error for figure 4.3(a) comparing the MGSR to the MoM solution.

Figure 4.3: Case study 1 Part A: Bi-static scattering from a homogeneous cylinder with $r = 1.5\lambda_0$, $q = 250$ and $\zeta = 1.1$ ($\epsilon_r = 2.1$), comparing MoM and MGSR.

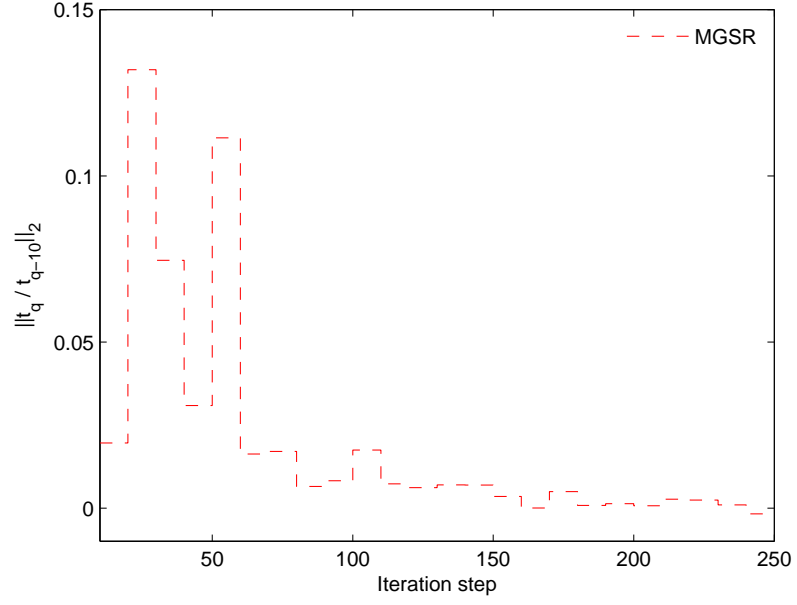


(a) Approximation residual relative error r_q - (Equation 4.50) for MGSR.

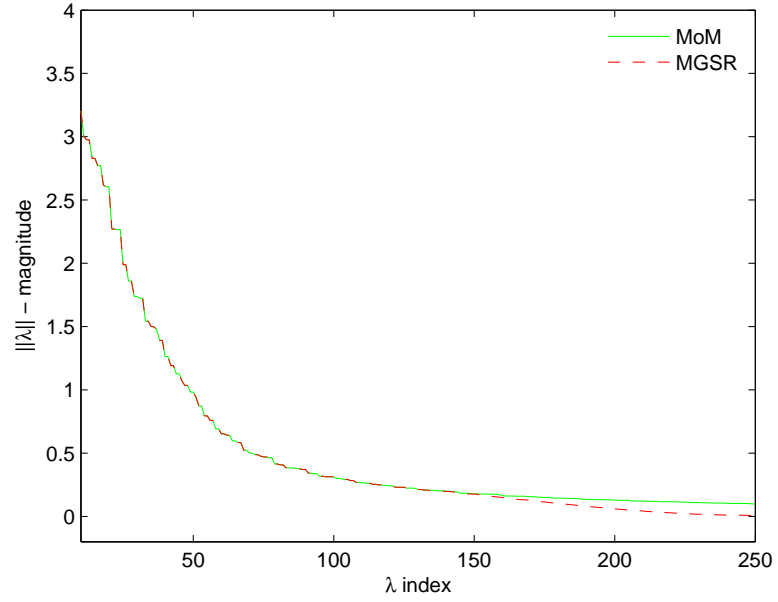


(b) Ritz residual norm $\|t_q\|_2$ - (Equation 4.59) for MGSR.

Figure 4.4: Case study 1 Part B: Bi-static scattering from a homogeneous cylinder with $r = 1.5\lambda_0$, $q = 250$ and $\zeta = 1.1$ ($\epsilon_r = 2.1$), comparing MoM and MGSR.

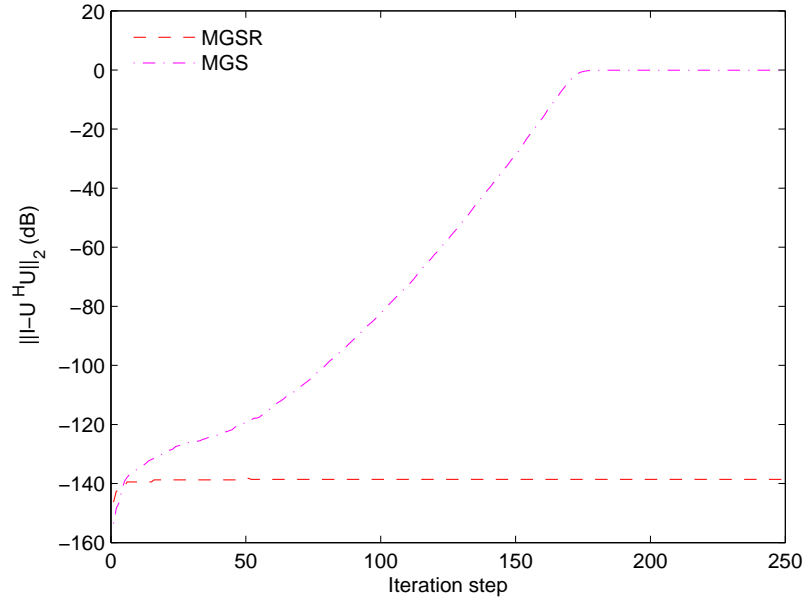


(a) Monitoring Ritz residual stagnation check for MGSR - $(\|t_q - t_{q-s}\|_2)$.



(b) $\|\lambda\|_2$ - comparing MoM against MGSR eigenvalues in order of magnitude.

Figure 4.5: Case study 1 Part C: Bi-static scattering from a homogeneous cylinder with $r = 1.5\lambda_0$, $q = 250$ and $\zeta = 1.1$ ($\epsilon_r = 2.1$), comparing MoM and MGSR.



(a) loss of orthogonality over iteration process for MGSR and MGS - $\|\mathbf{I} - \mathbf{U}^H \mathbf{U}\|_2$.

Figure 4.6: Case study 1 Part D: Bi-static scattering from a homogeneous cylinder with $r = 1.5\lambda_0$, $q = 250$ and $\zeta = 1.1$ ($\epsilon_r = 2.1$), comparing MoM and MGSR.

4.5.2 Case Study 1: Mono-static scattering homogeneous cylinder - Medium 1

In these examples, a similar numerical experiment is conducted, where the mono-static backscattered field E_z^s is computed over a range of contrast values of $\zeta_1 = 1.1 : 4$ in increments of 0.1. For this experiment, a fixed line source location is utilised and is located at Cartesian coordinates $(-10,0,0)$. Figures 4.7(a) and 4.7(b) shows the scattered field and associated error obtained from the MoM, MGS and the MGSR technique for $q = 250$, representing a 90% reduction in system size. It is clear from these figures that the MGSR outperforms the MGS, replicating the reference solution over the entire contrast range to within near-working precision, while retaining machine precision orthogonality. The effect of loss of orthogonality in the MGS process is evident in the condition number of the reduced order matrix $\text{cond}(\mathbf{T}) = 7.09^{+15}$.

The CPU time associated with the solution of the scattered field for the MoM, MGS and the MGSR for 45 samples is given in Table 4.3. These simulation were run on a 3.00 GHz Xeon CPU processor with 3.00 GB of RAM at 2.99 GHz. The MoM solution is solved using the accelerated solver Conjugate Gradient Normal Equation Fast Fourier Transform (CGNE-FFT). The CGNE-FFT can reduce the number of matrix vector multiplications from $\mathcal{O}(m^2)$ operations per iteration to $\mathcal{O}(m \log_2 m)$ operations. It is evident from this table that the MGSR significantly decreases the computational expense associated with the direct solution of each contrast value in a sweep analysis. As discussed in Section 4.4.2, the main computational cost is incurred in generating the Krylov matrix \mathbf{U}_q requiring 28.63 seconds. However, as the Krylov matrix need to be only calculated once, minimal computational expense is required for all subsequent solutions of $q \ll m$. For example, a 90% reduction in system size using the MGSR, with near-machine precision in accuracy over the entire contrast range, results in a speed-up of a factor 37.48 as compared to the MoM solution with FFT capability, where

$$\text{Speed-up} = \frac{\text{Total CPU time in seconds to generate and solve MoM solution}}{\text{Total CPU time in seconds to generate and solve MGSR}}.$$

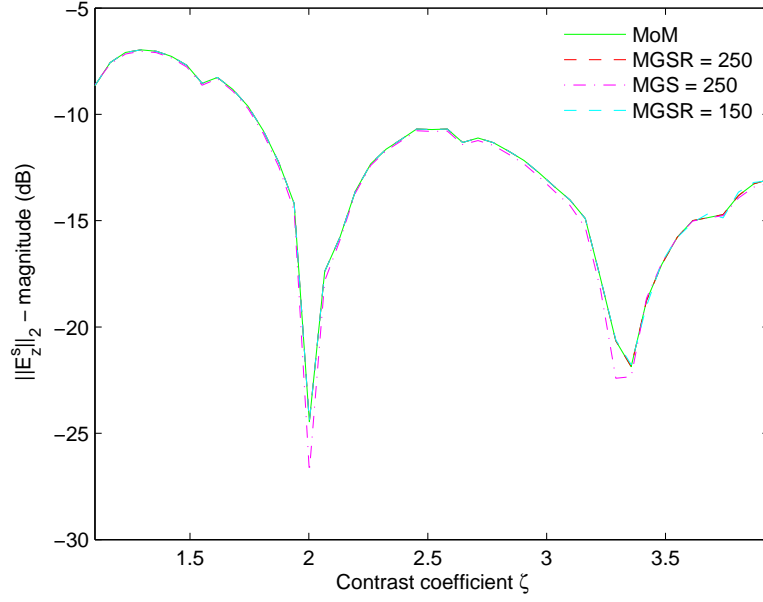
For a 94% reduction, the MGSR incurs an average percentage relative error of approximately 9% with a speed-up of a factor of 78.41.

In the final example, we consider the case where the contrast value is fixed and the source location is varying. Using Equation 4.30, the backscattered field E_z^s is observed at $\phi = 0$ and computed over a range of line source location of

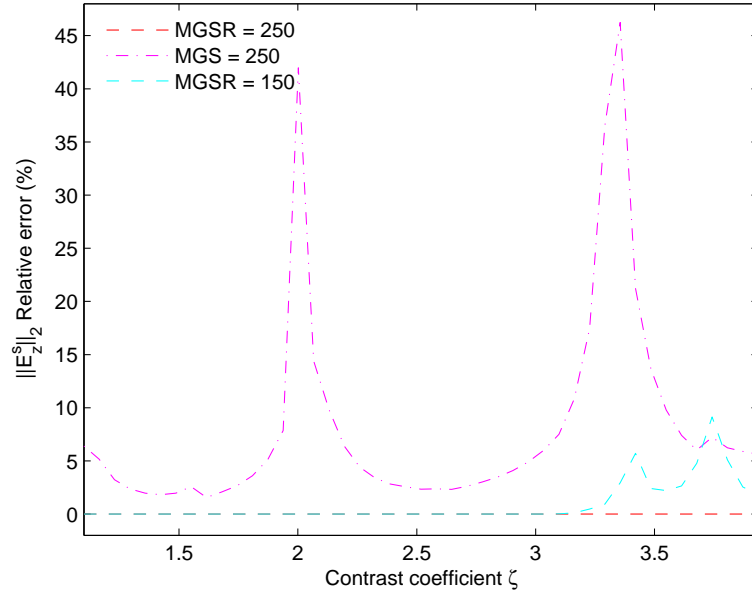
$\phi = 0 : 2\pi$ in increments of 8 degrees. The source location is set at a radius of $10\lambda_0$ and the contrast is fixed at $\zeta = 1.1$. From Figures 4.8(a) and 4.8(b), it is clear that the MGSF replicating the reference solution over the entire range of source location to within machine precision for $q = 250$.

Legend	Technique				
	MoM (CGNE-FFT)	Arnoldi MGSR (CGNE)			MGS
Order	$m = 2500$	$q = 150$	$q = 250$	$q = 250$	$q = 250$
c_n	891.65	870.36	885.45	885.45	7.09^{+15}
ζ	1.1 : 0.1 : 4	1.1 : 0.1 : 4	1.1 : 0.1 : 4	1.1 : 0.25 : 10	1.1 : 0.1 : 4
σ	0	0	0	0	0
n_s	45	45	45	45	45
$t_u(s)$	-	13.92	28.63	28.63	25.56
$t_s(s)$	26.766	0.032	0.078	0.078	1.063
n_i	887	12	12	12	170
o_q	-	-	1.38^{-14}	1.38^{-14}	1.0
$t_\sigma(s)$	-	-	-	-	-
$t_t(s)$	1204.5	15.36	32.14	32.14	73.395
r_q	-	0.027	0.015	0.015	-
$p_r(\%)$	-	94	90	90	90
$e_r(\%)$	-	9.13	8.21^{-11}	60.61	46
Speed-up	-	78.41	37.48	37.48	16.41
					9.38

Table 4.3: CPU time analysis (Case study 1,2 - Homogeneous cylinder, $f = 300$ MHz, $\lambda_0 = 1m$, $r = 1.5\lambda_0$, $m =$ size of MoM matrix, $q =$ size of ROM, c_n - condition number of MoM or ROM matrix accordingly, $\zeta =$ contrast range, $\sigma =$ expansion point, n_s - number of contrast samples, $t_u =$ CPU time in seconds to generate Krylov \mathbf{U}_q matrix, $t_s =$ average CPU time in seconds to solve for \mathbf{E}_z at each contrast value using CGNE or CGNE-FFT accordingly, $n_i =$ number of iteration of the solver required to reach the tolerance 10^{-5} , $o_q =$ value for the orthogonality check $\|\mathbf{I} - \mathbf{U}_q^H \mathbf{U}_q\|_2$ at iteration q , $t_\sigma =$ average CPU time in seconds to solve the model at each expansion point σ using CGNE-FFT, $t_t =$ total CPU time in seconds to generate and solve case study problem, $r_q =$ Ritz residual norm at iteration q , $p_r =$ ROM size reduction expressed in %, $e_r = \mathbf{E}_r^s / \mathbf{E}_z^s$ max relative error expressed as % over the entire contrast range).

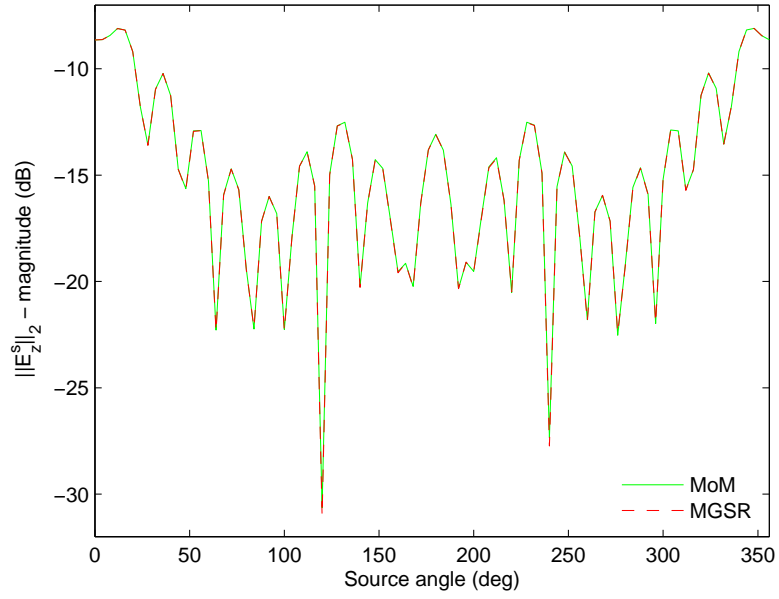


(a) $\|E_z^s\|_2$ - magnitude in dB for mono-static scattering over range of contrast $\zeta = 1.1 : 0.1 : 4$ comparing MoM, MGSR and the MGS from a homogeneous cylinder for $q = 150, 250$.

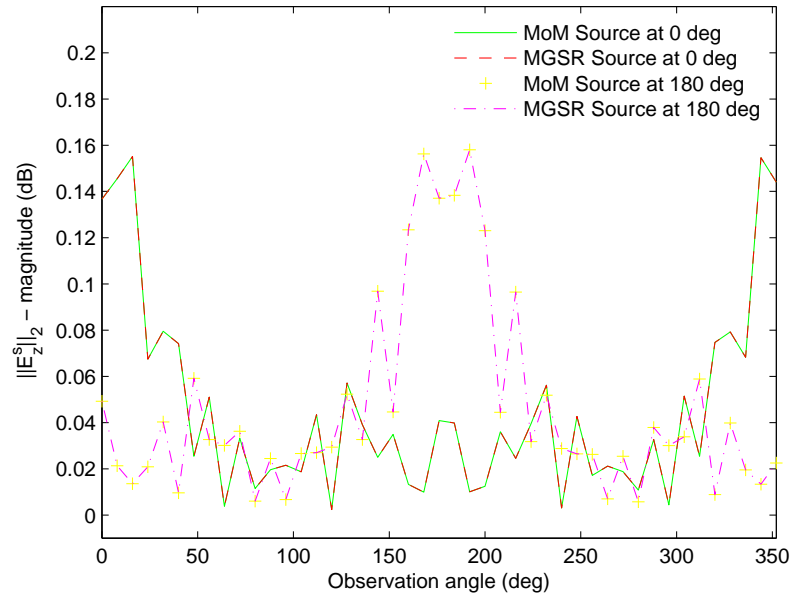


(b) Percentage relative error for Figure 4.7(a).

Figure 4.7: Case study 1: Mono-static scattering from a homogeneous cylinder with $r = 1.5\lambda_0$, $q = 150, 250$ and $\zeta = 1.1 : 0.1 : 4$, comparing MoM and MGSR.



(a) $\|E_z^s\|_2$ - magnitude in dB observed at receiver location 0 degrees over a range of source locations for $\phi = 0:2\pi$ and at a radius of $10\lambda_0$.



(b) $\|E_z^s\|_2$ - magnitude in dB for bi-static scattering over range of angle $\phi = 0 : 2\pi$ comparing MoM, MGSR for a constant contrast of $\zeta = 1.1$ and two source locations (0 and 180 degrees).

Figure 4.8: Case study 1: Scattering from a homogeneous cylinder with constant contrast and varying source location, comparing MoM and MGSR.

4.6 Shift-and-invert Arnoldi

In order to improve the range of the Arnoldi iteration in a contrast-sweep analysis, either the size of the ROM must increase or a variant of the shift-and-invert Arnoldi needs to be implemented [31, 44, 45, 65]. As demonstrated earlier, the Arnoldi algorithm rapidly approximates well-separated external eigenvalues better than the internal eigenvalues. Since the external eigenvalues are the most dominant eigenvalues of the matrix \mathbf{G} , an accurate approximation can be achieved from a relative low-order subspace. However, often the eigenvalues are clustered, leading to slower convergence and an unacceptable number of steps are required to achieve an accurate approximation.

Even if the size of the q is increased, the reduced order scaled matrix $\zeta \mathbf{H}_q$ approximation to $\zeta \mathbf{G}$ decreases as the ζ value is increased. This is illustrated in Figure 4.10(a), which clearly shows that as we scale the \mathbf{G} matrix by the constant ζ from 1 : 10, the error between $\lambda(\zeta \mathbf{G})$ and $\lambda(\zeta \mathbf{H}_q)$ linearly increases

$$\gamma_i = \text{abs}(\lambda(\zeta_i \mathbf{G}) - \lambda(\zeta_i \mathbf{H}_q)) \quad \text{For } \zeta_i = 1 : 10. \quad (4.63)$$

An alternative is to employ a variant of the shift-and-invert Arnoldi, where the \mathbf{G} matrix is substituted by the shifted and inverted matrix $(\mathbf{I} + \sigma \mathbf{G})^{-1}$ in line 3 of the Arnoldi algorithm. This produced the shift-and-invert modified Gram-Schmidt with re-orthogonalisation algorithm (SIMGSR) as given in Table 4.4. The shift point σ is chosen to be equal to the value of the contrast ζ where the approximation loses accuracy. In effect, the original system is solved exactly at ζ , resulting in the approximation being exact at the shift point. The Arnoldi algorithm now approximates the external eigenvalues of the shifted-and-inverted matrix, where the eigenvalues of the \mathbf{G} matrix are related to the shifted-and-inverted matrix by

$$\begin{aligned} \mathbf{G}\mathbf{x} &= \lambda\mathbf{x} \\ (\mathbf{I} + \sigma\mathbf{G})\mathbf{x} &= (1 + \sigma\lambda)\mathbf{x} \\ \frac{1}{(1 + \sigma\lambda)}\mathbf{x} &= (\mathbf{I} + \sigma\mathbf{G})^{-1}\mathbf{x} \end{aligned} \quad (4.64)$$

In the above equation, λ is an eigenvalue of \mathbf{G} and $\frac{1}{(1+\sigma\lambda)}$ is an eigenvalue of $(\mathbf{I} + \sigma\mathbf{G})^{-1}$.

The subsequent Arnoldi vectors \mathbf{u} generated in SIMGSR define an orthonormal basis for the following union of Krylov subspaces

$$\text{span}\{\mathbf{U}_q\} = \mathcal{K}_{a_1}(\mathbf{G}, \mathbf{u}_1) \bigcup_{j=2}^p \mathcal{K}_{a_j}((\mathbf{I} + \sigma_j \mathbf{G})^{-1}, \mathbf{u}_1) \quad (4.65)$$

where p is the number of shift points σ_j and a_j is the number of iterations at each shift

$$\sum_{j=1}^p p a_j = q. \quad (4.66)$$

The (if, else) condition of line 5, Table 4.4, determines how to pass from a shift point at the origin to the shifted-and-inverted matrix. As long as $j = 1$, the algorithm proceeds as the standard Arnoldi algorithm described in Section 4.2. The occurrence of the condition $j \neq 1$ signals that the Krylov subspace \mathbf{K}_{a_j} has been completely spanned and that the spanning of the Krylov subspace $\mathbf{K}_{a_{j+1}}$ is about to start.

The selection of how many shift points (σ_j) and the number of eigenvalues to be approximated at each point can be automated by utilising the approximation residual error r_q and the Ritz residual norm stagnation check. When the Ritz residual norm stagnates, the iteration is terminated and the ROM is created. The approximation residual error is then calculated for each value of contrast. If a particular ζ approximation error is below the tolerance tol_{r_q} , the Arnoldi iteration can then be restarted at step $q + 1$. A shift-and-inverted matrix is then solved at the ζ value where the tolerance tol_{r_q} was met. The Ritz residual norm and approximation residual error are repeatedly checked until all of the contrast values are below the tolerance tol_{r_q} .

Finally, after the iteration is terminated, the approximation matrix is produced by projecting the \mathbf{G} matrix onto the space defined by the columns of the orthonormal matrix \mathbf{U}_q . This is given by the operation

$$\mathbf{H}_q = \mathbf{U}_q^H \mathbf{G} \mathbf{U}_q. \quad (4.67)$$

```

 $\mathbf{u}_1 = \mathbf{b} / \|\mathbf{b}\|_2$ 
 $n = 1$ 
for  $j = 1, \dots, p$ 
  for  $k = 1, \dots, a_j$ 
    if  $j = 1$ 
       $\mathbf{w}_n = \mathbf{G}\mathbf{u}_n$ 
    else
       $\mathbf{w}_n = (\mathbf{I} + \sigma_j \mathbf{G})^{-1} \mathbf{u}_n$ 
    end
     $v_n = \|\mathbf{w}_n\|_2$ 
    for  $i = 1, \dots, n$ 
       $h_{i,n} = \mathbf{u}_i^H \mathbf{w}_n$ 
       $\mathbf{w}_n = \mathbf{w}_n - \mathbf{u}_i h_{i,n}$ 
    end  $i$ 
    if  $\|\mathbf{w}_n\|_2 < \eta * v_n$ 
      for  $i = 1, \dots, n$ 
         $h_{i,n} = \mathbf{u}_i^T \mathbf{w}_n$ 
         $\mathbf{w}_n = \mathbf{w}_n - \mathbf{u}_i h_{i,n}$ 
      end  $i$ 
       $h_{n,n} = h_{n,n} + y_{n,n}$ 
    endif
     $h_{n+1,n} = \|\mathbf{w}_n\|_2$ 
    if  $h_{n+1,n} = 0$  Quit
     $\mathbf{u}_{n+1} = \mathbf{w}_n / h_{n+1,n}$ 
     $n = n + 1$ 
  end  $k$ .
end  $j$ .
 $\mathbf{H}_q = \mathbf{U}_q^H \mathbf{G} \mathbf{U}_q$ 

```

Table 4.4: Shift and invert Arnoldi - modified Gram-Schmidt algorithm with re-orthogonalisation (SIMGSR), p = number of expansion points, a_j = number of eigenvalues approximated at each expansion point.

4.6.1 Case Study 2: Mono-static scattering homogeneous cylinder - Medium 1

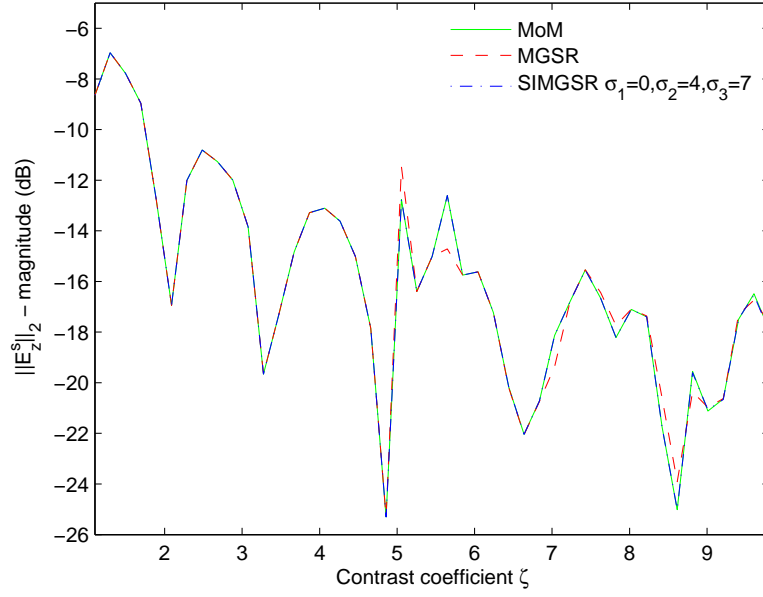
In this section, the application of the SIMGSR to a contrast sweep analysis is investigated. A similar numerical experiment is conducted where the mono-static backscattered field E_z^s is computed over an extended range of contrast values of $\zeta_1 = 1.1 : 10$ in increments of 0.25. As before, a fixed line source location is used and is located at Cartesian coordinates $(-10,0,0)$. Figures 4.9(a) and 4.9(b) shows the scattered field and associated error obtained from the MoM, MGSR and the SIMGSR technique for $q = 250$, representing a 90% reduction in system size. It is clear from these figures that the MGSR approximation is limited to a max value of $\zeta = 4.8$ for $q = 250$. Using three shift points $\zeta_1 = 0, \zeta_2 = 4$ and $\zeta_3 = 7$ with $q = 84 + 83 + 83 = 250$, the SIMGSR replicates the reference solution over the entire contrast range to within a max average percentage error of 10%.

Comparing Figures 4.10(a) and 4.10(b) clearly shows that as we scale the \mathbf{G} matrix by the contrast ζ from $1 : 10$, the error between $\lambda(\zeta\mathbf{G})$ and $\lambda(\zeta\mathbf{H}_q)$ is significantly decreased using the SIMGSR algorithm. The effect of reducing this error, as ζ increases, ensures that a wider contrast range can be accurately approximated using multiple shift points. This can be clearly demonstrated by plotting the average absolute error between $\lambda(\zeta\mathbf{G})$ and $\lambda(\zeta\mathbf{H}_q)$ for a range of $\zeta = 0 : 10$ comparing the first q eigenvalues of the MoM \mathbf{G} matrix against the eigenvalues of the ROM \mathbf{H}_q created using the MGSR and SIMGSR

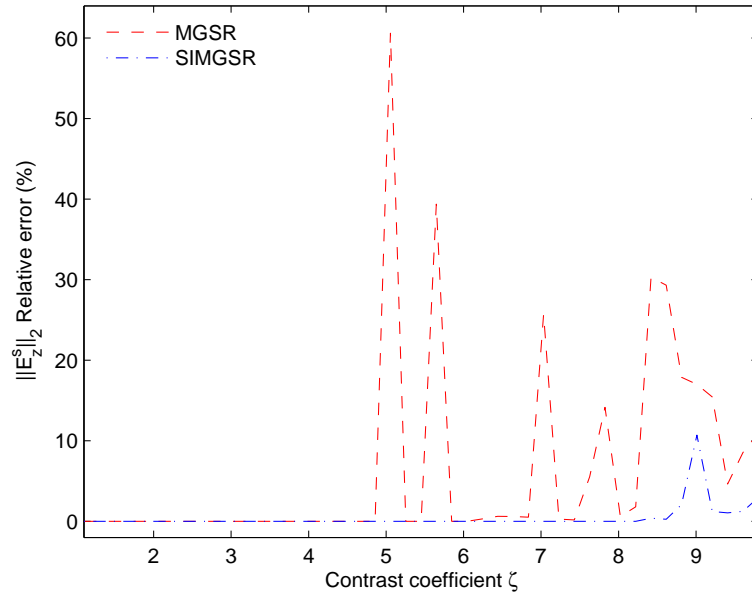
$$\alpha_i = \frac{\sum_{n=1}^q \text{abs}(\lambda_n(\zeta_i\mathbf{G}) - \lambda_n(\zeta_i\mathbf{H}_q))}{q}. \quad (4.68)$$

As evident from Figure 4.11(a) the SIMGSR incurs a slower increase in error between the scaled eigenvalues, subject to an average error of 0.048 as compared to the MGSR with 0.138.

The CPU time comparing the MGSR and SIMGSR for 45 samples over the extended range of contrast is given in Table 4.3. The additional computational time associated with the SIMGSR is due to the solution of the linear system $(\mathbf{I} + \sigma\mathbf{G})$ for each shift value. This is accompanied using the CGNE-FFT at a cost of 26.76 seconds for each shift. This significantly increases the time required to generate the \mathbf{U}_q matrix. However, the SIMGSR ROM still results in a considerable speed-up of 9.38 as compared to the direct solution over the entire contrast range.

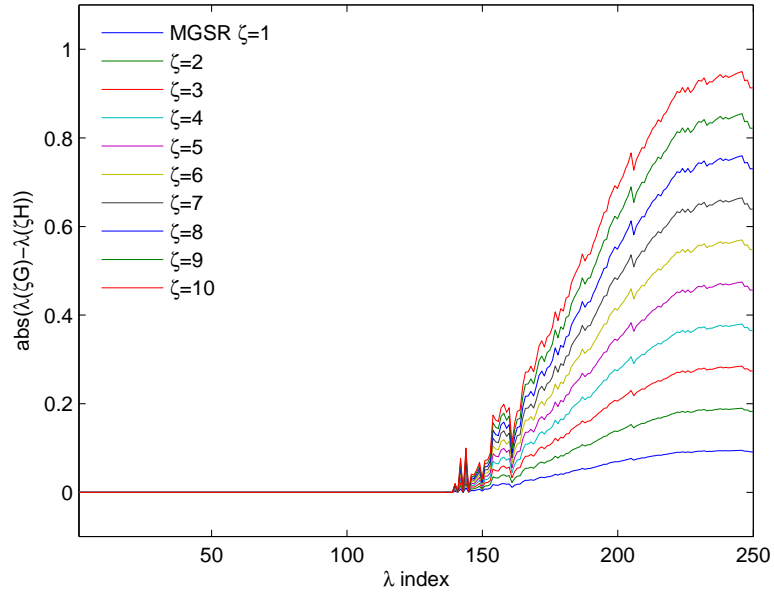


(a) $\|E_z^s\|_2$ - magnitude in dB for mono-static scattering over range of contrast $\zeta = 1.1 : 0.25 : 10$ comparing MoM, MGSR and the SIMGSR using 3 shift points ($\sigma_1 = 0$ $q = 84, \sigma_2 = 4$ $q = 83, \sigma_3 = 7$ $q = 83$) from a homogeneous cylinder).

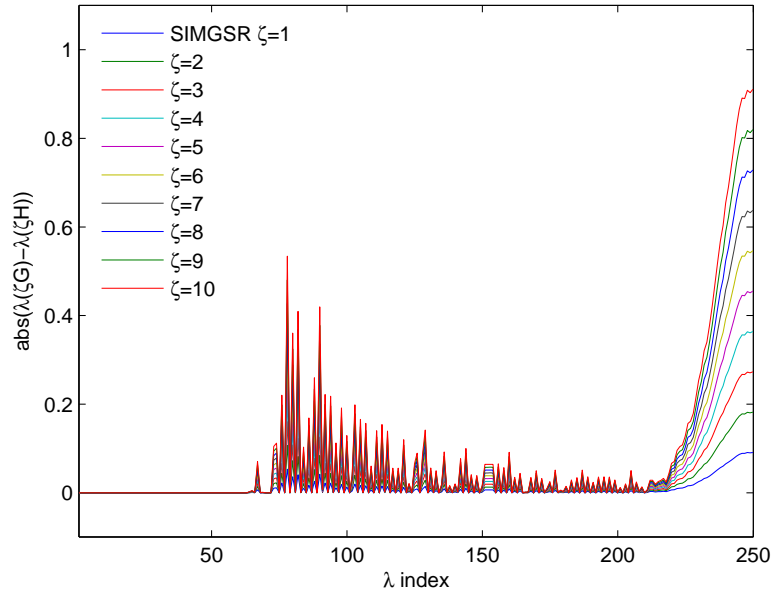


(b) Percentage relative error for Figure 4.9(a).

Figure 4.9: Case study 2: Mono-static scattering from a homogeneous cylinder with $r = 1.5\lambda_0$, $q = 250$ and $\zeta = 1.1 : 0.25 : 10$, comparing MoM, MGSR and SIMGSR.

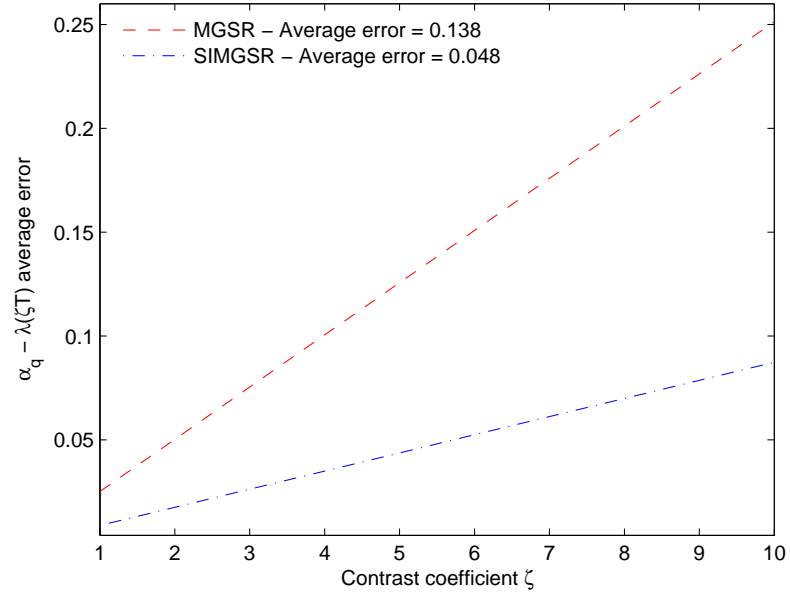


(a) $|\lambda(\zeta G) - \lambda(\zeta H)|$ for a range of $\zeta = 0 : 10$ - comparing the first q eigenvalues of the MoM G matrix against the eigenvalues of the ROM H created using the MGSR.



(b) $|\lambda(\zeta G) - \lambda(\zeta H)|$ for a range of $\zeta = 0 : 10$ - Comparing the first q eigenvalues of the MoM G matrix against the eigenvalues of the ROM H created using the SIMGSR.

Figure 4.10: Case study 2 Part A: Error analysis of the approximate eigenvalues of the ROM created using the MGSR and SIMGSR for a range of ζ values.



(a) α_q (Equation 4.68) - Average absolute error between $\lambda(\zeta G)$ and $\lambda(\zeta H)$ for a range of $\zeta = 0 : 10$, comparing the first q eigenvalues of the MoM G matrix against the eigenvalues of the ROM H created using the MGSR and SIMGSR.

Figure 4.11: Case study 2 Part A: Error analysis of the approximate eigenvalues of the ROM created using the MGSR and SIMGSR for a range of ζ values.

4.6.2 Case Study 3: Bi-static scattering inhomogeneous cylinder - Medium 1,2,3,4

In this section, we consider an inhomogeneous circular cylinder composed of four concentric regions centred at the origin, with radii $r_1 = 1.5\lambda_0$, $r_2 = 1.125\lambda_0$, $r_3 = 0.75\lambda_0$, $r_4 = 0.375\lambda_0$, and assumed to be embedded in free space. The structure is illuminated by a transverse magnetic (TM^z) wave emanating from a line source located at $(-10, 0)$ and radiating at a frequency of $f = 300$ MHz. The cylinder was discretised using $m = 2500$ cells and the bi-static backscattered field E_z^s is computed for the particular case of $\zeta_1 = 4$, $\zeta_2 = 3$, $\zeta_3 = 2$, $\zeta_4 = 1.1$, over an observation angle of $\phi = 0 : 2\pi$ with a fixed source location.

The scattered field and associated percentage relative error calculated by comparing the MoM against the MGSR for $q = 250$, are shown in Figures 4.12(a) and 4.12(b) respectively. The MGSR represents a 90% reduction in system size while yielding a maximum relative error of 6.3%.

As indicated in the previous section, the approximation residual error t_q (Equation 4.50) and the Ritz residual norm (Equation 4.59) are used to determine when to terminate the MGSR iteration. It can be seen from Figure 4.4(a) that a value of $q = 200$ results in $r_q < 10^{-3}$; this indicates that the approximation $\tilde{\mathbf{e}}$ has converged to \mathbf{e} within this tolerance. The Ritz residual is monitored to check for stagnation in the Arnoldi iteration. A value of $q = 160$ signals that the tolerance of $\text{tol}_{t_q} = 10^{-4}$ has been reached and the iteration terminated as illustrated in Figure 4.14(a).

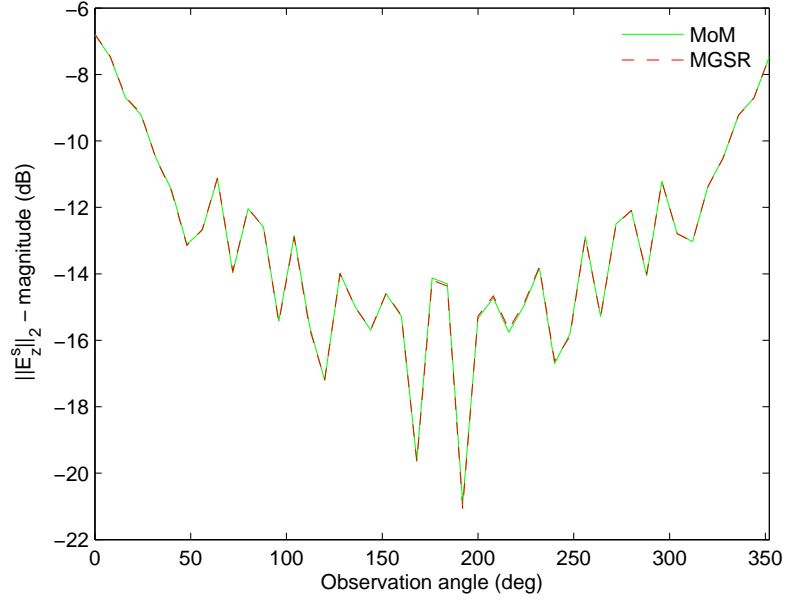
A plot of the approximation eigenvalue $\lambda(\mathbf{H}_q)$ and the corresponding eigenvalue $\lambda(\mathbf{G})$, in order of magnitude, is compared in Figure 4.14(b). From this figure, it is clear that the Arnoldi iteration initially approximates the largest eigenvalues of the matrix \mathbf{G} . As q is increased, the process rapidly approximates these external eigenvalues to a higher level of accuracy than the internal eigenvalues.

Figure 4.6(a) illustrates that the MGSR algorithm retains near-machine precision orthogonality amongst the computed Krylov vectors in the matrix \mathbf{U}_n (Equation 6.13).

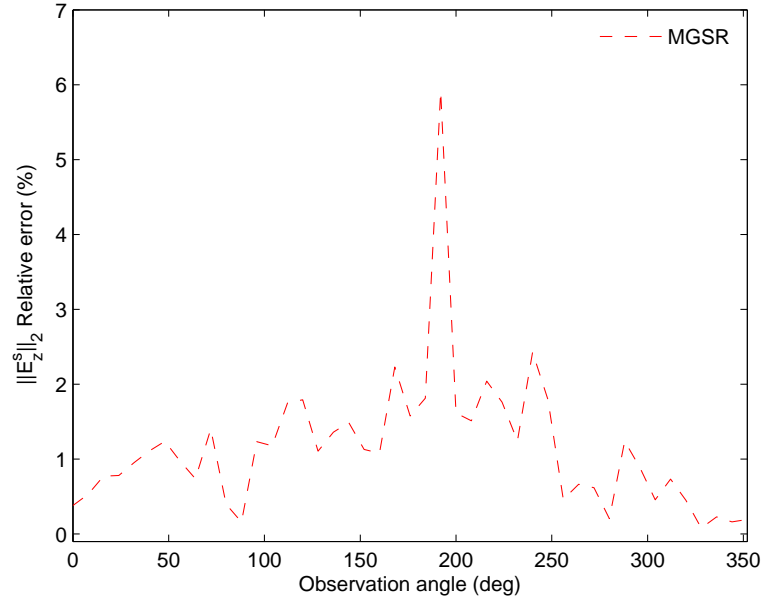
Finally, Figure 4.7(b) depicts the subspace residual error

$$\frac{\|(\mathbf{x} - \mathbf{U}_q \mathbf{a}_q - \mathbf{G} \mathbf{A} \mathbf{U}_q \mathbf{a}_q) - (\mathbf{x} - \mathbf{U}_q \mathbf{a}_q - \mathbf{G} \mathbf{U}_q \tilde{\mathbf{A}}_q \mathbf{a}_q)\|_2}{\|\mathbf{x} - \mathbf{U}_q \mathbf{a}_q - \mathbf{G} \mathbf{U}_q \tilde{\mathbf{A}}_q \mathbf{a}_q\|_2}. \quad (4.69)$$

This plot substantiates the argument for the approximation of Equation 4.36, by clearly showing that as q increases this approximation converges to working precision.

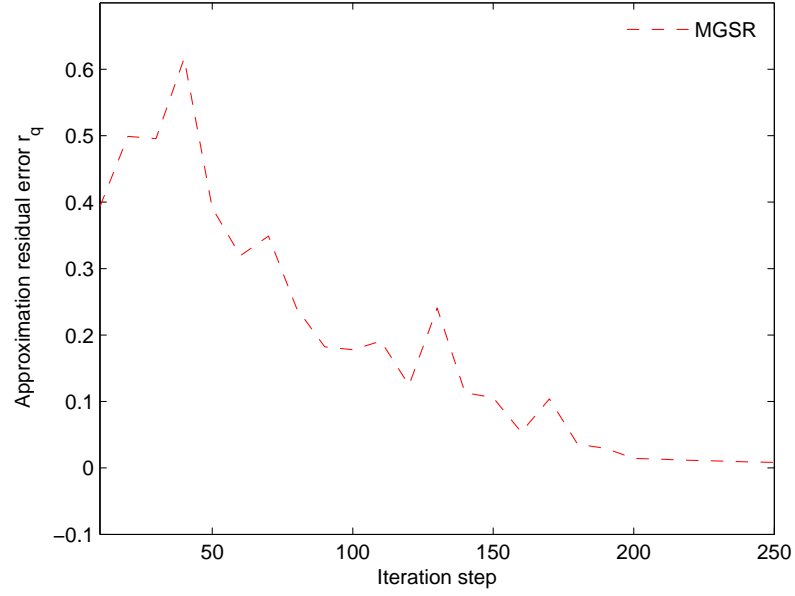


(a) $\|E_z^s\|_2$ - magnitude in db for bi-static scattering over range of angle $\phi = 0 : 2\pi$ comparing MoM and MGSR for a constant contrast profile of $\zeta_1 = 4, \zeta_2 = 3, \zeta_3 = 2$ and $\zeta_4 = 1.1$ from an inhomogeneous cylinder.

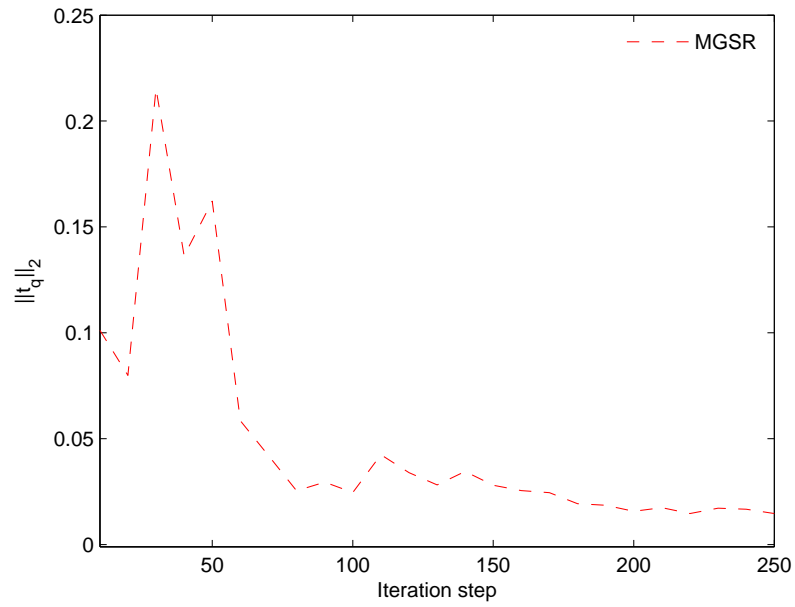


(b) Percentage relative error for Figure 4.3(a).

Figure 4.12: Case study 3 Part A: Bi-static scattering from an inhomogeneous cylinder with $r = 1.5\lambda_0$, $q = 250$, $\zeta_1 = 4, \zeta_2 = 3, \zeta_3 = 2$ and $\zeta_4 = 1.1$.

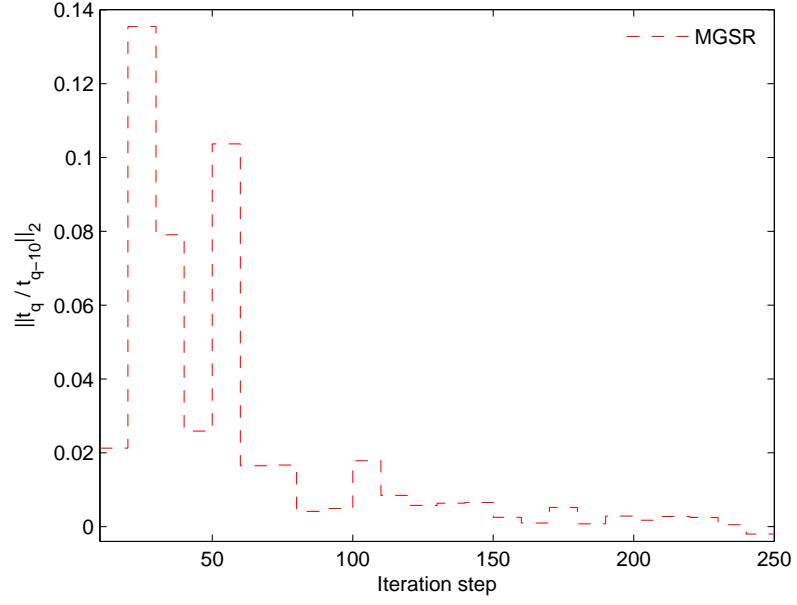


(a) Approximation residual relative error r_q - (Equation 4.50) for MGSR.

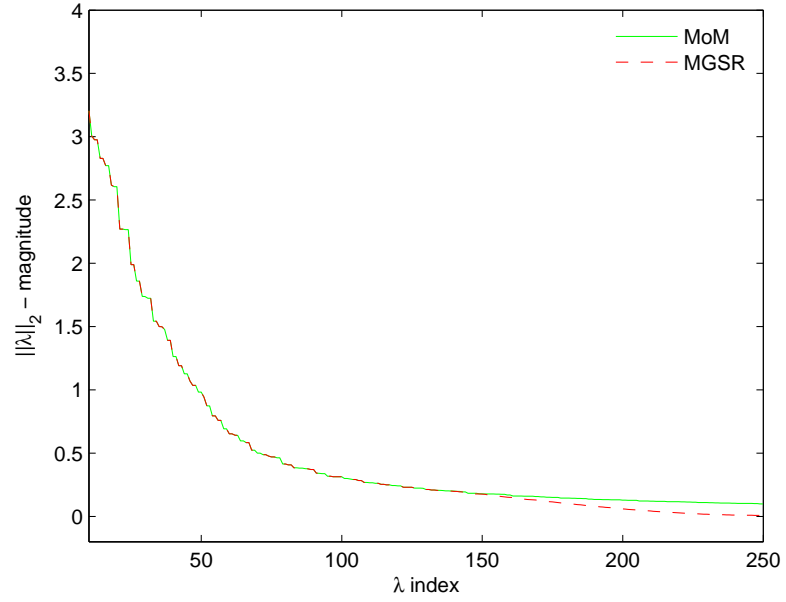


(b) Ritz residual norm $\|t_q\|_2$ - (Equation 4.59) for MGSR.

Figure 4.13: Case study 3 Part B: Bi-static scattering from an inhomogeneous cylinder with $r = 1.5\lambda_0$, $q = 250$, $\zeta_1 = 4$, $\zeta_2 = 3$, $\zeta_3 = 2$ and $\zeta_4 = 1.1$.

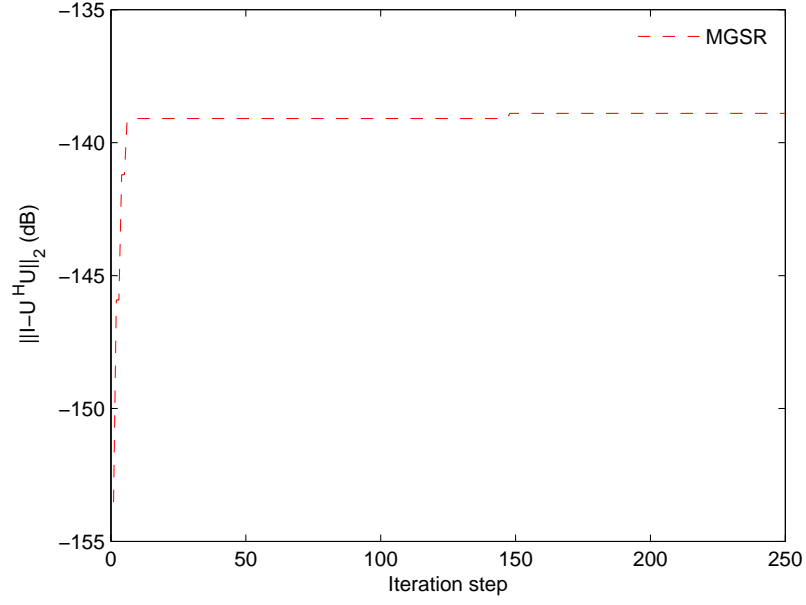


(a) Monitoring Ritz residual stagnation check for MGSR - $(\|\mathbf{r}_q - \mathbf{r}_{q-s}\|_2)$.

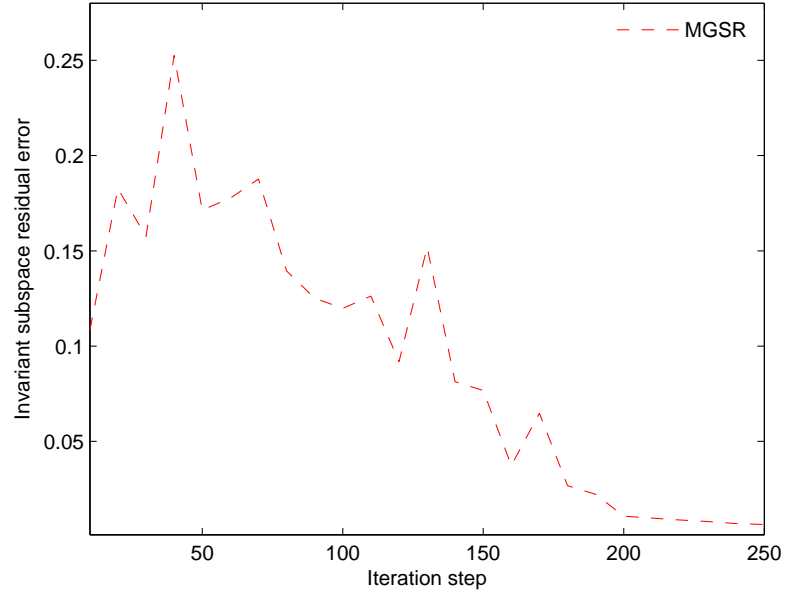


(b) $\|\lambda\|_2$ - comparing MoM against MGSR eigenvalues in order of magnitude.

Figure 4.14: Case study 3 Part C: Bi-static scattering from an inhomogeneous cylinder with $r = 1.5\lambda_0$, $q = 250$, $\zeta_1 = 4$, $\zeta_2 = 3$, $\zeta_3 = 2$ and $\zeta_4 = 1.1$.



(a) Loss of orthogonality over iteration process for MGSR and MGS - $\|\mathbf{I} - \mathbf{U}^H \mathbf{U}\|_2$.



(b) Equation 4.36 invariant subspace approximation relative error.

Figure 4.15: Case study 3 Part D: Bi-static scattering from an inhomogeneous cylinder with $r = 1.5\lambda_0$, $q = 250$, $\zeta_1 = 4$, $\zeta_2 = 3$, $\zeta_3 = 2$ and $\zeta_4 = 1.1$.

4.6.3 Case Study 4: Mono-static scattering from an inhomogeneous cylinder - Medium 1,2,3,4

In this section, the MGSR is applied to an inhomogeneous cylinder for a contrast-sweep analysis. A similar numerical experiment is conducted where the mono-static backscattered field E_z^s is computed over a range of contrast values of $\zeta_4 = 1.1 : 0.1 : 4$ while $\zeta_3 = 2$, $\zeta_2 = 3$, $\zeta_1 = 4$ are kept constant, for a fixed line source location. Figures 4.16(a) and 4.16(b) show the scattered field and associated error obtained from the MoM and the MGSR technique for $q = 250$ and $q = 150$. From Table 4.5 and the above figures, a reduction in system size of 94% results in a maximum relative error of $< 6.3\%$ and a Ritz residual norm of 0.1056. Machine precision accuracy over the entire contrast range can be achieved by a 90% reduction in system size with a Ritz residual norm of 8.43×10^{-3} . As discussed in the previous section, the Ritz residual norm r_q and approximation residual error t_q can be used to determine the order of the Arnoldi iteration.

Unfortunately, unlike the homogeneous case, the SIMGSR techniques can not be used to extend the range of accuracy of the Arnoldi algorithm. This is due to the contrast ζ being replaced with a contrast profile matrix \mathbf{A} . In this case, there is no singular value of ζ to use as an expansion point. Even if the \mathbf{A} matrix is used in a SIMGSR iteration, since the \mathbf{G} matrix is not being scaled by a contrast value, the columns of the subsequent \mathbf{U}_q matrix will not all span the same solution space. Consequentially, when the \mathbf{G} matrix is projected into the solution space by the operator \mathbf{U}_q (Equation 4.67), an inaccurate approximation matrix \mathbf{H}_q will be generated.

As is evident from Table 4.5, the MGSR algorithm can significantly decrease the computational expense associated with the direct solution of each contrast value in a sweep analysis. Unlike the homogeneous case as discussed in Section 4.4.2, the main computational cost of this approach is incurred in generating the Krylov matrix \mathbf{U}_q and the initial $\tilde{\mathbf{A}}_q$. However, once generated, the \mathbf{U}_q matrix and non-varying components of $\tilde{\mathbf{A}}_q$ can be used in subsequent simulations. Specifically, only the component of $\tilde{\mathbf{A}}_q$ associated with each varying homogeneous region needs to be re-calculated. The CPU time associated with the solution of the scattered field for the MoM using the CGNE-FFT against the MGSR with CGNE for 45 samples is given in Table 4.5. This is confirmed in this table where a combined time of 36.63 seconds is required to generate the initial \mathbf{U}_q and $\tilde{\mathbf{A}}_q$. However, the CPU time is significantly reduced for all subsequent generation of the amended $\tilde{\mathbf{A}}_q$ at a cost of 0.4219 seconds. From this table, it is also clear that as the size of the ROM increases, the CPU overhead associated with the creation and updating of the contrast profile matrix significantly

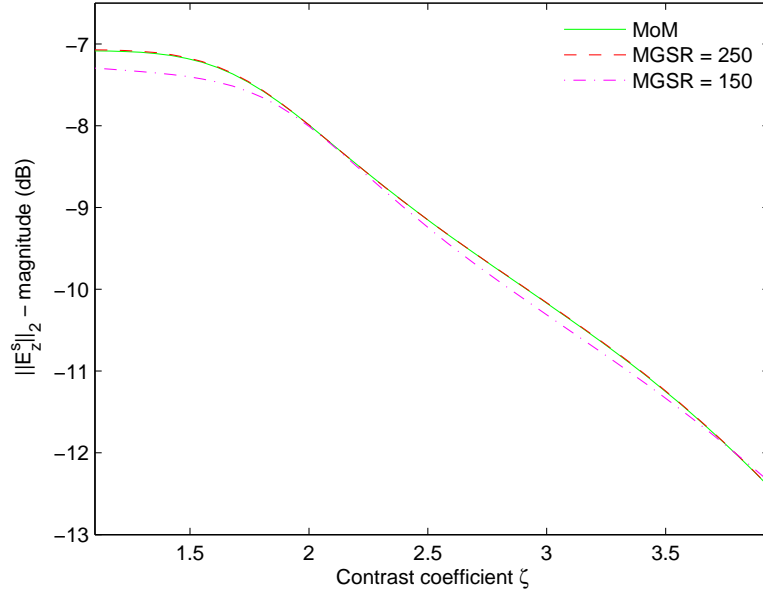
increases.

However, considerable CPU time saving can be achieved by utilising this method. For a 90% reduction in system size using the MGSR, near-machine precision in accuracy is observed over the entire contrast range. This reduction achieves a speed-up of 20.52 as compared to the MoM solution with FFT capability. Similarly, for a 94% reduction, the MGSR incurs an average percentage relative error of approximately 6.3% with a speed-up of 43.3.

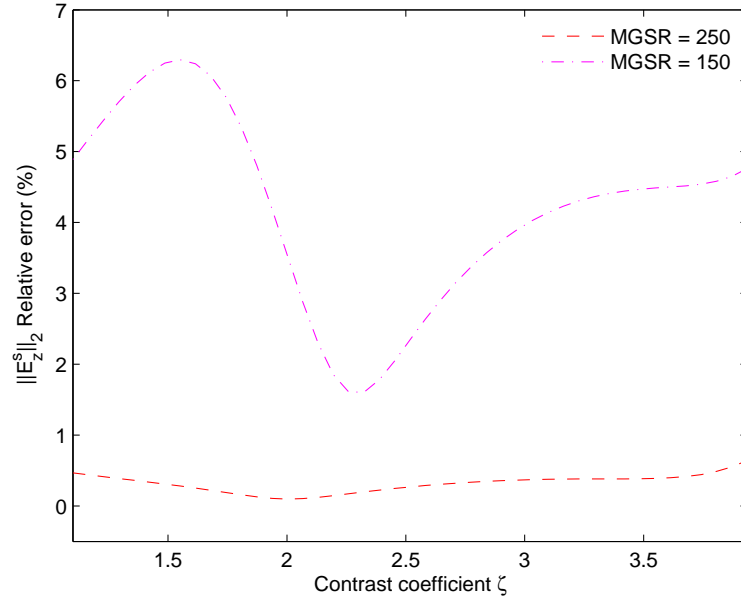
In the final example, we consider the case where the contrast value is fixed and the source location is varying, and the approximation solution is generated using Equation 4.42. Using this formulation, the backscattered field E_z^s is observed at $\phi = 0$ and computed over a range of line source location of $\phi = 0 : 2\pi$ in increments of 8 degrees. The source location is set at a radius of $10\lambda_0$ and the contrasts are fixed at $\zeta_4 = 1.1$, $\zeta_3 = 2$, $\zeta_2 = 3$ and $\zeta_1 = 4$. From Figures 4.17(a) and 4.17(b), it is clear that the MGSR duplicates the reference solution over the entire range of source location to within machine precision for $q = 250$.

Legend	Technique	
	MoM (CGNE-FFT)	Arnoldi MGSR (CGNE)
Order	$m = 2500$	$q = 150$
c_n	891.65	870.36
n_s	45	45
$t_u(s)$	-	13.92
$t_i(s)$	-	4.89
$t_v(s)$	-	0.1718
$t_s(s)$	26.766	0.032
n_i	887	12
o_q	-	1.29×10^{-14}
$t_t(s)$	1204.5	27.81
r_q	-	0.1056
$p_r(\%)$	-	94
$e_r(\%)$	-	3.05^{-15}
Speed-up	-	43.3
		20.52

Table 4.5: CPU time analysis (Case study 3,4 - Inhomogeneous structure with 4 homogeneous regions, $f = 300$ MHz, $\lambda_0 = 1m$, $r = 1.5\lambda_0$, Region 4 - $\zeta_4 = 1.1:0.1:4$ ($\zeta_1, \zeta_2, \zeta_3 = 4, 3, 2$), $m =$ size of MoM matrix, $q =$ size of ROM, c_n - condition number of MoM or ROM matrix accordingly, n_s - number of contrast samples, $t_u =$ CPU time in seconds to generate Krylov U_q matrix, $t_i =$ CPU time in seconds to generate initial \hat{A}_q , $t_v =$ CPU time in seconds to generate the amended component of \hat{A} , $t_s =$ average CPU time in seconds to solve for E_z at each contrast value using CGNE or CGNE-FFT accordingly, $n_i =$ number of iteration of the solver required to reach the tolerance 10^{-5} , $e_i =$ solvers relative error after n_i iterations, $o_q =$ value for the orthogonality check $\|\mathbf{I} - \mathbf{U}_q^H \mathbf{U}_q\|_2$ at iteration q , $t_t =$ total CPU time in seconds to generate and solve case study problem, $r_q =$ Ritz residual norm at iteration q , $p_r =$ ROM size reduction expressed in %, $e_r = E_z^s$ max absolute error over the entire contrast range).

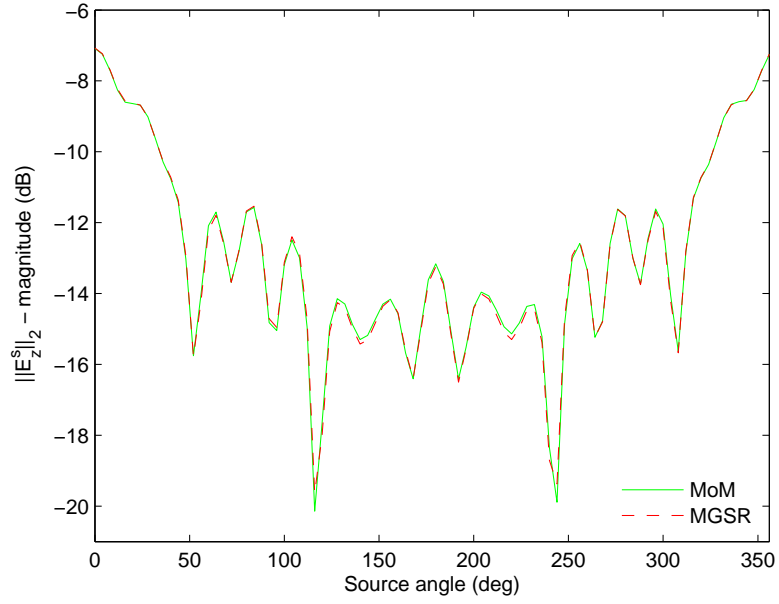


(a) $\|E_z^s\|_2$ - magnitude in db for mono-static scattering over range of contrast $\zeta_4 = 1.1:0.1:4$ with $\zeta_1 = 4, \zeta_2 = 3$ and $\zeta_3 = 2$, comparing MoM and MGSR from an inhomogeneous cylinder for $q = 250$ and 150).

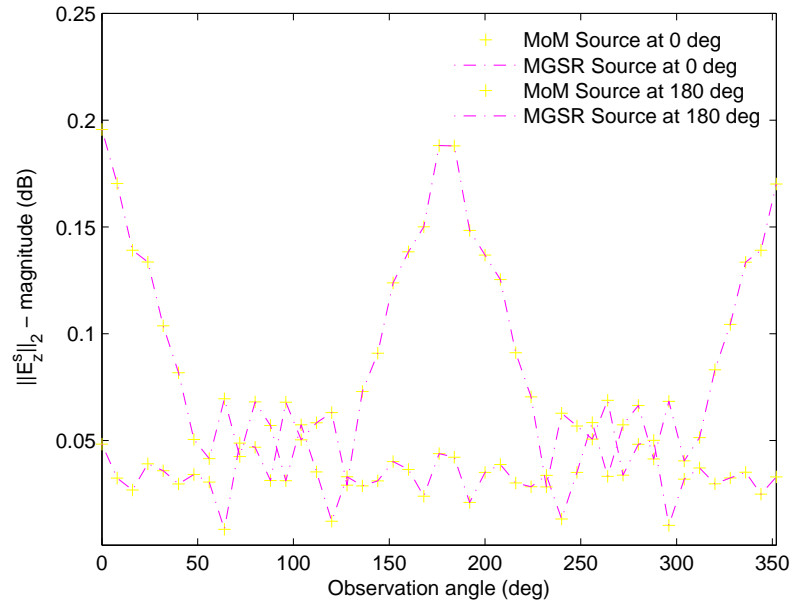


(b) Percentage relative error for Figure 4.16(a).

Figure 4.16: Case study 3: Mono-static scattering from an inhomogeneous cylinder with $r = 1.5\lambda_0$, $q = 250, 150$, $\zeta = 1.1:0.1:4$, $\zeta_1 = 4, \zeta_2 = 3$ and $\zeta_3 = 2$.



(a) $\|E_z^s\|_2$ - magnitude in db observed at source location 0 degrees over a range of source locations for $\phi = 0:2\pi$ and at a radius of $10\lambda_0$.



(b) $\|E_z^s\|_2$ - magnitude in db for bi-static scattering over range of angle $\phi = 0:2\pi$ comparing MoM, MGSR for a constant contrast of $\zeta = 1.1$ and two source locations (0 and 180 degrees).

Figure 4.17: Case study 4: Scattering from an inhomogeneous cylinder with constant contrast and varying source location.

Chapter 5

Well-Conditioned Asymptotic Waveform Evaluation

“The important thing in science is not so much to obtain new facts as to discover new ways of thinking about them.”

Sir William Bragg

This chapter is dedicated to the application of the WCAWE algorithm for fast frequency-sweep analysis with the EFIE. The evolution of the WCAWE algorithm is explored in detail. The WCAWE algorithm introduces correction factors that eliminate the ill-conditioning associated with explicit moment-matching techniques in order to obtain a high-order approximation in a numerically stable manner. Other numerical implementation issues are discussed in Section 5.6, including how to terminate the WCAWE iteration process and the extension of the WCAWE algorithm to wideband applications.

5.1 Well-Conditioned Asymptotic Waveform Evaluation (WCAWE)

In Section 2.5, the GAWE technique was presented. It has been shown in [11, 51] that the GAWE approximation will not significantly improve the bandwidth achieved compared to an AWE approximation of the same order. This is due to the fact that the GAWE is still building the subspace \mathcal{W}_q through the same ill-conditioned moment-matching process as is present in the AWE process (Equation 2.16). More specifically, the GAWE orthonormalises \mathbf{W}_q onto the basis defined by the columns of the matrix $\overline{\mathbf{W}}_q$ which is then used in Equation 2.30. Indeed, using the AWE with the adaptive zeta will outperform the GAWE. Therefore, the AWE with adaptive zeta will be used as the method for comparison for the WCAWE.

In order to understand the WCAWE process, examination of the possible solution to the problems encountered by the GAWE technique is required - which is to orthonormalise the GAWE vectors \mathbf{w}_n onto the columns of $\overline{\mathbf{W}}_q$ before \mathbf{W}_q is generated. This approach is called the alternative GAWE (AGAWE) and is outlined in Table 5.1. At step n the AGAWE algorithm immediately orthonormalised $\widehat{\mathbf{w}}_n$ against $\overline{\mathbf{W}}_{n-1}$ ($\widehat{\mathbf{w}}_n$ is explicitly orthogonalised against all the previous vectors $\widehat{\mathbf{w}}_1, \widehat{\mathbf{w}}_2, \dots, \widehat{\mathbf{w}}_{n-1}$), which subsequently is used to form $\widehat{\mathbf{w}}_n$. The orthonormal matrix $\overline{\mathbf{W}}_q$ can then be substituted into Equation 2.27 to form an AGAWE approximation.

However, this approach in general will not match moments and thus will produce an inaccurate approximation. To examine this point further, consideration of why this new approximation will not match moments is required and subsequently, how the WCAWE technique resolves these issues. The recursive forms for the vector in the AGAWE approximation are given as

$$\begin{aligned}\widehat{\mathbf{w}}_1 &= \mathbf{Z}^{-1}\mathbf{b} \\ \widehat{\mathbf{w}}_2 &= \mathbf{Z}^{-1} \left(\mathbf{b}^{[1]} - \mathbf{Z}^{[1]}\widehat{\mathbf{w}}_1 \right) \\ \widehat{\mathbf{w}}_3 &= \mathbf{Z}^{-1} \left(\mathbf{b}^{[2]} - \mathbf{Z}^{[1]}\widehat{\mathbf{w}}_2 - \mathbf{Z}^{[2]}\widehat{\mathbf{w}}_1 \right) \\ &\vdots \\ \widehat{\mathbf{w}}_q &= \mathbf{Z}^{-1} \left(\mathbf{b}^{[q-1]} - \sum_{m=1}^{q-1} \mathbf{Z}^{[m]}\widehat{\mathbf{w}}_{q-m} \right).\end{aligned}$$

from Algorithm 5.1. If the columns of the matrix $\overline{\mathbf{W}}_q$ matches moments, then it must be the case that

$$\text{span}(\overline{\mathbf{W}}_n) = \text{span}(\mathbf{W}_n) \quad \text{for all } 1 \leq n \leq q. \quad (5.1)$$

That is to say, the span of columns of the AGAWE approximation $\overline{\mathbf{W}}_n$ must be equal to the span of the AWE subspace \mathcal{W}_n (Note: The AWE is explicitly formulated to match moments of the Taylor expansion and as such if the AGAWE match moments the span of the corresponding subspaces will be equivalent) for all n such that $1 \leq n \leq q$. However, since $\overline{\mathbf{W}}_q$ is generated from $\widehat{\mathbf{W}}_q$ by an orthonormalisation process, it is always the case that

$$\text{span}(\overline{\mathbf{W}}_n) = \text{span}(\widehat{\mathbf{W}}_n) \quad \text{for all } 1 \leq n \leq q. \quad (5.2)$$

Therefore, the requirement given in Equation 5.1 is equivalent to the following requirement:

$$\text{span}(\widehat{\mathbf{W}}_n) = \text{span}(\mathbf{W}_n) \quad \text{for all } 1 \leq n \leq q. \quad (5.3)$$

The following examples show that Equation 5.3 does not hold for the case outlined. The requirement given in Equation 5.3 can fail to be true for values of n as low as 2. For example, $\mathbf{w}_1 = \widehat{\mathbf{w}}_1$ therefore

$$\widehat{\widehat{\mathbf{w}}}_1 = \widehat{\mathbf{w}}_1 \mathbf{T}_{[1,1]}^{-1} = \mathbf{w}_1 \mathbf{T}_{[1,1]}^{-1} \in \text{span}(\mathbf{W}_1) \quad (5.4)$$

(where \mathbf{T} is defined on line 2, 7 and 10 of Algorithm 5.1) and so

$$\begin{aligned} \widehat{\mathbf{w}}_2 &= \mathbf{Z}^{-1} \left(\mathbf{b}^{[1]} - \mathbf{Z}^{[1]} \widehat{\widehat{\mathbf{w}}}_1 \right) \\ &= \mathbf{Z}^{-1} \left(\mathbf{b}^{[1]} - \mathbf{Z}^{[1]} \mathbf{w}_1 \mathbf{T}_{[1,1]}^{-1} \right) \notin \text{span}(\mathbf{W}_2). \end{aligned} \quad (5.5)$$

Therefore, $\text{span}(\widehat{\mathbf{W}}_2) \neq \text{span}(\mathbf{W}_2)$. Thus, in general, the requirement that Equation 5.3 is not fulfilled and Equation 5.1 does not match moments for $n > 1$. $n = 3$ is generated as a comparison to show how the WCAWE corrects the AGAWE which will be outlined later in this section

$$\begin{aligned} \widehat{\mathbf{w}}_3 &= \mathbf{Z}^{-1} \left(\mathbf{b}^{[2]} - \mathbf{Z}^{[1]} \widehat{\widehat{\mathbf{w}}}_2 - \mathbf{Z}^{[2]} \widehat{\widehat{\mathbf{w}}}_1 \right) \\ &= \mathbf{Z}^{-1} \left(\mathbf{b}^{[2]} - \mathbf{Z}^{[1]} \widehat{\mathbf{w}}_2 \mathbf{T}_{[2,2]}^{-1} - \mathbf{Z}^{[2]} \mathbf{w}_1 \mathbf{T}_{[1,1]}^{-1} \right) \\ &= \mathbf{Z}^{-1} \left(\mathbf{b}^{[2]} - \mathbf{Z}^{[1]} \left(\mathbf{Z}^{-1} \left(\mathbf{b}^{[1]} - \mathbf{Z}^{[1]} \mathbf{w}_1 \mathbf{T}_{[1,1]}^{-1} \right) \right) \right. \\ &\quad \left. \mathbf{T}_{[2,2]}^{-1} - \mathbf{Z}^{[2]} \mathbf{w}_1 \mathbf{T}_{[1,1]}^{-1} \right) \notin \text{span}(\mathbf{W}_3). \end{aligned} \quad (5.6)$$

5.1.1 Summary of terms

- $\mathcal{W}_q = \{\mathbf{w}_1, \mathbf{w}_2, \dots, \mathbf{w}_q\}$ - AWE and GAWE subspace
- $\widehat{\mathcal{W}}_q = \{\widehat{\mathbf{w}}_1, \widehat{\mathbf{w}}_2, \dots, \widehat{\mathbf{w}}_q\}$ - AGAWE subspace
- $\overline{\mathbf{W}}_q = [\overline{\mathbf{w}}_1, \overline{\mathbf{w}}_2, \dots, \overline{\mathbf{w}}_q]$ - GAWE orthonormal matrix whose columns define an orthonormal basis $\{\overline{\mathbf{w}}_1, \overline{\mathbf{w}}_2, \dots, \overline{\mathbf{w}}_q\}$
- $\widehat{\overline{\mathbf{W}}}_q = [\widehat{\overline{\mathbf{w}}}_1, \widehat{\overline{\mathbf{w}}}_2, \dots, \widehat{\overline{\mathbf{w}}}_q]$ - AGAWE orthonormal matrix whose columns define an orthonormal basis $\{\widehat{\overline{\mathbf{w}}}_1, \widehat{\overline{\mathbf{w}}}_2, \dots, \widehat{\overline{\mathbf{w}}}_q\}$
- $\text{span}(\overline{\mathbf{W}}_q) = \text{span}(\mathbf{W}_q)$
- $\text{span}(\widehat{\overline{\mathbf{W}}}_q) \neq \text{span}(\mathbf{W}_q)$

```

 $\hat{\mathbf{w}}_1 = \mathbf{Z}^{-1}\mathbf{b}$ 
 $\mathbf{T}_{[1,1]} = \|\hat{\mathbf{w}}_1\|_2$ 
 $\hat{\tilde{\mathbf{w}}}_1 = \hat{\mathbf{w}}_1 \mathbf{T}_{[1,1]}^{-1}$ 
for  $n = 2, \dots, q$ 
     $\hat{\mathbf{w}}_n = \mathbf{Z}^{-1}(\mathbf{b}^{[n-1]} - \sum_{m=1}^{n-1} \mathbf{Z}^{[m]} \hat{\tilde{\mathbf{w}}}_{n-m})$ 
    for  $i = 1, \dots, n-1$ 
         $\mathbf{T}_{[i,n]} = \hat{\tilde{\mathbf{w}}}_i^H \hat{\mathbf{w}}_n$ 
         $\hat{\mathbf{w}}_n = \hat{\mathbf{w}}_n - \mathbf{T}_{[i,n]} \hat{\tilde{\mathbf{w}}}_i$ 
    end  $i$ 
     $\mathbf{T}_{[n,n]} = \|\hat{\mathbf{w}}_n\|_2$ 
     $\hat{\tilde{\mathbf{w}}}_n = \hat{\mathbf{w}}_n \mathbf{T}_{[n,n]}^{-1}$ 
end  $n$ .

```

Table 5.1: AGAWE Algorithm.

5.2 WCAWE algorithm

A proposed approach that avoids the unattractive properties of the AWE and the GAWE is the WCAWE [10,11,51]. It introduces correction factors that significantly reduce ill-conditioning in order to obtain a high-order approximation in a numerically stable manner. The WCAWE process, outlined in Table 5.2, also rectifies the problem of not matching moments by the introduction of correction terms in the orthogonalisation process. In doing so, the WCAWE method can remain a moment-matching process while simultaneously producing an orthonormalised basis. As with the alternative GAWE, the WCAWE process constructs the columns of the orthonormal matrix

$$\mathbf{V}_q = [\mathbf{v}_1, \mathbf{v}_2, \dots, \mathbf{v}_q] \quad (5.7)$$

iteratively by using a modified Gram-Schmidt process. This procedure is used to orthogonalise \mathbf{v}_n onto the basis:

$$\tilde{\mathbf{V}}_{q-1} = \{\tilde{\mathbf{v}}_1, \tilde{\mathbf{v}}_2, \dots, \tilde{\mathbf{v}}_{q-1}\} \quad (5.8)$$

(\mathbf{v}_n is explicitly orthogonalised against all the previous vectors $\tilde{\mathbf{v}}_{q-1}$). This is achieved by computing the orthogonal projection of $\tilde{\mathbf{v}}_n$ onto

$$\text{span}\{\mathbf{v}_1, \mathbf{v}_2, \dots, \mathbf{v}_{q-1}\}. \quad (5.9)$$

This projection is subtracted from the original vector and the result is normalised to obtain \mathbf{v}_q . This is by construction, orthogonal to all previously computed vectors $\tilde{\mathbf{v}}_1, \tilde{\mathbf{v}}_2, \dots, \tilde{\mathbf{v}}_{q-1}$ with unit norm. In this way, the orthogonality of the basis vectors is guaranteed and the moment-matching process can be maintained. The resultant vector generated in Table 5.2 is given by:

$$\begin{aligned} \tilde{\mathbf{v}}_1 &= \mathbf{Z}^{-1} \mathbf{b} \\ \tilde{\mathbf{v}}_2 &= \mathbf{Z}^{-1} \left(\mathbf{b}^{[1]} \mathbf{e}_1^T \mathbf{P}_{\mathbf{T}_1} (2, 1) \mathbf{e}_1 - \mathbf{Z}^{[1]} \mathbf{v}_1 \right) \\ \tilde{\mathbf{v}}_3 &= \mathbf{Z}^{-1} \left(\mathbf{b}^{[1]} \mathbf{e}_1^T \mathbf{P}_{\mathbf{T}_1} (3, 1) \mathbf{e}_2 + \mathbf{b}^{[2]} \mathbf{e}_1^T \mathbf{P}_{\mathbf{T}_1} (3, 2) \mathbf{e}_1 - \mathbf{Z}^{[1]} \mathbf{v}_2 - \mathbf{Z}^{[2]} \mathbf{V}_1 \mathbf{P}_{\mathbf{T}_2} (3, 2) \mathbf{e}_1 \right) \\ &\vdots \\ \tilde{\mathbf{v}}_n &= \mathbf{Z}^{-1} \left(\sum_{m=1}^{n-1} \left(\mathbf{b}^{[m]} \mathbf{e}_1^T \mathbf{P}_{\mathbf{T}_1} (n, m) \mathbf{e}_{n-m} \right) - \mathbf{Z}^{[1]} \mathbf{v}_{n-1} \right. \\ &\quad \left. - \sum_{m=2}^{n-1} \mathbf{Z}^{[m]} \mathbf{V}_{n-m} \mathbf{P}_{\mathbf{T}_2} (n, m) \mathbf{e}_{n-m} \right) \end{aligned} \quad (5.10)$$

where \mathbf{e}_r is the vector with all entries equal to zero except the r^{th} entry which is equal to unity. The length of \mathbf{e}_r conforms to the matrix that operates on it. The correction term in Equation 5.10 is given by:

$$\mathbf{P}_{\mathbf{T}_w}(n, m) = \prod_{t=w}^m \mathbf{T}_{[t:n-m+t-1, t:n-m+t-1]}^{-1} \quad (5.11)$$

where

$$\prod_{t=1}^2 \mathbf{T}_t^{-1} = \mathbf{T}_1^{-1} \mathbf{T}_2^{-1} \quad (5.12)$$

and $w = 1$ or 2 .

Definition 5.2.1. Given a $q \times q$ matrix \mathbf{T} and four integers i_1, i_2, j_1 and j_2 such that $1 \leq i_1 \leq i_2 \leq q$ and $1 \leq j_1 \leq j_2 \leq q$, let $\mathbf{T}_{[i_1, j_1]}$ be the entry in \mathbf{T} at the intersection of row i_1 and column j_1 . Furthermore, let $\mathbf{T}_{[i_1:i_2, j_1:j_2]}$ denote the block matrix extracted from \mathbf{T} starting from row i_1 and going through row i_2 from columns j_1 through j_2 .

The $n - m \times n - m$ matrix $\mathbf{P}_{\mathbf{T}_w}(n, m)$ is a composition of many blocks extracted from the matrix \mathbf{T} . The \mathbf{T} matrix is a $q \times q$ upper triangular, nonsingular matrix created by the coefficients of the Gram-Schmidt process. Each column in the \mathbf{T} matrix is the projection of the newly created vector $\tilde{\mathbf{v}}_q$ onto the basis $\mathbf{V}_{q-1} = \{\mathbf{v}_1, \mathbf{v}_2, \dots, \mathbf{v}_{q-1}\}$.

$$\mathbf{T} = \begin{pmatrix} t_{1,1} & t_{1,2} & t_{1,3} & \cdots & t_{1,q} \\ & t_{2,2} & t_{2,3} & \cdots & t_{2,q} \\ & & t_{3,3} & \cdots & t_{3,q} \\ & & & \ddots & \vdots \\ & & & & t_{q,q} \end{pmatrix} = \begin{pmatrix} \|\tilde{\mathbf{v}}_1\|_2 & \mathbf{v}_1^H \tilde{\mathbf{v}}_2 & \mathbf{v}_1^H \tilde{\mathbf{v}}_3 & \cdots & \mathbf{v}_1^H \tilde{\mathbf{v}}_q \\ & \|\tilde{\mathbf{v}}_2\|_2 & \mathbf{v}_2^H \tilde{\mathbf{v}}_3 & \cdots & \mathbf{v}_2^H \tilde{\mathbf{v}}_q \\ & & \|\tilde{\mathbf{v}}_3\|_2 & \cdots & \mathbf{v}_3^H \tilde{\mathbf{v}}_q \\ & & & \ddots & \vdots \\ & & & & \|\tilde{\mathbf{v}}_q\|_2 \end{pmatrix}.$$

As such, \mathbf{T} is a matrix that tracks the mapping from one vector basis to another. It should be noted that if \mathbf{T} is chosen to be the identity matrix, then the WCAWE vectors $\tilde{\mathbf{v}}_q$ from Equation 5.10 reduce to AWE vectors \mathbf{w}_q from Equation 2.16. Indeed, the WCAWE process is actually a generalisation of both the AWE and Arnoldi processes. Central to being able to maintain a moment-matching process, the $\tilde{\mathbf{V}}_q$ and \mathbf{V}_q matrices are related by the \mathbf{T} matrix which is used to orthonormalise $\tilde{\mathbf{V}}_q$, given by:

$$\mathbf{V}_q = \tilde{\mathbf{V}}_q \mathbf{T}^{-1}. \quad (5.13)$$

5.2.1 Summary of terms

- $\mathcal{W}_q = \{\mathbf{w}_1, \mathbf{w}_2, \dots, \mathbf{w}_q\}$ - AWE and GAWE subspace
- $\widehat{\mathcal{W}}_q = \{\widehat{\mathbf{w}}_1, \widehat{\mathbf{w}}_2, \dots, \widehat{\mathbf{w}}_q\}$ - AGAWE subspace
- $\tilde{\mathcal{V}}_q = \{\tilde{\mathbf{v}}_1, \tilde{\mathbf{v}}_2, \dots, \tilde{\mathbf{v}}_q\}$ - WCAWE subspace
- $\overline{\mathbf{W}}_q = [\bar{\mathbf{w}}_1, \bar{\mathbf{w}}_2, \dots, \bar{\mathbf{w}}_q]$ - GAWE orthonormal matrix whose columns define an orthonormal basis $\{\bar{\mathbf{w}}_1, \bar{\mathbf{w}}_2, \dots, \bar{\mathbf{w}}_q\}$
- $\widehat{\overline{\mathbf{W}}}_q = [\widehat{\bar{\mathbf{w}}}_1, \widehat{\bar{\mathbf{w}}}_2, \dots, \widehat{\bar{\mathbf{w}}}_q]$ - AGAWE orthonormal matrix whose columns define an orthonormal basis $\{\widehat{\bar{\mathbf{w}}}_1, \widehat{\bar{\mathbf{w}}}_2, \dots, \widehat{\bar{\mathbf{w}}}_q\}$
- $\mathbf{V}_q = [\mathbf{v}_1, \mathbf{v}_2, \dots, \mathbf{v}_q]$ WCAWE orthonormal matrix whose columns define an orthonormal basis $\{\mathbf{v}_1, \mathbf{v}_2, \dots, \mathbf{v}_q\}$
- $\text{span}(\overline{\mathbf{W}}_q) = \text{span}(\mathbf{W}_q)$
- $\text{span}(\widehat{\overline{\mathbf{W}}}_q) \neq \text{span}(\mathbf{W}_q)$
- $\text{span}(\mathbf{V}_q) = \text{span}(\mathbf{W}_q)$

```

 $\tilde{\mathbf{v}}_1 = \mathbf{Z}^{-1} \mathbf{b}$  (compute first moment);
 $t_{1,1} = \|\tilde{\mathbf{v}}_1\|_2$ 
 $\mathbf{v}_1 = \tilde{\mathbf{v}}_1/t_{1,1}$  (compute first WCAWE vector);
for  $n = 2, \dots, q$ 
     $\tilde{\mathbf{v}}_n = \mathbf{Z}^{-1} \left( \sum_{m=1}^{n-1} (\mathbf{b}^{[m]} \mathbf{e}_1^T \mathbf{P}_{\mathbf{T}_1}(n, m) \mathbf{e}_{n-m}) - \mathbf{Z}^{[1]} \mathbf{v}_{n-1} \right.$ 
     $\left. - \sum_{m=2}^{n-1} \mathbf{Z}^{[m]} \mathbf{v}_{n-m} \mathbf{P}_{\mathbf{T}_2}(n, m) \mathbf{e}_{n-m} \right)$  (compute next corrected vector);
    for  $i = 1, \dots, n-1$ 
         $t_{i,n} = \mathbf{v}_i^H \tilde{\mathbf{v}}_n$  (compute projections of new vector  $\tilde{\mathbf{v}}_n$  onto  $\text{span}\{\mathbf{v}_1, \mathbf{v}_2, \dots, \mathbf{v}_{q-1}\}$ );
         $\tilde{\mathbf{v}}_n = \tilde{\mathbf{v}}_n - t_{i,n} \mathbf{v}_i$  (subtract the projections to make  $\tilde{\mathbf{v}}_n$  orthogonal to the previously
        calculated orthonormal vectors  $\mathbf{v}_i$ );
    end  $i$ 
     $t_{n,n} = \|\tilde{\mathbf{v}}_n\|_2$ 
     $\mathbf{v}_n = \tilde{\mathbf{v}}_n/t_{n,n}$  (make  $\mathbf{v}_n$  a unit vector);
end  $n$ .

```

Table 5.2: Well-Conditioned Asymptotic Waveform Evaluation Algorithm (WCAWE).

5.3 Example showing that the WCAWE algorithm matches moments

As before, the proof that the WCAWE process matches moments is conditional on the requirement of Equation 5.3, which corresponds to:

$$\text{span}(\mathbf{V}_n) = \text{span}(\mathbf{W}_n) \quad \text{for all } 1 \leq n \leq q. \quad (5.14)$$

To start this example, some facts and definitions must be stated.

Definition 5.3.1. Let \mathbf{X} be a $q \times q$ upper triangular matrix whose entries are

$$\mathbf{X}_{[j_1, j_2]} = \begin{cases} \mathbf{e}_1^T \mathbf{P}_{\mathbf{T}_1}(j_2, j_1 - 1) \mathbf{e}_{j_2 - j_1 + 1} & \text{for } 2 \leq j_1 \leq j_2 \leq q \\ 1 & \text{for } j_1 = j_2 = 1 \\ 0 & \text{otherwise.} \end{cases}$$

Remark. The \mathbf{X} matrix is never actually computed, but its definition is necessary to facilitate this proof. $\mathbf{X}_{[q, q]}$ is the product of the diagonal coefficients of the $\mathbf{T}_{[q-1, q-1]}^{-1}$ matrix that implicitly scales the n th AWE vector \mathbf{w}_n to generate the n th vector of the well-conditioned process \mathbf{v}_n that is presented in Equation 5.10

$$\mathbf{X}_{[q, q]} = \mathbf{T}_{[1, 1]}^{-1} \mathbf{T}_{[2, 2]}^{-1} \cdots \mathbf{T}_{[q-1, q-1]}^{-1}. \quad (5.15)$$

The \mathbf{X} matrix ensures that the columns of \mathbf{V}_n are orthogonal and match moments. This will be clearly demonstrated in the proceeding example. \square

Fact 5.3.1. Since \mathbf{T} is nonsingular, $\text{span}(\mathbf{V}_q) = \text{span}(\tilde{\mathbf{V}}_q)$. This follows from Equation 5.13 and the fact that a subspace is closed under multiplication.

The following example will explicitly show that Equation 5.14 is true for $n = 1, 2, 3$. A complete proof for $n = q$ is given in [11, 51]. Let \mathbf{W}_q be as given in Equation 2.16, \mathbf{X} as given in Definition 5.3.1 and $\tilde{\mathbf{V}}_q$ as given in Equation 5.10. Then by showing that

$$\tilde{\mathbf{V}}_q = \mathbf{W}_q \mathbf{X}_{[1:q, 1:q]} \quad (5.16)$$

it follows that

$$\text{span}(\tilde{\mathbf{V}}_q) = \text{span}(\mathbf{W}_q) \quad (5.17)$$

which in conjunction with Fact 5.3.1 proves that

$$\text{span}(\mathbf{V}_q) = \text{span}(\mathbf{W}_q). \quad (5.18)$$

Initially, it is clear that for $q = 1$ that $\tilde{\mathbf{v}}_1 = \mathbf{w}_1 = \mathbf{w}_1 \mathbf{X}_{[1,1]}$. Therefore $\text{span}(\tilde{\mathbf{v}}_1) = \text{span}(\mathbf{w}_1)$ (see Definition A.0.1).

For the case $q = 2$,

$$\begin{aligned}\tilde{\mathbf{v}}_2 &= \mathbf{Z}^{-1} \left(\mathbf{b}^{[1]} \mathbf{e}_1^T \mathbf{P}_{\mathbf{T}_1} (2, 1) \mathbf{e}_1 - \mathbf{Z}^{[1]} \mathbf{v}_1 \right) \\ &= \mathbf{Z}^{-1} \left(\mathbf{b}^{[1]} \mathbf{T}_{[1,1]}^{-1} - \mathbf{Z}^{[1]} \tilde{\mathbf{v}}_1 \mathbf{T}_{[1,1]}^{-1} \right) \\ &= \mathbf{Z}^{-1} \left(\mathbf{b}^{[1]} - \mathbf{Z}^{[1]} \mathbf{w}_1 \right) \mathbf{T}_{[1,1]}^{-1} \quad (5.19)\end{aligned}$$

$$\begin{aligned}&= \mathbf{w}_2 \mathbf{T}_{[1,1]}^{-1} \\ &= \mathbf{w}_2 \mathbf{e}_1^T \mathbf{P}_{\mathbf{T}_1} (2, 1) \mathbf{e}_1 \text{ (see Equation 5.11)} \\ &= \mathbf{w}_2 \mathbf{X}_{[2,2]} \cdot \text{(see Definition 5.3.1)} \quad (5.20)\end{aligned}$$

Therefore, $\tilde{\mathbf{V}}_2 = \mathbf{W}_2 \mathbf{X}_{[1:2,1:2]}$ and $\text{span}(\tilde{\mathbf{V}}_2) = \text{span}(\mathbf{W}_2)$. If Equations 5.5 and 5.19 are compared, it becomes clear how the WCAWE process matches moments. In Equation 5.5, the orthogonalisation matrix $\mathbf{T}_{[1,1]}^{-1}$ fails to scale the generated vector appropriately to ensure that the vector $\hat{\mathbf{w}}_2$ spans the same space as \mathbf{W}_2 . This is rectified in Equation 5.19 where the vector \mathbf{w}_2 is scaled correctly, ensuring that $\tilde{\mathbf{v}}_2$ spans the same space as the columns of \mathbf{W}_2 .

For the case $q = 3$,

$$\begin{aligned}\tilde{\mathbf{v}}_3 &= \mathbf{Z}^{-1} \left(\mathbf{b}^{[1]} \mathbf{e}_1^T \mathbf{P}_{\mathbf{U}_1} (3, 1) \mathbf{e}_2 + \mathbf{b}^{[2]} \mathbf{e}_1^T \mathbf{P}_{\mathbf{U}_1} (3, 2) \mathbf{e}_1 - \mathbf{Z}^{[1]} \mathbf{v}_2 - \mathbf{Z}^{[2]} \mathbf{V}_1 \mathbf{P}_{\mathbf{U}_2} (3, 2) \mathbf{e}_1 \right) \\ &\quad \text{Note: } (\mathbf{e}_1^T \mathbf{P}_{\mathbf{U}_1} (3, 1) \mathbf{e}_2 = 0) \text{ since } j_1 = 0 \text{ (see Definition 5.3.1)} \\ &= \mathbf{Z}^{-1} \left(\mathbf{b}^{[2]} \mathbf{T}_{[1,1]}^{-1} \mathbf{T}_{[2,2]}^{-1} - \mathbf{Z}^{[1]} \mathbf{v}_2 - \mathbf{Z}^{[2]} \mathbf{v}_1 \mathbf{T}_{[2,2]}^{-1} \right) \\ &= \mathbf{Z}^{-1} \left(\mathbf{b}^{[2]} \mathbf{T}_{[1,1]}^{-1} \mathbf{T}_{[2,2]}^{-1} - \mathbf{Z}^{[1]} \tilde{\mathbf{v}}_2 \mathbf{T}_{[2,2]}^{-1} - \mathbf{Z}^{[2]} \tilde{\mathbf{v}}_1 \mathbf{T}_{[1,1]}^{-1} \mathbf{T}_{[2,2]}^{-1} \right) \\ &\quad \text{since } \mathbf{V}_q = \tilde{\mathbf{V}}_q \mathbf{T}_{[1:q,1:q]}^{-1} \text{ (see Equation 5.13)} \\ &= \mathbf{Z}^{-1} \left(\mathbf{b}^{[2]} \mathbf{T}_{[1,1]}^{-1} \mathbf{T}_{[2,2]}^{-1} - \mathbf{Z}^{[1]} \mathbf{w}_2 \mathbf{T}_{[1,1]}^{-1} \mathbf{T}_{[2,2]}^{-1} - \mathbf{Z}^{[2]} \mathbf{w}_1 \mathbf{T}_{[1,1]}^{-1} \mathbf{T}_{[2,2]}^{-1} \right) \\ &= \mathbf{Z}^{-1} \left(\mathbf{b}^{[2]} - \mathbf{Z}^{[1]} \mathbf{w}_2 - \mathbf{Z}^{[2]} \mathbf{w}_1 \right) \mathbf{T}_{[1,1]}^{-1} \mathbf{T}_{[2,2]}^{-1} \\ &= \mathbf{w}_3 \mathbf{T}_{[1,1]}^{-1} \mathbf{T}_{[2,2]}^{-1} \\ &= \mathbf{w}_3 \mathbf{e}_1^T \mathbf{P}_{\mathbf{U}_1} (3, 2) \mathbf{e}_1 \\ &= \mathbf{w}_3 \mathbf{X}_{[3,3]} \quad (5.21)\end{aligned}$$

Therefore, $\tilde{\mathbf{V}}_3 = \mathbf{W}_3 \mathbf{X}_{[1:3,1:3]}$ and $\text{span}(\tilde{\mathbf{V}}_3) = \text{span}(\mathbf{W}_3)$. The proof that $\tilde{\mathbf{V}}_q = \mathbf{W}_q \mathbf{X}_{[1:q,1:q]}$ is given in [11, 51]. Since the $\text{span}(\mathbf{V}_q) = \text{span}(\tilde{\mathbf{V}}_q)$, then it is the case that $\text{span}(\mathbf{V}_q) = \text{span}(\mathbf{W}_q)$. This proves that the space \mathbf{V}_q matches mo-

ments and consequently, that the WCAWE technique can maintain a moment-matching process while simultaneously generating an orthonormal space. By imposing this orthogonality relation amongst the generated vectors, linear independence can be maintained and so high-order approximations can be constructed. Thus, the WCAWE process does not suffer from the numerical difficulties associated with the explicit moment computation methods as discussed in Section 2.4.1. However, due to finite precision computation, loss of orthogonality between the computed vectors can occur.

Ultimately, this process results in the approximation to the solution vector \mathbf{x}_q for any frequency f in the range $f_{min} \leq f \leq f_{max}$ given by Equation 2.27 defined in Section 2.5, which corresponds to:

$$\mathbf{x}_q = \mathbf{V}_q \mathbf{a}_q \quad (5.22)$$

with

$$\mathbf{a}_q = \left(\sum_{n=0}^q \mathbf{V}_{q \times m}^H \mathbf{Z}_{m \times m}^{[n]} \mathbf{V}_{m \times q} \beta^n \right)^{-1} \left(\sum_{n=0}^q \mathbf{V}_{q \times m}^H \mathbf{b}_{m \times 1}^{[n]} \beta^n \right) \quad (5.23)$$

Clearly Equation 5.22 can be used to solve efficiently over a wide range of frequencies as it requires the inversion of a matrix of order $q \ll m$ for each frequency value.

5.4 Recursive formulation of the matrix derivatives

In this section, the q^{th} order recursive equation for the differentiation of the volume EFIE formulation of a two-dimensional inhomogeneous lossy dielectric object with real permittivity is reviewed. In order to model the frequency-dependent variations evident in Equations 3.82 and 3.83, obtained using the circular-cell approximation as outlined in Section 3.6.1, care needs to be taken.

The following identities give the q^{th} order recursive form of the derivatives of a function $a(k_b)$ expanded as a product [71]

$$\text{if } a(k_b) = b(k_b) c(k_b), \text{ then} \quad a^{[q]}(k_b) = \sum_{p=0}^q \binom{q}{p} b^{[q-p]}(k_b) c^{[p]}(k_b) \quad (5.24)$$

or a quotient [71]

$$\text{if } a(k_b) = \frac{b(k_b)}{c(k_b)}, \text{ then} \quad a^{[q]}(k_b) = \frac{1}{c(k_b)} \left[b^{[q]}(k_b) - \sum_{p=1}^q c^{[p]}(k_b) a^{[q-p]}(k_b) \right] \quad (5.25)$$

where

$$\binom{q}{p} = \frac{q!}{p!(q-p)!} \quad (5.26)$$

is the binomial coefficient. Using the above identities, the q^{th} derivative with respect to k of the matrix entry $\mathbf{Z}_{i,j}(k)$, evaluated at k_b , is given by

$$Z_{i,j}^{[q]} = \frac{\eta\pi a_i}{2} \sum_{p=0}^q \binom{q}{p} J_1(k_{b0} a_i)^{[p]} H_0^{(2)}(k_{b0} |\mathbf{r}_i - \mathbf{r}_j|)^{[q-p]} \quad i \neq j \quad (5.27)$$

and

$$Z_{i,j}^{[q]} = \frac{\eta\pi a_i}{2} H_1^{(2)}(k_{b0} a_i)^{[q]} - \frac{(-1)^{[q]} j \eta \epsilon_{ri} q!}{(k_{b0})^{[q+1]} (\epsilon_{ri} - 1)} \quad i = j. \quad (5.28)$$

Careful consideration needs to be taken when differentiating the Bessel and Hankel functions by using the following recursive relation [72]:

$$\Psi_v^{[q]} = \frac{1}{2^q} \sum_{p=0}^q (-1)^{(p+2)} \binom{q}{p} \Psi_{v-q+2p} \quad (5.29)$$

where $\Psi_v^{[q]}$ denotes the q^{th} derivative of $J, Y, H^{(1)}, H^{(2)}$ of order v .

5.5 Numerical results and validations

In this section, the radar cross-section (RCS) is calculated for profiles of varying geometry, size and contrast with the objective of validating the WCAWE Algorithm by comparison with the MoM using a two-dimensional volume EFIE formulation.

5.5.1 Case Study 1: Homogeneous cylinder - Medium 1

We initially consider a homogeneous cylinder of radius $r = \lambda_0/2 = 0.08m$, $\epsilon_r = 2$, centred at the origin and assumed to be embedded in free space. The structure is illuminated by a TM^z wave emanating from a plane wave source. The cylinder was discretised using $m = 170$ cells and the RCS was computed over a band of frequencies $f = 0.5 : 2.5$ GHz with 0.014 GHz increments for a monostatic setup $\phi = 0$.

The Mie series, as described in Section 3.7, is used to validate independently the accuracy of the MoM solution. This is illustrated in Figure 5.1(a), where the Euclidean norm of the current density is plotted comparing the MoM solution to the Mie series. The RCS and associated percentage relative error are shown in Figures 5.1(b) and 5.2(a), respectively. The MoM is the true value and is compared against the Padé via AWE with adaptive zeta and the WCAWE for $q = 15$. Although scaling reduces the ill-conditioning of the Padé coefficient matrix as discussed in Section 2.4.1, these strategies still result in significant round-off error for relatively small values of q . This is confirmed in Table 2.1 where the condition number for the Padé via AWE with and without the scaling factor Zeta is listed. Indeed, for values of $q > 10$, the condition number greatly increases and the AWE results start to deteriorate.

From Figures 5.1(b) and 5.2(a), it is clear the WCAWE out-performs the Padé via AWE with adaptive Zeta, duplicating the MoM solution over the entire band of frequencies to within a 1% relative error. The Padé via AWE with adaptive zeta achieves the same accuracy over a much smaller range of $f = 0.66 : 2.3$ GHz. As an additional means to measure the accuracy of the approximation solution \mathbf{x}_q at each frequency sample, the relative residual [11, 49, 73] is generated. After the approximate solution \mathbf{x}_q has been generated the relative residual

$$\mathbf{r}_q = \frac{\|\mathbf{a}_q\|_2}{\left\| \sum_{n=0}^q \mathbf{b}^{[n]} \beta^n \right\|_2} \quad (5.30)$$

is generated for all frequencies f_j in the range $f_{min} \leq f_j \leq f_{max}$ where

$$\mathbf{a}_q = \sum_{n=0}^q \left(\mathbf{z}^{[n]} \beta^n \right) \mathbf{x}_q - \sum_{n=0}^q \mathbf{b}^{[n]} \beta^n. \quad (5.31)$$

If $r_q < \text{tol}_{r_q}$ for some pre-specified tolerance value tol_{r_q} , the solution is considered to have converged at frequency f_j . Figure 5.2(b) depicts the relative residual r_q calculated over the entire band of frequencies. It indicates that the range of frequencies $f = 0.5 : 2.5$ GHz has converged to within $\text{tol}_{r_q} = 10^{-2}$ of the MoM solution for the WCAWE, confirming Figure 5.2(a). Additionally Table 5.3 illustrates the decline in accuracy of the Padé via AWE with adaptive Zeta as the moment order increases as compared to the WCAWE (Line 6 - n_m).

As an indicator of the rate of convergence of the frequency points to the $\text{tol}_{r_q} = 10^{-2}$ over the iteration process, Figure 5.3(a) depicts the number of converged frequency points that has been achieved in total at each iteration. From this figure, we note the WCAWE process results in a regular addition of converged frequency points at each iteration.

Figure 5.3(b) illustrates the loss of orthogonality of a computed set of moments \mathbf{m}_n at each iteration step

$$\|\mathbf{I}_{n \times n} - \mathbf{M}_{n \times m}^H \mathbf{M}_{m \times n}\|_2 \quad \text{for all } 1 \leq n \leq q \quad (5.32)$$

where

$$\mathbf{M} = [\mathbf{m}_1, \mathbf{m}_2, \dots, \mathbf{m}_n] \quad (5.33)$$

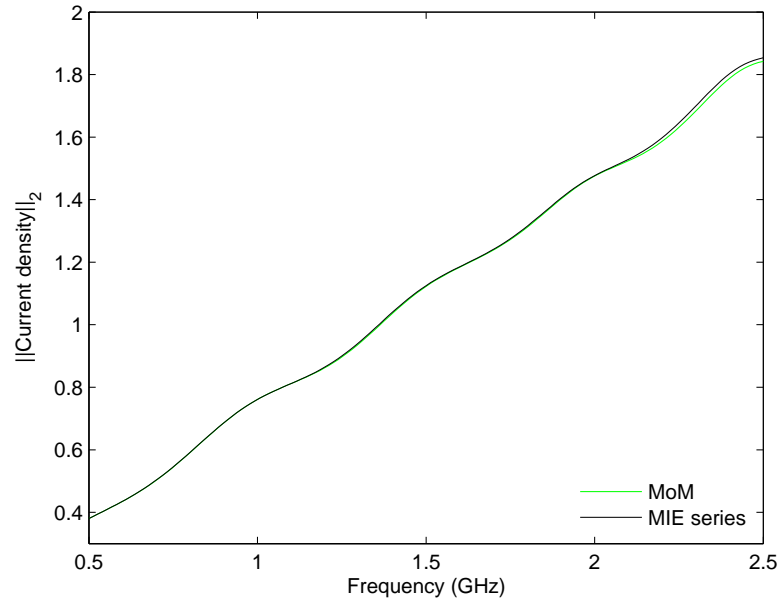
and \mathbf{I}_n is an $n \times n$ identity matrix. It should be noted that if the moments are exactly orthogonal, Equation 5.32 will equate to zero. However, due to finite precision this eventuality will not occur. From this figure, it is clear that the computed moments remain close to machine precision, ensuring that each new moment contains additional new useful information. The total scattered field E_z^s , at an observation radius of $1m$ and angles $\theta = 0 : 2\pi$, for a converged approximation frequency $f = 0.5$ GHz is illustrated in Figure 5.4(a).

The CPU time associated with the solution of the RCS for the MoM, Padé via AWE with adaptive Zeta and WCAWE is given in Table 5.3. It is evident from this table that the WCAWE significantly decreases the computational expense associated with the direct solution of each frequency sample in a sweep analysis. Additionally, it is clear from this table that as the number of moments increase, the WCAWE technique significantly outperforms the AWE in the number of frequency points that have converged to tol_{r_q} . The Padé via AWE with adaptive Zeta and WCAWE CPU times are similar due to the additional times

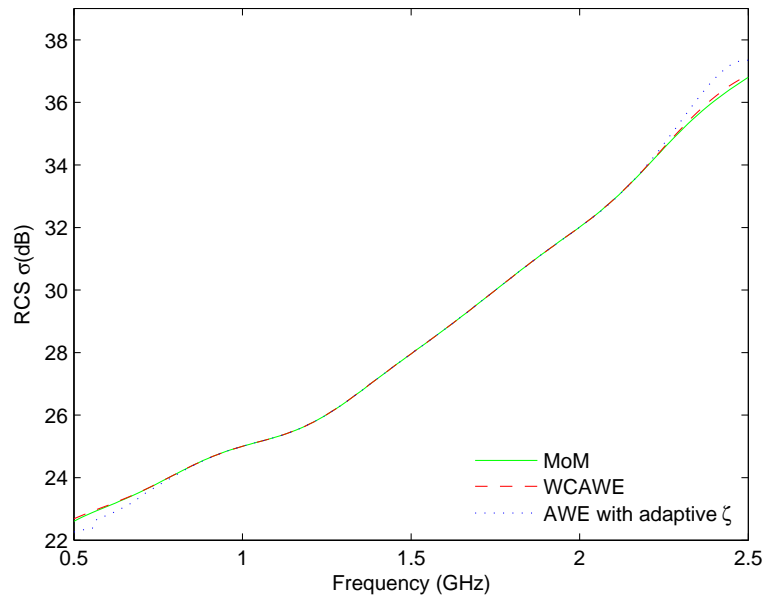
required to scale the Padé via AWE with adaptive Zeta moments. The main computational overhead is due to the generation of the derivatives and this is clearly illustrated in Figure 5.4(b). However, as the derivatives need only be calculated once, minimal computational expense is required for all subsequent solutions. Additionally, this figure indicates the number of frequency samples required to achieve a computational saving when compared against generating the MoM solution at each frequency point. For example, for $q = 10$ moments in order for the WCAWE to break even computationally with the MoM solution, 35 frequency samples would be required, taking 9.8 seconds to generate and solve. This figure demonstrates that as the order of the moments increases, the number of samples required to break even rapidly increases. Consequently careful consideration is required when choosing the order of the WCAWE technique.

Legend	Technique						
	MoM	Padé via AWE with adaptive ζ			WCAWE		
Order	$m = 170$	$q = 15$	$q = 10$	$q = 5$	$q = 15$	$q = 10$	$q = 5$
$t_m(s)$	172.9	-	-	-	-	-	-
n_s	145	145	145	145	145	145	145
$t_g(s)$	-	120.8	37.7	6.35	120.98	38.03	6.73
n_m	-	92	62	25	134	94	25
$t_s(s)$	0.019	0.012	0.012	0.012	0.015	0.015	0.015
$t_t(s)$	175.6	122.54	39.4	8.09	121.42	38.46	7.16
Speed-up	-	1.43	4.45	21.7	1.43	4.37	19.72

Table 5.3: CPU time analysis (Case study 1 - $f = 0.5 : 2.5$ GHz, $\lambda_0 = 0.2m$, $r = 0.08m$, $m =$ size of MoM matrix, $q =$ number of moments, $t_m =$ CPU time in seconds to generate MoM matrices for all samples, $n_s =$ number of frequency samples, $t_g =$ CPU time in seconds to generate moments, $n_m =$ number of frequency samples converged to predefined tolerance $tol_{r_q} = 10^{-2}$ of the MoM solution, $t_s =$ average CPU time in seconds to solve for RCS at each frequency, $t_t =$ total CPU time in seconds to generate and solve case study problem).

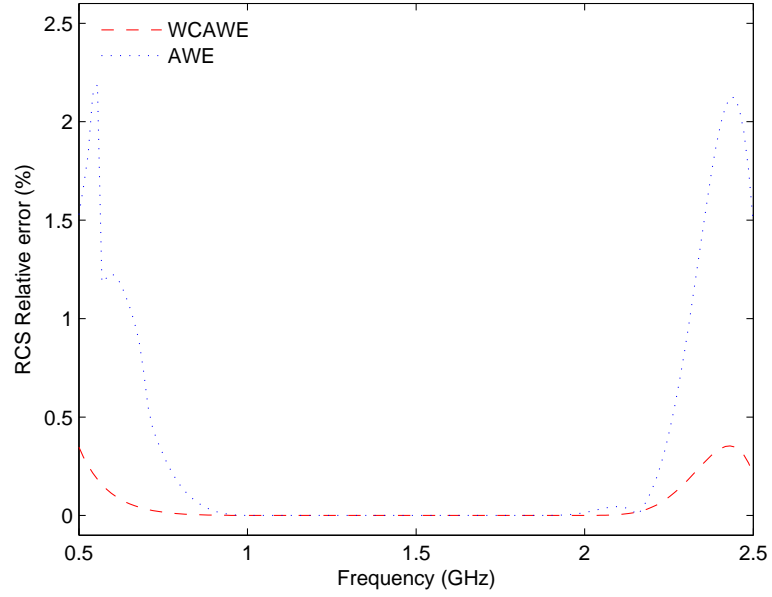


(a) $\|J_z\|_2$ Current density frequency sweep comparing the analytical solution (MIE series) against the MoM.

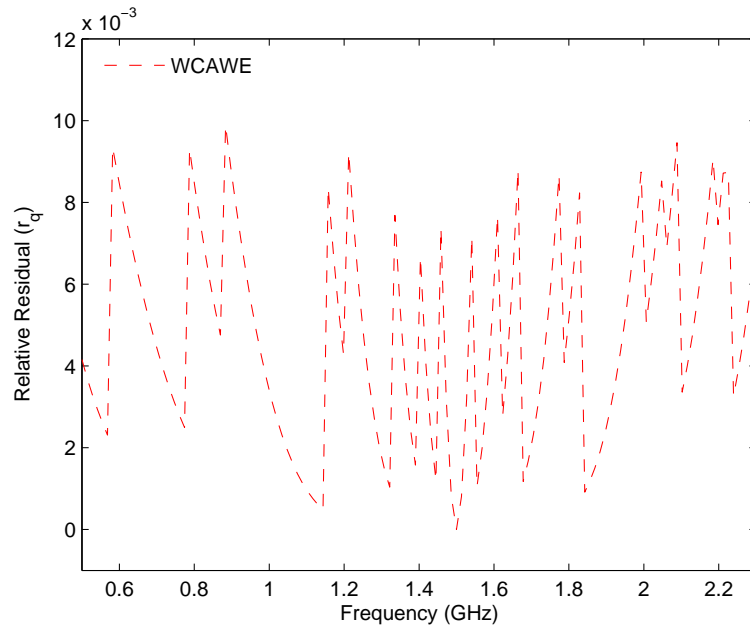


(b) $\sigma_{TM}(\Phi)$ RCS frequency sweep comparing MoM, Padé via AWE with adaptive zeta and WCAWE).

Figure 5.1: Case study 1 Part A: Single point expansion - Homogeneous cylinder.

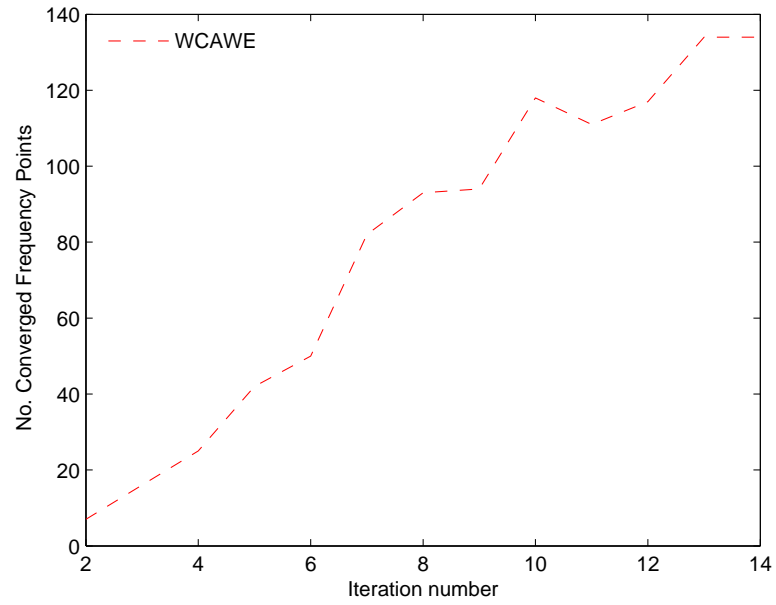


(a) Percentage relative error for Figure 5.1(b) comparing the AWE and WCAWE to the MoM solution.

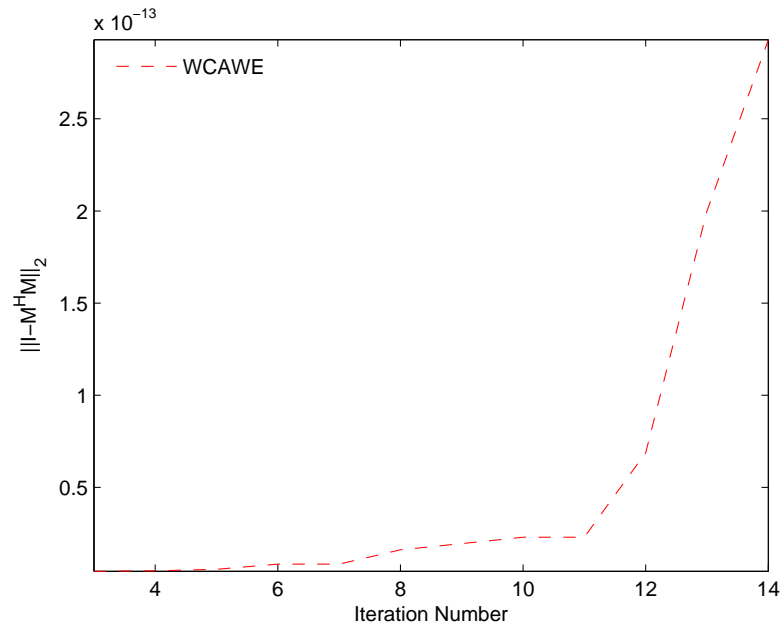


(b) Relative residual r_q for WCAWE.

Figure 5.2: Case study 1 Part B: Single point expansion - Homogeneous cylinder.

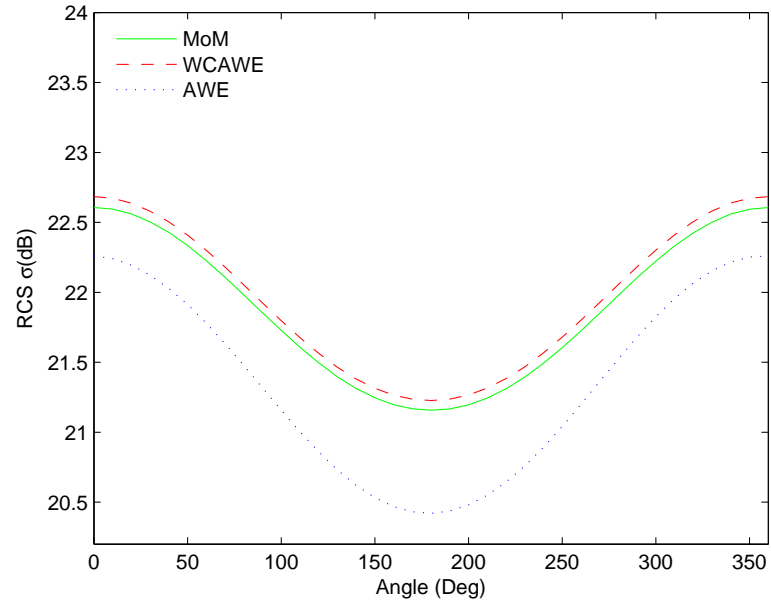


(a) Number of converged frequency points at each moment for WCAWE.

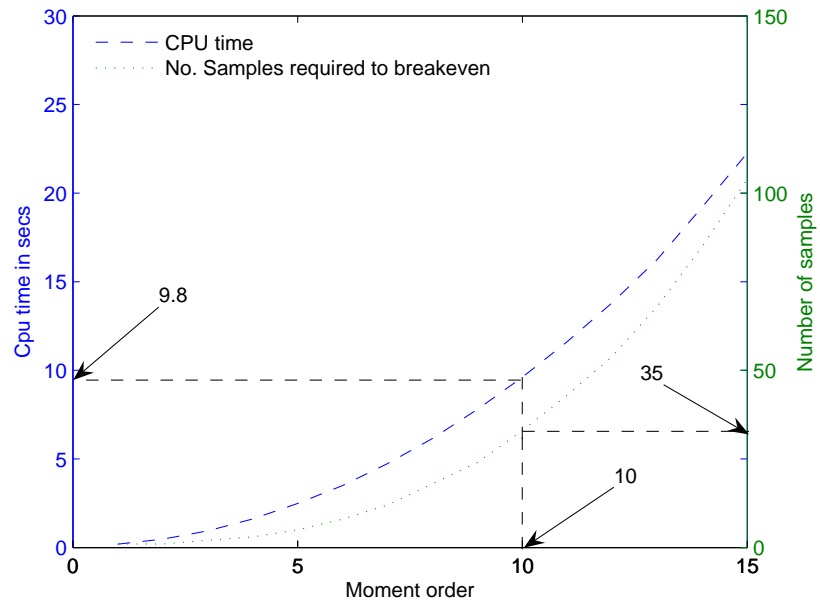


(b) Loss of orthogonality of the WCAWE moments over iteration process - $\|I - M^H M\|_2$.

Figure 5.3: Case study 1 Part C: Single point expansion - Homogeneous cylinder.



(a) $\sigma_{TM}(\Phi)$ RCS for a converged frequency $f = 0.5$ GHz.



(b) WCAWE CPU break-even analysis.

Figure 5.4: Case study 1 Part D: Single point expansion - Homogeneous cylinder.

5.6 Multipoint Well-Conditioned Asymptotic Waveform Evaluation (MWCAWE)

In order to extend the bandwidth in a frequency sweep, a multipoint approach should be implemented. Several practical implementation issues must therefore be addressed. These include:

- how many expansion points to use
- where to place them
- the approximation order at each expansion point

Determining the optimum size of the approximation order q at each expansion point will result in a more efficient approximation. As evident in Table 5.3 (line 6 - t_g), most of the computational cost of generating the approximation is due to the calculation of the derivatives. Figure 5.4(b) illustrates the CPU break-even analysis comparing the cost of generating the derivatives to the number of frequency samples required. As the number of moments increase there is a rapid increase in the number of samples required to achieve a CPU saving using the WCAWE over the MoM. These data can be used as a guide to determine the maximum number of moments that should be matched at each expansion point.

After determining the maximum value for q at the central expansion point β_0 , one must consider if further expansion points are required and where they must be located, such that the approximate solution can converge to a pre-specified tolerance. After β_0 has been chosen, the approximate solution \mathbf{x}_q and the relative residual r_q should be generated for all frequencies f_j in the range $f_{min} \leq f_j \leq f_{max}$. If $r_q < \text{tol}_{r_q}$ for some pre-specified tolerance value tol_{r_q} , the solution is considered to have converged at frequency f_j . If either f_{min} or f_{max} is not converged, another expansion point is selected at the centre of the region in which convergence did not take place and r_q generated. The unconverged region is continually divided and tested until all values of f_j are marked as converged. Figure 5.5 clearly illustrates this strategy.

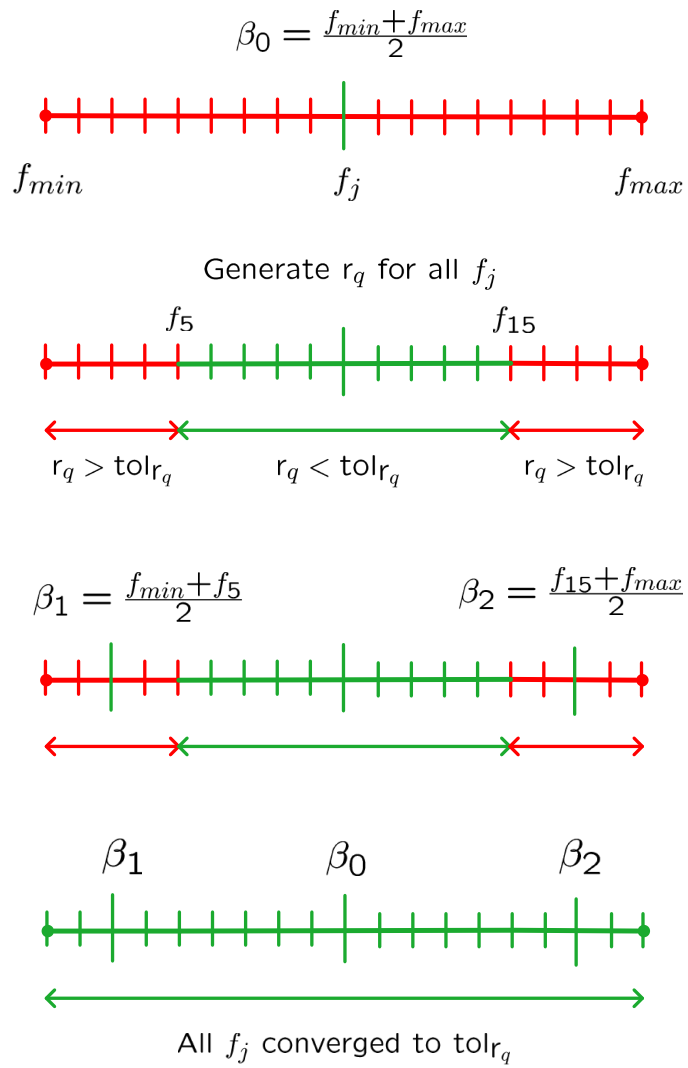


Figure 5.5: Multipoint WCAWE procedure.

5.6.1 Case Study 2: Inhomogeneous square - Medium 1,2

In the second example, a similar numerical experiment is conducted for an inhomogeneous square of length $l = \lambda_0 = 0.36m$, centred at the origin, with broadside incidence. The square is composed of two equally sized regions, with $(x < 0, \epsilon_r = 2, \text{medium 1})$ and $(x \geq 0, \epsilon_r = 3, \text{medium 2})$. The square was discretised using $m = 990$ cells and the RCS was computed over a band of frequencies $f = 0.5 : 1.2$ GHz with 5 MHz increments for a monostatic setup $\phi = 0$.

Figures 5.6(a) and 5.6(b) show the RCS results obtained which compare the MoM results against the WCAWE for $q = 12$. Figure 5.6(a) shows the RCS versus frequency with one expansion point at $\beta_0 = 850$ MHz. The WCAWE algorithm duplicates the reference solution over the band of frequencies $f = 0.66 : 1.06$ GHz. This is confirmed in Figure 5.6(b), which shows that the relative residual $r_q < 10^{-2}$ (1% relative error) over the range of frequencies $f = 0.66 : 1.06$ GHz. In order to achieve additional bandwidth, a multipoint WCAWE (MWCAWE) approach must be implemented. From Figure 5.6(a), it is clear that for such an approach, we need to place two additional expansion points. These are automatically positioned at the centre of the two unconverged bands of frequency ($\beta_1, \beta_2 = 580, 1130$ MHz respectively) for ($q_1 = 7, q_2 = 8$).

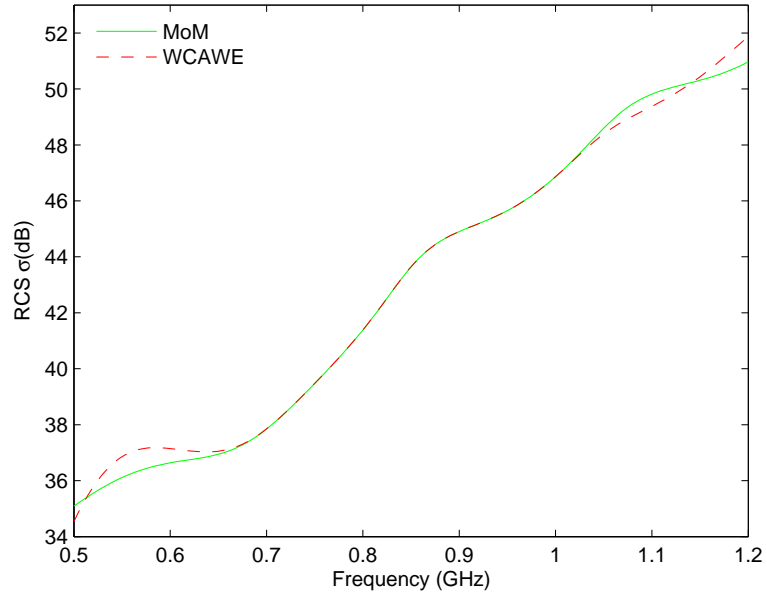
Figures 5.7(a) and 5.7(b) indicate that the Multipoint WCAWE can provide accurate and robust fast frequency sweeps in broadband applications. The CPU results using the WCAWE and MWCAWE are compared with the MoM direct calculation to demonstrate the efficiencies of these approaches, as shown in Table 5.4. From these results, the computational saving associated with the multipoint approach is clearly evident with the MWCAWE approximately achieving a speed-up of 1.57, while achieving $< 1\%$ relative error over the entire frequency range. Achieving the same level of accuracy using a single point expansion would incur significantly more computational cost. This is due to the computational cost required to generate the high-order moments, which take significantly more computational time to compute, as compared to low order moments. However, it should be noted that although multiple expansion points with low-order moments can significantly reduce the CPU times, this approach can become computationally expensive for large-scale simulations. This is due to the need to make and invert a \mathbf{Z} matrix at the expansion frequency for each new expansion point.

The rate of convergence of the frequency points to the $\text{tol}_{r_q} = 10^{-2}$ over the iteration process is depicted in Figure 5.8(a) for each expansion point. From this figure, we note that the WCAWE process results in a regular addition of converged frequency points at each iteration. Finally Figure 5.8(b) illustrates the

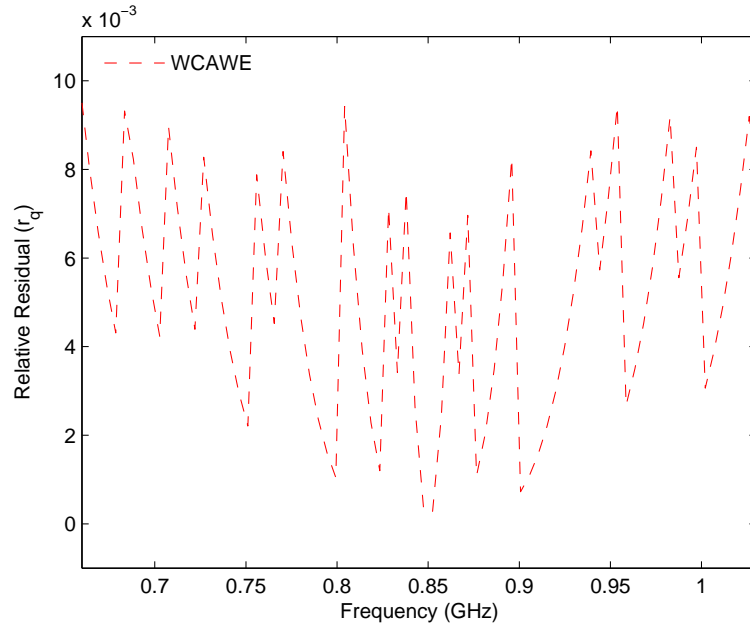
loss of orthogonality of a computed set of moments \mathbf{m}_n at each iteration step for each expansion point (see Equation 6.13). It is clear from this figure that the computed moments remain close to machine precision, ensuring that each new moment contains additional new useful information.

Legend	Technique		
	MoM	WCAWE	MWCAWE
Order	$m = 990$	$q = 12$	$q = 12 + 7 + 8 = 27$
$t_m(s)$	4886.2	-	-
n_s	145	145	145
$t_g(s)$	-	2132.8	3324.3
n_m	-	79	145
$t_s(s)$	2.4	0.09	0.09
$t_t(s)$	5234.2	2145.85	3337.35
Speed-up	-	2.44	1.57

Table 5.4: CPU time analysis (Case study 2 - $f = 0.5 : 1.2$ GHz, $m =$ size of MoM matrix, $q =$ number of moments, $t_m =$ CPU time in seconds to generate MoM matrices for all samples, $n_s =$ number of frequency samples, $t_g =$ CPU time in seconds to generate moments, $n_m =$ number of frequency samples converged to predefined tolerance $\text{tol}_{r_q} = 10^{-2}$, $t_s =$ average CPU time in seconds to solve for RCS at each frequency, $t_t =$ total CPU time in seconds to generate and solve case study problem).

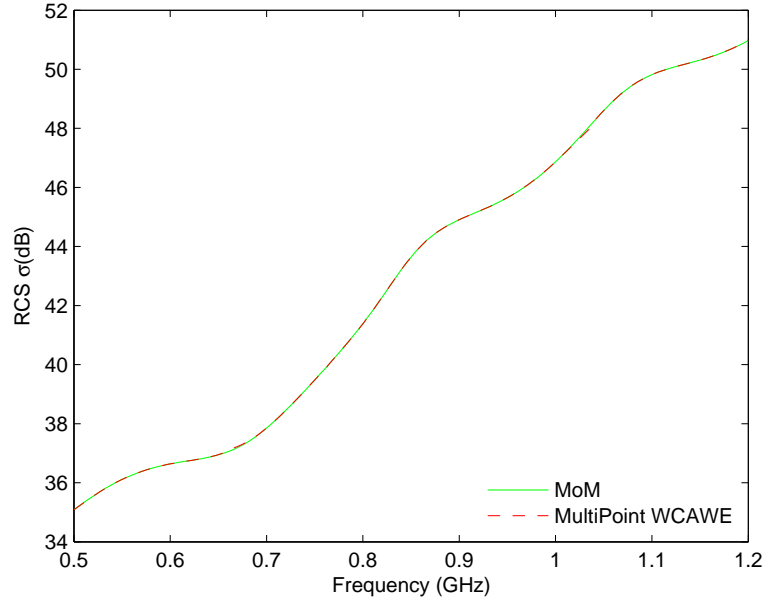


(a) $\sigma_{TM}(\Phi)$ RCS frequency sweep comparing MoM and WCAWE - Medium 1, $\epsilon_r = 2$ Medium 2, $\epsilon_r = 3$.

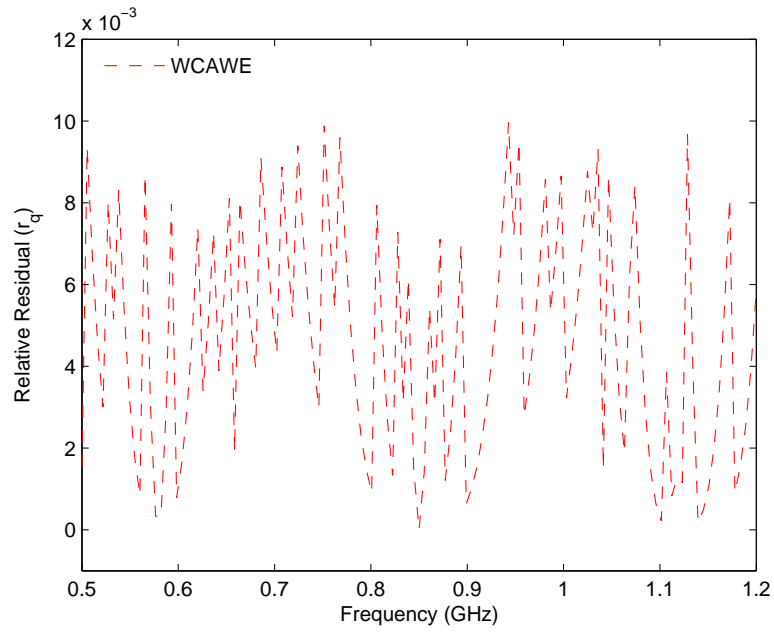


(b) Relative residual r_q for WCAWE.

Figure 5.6: Case study 2 Part A: Single point expansion - Inhomogeneous square.

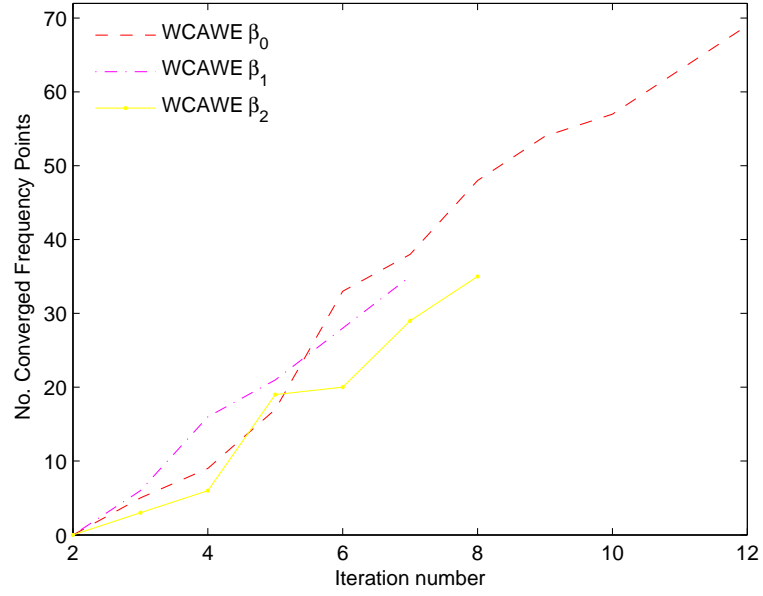


(a) Multipoint $\sigma_{TM}(\Phi)$ RCS frequency sweep using MoM and WCAWE ($\sigma_1 = 850$ MHz $n_1 = 12$, $\sigma_2 = 580$ MHz $n_2 = 7$, $\sigma_3 = 1.13$ GHz $n_3 = 8$).

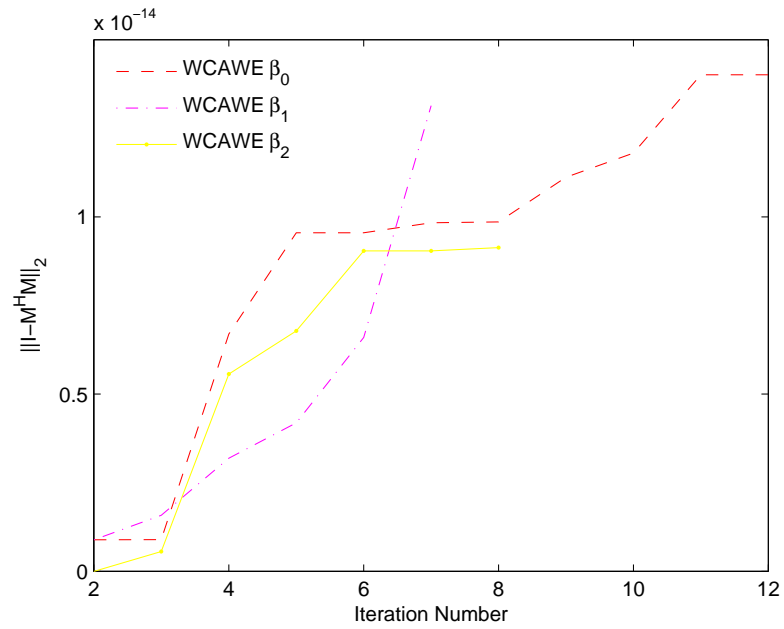


(b) Relative residual r_q for WCAWE.

Figure 5.7: Case study 2 Part A: Multipoint expansion - Inhomogeneous square.



(a) Number of converged frequency points at each moment for WCAWE.



(b) Loss of orthogonality of the WCAWE moments over iteration process - $\|I - M^H M\|_2$.

Figure 5.8: Case study 2 Part B: Multipoint expansion - Inhomogeneous square.

5.7 Three-dimensional surface EFIE for a perfectly conducting object

In this section, the results for the three-dimensional surface integral formulation for a perfect electrically conducting (PEC) square are introduced. For a PEC, the total tangential electric field is zero at the surface. The governing equations and q^{th} derivative are given by [2].

5.8 Numerical results and validations

The RCS is calculated for a three-dimensional PEC square with the objective of validating the WCAWE Algorithm by comparison with the method of moments using a 3-dimensional surface EFIE formulation.

5.8.1 Case Study 1: Perfect electrically conducting square

We consider a homogeneous square plate of side length $l = \lambda_0 = 0.02m$, $\epsilon_r = 2$, centred at the origin. The plate is illuminated by a plane wave with broad-side incidence $\theta_{inc} = \pi/2$, $\phi_{inc} = 0$ and polarisation $\alpha_{inc} = \pi/2$. The plate was discretised using $m = 930$ cells and the RCS was computed over a band of frequencies $f = 0.5 : 35.0$ GHz with 0.25 GHz increments for a monostatic setup $\phi_{sca} = 0$. Figure 5.9(a) compares the RCS MoM results against the Padé via AWE with adaptive zeta and WCAWE for $q = 24$ with one expansion point at $\beta_0 = 17.75$ GHz. The increased accuracy of the WCAWE algorithm over the AWE is clearly evident as it duplicates the reference solution over the band of frequencies $f = 5.25 : 34.5$ GHz with a 1% relative error, while the Padé is limited to a similar error over the band $f = 10.75 : 27.5$ GHz. This is confirmed in Figures 5.9(b) and 5.10(a), which illustrate the percentage relative error and the relative residual r_q (see Equation 5.30), respectively. They demonstrate that the range of frequencies $f = 5.25 : 34.5$ GHz has converged to the pre-specified $\text{tol}_{r_q} = 10^{-2}$ (1% relative error). It should be noted that the spike in error associated with the AWE in Figure 5.9(b) at approximately 10 and 30 GHz can not be accounted for.

Figure 5.10(b) illustrates the loss of orthogonality of a computed set of moments \mathbf{m}_n at each iteration step (Equation 6.13). From this figure, it is clear that the computed moments remain close to machine precision, ensuring that each new moment contains additional new useful information. The total scattered field E_z^s , at an observation radius of $1m$ and angles $\theta = 0 : 2\pi$, for a converged approximation frequency $f = 0.5$ GHz is illustrated in Figure 5.11(a).

The CPU time associated with the solution of the RCS for the MoM, Padé via AWE with adaptive Zeta and WCAWE is given in Table 5.5. It is evident from

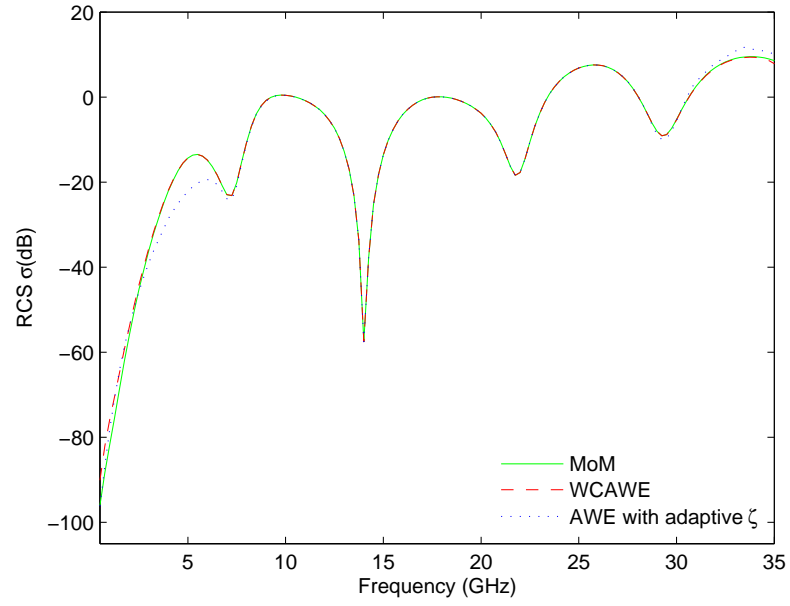
this table that the WCAWE significantly decreases the computational expense associated with the direct solution of each frequency sample in a sweep analysis. Significantly, a CPU speed-up of 1.32 is achieved using the WCAWE technique over the MoM using $q = 24$ moments while duplicating the reference solution over the entire bandwidth to within a 10% relative error.

Additionally, it is clear from this table that as the number of moments increases the WCAWE technique significantly outperforms the AWE in the number of frequency points that have converged to tol_{r_q} . The Padé via AWE with adaptive Zeta and WCAWE CPU times are similar due to the additional times required to scale the Padé via AWE with adaptive Zeta moments.

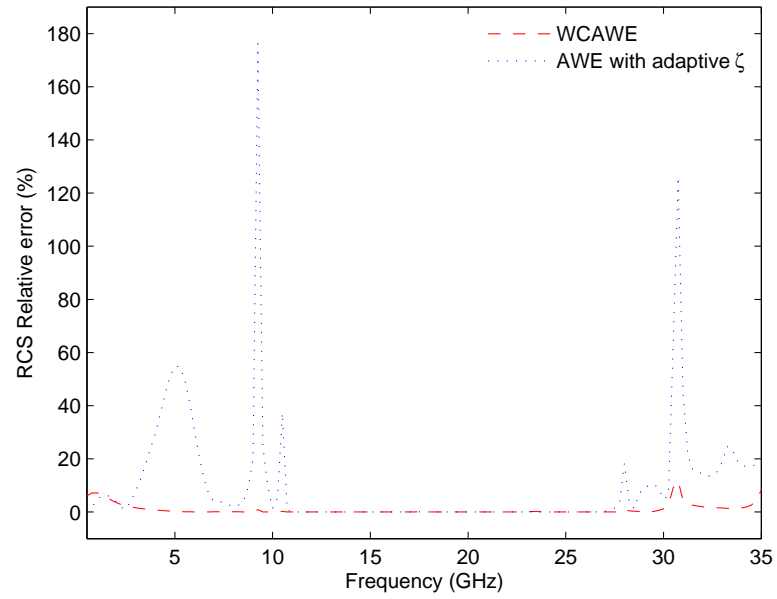
The main computational overhead is due to the generation of the derivatives, and this is clearly illustrated in Figure 5.11(b). However, as the derivatives need only be calculated once, minimal computational expense is required for all subsequent solutions. Additionally, this figure indicates the number of frequency samples required to achieve a computational saving when compared against generating the MoM solution at each frequency point. It should be noted that there is a much slower increase in the computational expense for generating higher order moments than that of the equivalent order volume EFIE illustrated in Figure 5.4(b). Consequently, the surface EFIE can utilise higher order moments while still producing significant computational time savings.

Legend	Technique						
	MoM	Padé via AWE with adaptive ζ			WCAWE		
		$q = 24$	$q = 16$	$q = 6$	$q = 24$	$q = 16$	$q = 6$
Order	$m = 930$						
$t_m(s)$	45354	-	-	-	-	-	-
n_s	145	145	145	145	145	145	145
$t_g(s)$	-	34542	18759	4811.3	34559	18764	4824.6
n_m	-	69	44	23	120	68	31
$t_s(s)$	1.99	0.046	0.046	0.046	0.09	0.09	0.09
$t_t(s)$	45642.5	34656.69	18765.67	4817.97	34574.8	18777.05	4837.65
Speed-up	-	1.32	2.43	9.47	1.32	2.43	9.43

Table 5.5: CPU time analysis (Case study 1 - $f = 0.5 : 35.0$ GHz, $\lambda_0 = 0.2m$, $m =$ size of MoM matrix, $q =$ number of moments, $t_m =$ CPU time in seconds to generate MoM matrices for all samples, $n_s =$ number of frequency samples, $t_g =$ CPU time in seconds to generate moments, $n_m =$ number of frequency samples converged to predefined tolerance $\text{tol}_q = 10^{-2}$, $t_s =$ average CPU time in seconds to solve for RCS at each frequency, $t_t =$ total CPU time in seconds to generate and solve case study problem).

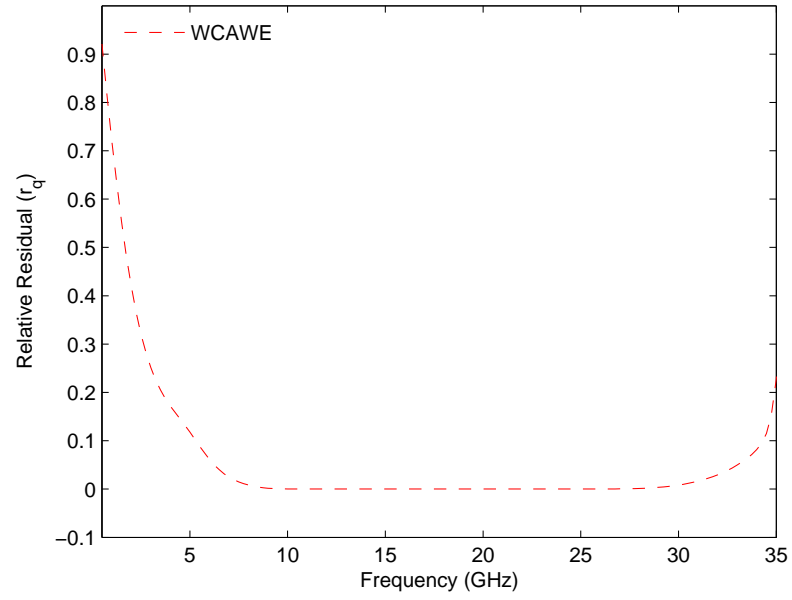


(a) $\sigma_{TM}(\Phi)$ RCS frequency sweep comparing MoM, Padé via AWE with adaptive zeta and WCAWE).

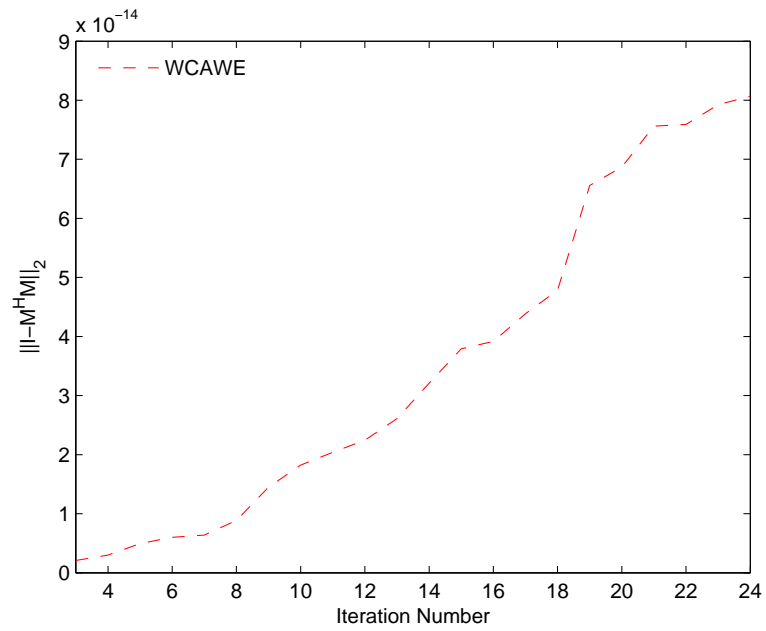


(b) Percentage relative error for Figure 5.9(a) comparing the Padé via AWE with adaptive zeta and WCAWE to the MoM solution.

Figure 5.9: Case study 1 Part A: Single point expansion - Homogeneous square.

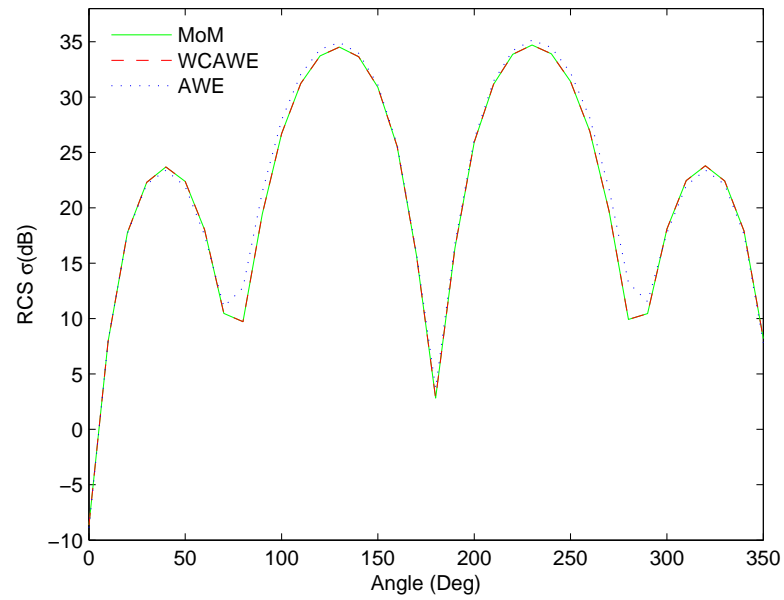


(a) Relative residual r_q for WCAWE.

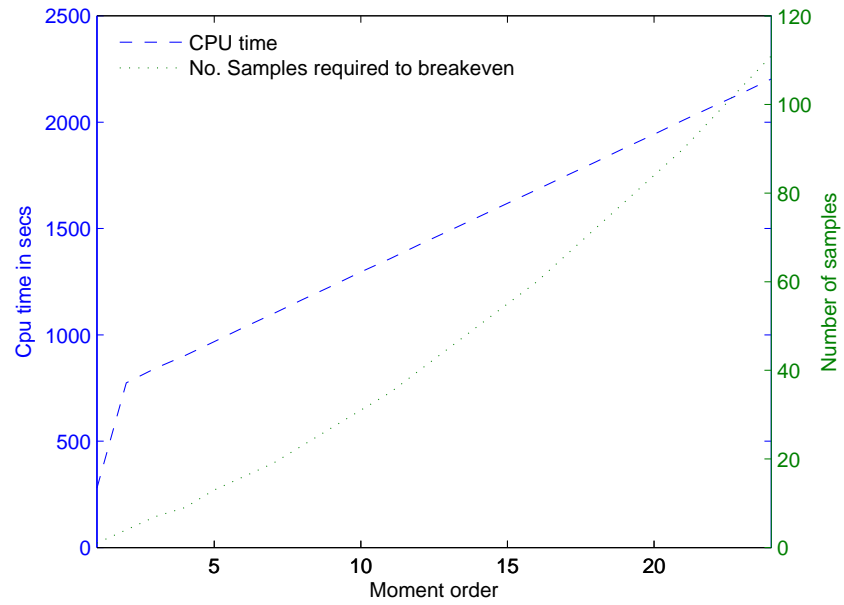


(b) Loss of orthogonality of the WCAWE moments over iteration process - $\|I - M^H M\|_2$.

Figure 5.10: Case study 1 Part B: Single point expansion - Homogeneous square.



(a) $\sigma_{TM}(\Phi)$ RCS for a converged frequency $f = 0.5$ GHz.



(b) WCAWE CPU break-even analysis.

Figure 5.11: Case study 1 Part C: Single point expansion - Homogeneous square.

Chapter 6

Fast frequency-sweep analysis for object with frequency-dependent dielectrics

“Science... never solves a problem without creating ten more.”

George Bernard Shaw

In this chapter, an extension of the WCAWE to account for frequency-dependent dielectric properties in a fast-frequency analysis is formulated. In particular, the variation in the dielectric properties of the lanthanum substituted barium titanate microwave ceramic $\text{Ba}_x\text{La}_4\text{Ti}_{2+x}\text{O}_{12+3x}$ in the sub 1 GHz frequency range is investigated for various values of x in a frequency-sweep analysis. This ceramic is chosen because it displays a marked variation in its dielectric properties with frequency.

6.1 Frequency dependence of the dielectric properties

Frequency-dependent dielectric variations will occur in all material and typically follow a decrease in the real and complex part of the permittivity as the frequency increases. As discussed in [74, 75], there are several regimes in which the dielectric permittivity is changing. This is due to the fact, that at frequencies approaching 1 GHz and above, the molecules of a material can no longer rotate fast enough to remain in phase with the applied field [74, 75]. Consequently, the contribution of the molecular polarization to the net polarisation declines, which causes a decrease in the dielectric permittivity as the applied field frequency increases.

Over the past decade, much research has been carried out on the electromagnetic characterisation of materials over different frequency ranges [76–78]. Propagation of ultrawideband signals through wall and floors has been the main

focus of the current research. Work described in [76–80] has tabulated the electromagnetic properties of various materials, in particular the complex dielectric constants recorded using experimental techniques and their variation against frequency.

To date, no research has applied MOR to problems examining the wave scattering from a lossy dielectric object with complex permittivity which varies with frequency, using the EFIE formulations. In particular, the importance of the contribution of frequency dependence of these dielectric constants in the accuracy of a MOR frequency sweep analysis has not been researched.

For a lossy dielectric, the matrix element for the impedance matrix using the circle-cell approximation in Section 3.6.1 is given by

$$Z_{i,j} = \frac{\eta\pi a_i}{2} J_1(k_b a_i) H_0^{(2)}(k_b |\mathbf{r}_i - \mathbf{r}_j|) \quad i \neq j \quad (6.1)$$

and

$$Z_{i,j} = \frac{\eta\pi a_i}{2} H_1^{(2)}(k_b a_i) - \frac{j\eta\epsilon_c}{k_b(\epsilon_c - \epsilon_0)} \quad i = j \quad (6.2)$$

The complex permittivity is given by [29,81]

$$\epsilon_c(\omega) = \epsilon' - j\frac{\sigma}{2\pi f} = \epsilon' - j\epsilon'' \quad (6.3)$$

while the real permittivity is given by $\epsilon' = \epsilon_r \epsilon_0$, with ϵ_r being the relative permittivity constant. The real part determines the ability of a material to transmit an electric field and is determined by the ability of a material to polarise in response to the field. The imaginary part of the complex permittivity, ϵ'' , represents all the dielectric loss of the medium [29,81]. In dielectric materials, this loss can be attributed to defects, space charge formation and lattice distortions in the material which can produce an absorption current. A measure of the power loss in the medium is given by the ratio [29,81]

$$\tan \delta_c = \frac{\epsilon''}{\epsilon'} \cong \frac{\sigma}{2\pi f \epsilon'} \quad (6.4)$$

where δ_c is the loss angle. Both the real and imaginary parts are functions of frequency and are in fact related to each other by the Kramers-Kronig relation [82–84]

$$\epsilon'(\omega) = \frac{1}{\pi} \mathcal{P} \int_{-\infty}^{\infty} \frac{\epsilon''(\omega_1)}{\omega_1 - \omega} d\omega_1 \quad (6.5)$$

$$\epsilon''(\omega) = -\frac{1}{\pi} \mathcal{P} \int_{-\infty}^{\infty} \frac{\epsilon'(\omega_1)}{\omega_1 - \omega} d\omega_1 \quad (6.6)$$

where \mathcal{P} means that the Cauchy principal value of the integral is used. The Cauchy principal value is used to exclude the singularity $\omega_1 = \omega$ from the region of integration [83,84]. The dependence of the real and imaginary parts of permittivity on frequency is clearly evident in these equations. The Kramers-Kronig relation shows that as a consequence of causality, the real part of the permittivity could be related to the Hilbert transform of the imaginary part [83,84]. Causality is the principle that the state of a system depends upon its past but not its future. It is expressed in the frequency domain as the principle that a causal response function has no poles in the closed upper half plane [83,84]. Cauchy's theorem may then be used to derive the relationship between the real and imaginary parts of such a function, as seen in the above relations.

6.2 Dielectric ceramic $\text{Ba}_x\text{La}_4\text{Ti}_{2+x}\text{O}_{12+3x}$

Dielectric ceramics are used extensively in microwave devices such as resonators and antennas. These materials are required to have high dielectric constants (ϵ') and low tangent losses ($\tan \delta$) in order to satisfy the demands of high electrical loads [79,80]. Due to the precise nature of these devices, it is essential that the frequency-dependent fluctuation of ϵ is accounted for in a frequency sweep analysis. Recently, several new microwave dielectric ceramics were reported in [80] with excellent dielectric properties that will be used as the basis for this study. In this research, the contribution of this variation in the dielectric properties of ceramics in the MHz frequency range will be investigated.

6.3 Recursive formulation of the matrix derivatives

In order to model the frequency-dependent variations in ϵ evident in Equations 6.5 and 6.6, careful consideration needs to be taken when differentiating Equations 6.1 and 6.2. To model this dependence, initially a third-order polynomial is fitted to the tabulated dielectric properties of the ceramic

$\text{Ba}_x\text{La}_4\text{Ti}_{2+x}\text{O}_{12+3x}$ listed in [80] and illustrated in Figures 6.1(a) and 6.1(b) for two distinct values of x . An analytical expression is independently fitted for both the real and imaginary permittivity of the form

$$\epsilon'(k_b) = a'k_b^3 + b'k_b^2 + c'k_b + d' \quad \text{and} \quad \epsilon''(k_b) = a''k_b^3 + b''k_b^2 + c''k_b + d'' \quad (6.7)$$

where (a', b', c', d') and (a'', b'', c'', d'') are the polynomial constants for real and imaginary permittivity in each basis cell respectively. Using Equation 6.7 and the identities Equation 5.24 and 5.25, the q^{th} derivative with respect to k of the matrix entry $Z_{i,j}(k)$, evaluated at k_b , is given by

$$Z_{i,j}^{[q]} = \frac{\eta\pi a_i}{2} \sum_{p=0}^q \binom{q}{p} J_1(k_b a_i)^{[p]} H_0^{(2)}(k_b |\mathbf{r}_i - \mathbf{r}_j|)^{[q-p]} \quad i \neq j \quad (6.8)$$

and

$$Z_{i,j}^{[q]} = \frac{\eta\pi a_i}{2} H_1^{(2)}(k_b a_i)^{[q]} - C_q \quad i = j \quad (6.9)$$

where

$$C_q = \frac{1}{k_b (\epsilon_{ci}(k_b) - \epsilon_0)} \left[(j\eta\epsilon_{ci}(k_b))^{[q]} \left[\sum_{j=1}^q \right. \right. \\ \left. \left. - \left[\sum_{p=0}^j \binom{j}{p} (k_b)^{[p]} (\epsilon_{ci}(k_b) - \epsilon_0)^{[j-p]} \right] C^{[q-j]} \right] \right]. \quad (6.10)$$

In particular

$$(j\eta\epsilon_{ci}(k_b))^{[q]} = (j\eta)^{[q]} \left((a'_i k_b^2 + b'_i k_b + c'_i)^{[q]} - j (a''_i k_b^2 + b''_i k_b + c''_i)^{[q]} \right). \quad (6.11)$$

The following recursive relation is used [72]

$$\Psi_v^{[q]} = \frac{1}{2^q} \sum_{p=0}^q (-1)^{(p+2)} \binom{q}{p} \Psi_{v-q+2p} \quad (6.12)$$

when differentiating the Bessel and Hankel functions, where $\Psi_v^{[q]}$ denotes the q^{th} derivative of $J, Y, H^{(1)}, H^{(2)}$ of order v .

6.4 Numerical results and validations

In this section, the RCS is calculated for profiles of varying contrast with the objective of validating the WCAWE Algorithm by comparison with the method of moments. The effect of the frequency-dependent variation in the dielectric properties of the ceramic $\text{Ba}_x\text{La}_4\text{Ti}_{2+x}\text{O}_{12+3x}$ for two values of x is examined in a frequency-sweep analysis using a two-dimensional volume EFIE formulation.

6.4.1 Case Study 1: Homogeneous cylinder - Medium 1

We initially consider a homogeneous cylinder of radius $r = \lambda_0/3 = 0.2m$, centred at the origin and assumed to be embedded in free space. The frequency dependent dielectric properties for this object are illustrated in Figure 6.1(a) for $x = 0$. The structure is illuminated by a TM^z wave emanating from a plane wave source. The cylinder is discretised using $m = 1020$ cells and the RCS was computed over a band of frequencies $f = 400 : 500$ MHz with 0.68 MHz increments for a monostatic setup $\phi = 0$.

Figures 6.2(a) and 6.2(b) show the RCS and associated percentage relative error obtained in comparing the MoM against the Padé via AWE with adaptive Zeta and the WCAWE for $q = 15$. To demonstrate the significant effect of the frequency dependence of the permittivity ϵ , the RCS is calculated using the MoM with an average value for the dielectric properties for $x = 0$ (Figure 6.1(a)) ($\epsilon' = 104.46$, $\tan \delta = 0.087$). This is evident in Figure 6.2(a) where this approximation results in a significant error over the entire frequency range, thereby justifying the need to account for the frequency dependence of the dielectric properties.

Although scaling reduces the ill-conditioning of the Padé coefficient matrix as discussed in Section 2.4.1, these strategies still result in significant round-off error for relatively small values of q . From Figures 6.2(a) and 6.2(b), it is clear the WCAWE outperforms the Padé via AWE with adaptive Zeta, duplicating the reference solution over the entire band of frequencies to within a 1% relative error. This is confirmed in Figure 6.3(a), where the relative residual r_q (Equation 5.30) demonstrates that each sample in the range $f = 400 : 500$ MHz has converged to a pre-specified $\text{tol}_{r_q} = 10^{-2}$.

As an indicator of the rate of convergence of the frequency points to the $\text{tol}_{r_q} = 10^{-2}$ over the iteration process, Figure 6.3(b) depicts the number of converged frequency points that has been achieved in total at each iteration. From this figure, we note that the WCAWE process results in a regular addition of converged frequency points at each iteration. Figure 6.4(a) illustrates the loss of orthogonality of a computed set of moments \mathbf{m}_n at each iteration step

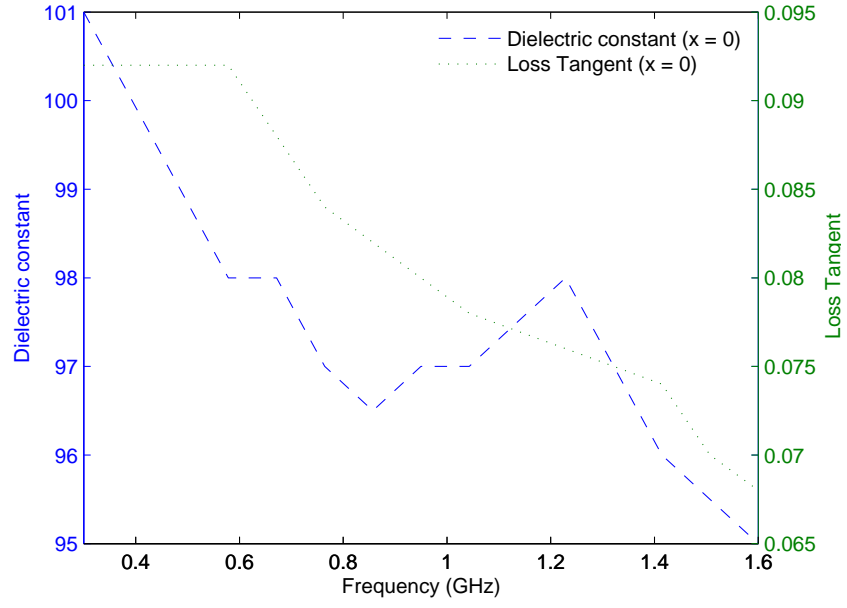
$$\|\mathbf{I}_{n \times n} - \mathbf{M}_{n \times m}^H \mathbf{M}_{m \times n}\|_2 \quad \text{for all } 1 \leq n \leq q \quad (6.13)$$

From this figure, it is clear that the computed moments remain close to machine precision, ensuring that each new moment contains additional new useful information.

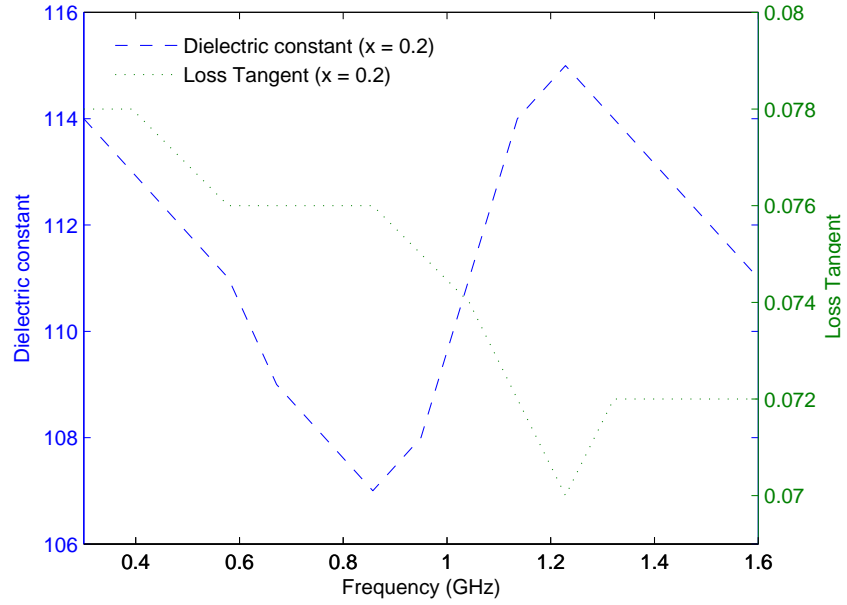
The CPU time associated with the solution of the RCS for the MoM, Padé via AWE with adaptive Zeta and WCAWE is given in Table 6.1. It is evident from this table that the WCAWE significantly decreases the computational expense associated with the direct solution of each frequency sample in a sweep analysis. Additionally, it is clear from this table that as the number of moments increases the WCAWE technique significantly outperforms the AWE in the number of frequency points that have converged to r_q . The Padé via AWE with adaptive Zeta and WCAWE CPU times are similar due to the additional times required to scale the Padé via AWE with adaptive Zeta moments. The main computational overhead is due to the generation of the derivatives and this is clearly illustrated in Figure 6.4(b). However, as the derivatives need only be calculated once, minimal computational expense is required for all subsequent solutions. Additionally, this figure indicates the number of frequency samples required to achieve a computational saving.

Legend	Technique						
	MoM	Padé via AWE with adaptive ζ			WCAWE		
Order	$m = 1020$	$q = 15$	$q = 10$	$q = 5$	$q = 15$	$q = 10$	$q = 5$
$t_m(s)$	5829	-	-	-	-	-	-
n_s	145	145	145	145	145	145	145
$t_g(s)$	-	4385	1333.2	213.2	4390	1334.9	213.23
n_m	-	113	81	33	145	113	60
$t_s(s)$	2.54	0.05	0.05	0.05	0.08	0.08	0.08
$t_t(s)$	6197.3	4392.25	1340.45	220.45	4402	1346.5	224.83
Speed-up	-	1.41	4.62	28.11	1.41	4.6	27.56

Table 6.1: CPU time analysis (Case study 1 - $f = 0.4 : 0.5$ GHz, $\lambda_0 = 0.6m$, $r = 0.2m$, $m =$ size of MoM matrix, $q =$ number of moments, $t_m =$ CPU time in seconds to generate MoM matrices for all samples, $n_s =$ number of frequency samples, $t_g =$ CPU time in seconds to generate moments, $n_m =$ number of frequency samples converged to predefined tolerance $tol_{r_q} = 10^{-2}$, $t_s =$ average CPU time in seconds to solve for RCS at each frequency, $t_t =$ total CPU time in seconds to generate and solve case study problem).

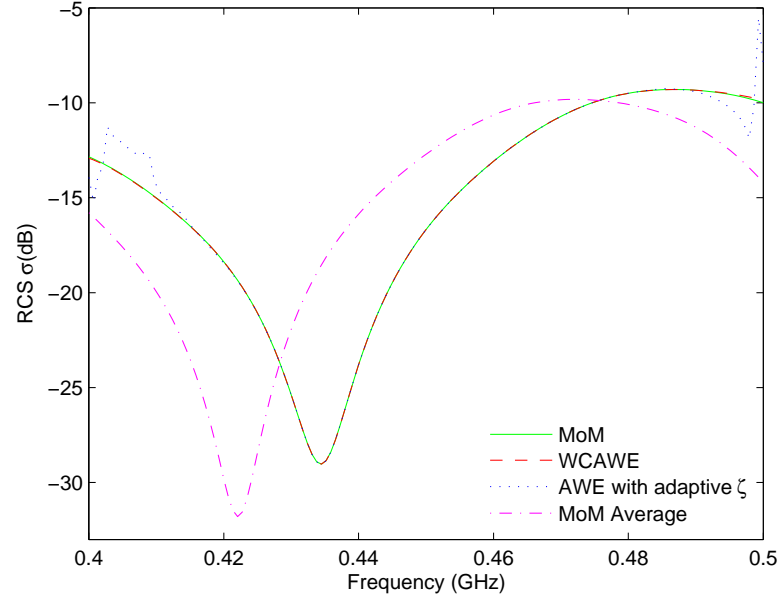


(a) Dielectric constant and loss tangent of $\text{Ba}_x\text{La}_4\text{Ti}_{2+x}\text{O}_{12+3x}$ for $x = 0.0$.

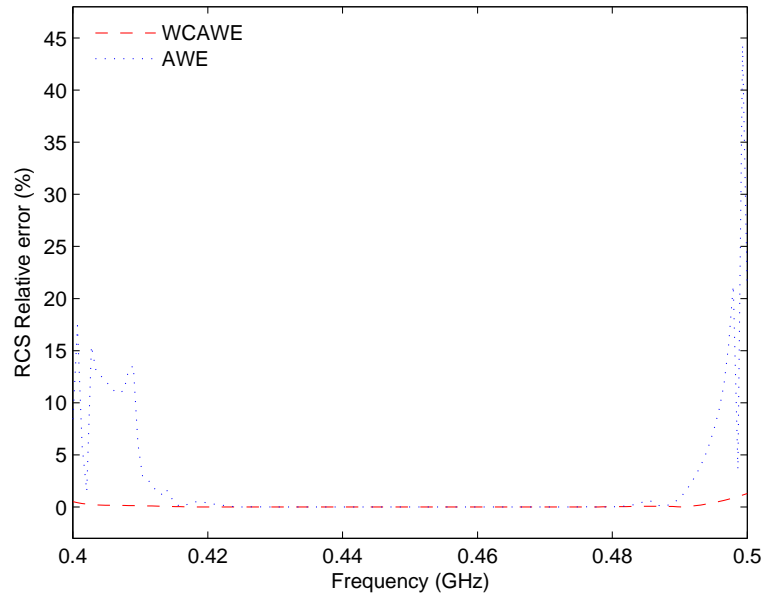


(b) Dielectric constant and loss tangent of $\text{Ba}_x\text{La}_4\text{Ti}_{2+x}\text{O}_{12+3x}$ for $x = 0.2$.

Figure 6.1: Microwave dielectric properties of $\text{Ba}_x\text{La}_4\text{Ti}_{2+x}\text{O}_{12+3x}$ as a function of frequency for two specific values of x .

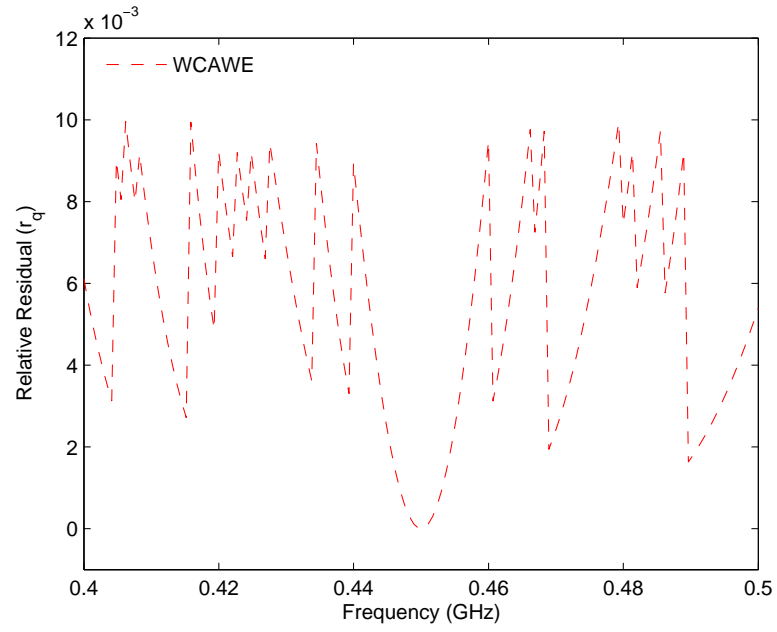


(a) $\sigma_{TM}(\Phi)$ RCS frequency sweep comparing MoM, Padé via AWE with adaptive zeta, WCAWE, and MoM using average value for dielectric constant $\epsilon' = 104.46$ and $\tan \delta = 0.087$ (Figure 6.1(a) $x = 0.0$).

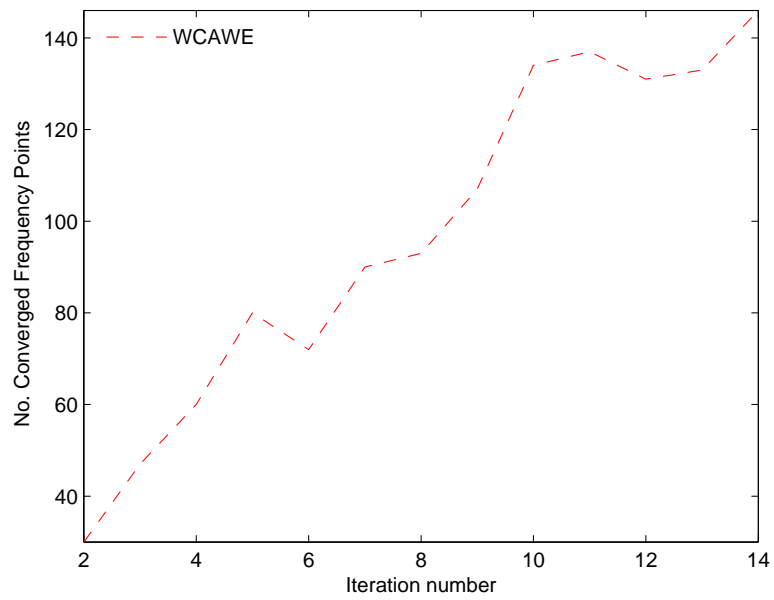


(b) Percentage relative error for Figure 6.2(a) comparing the AWE and WCAWE to the MoM solution.

Figure 6.2: Case study 1 Part A: Single point expansion - Homogeneous cylinder.

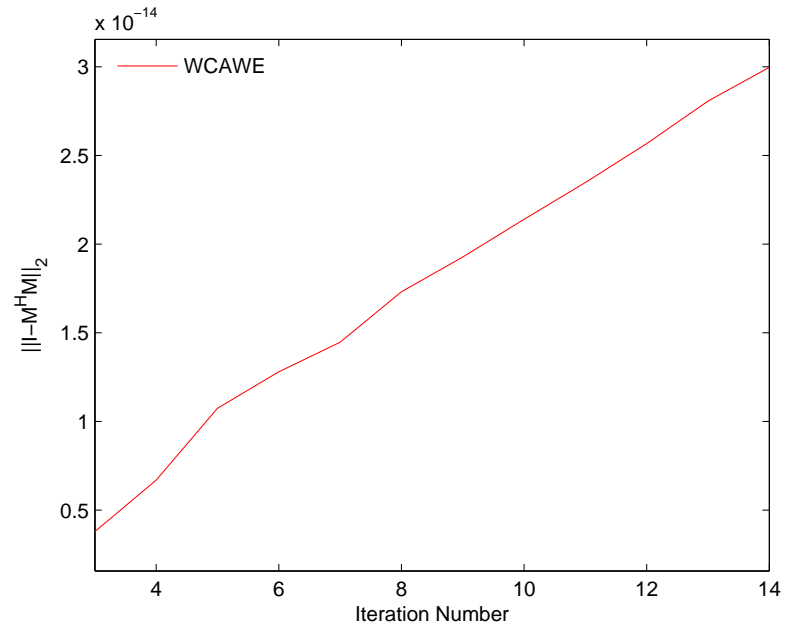


(a) Relative residual r_q for WCAWE.

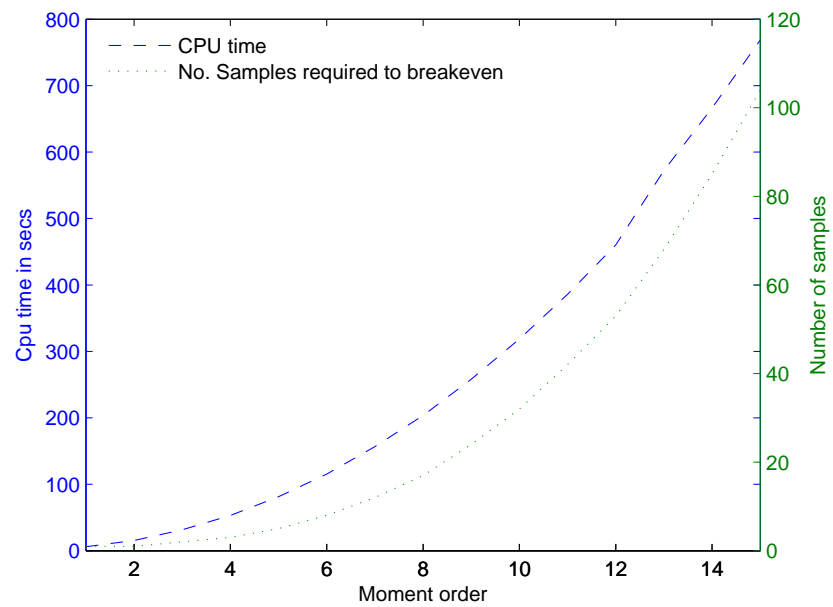


(b) Number of converged frequency points at each moment for WCAWE.

Figure 6.3: Case study 1 Part B: Single point expansion - Homogeneous cylinder.



(a) Loss of orthogonality of the WCAWE moments over iteration process - $\|I - M^H M\|_2$.



(b) CPU break-even analysis.

Figure 6.4: Case study 1 Part C: Single point expansion - Homogeneous cylinder.

6.4.2 Case Study 2: Inhomogeneous cylinder - Medium 1,2

In the second example, a similar numerical experiment is conducted for an inhomogeneous circular cylinder composed of two concentric regions centred at the origin, with radius $(r_1 = \lambda_0/3 = 0.2m, \text{medium 1}), (r_2 = \lambda_0/6, \text{medium 2})$. The cylinder is discretised using $m = 1020$ cells and the RCS was computed over a band of frequencies $f = 400 : 600$ MHz with 0.68 MHz increments for a monostatic setup $\phi = 0$.

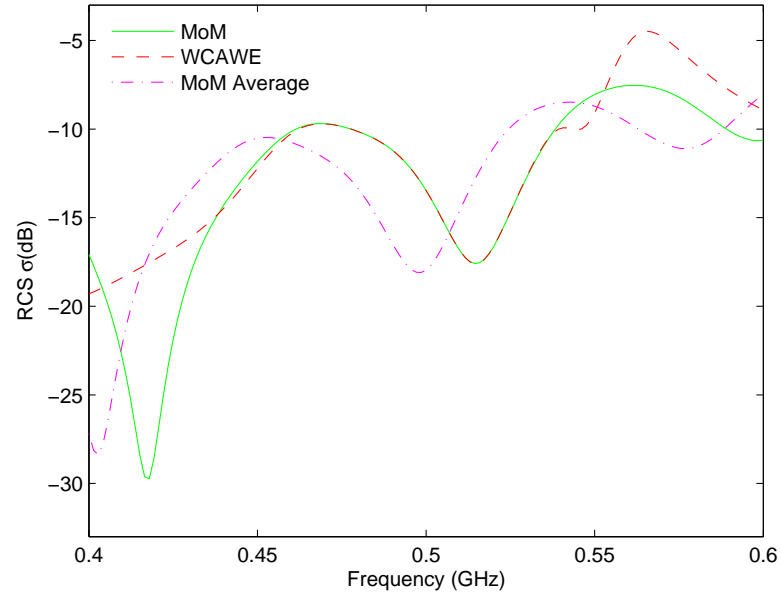
Figure 6.5(a) shows the RCS results obtained in comparing the MoM results against the WCAWE ($q = 12$) and using an average value for the dielectric properties in medium 1 and 2 with one expansion point at $\beta_0 = 500$ MHz (medium 1 - $\epsilon' = 104.46, \tan \delta = 0.087$, Figure 6.1(a) $x = 0.0$ and medium 2 - $\epsilon' = 119.43, \tan \delta = 0.079$, Figure 6.1(b) $x = 0.2$). The WCAWE algorithm duplicates the reference solution over the band of frequencies $f = 450 : 540$ MHz to within an 1% relative error and degrades thereafter. Again, we note the need to include the frequency-dependent variation of the dielectric properties in the WCAWE process. This is shown in Figure 6.5(a) where there is a significant error over the entire frequency range for the MoM solution based on the average value for the complex permittivity.

In order to achieve additional bandwidth, a MWCAWE approach must be implemented. From Figure 6.5(a), it is clear that for such an approach, we need to place two additional expansion points. These are automatically positioned at the centre of the two unconverged bands of frequency ($\beta_1, \beta_2 = 425, 574$ MHz respectively) for ($q_1 = 6, q_2 = 5$). Figures 6.5(b) indicate that the Multipoint WCAWE can provide accurate and robust fast frequency sweeps in broadband applications.

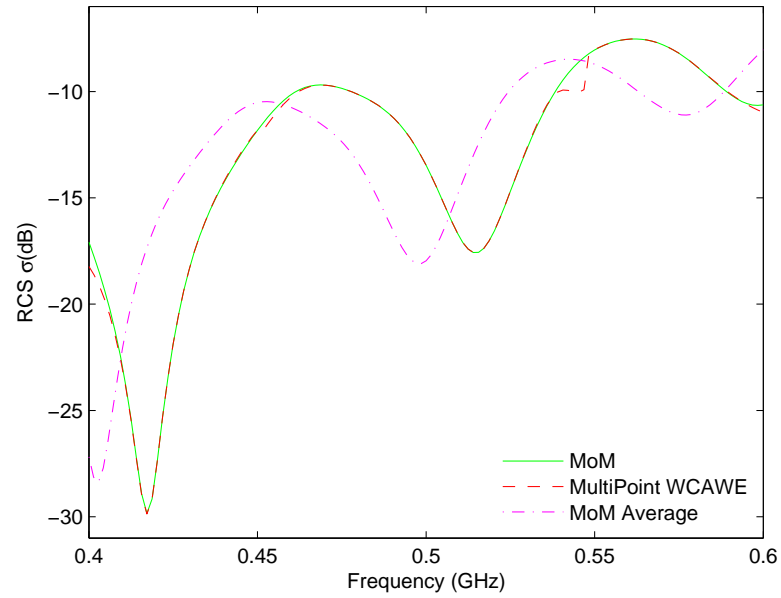
The CPU results using the WCAWE and MWCAWE are compared with the MoM direct calculation to demonstrate the efficiencies of these approaches, as shown in Table 6.2. It can be seen that using the MWCAWE is approximately 2.22 times faster while achieving within 1% relative error over the entire frequency range. Although multiple expansion points with low-order moments can significantly reduce the CPU times, it should be noted that this approach can become computationally expensive for large-scale simulations. This is due to the need to make and invert a \mathbf{Z} matrix at the expansion frequency for each new expansion point.

Legend	Technique		
	MoM	WCAWE	MWCAWE
Order	$m = 1020$	$q = 12$	$q = 12 + 6 + 5 = 23$
$t_m(s)$	5829	-	-
n_s	145	145	145
$t_g(s)$	-	2337	2768
n_m	-	66	145
$t_s(s)$	2.54	0.08	0.08
$t_t(s)$	6197.3	2348.6	2779.6
Speed-up	-	2.64	2.22

Table 6.2: CPU time analysis (Case study 2 - $f = 0.4 : 0.6$ GHz, $m =$ size of MoM matrix, $n_0 =$ number of moments, $t_m =$ CPU time in seconds to generate MoM matrices for all samples, n_s - number of frequency samples, $t_g =$ CPU time in seconds to generate moments, $n_m =$ number of frequency samples converged to predefined tolerance $\text{tol}_{r_g} = 10^{-2}$, $t_s =$ average CPU time in seconds to solve for RCS at each frequency, $t_t =$ total CPU time in seconds to generate and solve case study problem).



(a) $\sigma_{TM}(\Phi)$ RCS frequency sweep comparing MoM, WCAWE, and MoM using average value for dielectric constant - Medium 1, $\epsilon' = 104.46$ and $\tan \delta = 0.087$ (Figure 6.1(a) $x = 0.0$.) Medium 2, $\epsilon' = 119.43$ and $\tan \delta = 0.079$ (Figure 6.1(a) $x = 0.2$)



(b) Multipoint $\sigma_{TM}(\Phi)$ RCS frequency sweep using MoM, WCAWE and MoM using average value for dielectric constant ($\beta_0 = 500$ MHz $q_0 = 12$, $\beta_1 = 425$ MHz $q_1 = 6$, $\beta_2 = 574$ MHz $q_2 = 5$).

Figure 6.5: Case study 2: Multipoint expansion - Inhomogeneous cylinder.

Chapter 7

Conclusions

"I know not with what weapons World War III will be fought, but World War IV will be fought with sticks and stones."

Albert Einstein

The main focus of this work is a contribution to the development of MOR techniques for EFIE formulations for fast-sweep analysis. Although much research has been done in the area of MOR, application of these techniques to the area of the EFIE formulation has been limited. The EFIE results in difficulties when forming low-order accurate ROMs, due to the dense nature of the matrices associated with the discretisation of IEs. In particular, this property leads to several numerical difficulties, which result in an increase in the order of the ROM to generate accurate approximations. Krylov-based methods suffer from early loss of orthogonality amongst the vectors of the Krylov subspace. For AWE variants, there is a need for significantly more moments to be matched to achieve an accurate ROM over a wide bandwidth.

Fast-sweep problems are a very popular area of research with numerous applications. Of particular interest are contrast-and frequency-sweep analysis. In a fast-sweep analysis, some parameter on which the original problem depends is variable and it is required to solve this problem as the parameter changes over a desired parameter range. MOR techniques will generate ROMs that can be rapidly solved to characterise the parameter-dependent behaviour of the system over the entire parameter range.

Contrast-sweep problems are associated with scattering problems where the material properties such as the permittivity, permeability, and conductivity are varied over a range, to produce the equivalent scattered fields. There has been very limited research in the field of fast contrast-sweep problems. Much of the research has been restricted to the solution of the inverse problem through the

repeated direct simulation of the forward problem. This requires the repeated solution of the full-scattering problem for the total fields at each step in contrast. Problems associated with the repeated solution of a system over a wide bandwidth are commonplace in several areas of electromagnetics. In many areas, such as radar applications, it is necessary to determine the scattering from an object over a wide-frequency band. Since the discretised EFIE systems are frequency-dependent, this produces a nonlinear parameter dependence and restricts the use of several MOR techniques.

In Chapter 4 the Arnoldi algorithm was introduced and the procedure for generating ROMs using this algorithm was outlined for a contrast-sweep configuration. An extension of this algorithm to produce a ROM for inhomogeneous geometries using the volume EFIE formulation was formulated. Additionally, it was demonstrated that the Arnoldi algorithm can be used to efficiently solve problems involving multiple source locations.

As Chapter 4 demonstrated, the Arnoldi algorithm can produce accurate low-order approximations for a relatively low computational cost. The Arnoldi algorithm produces the ROM through the orthogonal similarity transformation, which projects the relevant variables onto a lower-order Krylov subspace. This reduced-order model representation is based on the shift-invariance property of the Arnoldi iteration. This means that the Arnoldi algorithm is applied only once for some particular choice of contrast profile matrix \mathbf{A} . Due to the shift-invariance, the resultant Arnoldi matrix can be used for a whole range of contrast profiles. The computational expense for any subsequent simulation with an alternative contrast distribution is reduced to the formation of a revised $\tilde{\mathbf{A}}$ and the inversion of a matrix of order $q \ll m$.

The approximate extension of the Arnoldi algorithm to deal with inhomogeneous structures is a consequence of the approximate subspace generated. This has been shown to be a valid approximation due to the independence of the columns of the generated orthonormal matrix, imposed by the re-orthogonalisation process. Notably, this approximation was demonstrated to produce a significant reduction in the system size for varying geometries, sizes and contrast profiles while still resulting in an accurate approximation over a wide contrast range.

Finally, a process for monitoring the linear independence of the generated Arnoldi vectors has been applied in conjunction with a relative residual in order to automate the termination of the Arnoldi iteration.

In Chapter 5, a fast frequency-sweep method for a two-dimensional volume EFIE formulation for inhomogeneous lossy dielectric objects was demonstrated, using the WCAWE approach. Additionally, this algorithm was applied to pro-

duce a ROM for three-dimensional surface EFIE formulation, to achieve fast and accurate frequency-sweep calculations of electromagnetic wave scattering from perfectly conducting three-dimensional objects.

The WCAWE method provides the flexibility needed to handle efficiently the shortcoming of the AWE with Padé; specifically, the loss of accuracy as q increases due to the explicit moment-matching process and the ill-conditioned Padé coefficient matrix. We have demonstrated that a significant reduction in the system size can be achieved while still resulting in an accurate approximation over a wide frequency range. We considered homogeneous and inhomogeneous geometries of various sizes and contrasts over a wide bandwidth and compared the RCS using the MoM with AWE and the WCAWE algorithm. Practical implementation issues were addressed, and numerical examples were given to illustrate the accuracy and robustness of the proposed methods. These examples demonstrated that the WCAWE can produce a numerically stable and robust high-order approximation from a single expansion point as compared to the Padé via AWE with adaptive zeta. It has been shown that, in order to achieve a much broader bandwidth, a multipoint approach is necessary to produce an efficient and accurate response throughout the entire bandwidth. Finally, a process for monitoring the linear independence of the generated moment vectors was applied, in conjunction with a relative residual in order to automate the multipoint approach.

The final contribution was to achieve a fast full-wave frequency-sweep analysis using the WCAWE technique for materials with frequency-dependent dielectric properties. Over the past decade, much research has been carried out on the electromagnetic characterisation of materials over different frequency ranges. Propagation of ultrawideband signals through walls and floors has been the main focus of the current research. To date, no research has applied MOR to problems examining the wave scattering from a lossy dielectric object with complex permittivity which varies with frequency, using the EFIE formulations. In particular, the importance of the contribution of frequency dependence of these dielectric constants in the accuracy of a MOR frequency sweep analysis has not been researched.

We used experimental tabulated results showing the electromagnetic properties of various materials. Specifically, the complex dielectric constants were recorded and their variation against frequency. We then applied a third-order polynomial to achieve an analytical expression for the real and imaginary permittivity independently for each material using the tabulated material constants. Using this analytical expression and a recursive derivative formulation, a fast

frequency-sweep analysis that takes account of the frequency dependence of the permittivity and conductivity parameters was achieved. Various configurations of homogeneous and inhomogeneous cylinders of differing radii and contrasts were analysed. By comparing the RCS using the MoM with an average value for the dielectric constant and the loss tangent against the frequency-dependent counterpart, the significant effect of the frequency dependence of the permittivity ϵ and conductivity σ was demonstrated.

Finally it should be noted that all numerical formulations employed in this thesis were validated against the exact Mie series solution.

7.1 Future study

Krylov space methods have been shown to be very well suited for reducing the size of linear systems. However, as with the WCAWE algorithm, more efficient and stricter error controls need to be developed to help in the termination of the iterative process.

The application of Krylov-based methods when there are nonlinear dependencies and largescale simulations is an area of research that requires significant work. One way to enhance the performance of Krylov-based model reduction could be to execute the algorithm on multiple processors. One can break the algorithm into portions that can be treated in a parallel fashion. There are at least two types of exploitable parallelism within model reduction via projection. The first is the parallelism that exists in the basic matrix operations of matrix-vector products. The second type arises from the unions of the subspaces in multipoint expansions; accordingly, the interpolation points could be distributed across the processors. These strategies could result in two levels of parallelism where the second type of parallelism could be combined with that in the basic matrix operations.

The solution of symmetric matrix systems is computationally less expensive than that of non-symmetric systems, and results in considerably lower storage costs. Non-symmetric systems can be preconditioned to produce corresponding symmetric matrix systems. The use of generating ROM, from such symmetric matrix systems, using Krylov based algorithms is an area which merits further investigation.

As with the WCAWE, the Arnoldi algorithm required some tuning to address some practical implementation issues. These include finding more robust, efficient termination schemes to find the value needed for q and creating adaptive interpolation point strategies.

In relation to the WCAWE further investigation is required to find ways to

decrease the number of moments required to achieve a wide bandwidth using a single-point analysis. This may be achieved by using the WCAWE algorithm in conjunction with other techniques such as the model-based parameter estimation approach [19]. Future work should analyse the application of WCAWE to largescale problems such as three-dimensional structures. This would require orchestrating several different approaches to make the WCAWE procedure viable, such as incorporation of sparsification techniques, iterative methods, preconditioning, higher-order basis functions and parallelisation.

Extension of the full-wave frequency-sweep analysis using the WCAWE technique to consider three-dimensional structures with frequency-dependent dielectric properties could also be investigated. Comparison of these results against experimental and ray-based techniques would be another area of worthwhile research. There is a need to understand how the dielectric material properties over a bandwidth will influence device functionality and design. Consequently, a comprehensive compilation of dielectric properties over the complete microwave range is required. This database would be valuable in designing accurate simulators that take into account the significant contribution of this frequency dependence of dielectric values.

Appendix A

Basic definitions and proofs

This Section introduces some basic definitions and proofs that are used extensively throughout this work. In particular , it shows how to produce an orthonormal basis for a subspace and gives the background to orthogonal projection techniques.

Span

Definition A.0.1. Given a collection of vectors $\mathbf{U} = \{\mathbf{u}_1, \mathbf{u}_1, \dots, \mathbf{u}_q\}$, the set of linear combinations of these vectors is a subspace and is referred to as the span of \mathbf{U} [36,85]:

$$\text{span}\{\mathbf{U}\} = \text{span}\{\mathbf{u}_1, \mathbf{u}_2, \dots, \mathbf{u}_q\} = \sum_{n=1}^q \alpha_n \mathbf{u}_n. \quad (\text{A.1})$$

Range

The range of a matrix $\mathcal{R}(\mathbf{Z})$ is defined as the span of the columns of \mathbf{Z} .

Independence

A set of vectors are linearly independent if none of them can be written as a linear combination of a finite number of many other vectors in the collection [36, 85].

Definition A.0.2. A set of vectors $\mathbf{U} = \{\mathbf{u}_1, \mathbf{u}_1, \dots, \mathbf{u}_q\}$ is linearly dependent if there exist some non-zero α_q for $1 \leq q \leq n$ such that

$$\sum_{n=1}^q \alpha_q \mathbf{u}_q = 0. \quad (\text{A.2})$$

Otherwise, the set \mathbf{U} is called linearly independent.

Basis

A basis is a set of vectors that, in a linear combination, can represent every vector in a given vector space, and such that no element of the set can be represented as a linear combination of the others [36,85]. In other words, a basis is a linearly independent spanning set.

Definition A.0.3. A basis \mathbf{U} of a subspace \mathbf{W} is a linearly independent subset of \mathbf{W} that spans \mathbf{W} .

Invariant Subspace

Definition A.0.4 ([36,44]). An invariant subspace \mathbf{W} of \mathbf{Z} satisfies $\mathbf{Z}\mathbf{u} \in \mathbf{W}$ for all $\mathbf{u} \in \mathbf{W}$.

Proposition A.0.1 ([36,44]). Let \mathbf{Z} be $m \times m$, let $\mathbf{U} = [\mathbf{u}_1, \mathbf{u}_2, \dots, \mathbf{u}_q]$ be any $m \times q$ matrix with independent columns, and let $\mathbf{W} = \text{span}(\mathbf{U})$ (the q -dimensional space spanned by the columns of \mathbf{U}). Then \mathbf{W} is an invariant subspace if and only if there is an $q \times q$ matrix \mathbf{H} such that $\mathbf{Z}\mathbf{U} = \mathbf{U}\mathbf{H}$.

Orthogonal Basis

A set of vectors $\mathbf{U} = \{\mathbf{u}_1, \mathbf{u}_2, \dots, \mathbf{u}_q\}$ is said to be an orthogonal set if each pair of distinct vectors from the set are orthogonal, that is, if $\mathbf{u}_j^H \mathbf{u}_q = 0$ whenever $j \neq q$ [85,86].

Theorem A.0.1 (Orthogonal Basis [86]). If $\mathbf{U} = \{\mathbf{u}_1, \mathbf{u}_2, \dots, \mathbf{u}_q\}$ is an orthogonal set of nonzero vectors, then \mathbf{U} is linearly independent and hence is a basis for the subspace spanned by \mathbf{U} .

The set of vectors \mathbf{U} are said to be orthonormal if every vector of \mathbf{U} has a 2-norm equal to unity [85,86].

Orthonormal Matrix

Theorem A.0.2 ([85,86]). An $m \times n$ matrix \mathbf{U} has orthonormal columns if and only if $\mathbf{U}^H \mathbf{U} = \mathbf{I}$.

This theorem is particularly usefully when applied to square matrices. An orthonormal matrix is a square invertible matrix \mathbf{U} such that $\mathbf{U}^{-1} = \mathbf{U}^H$. A square matrix $\mathbf{U} \in \mathbb{C}^n$ is unitary if $\mathbf{U}^{-1} = \mathbf{U}^H$.

Orthonormal Projection

Theorem A.0.3 ([85, 86]). If $\{\mathbf{u}_1, \dots, \mathbf{u}_n\}$ is an orthonormal basis for a subspace \mathbf{W} , then

$$\begin{aligned}\text{proj}_{\mathbf{W}}\mathbf{z} &= (\mathbf{z} \cdot \mathbf{u}_1) \mathbf{u}_1 + (\mathbf{z} \cdot \mathbf{u}_2) \mathbf{u}_2 + \dots + (\mathbf{z} \cdot \mathbf{u}_n) \mathbf{u}_n \\ &= (\mathbf{u}_1^H \mathbf{z}) \mathbf{u}_1 + (\mathbf{u}_2^H \mathbf{z}) \mathbf{u}_2 + \dots + (\mathbf{u}_n^H \mathbf{z}) \mathbf{u}_n\end{aligned}\quad (\text{A.3})$$

If $\mathbf{U} = [\mathbf{u}_1, \dots, \mathbf{u}_n]$, then

$$\text{proj}_{\mathbf{W}}\mathbf{z} = \mathbf{U}\mathbf{U}^H\mathbf{z} \quad (\text{A.4})$$

is the orthogonal projection of a vector \mathbf{z} onto the subspace \mathbf{W} .

Similarity Transformations

Definition A.0.5 ([87]). Let \mathbf{U} be a square nonsingular matrix having the same size as a matrix \mathbf{Z} . We say that the matrices \mathbf{Z} and $\mathbf{U}^{-1}\mathbf{Z}\mathbf{U}$ are similar, and the transformation from \mathbf{Z} to $\mathbf{U}^{-1}\mathbf{Z}\mathbf{U}$ is called a similarity transformation. If \mathbf{U} is orthogonal

$$\mathbf{H} = \mathbf{U}^{-1}\mathbf{Z}\mathbf{U} = \mathbf{U}^H\mathbf{Z}\mathbf{U} \quad (\text{A.5})$$

is an orthogonal similarity transformation. Moreover, we say that the two matrices are unitarily similar if \mathbf{U} is unitary.

By using similarity transformations, it is possible to reduce a given matrix to any one of several similar, or canonical forms [36, 44, 65]. Of particular interest in this thesis is the similarity transformation to Hessenberg form. Two similar matrices share the same spectrum and the same characteristic polynomial. As described above in Theorem A.4, any similarity transformation is also a change of basis operation [65]. If \mathbf{U} is orthogonal, square and nonsingular, then $\lambda(\mathbf{Z}) = \lambda(\mathbf{H})$ and we say that \mathbf{Z} and \mathbf{H} are similar. In this context, \mathbf{U} is called an orthogonal similarity transformation and \mathbf{W} is an invariant subspace for \mathbf{Z} [36, 44].

Gram-Schmidt Process

The Gram-Schmidt process is an algorithm for producing an orthogonal or orthonormal basis for any nonzero subspace [36, 85, 86].

Example A.0.1 ([85]). Let $\mathbf{W} = \text{span}\{\mathbf{z}_1, \mathbf{z}_2, \mathbf{z}_3\}$. Construct an orthogonal basis for \mathbf{W} .

Solution. Let $\mathbf{v}_1 = \mathbf{z}_1$ and $\mathbf{W}_1 = \text{Span}\{\mathbf{z}_1\} = \text{Span}\{\mathbf{v}_1\}$. Let \mathbf{v}_2 be the vector produced by subtracting from \mathbf{z}_2 its projection onto the subspace \mathbf{W}_1 . That is, let

$$\begin{aligned}\mathbf{v}_2 &= \mathbf{z}_2 - \text{proj}_{\mathbf{W}_1} \mathbf{z}_2 \\ &= \mathbf{z}_2 - \frac{\mathbf{z}_2 \cdot \mathbf{v}_1}{\mathbf{v}_1 \cdot \mathbf{v}_1} \mathbf{v}_1\end{aligned}\tag{A.6}$$

where \mathbf{v}_2 is the component of \mathbf{z}_2 orthogonal to \mathbf{z}_1 and $\{\mathbf{v}_1, \mathbf{v}_2\}$ is an orthogonal basis for the subspace \mathbf{W}_2 spanned by \mathbf{z}_1 and \mathbf{z}_2 . Now let \mathbf{v}_3 be the vector produced by subtracting from \mathbf{z}_3 its projection onto the subspace \mathbf{W}_2 . Use the orthogonal basis $\{\mathbf{v}_1, \mathbf{v}_2\}$ to compute the projection onto \mathbf{W}_2

$$\begin{aligned}\text{proj}_{\mathbf{W}_2} \mathbf{z}_3 &= \text{Projection of } \mathbf{z}_3 \text{ onto } \mathbf{v}_1 + \text{Projection of } \mathbf{z}_3 \text{ onto } \mathbf{v}_2 \\ &= \frac{\mathbf{z}_3 \cdot \mathbf{v}_1}{\mathbf{v}_1 \cdot \mathbf{v}_1} \mathbf{v}_1 + \frac{\mathbf{z}_3 \cdot \mathbf{v}_2}{\mathbf{v}_2 \cdot \mathbf{v}_2} \mathbf{v}_2.\end{aligned}\tag{A.7}$$

Then \mathbf{v}_3 is the component of \mathbf{z}_3 orthogonal to \mathbf{W}_2 , namely

$$\mathbf{v}_3 = \mathbf{z}_3 - \text{proj}_{\mathbf{W}_2} \mathbf{z}_3.\tag{A.8}$$

See Figure A.1 [85] for a diagram of this construction. Observe that \mathbf{v}_3 is in \mathbf{W} , because \mathbf{z}_3 and $\text{proj}_{\mathbf{W}_2} \mathbf{z}_3$ are both in \mathbf{W} . Thus $\{\mathbf{v}_1, \mathbf{v}_2, \mathbf{v}_3\}$ is an orthogonal set of nonzero linear independent vectors in \mathbf{W} . Hence, by Theorem A.0.1 $\{\mathbf{v}_1, \mathbf{v}_2, \mathbf{v}_3\}$ is an orthogonal basis for \mathbf{W} . \square

The generalised Gram-Schmidt formula for producing an orthogonal basis $\{\mathbf{v}_1, \mathbf{v}_2, \dots, \mathbf{v}_q\}$ is given by

$$\mathbf{v}_q = \mathbf{z}_q - \frac{\mathbf{z}_q \cdot \mathbf{v}_1}{\mathbf{v}_1 \cdot \mathbf{v}_1} \mathbf{v}_1 - \dots - \frac{\mathbf{z}_q \cdot \mathbf{v}_{q-1}}{\mathbf{v}_{q-1} \cdot \mathbf{v}_{q-1}} \mathbf{v}_{q-1}.\tag{A.9}$$

An orthonormal basis can be constructed from this orthogonal basis by normalising \mathbf{v}_q , to form the vector $\mathbf{u}_q = \mathbf{v}_q / \|\mathbf{v}_q\|$, to obtain a vector of length 1 at each step of the construction leading to replacement of Equation A.9 with

$$\mathbf{v}_q = \mathbf{z}_q - (\mathbf{z}_q \cdot \mathbf{u}_1) \mathbf{u}_1 - \dots - (\mathbf{z}_q \cdot \mathbf{u}_{q-1}) \mathbf{u}_{q-1}.\tag{A.10}$$

This is the basis for the classical Gram-Schmidt (CGS) and modified Gram-Schmidt (MGS) orthogonalisation processes outlined in Tables A.1 and A.2, re-

spectively. These algorithms are mathematically equivalent. However, the CGS method is numerically unstable in floating point arithmetic when the columns of \mathbf{U} are nearly linearly dependent resulting in loss of orthogonality amongst the computed \mathbf{u}_n vectors. A rearrangement of the calculation in line 4 of Table A.1 results in the MGS, which yields a more stable computation. As such the MGS will be the primary orthogonalisation process used in the Arnoldi algorithm. Figure A.2 illustrates an example of the modified Gram-Schmidt process when \mathbf{Z} is 2×2 matrix.

```

for  $n = 1, \dots, q$ 
   $\mathbf{v}_n = \mathbf{z}_n$  (compute next vector spanning the subspace);
  For  $i = 2, \dots, n$ 
     $h_{i,n} = \mathbf{u}_i^H \mathbf{z}_n$  (compute projections of new vector  $\mathbf{z}_n$  onto the subspace);
     $\mathbf{v}_n = \mathbf{v}_n - h_{i,n} \mathbf{u}_i$  (subtract the projections to make  $\mathbf{v}_n$  orthogonal to the previously
  end  $i$           calculated orthonormal vectors  $\mathbf{u}_i$ );
   $h_{n,n} = \|\mathbf{v}_n\|_2$ 
  if  $h_{n,n} = 0$  Quit ( $\mathbf{v}_n$  is linearly dependent on  $\mathbf{v}_1, \mathbf{v}_2, \dots, \mathbf{v}_{n-1}$ );
   $\mathbf{u}_n = \mathbf{v}_n / h_{n,n}$  (make  $\mathbf{u}_n$  a unit vector);
end  $n$ .

```

Table A.1: The classical Gram-Schmidt (CGS) algorithm.

```

for  $n = 1, \dots, q$ 
   $\mathbf{v}_n = \mathbf{z}_n$  (compute next vector spanning the subspace);
  for  $i = 2, \dots, n$ 
     $h_{i,n} = \mathbf{u}_i^H \mathbf{v}_n$  (compute projections of new vector  $\mathbf{v}_n$  onto the subspace);
     $\mathbf{v}_n = \mathbf{v}_n - h_{i,n} \mathbf{u}_i$  (subtract the projections to make  $\mathbf{v}_n$  orthogonal to the previously
  end  $i$           calculated orthonormal vectors  $\mathbf{u}_i$ );
   $h_{n,n} = \|\mathbf{v}_n\|_2$ 
  if  $h_{n,n} = 0$  Quit ( $\mathbf{v}_n$  is linearly dependent on  $\mathbf{v}_1, \mathbf{v}_2, \dots, \mathbf{v}_{n-1}$ );
   $\mathbf{u}_n = \mathbf{v}_n / h_{n,n}$  (make  $\mathbf{u}_n$  a unit vector);
end  $n$ .

```

Table A.2: The modified Gram-Schmidt (MGS) algorithm.

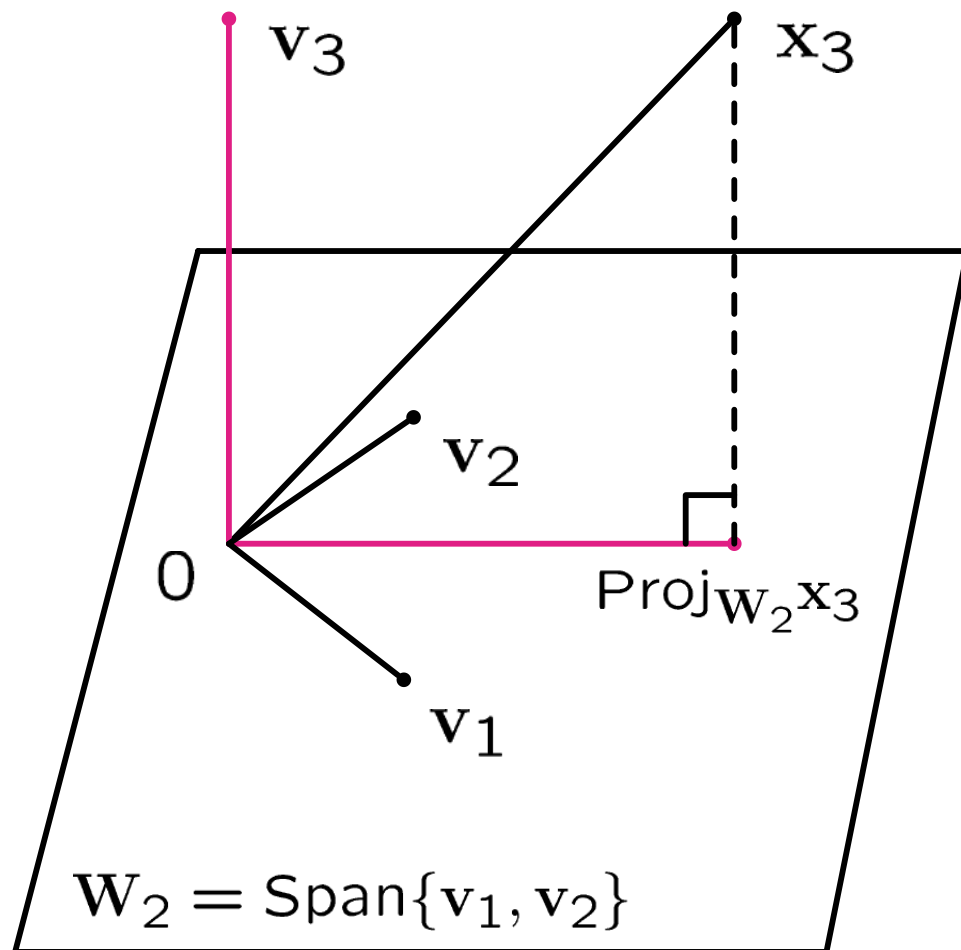


Figure A.1: Example A - The construction of \mathbf{v}_3 from \mathbf{z}_3 and W_2 .

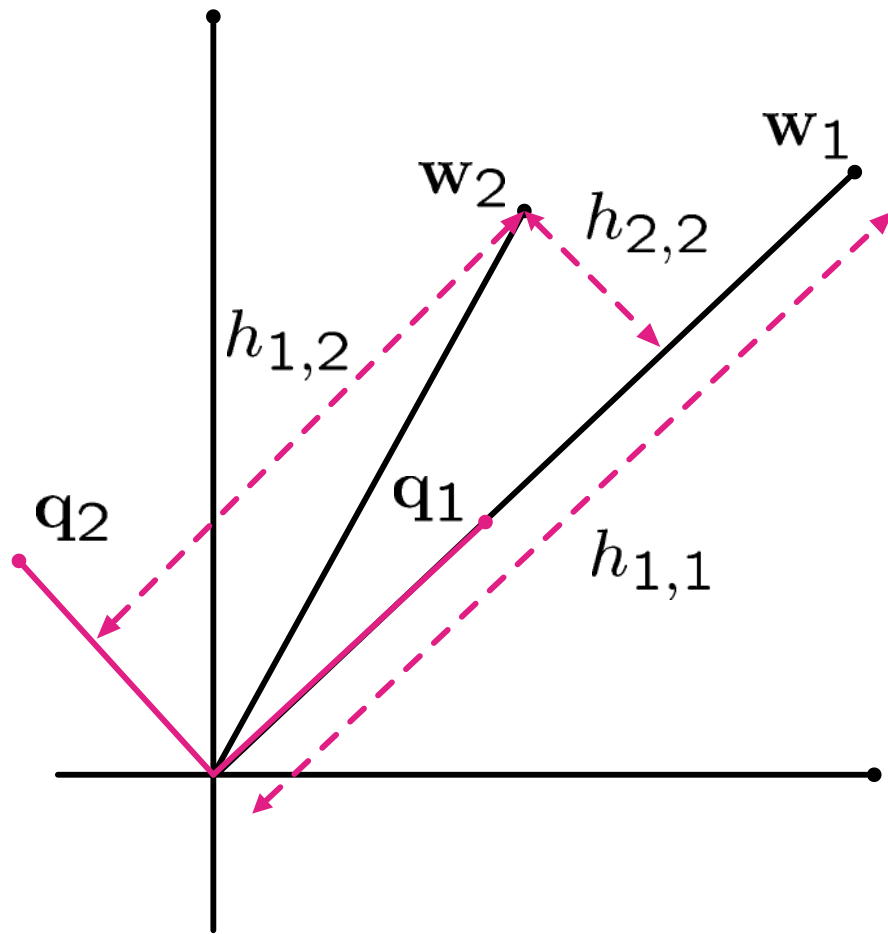


Figure A.2: Modified Gram-Schmidt when \mathbf{Z} is 2×2 matrix.

Appendix B

Acronyms

AGAWE	Alternative Galerkin Asymptotic Waveform Evaluation
AWE	Asymptotic Waveform Evaluation
CEM	Computational Electromagnetic
CG	Conjugate Gradient
CG – FFT	Conjugate Gradient - Fast Fourier Transform
CGNE – FFT	Conjugate Gradient Normal Equation - Fast Fourier Transform
CGS	classical Gram-Schmidt
EFIE	Electric Field Integral Equation
EM	Electromagnetic
ETAS	Expanded Taylor Approximation System
FEM	Finite Element Method
FDM	Finite Difference Method
FDTD	Finite-Difference Frequency Domain
FMM	Fast Multipole Method
GAWE	Galerkin Asymptotic Waveform Evaluation
GE	Gaussian Elimination
IE	Integral Equation
MBPE	Model-based parameter estimation
MGS	Arnoldi - modified Gram-Schmidt

MGSR	Arnoldi - modified Gram-Schmidt with re-orthogonalisation
MWCAWE	Multipoint Well-Conditioned Asymptotic Waveform Evaluation
MoM	Method of Moments
MOR	Model-order Reduction
ODE	Ordinary Differential Equation
PDE	Partial Differential Equation
PEC	Perfect Electric Conductor
PFFT	Precorrected Fast Fourier Transform
POD	Proper Orthogonal Decomposition
PVL	Padé via Lanczos
PVA	Projection via Arnoldi
RCS	Radar Cross Section
RF	Radio Frequency
RMM	Residual Minimising Methods
ROM	Reduced-order Model
SIE	Surface Integral Equation
SIMGS	Shift and Invert Arnoldi modified Gram-Schmidt
SPPT	Segregation by primary phase factors
TBR	Truncated Balanced Realisation
TM	Transverse Magnetic
VIE	Volume Integral Equation
WCAWE	Well-Conditioned Asymptotic Waveform Evaluation

Bibliography

- [1] C. J. Reddy, M. D. Deshpande, C. R. Cockrell, and F. B. Beck. Fast rcs computation over a frequency band using method of moments in conjunction with asymptotic waveform evaluation technique. *IEEE Trans. Antennas and Propagation*, 46(8):1229–1233, 1998.
- [2] C. J. Reddy and M. D. Deshpande. Application of awe for rcs frequency response calculations using method of moments. Technical Report 4758, National Aeronautics and Space Administration, October 1996.
- [3] Y. B. Wang and Y. M. Bo. Fast rcs computation with general asymptotic waveform evaluation. *Electromagn. Waves and Appl.*, 21:1873–1884, 2007.
- [4] N.V. Budko and R.F. Remis. Electromagnetic inversion using a reduced-order three-dimensional homogeneous model. *Inverse Problems*, 20(6):S17–S26, 2004.
- [5] R.F. Remis and N.V. Budko. A model order reduction approach to nonlinear effective inversion. In *Proc. International Conference on Electromagnetics in Advanced Applications (ICEAA 03)*, pages 695–698, Torino, Italy, September 2003.
- [6] Andreas Kirsch. *An introduction to the mathematical theory of inverse problems*. Springer-Verlag New York, Inc., New York, USA, 1996.
- [7] J. M. Jin, J. Chen, W. C. Chew, H. Gan, R. L. Magin, and P. J. Dimbylow. Computation of electromagnetic fields for high-frequency magnetic resonance imaging applications. *Phys. Med. Biol.*, 41:2719–2738, 1996.
- [8] S. Koulouridis, S. Konstantina, and S. Nikita. Study of the coupling between human head and cellular phone helical antennas. *IEEE Trans. on Electromagnetics Compatibility*, 46, 2004.
- [9] A. F. Peterson, S. L. Ray, and R. Mittra. *Computational Methods for Electromagnetics*. IEEE Press Series on Electromagnetic Wave Theory. Wiley-IEEE Press, Piscataway, New Jersey, USA, 1st edition, 1997.

- [10] R. D. Slone, R. Lee, and Jin-Fa Lee. Well-conditioned asymptotic waveform evaluation for finite elements. *IEEE Trans. Antennas and Propagation*, 51(9):2442–2447, Sep. 2003.
- [11] R. D. Slone. *Fast Frequency Sweep Model Order Reduction of Polynomial Matrix Equations Resulting from Finite Element Discretizations*. PhD thesis, Ohio State Univ., Columbus, 2002.
- [12] W. E. Arnoldi. The principle of minimized iteration in the solution of the matrix eigenproblem. *Quart. Appl. Math.*, 9:17–29, 1951.
- [13] C. Lanczos. An iteration method for the solution of the eigenvalue problem of linear differential and integral operators. *J. Res. Nat. Bur. Standards*, 45:225–280, 1950.
- [14] B. C. Moore. Principal component analysis in linear systems: controllability, observability, and model reduction. *IEEE Trans. Automatic control*, 26:17–31, 1981.
- [15] L. Sirovich. Turbulence and the dynamic of coherent structure. part 1: coherent structures. *Quart. Appl. Math.*, 45:561–571, 1987.
- [16] Joel Phillips and L. Miguel Silveira. Poor man’s tbr: A simple model reduction scheme. *IEEE Transactions on Computer-Aided Design of Integrated Circuits and Systems*, 24(1):42–55, January 2005.
- [17] G. J. Burke, E. K. Miller, S. Chakrabarti, and K. Demarest. Using model-based parameter estimation to increase the efficiency of computing electromagnetic transfer functions. *IEEE Trans. Magnetism*, 25:2807–2809, 1989.
- [18] C. J. Reddy. Application of model based parameter estimation for fast frequency response calculation of input characteristics of cavity-backed aperture antennas using hybrid fem/mom technique. Technical report, National Aeronautics and Space Administration, 1998.
- [19] E. K. Miller. Model-based parameter estimation in electromagnetics: Part 1. background and theoretical development. *IEEE Antennas Propagat. Mag.*, 40:42–52, 1998.
- [20] E. K. Miller. Model-based parameter estimation in electromagnetics: Part 3. application to em integral equations. *IEEE Antennas Propagat. Mag.*, 40:49–66, 1998.
- [21] L. T. Pillage and R. A Rohrer. Asymptotic waveform evaluation for timing analysis. *IEEE Trans. Computer-Aided Design*, 9:352–366, 1990.

- [22] B. Fasnfest, J. D. Rockway, N. J. Champagne, and R. M. Sharpe. A generalized fast frequency sweep algorithm for coupled circuit-em simulations. In *Proc. IEEE Antennas and Propagation Society International Symposium*, volume 4, pages 3944–3947, 20–25 June 2004.
- [23] J. X. Wan and C.-H. Liang. Rapid solutions of scattering from microstrip antennas using well-conditioned asymptotic waveform evaluation. In *Progress In Electromagnetics Research, PIER 49*, pages 39–52, 2004.
- [24] V. Raghavan, R. A. Rohrer, L. T. Pillage, J. E. Bracken, J. Y. Lee, and M. Alaybeyi. Awe-inspired. In *IEEE Custom Integrated Circuit Conference*, 1993.
- [25] P. Feldmann and R. W. Freund. Efficient linear circuit analysis by padé approximation via the lanczos process. *IEEE Trans. Computer-Aided Design*, 14:137–158, 1993.
- [26] A. Odabasioglu and M. Celik. Prima: Passive reduced-order interconnect macromodelling algorithm. *IEEE. Trans. Computer-Aided Design*, 17:645–654, 1998.
- [27] K. Gallivan, E. Grimme, and P. Van Dooren. Padé approximation of large-scale dynamic systems with lanczos methods. In *Proc. 33rd IEEE Conference on Decision and Control*, volume 1, pages 443–448, 14–16 Dec. 1994.
- [28] Thomas J. Klemas. *Full-wave algorithms for model order reduction and electromagnetic analysis of impedance and scattering*. PhD thesis, Massachusetts Institute of Technology. Dept. of Electrical Engineering and Computer Science, Boston, Ma, USA, 2005.
- [29] C. A. Balanis. *Advanced Engineering Electromagnetic*. John Wiley & sons, Inc., New York, USA, 1989.
- [30] O. Axelsson. *Iterative Solution Methods*. Cambridge University Press, Cambridge, 1996.
- [31] Y. Saad. *Iterative Methods for Sparse Linear Systems*. Society for Industrial and Applied Mathematics, Philadelphia, PA, USA, 2003.
- [32] Xiao-Chun Nie, Xiao-Chun Nie, Le-Wei Li, Ning Yuan, Tat Soon Yeo, and Yeow-Beng Gan. Precorrected-fft solution of the volume integral equation for 3-d inhomogeneous dielectric objects. *IEEE Trans. Antennas and Propagation*, 53(1):313–320, 2005.
- [33] J. R. Phillips, E. Chiprout, and D. D. Ling. Efficient full-wave electromagnetic analysis via model-order reduction of fast integral transforms. In *Proc. 33rd IEEE Design Automation Conf.*, pages 377–382, 3–7 June 1996.

- [34] W. C. Chew, E. Michielssen, J. M. Song, and J. M. Jin. *Fast and Efficient Algorithms in Computational Electromagnetics*. Artech House, Inc., Norwood, MA, USA, 2001.
- [35] Y. Quibo. *Electromagnetic scattering by numerical methods applicable for large structures*. PhD thesis, Electrical & Computer Engineering, University of Manitoba, 2000.
- [36] G. H Golub and C. F. Van Loan. *Matrix Computations*. Johns Hopkins University Press, Baltimore, MD, USA, 3rd edition, 1996.
- [37] T. Cwik, R. van de Geijn, and J. Patterson. Application of massively parallel computation to integral equation models of electromagnetic scattering. *J. Opt. Soc. Am. A*, 11(4), 1994.
- [38] K. D. Tatalias and J. M. Bornholdt. Mapping electromagnetic field computations to parallel processors. *IEEE Transactions on Magnetics*, 25(4):2901–2906, 1989.
- [39] O. S. Kim, P. Meincke, and O. Breinbjerg. A high-performance parallel finite element code for large-scale structural analysis based on domain-wise multifrontal technique. In *Conference on High Performance Networking and Computing IEEE Computer Society*, 2003.
- [40] O. Ergul, T. Malas, and L. Gurel. Solution of extremely large integral-equation problems. In *Proc. Int. Conf. on Electromagnetics in Advanced Applications (ICEAA 07)*, pages 970–973, 2007.
- [41] Soon Jae. Kwon, Kai Du, and Raj Mittra. Characteristic basis function method: A numerical efficient technique for analyzing microwave and rf circuits. *Microwave and Optical Technology Letter*, 38(6):444–448, 2003.
- [42] O. S. Kim, E. Jorgensen, P. Meincke, and O. Breinbjerg. Higher-order vsie-mom formulation for scattering by composite metallic and dielectric objects. In *URSI Int. Symp. on Electromagnetic Theory*, 2004.
- [43] V. S. Prakash, Junho Yeo, and R. Mittra. An adaptive algorithm for fast frequency response computation of planar microwave structures. *IEEE Trans. on Microwave Theory and Techniques*, 52(3):920–926, 2004.
- [44] James W. Demmel. *Applied numerical linear algebra*. Society for Industrial and Applied Mathematics, Philadelphia, PA, USA, 1997.
- [45] James Demmel, Jack Dongarra, Axel Ruhe, and Henk van der Vorst. *Templates for the solution of algebraic eigenvalue problems: a practical guide*. Society for Industrial and Applied Mathematics, Philadelphia, PA, USA, 2000.

- [46] M. Gutknecht and M. Rozlo. By how much can residual minimization accelerate the convergence of orthogonal error methods. *Numerical Algorithms*, 27(2):189–213, June 2001.
- [47] Chia-Chi Chu, Herng-Jer Lee, and Wu-Shiung Feng. Error estimations of arnoldi-based interconnect model-order reductions. *IEICE Trans. Fundam. Electron. Commun. Comput. Sci.*, E88-A(2):533–537, 2005.
- [48] R. D. Slone, Jin-Fa Lee, and R. Lee. Multipoint galerkin asymptotic waveform evaluation. In *Proc. IEEE Antennas and Propagation Society International Symposium*, volume 4, pages 2356–2359, 16–21 July 2000.
- [49] R. D. Slone, R. Lee, and Jin-Fa Lee. Automating multipoint galerkin awe for a fem fast frequency sweep. *IEEE Transactions on Magnetics*, 38(2):637–640, March 2002.
- [50] R. D. Slone, R. Lee, and Jin-Fa Lee. Terminating the iterative process for the galerkin asymptotic waveform evaluation model order reduction technique. In *Proc. IEEE Antennas and Propagation Society International Symposium*, volume 3, pages 200–203, 8–13 July 2001.
- [51] R. D Slone, R Lee, and Jin-Fa Lee. Broadband model order reduction of polynomial matrix equations using single-point well-conditioned asymptotic waveform evaluation: derivations and theory. *International Journal for Numerical Methods in Engineering*, 58:2325–2342, 2003.
- [52] Thomas J. Klemas, Luca Daniel, and Jacob K. White. Segregation by primary phase factors: A full-wave algorithm for model order reduction. In *DAC 2005*, Anaheim, USA, June 13-17 2005.
- [53] Pieter J. Heres. *Robust and efficient Krylov subspace methods for Model Order Reduction*. PhD thesis, Eindhoven University of Technology, Eindhoven, 2005.
- [54] Tingdong Zhu, Steven L. Dvorak, and John L. Prince. Application of subspace projection approaches for reduced-order modeling of electromagnetic systems. *IEEE Trans. on Advanced Packaging*, 3:353–360, 2003.
- [55] U. Andersson. *Time-Domain Methods for the Maxwell Equations*. PhD thesis, Pennsylvania State University, 2001.
- [56] J. L. Volakis and L. C. Kempel. Electromagnetics: computational methods and considerations. *IEEE Computational Science & Engineering*, 2(1):42–57, 1995.

- [57] D. McNamara, C. Pistorius, and J. Malherbe. *Introduction to the Uniform Geometrical Theory of Diffraction*. Artech House Microwave Library, Norwood, MA, USA, 1990.
- [58] Roger F. Harrington. *Field Computation by Moment Methods*. Wiley-IEEE Press, Chichester, UK, 1993.
- [59] J. Richmond. Scattering by a dielectric cylinder of arbitrary cross section shape. *IEEE Trans. Antennas and Propagation*, 13(3):334–341, May 1965.
- [60] L. Rossi and P. J. Cullen. On the fully numerical evaluation of the linear-shape function times the 3d green’s function on a plane triangle. *IEEE Transactions on Microwave Theory and Techniques*, 47(4):398–402, 1999.
- [61] Walter Rudin. *Real and Complex Analysis*. McGraw-Hill, 3rd edition, 1986.
- [62] C.J. Reddy and D. J. Shippy. Alternative integration formulae for triangular finite elements. *International Journal For Numerical Methods In Engineering*, 17:133–139, 1981.
- [63] R. Harrington. *Time-Harmonic Electromagnetic Fields*. McGraw-Hill, New York, 1961.
- [64] D. E. Lawrence and K. Sarabandi. Acoustic and electromagnetic wave interaction: analytical formulation for acousto-electromagnetic scattering behavior of a dielectric cylinder. *IEEE Trans. Antennas and Propagation*, 49(10):1382–1392, 2001.
- [65] L. Trefethen and D. Bau. *Numerical Linear Algebra*. SIAM, Philadelphia, PA, USA, 1997.
- [66] E. J. Grimme. *Krylov Projection Methods*. PhD thesis, Coordinated-Science Laboratory, University of Illinois at Urbana-Champaign, USA, Urbana-Champaign, IL, 1997.
- [67] D.C. Sorensen. Implicitly-restarted arnoldi/lanczos methods for large scale eigenvalue calculations. In *in: D.E. Keyes, A. Sameh, V. Venkatakrishnan (Eds.), Parallel Number Alogirthm Proceedings ICASE/LaRC Workshop*, Dordrecht, 1995. Kluwer Academic Publishers.
- [68] L. Giraud, J. Langou, and M. Rozlo. On the loss of orthogonality in the gram-schmidt orthogonalization process. *Computers and Mathematics with Applications*, 50:1069–1075, 2005.
- [69] R. B. Lehoucq. *Analysis and Implementation of an Implicitly Restarted Iteration*. PhD thesis, Rice University, Houston, TX, USA, 1995.

- [70] V. Hernandez, J. E. Roman, and V. Vidal. Orthogonalization routines in slepc. Technical report, Universidad Polit cnica de Valencia, 2005.
- [71] A. Jorba and M. Zou. A software package for the numerical integration of odes by means of high-order taylor methods. *Experimental Mathematics*, 14:99, 2000.
- [72] Milton Abramowitz and Irene A. Stegun. *Handbook of Mathematical Functions with Formulas, Graphs, and Mathematical Tables*. Dover, New York, 9th edition, 1964.
- [73] R. D. Slone, R. Lee, and Jin-Fa Lee. Multipoint galerkin asymptotic waveform evaluation for model order reduction of frequency domain fem electromagnetic radiation problems. *IEEE Trans. Antennas and Propagation*, 49(10):1504–1513, 2001.
- [74] Charles Kittel. *Introduction to Solid State Physics*. Wiley, 8 edition, 2005.
- [75] Mike Golio. *The RF and Microwave Handbook*. CRC Press, Boco Raton, FL, USA, 2001.
- [76] G. I. Torgivnikov. *Dielectric properties of wood and wood-based materials*. Springer-Verlag, New York, USA, 1993.
- [77] D. Pena, R. M. Feick, H. D. Hristov, and W. Grote. Measurement and modelling of propagation losses in brock and concrete walls for the 900-mhz band. *IEEE Trans. Antennas and Propagation*, 51:31–39, 2003.
- [78] A. Muqaibel, A. Safaai-Jazi, A. Bayram, A. M. Attiya, and S. M. Riad. Ultra-wideband through-the-wall propagation. *IEE Proceedings Microwaves, Antennas and Propagation*, pages 581–588, 2005.
- [79] H. Yamada, T. Okawa, T. Tohdo, and H. Ohsa. Microwave dielectric properties of $\text{Ba}_x\text{La}_4\text{Ti}_{3+x}\text{O}_{12+3x}$ ($x=0.0-1.0$) ceramics. *Journal of the European Ceramics Society*, 26:2059–2062, 2006.
- [80] S. B. Narang, D. Kaura, and S. Bahela. Dielectric properties of lanthanum substituted barium titanate microwave ceramics. *Journal of the European Ceramics Society*, 60(25–26):3179–3182, November 2006.
- [81] D. K. Cheng. *Field and Wave Electromagnetics*. Series in Electrical Engineering. Addison-Wesley, Boston, MA, USA, 2nd edition, 1992.
- [82] R. Lovell. Application of kramers-kronig relations to the interpretation of dielectric data. *J. Phys. C: Solid State Phys.*, 7:4378–4384, 1974.

- [83] E. M. Landau, L. D. Lifshitz. *Electrodynamics of Continuous Media*. Pergamon Press, 1982.
- [84] H. M. Nussenzveig. *Causality and Dispersion Relations*. Academic Press, 1972.
- [85] David C. Lay. *Linear Algebra and Its Applications*. Addison Wesley, Boston, MA, USA, 2nd edition, 1997.
- [86] John B. Fraleigh and Raymond A. Beauregard. *Linear Algebra*. Addison Wesley, Boston, MA, USA, 3rd edition, 1995.
- [87] Alfio Quarteroni, Riccardo Sacco, and Fausto Saleri. *Numerical Mathematics (Texts in Applied Mathematics)*. Springer-Verlag, Secaucus, NJ, USA, 2006.

Publications

P. Bradley, C. Brennan, and M. Condon, "Multipoint Arnoldi model order reduction for electromagnetic wave scattering computation," 6th Intl. Conference on Computation in Electromagnetics (CEM 2006), Aachen, Germany, April 2006. - Winner Best Paper

P. Bradley, C. Brennan, and M. Condon, "Well-conditioned Asymptotic Waveform Evaluation for model order reduction of volume integral equation based wave scattering computation," China Ireland International conference on Information and Communications Technology (CIICT 2007), Dublin, Ireland, August 2007. - Winner Best Paper

P. Bradley, C. Brennan, and M. Condon, "Arnoldi model order reduction for electromagnetic wave scattering computation," International Conference on Electromagnetics in Advanced Applications (ICEAA 2007), Torino, Italy, September 2007.

P. Bradley, C. Brennan, and M. Condon, "Well-conditioned Asymptotic Waveform Evaluation for efficient computation of wave-scattering from perfectly conducting bodies," Asia-Pacific Microwave Conference (APMC 2007), Bangkok, Thailand, December 2007.

M. Mullen, P. Bradley, C. Brennan, and M. Condon, "Efficient wideband computation of radar cross section for perfectly electrically conducting objects," URSI Emerging Trends in Wireless Communications, Dublin, Ireland, April 2008.

P. Bradley, C. Brennan, and M. Condon, "Efficient wideband electromagnetic scattering computation using Well-Conditioned Asymptotic Waveform Evaluation for a lossy dielectric," IEEE Transactions on Antennas and Propagation, 2009.

Acknowledgements

The last lines of this text should be words of gratitude to all those who helped to make this thesis possible. Foremost are my supervisors Dr. Conor Brennan and Dr. Marissa Condon. Without their enthusiastic supervision, direction, ideas, support and criticism this work would not have been possible. I thank my fellow postgraduates of the RINCE Research Group, in particular John Diskin, Aubrey Dunne, Barry Kirkpatrick and Marie Mullen for their help and moral support throughout my stay in DCU. I am grateful to all my friends especially Paul denning and Paul Sheridan for standing by me in the good time and bad. Finally, I am forever indebted to my parents Christopher and Ann Bradley, my Uncle and Aunt John Conaty and Philomena Bradley, for their endless support, and never failing faith in me.

Patrick Bradley
Dublin
July 13, 2009